



JOHANNES GUTENBERG  
UNIVERSITÄT MAINZ

Dissertation zur Erlangung des akademischen Grades

**"Doktor der Naturwissenschaften"**

im Promotionsfach Chemie

am Fachbereich Chemie, Pharmazie und Geowissenschaften  
der Johannes Gutenberg-Universität Mainz

# **Thermodynamics and Kinetics of Molecular Structure Formation on Surfaces**

Vorgelegt von

**Simon Aeschlimann**

aus Rochester, USA

Mainz, den 12. Mai 2020



This thesis was supervised by [Personal data removed] and was carried out at the Institute of Physical Chemistry at the Johannes Gutenberg University Mainz from April 2017 to May 2020.

**D77** (Dissertation Johannes Gutenberg-Universität Mainz)

**Dean of the Faculty** [Personal data removed]

**1<sup>st</sup> report** [Personal data removed]  
Johannes Gutenberg University Mainz

**2<sup>nd</sup> report** [Personal data removed]  
Max Planck Institute for Polymer Research Mainz

**3<sup>rd</sup> report** [Personal data removed]  
Bielefeld University

**Submitted:** 12<sup>th</sup> May 2020

**Oral examination:** 22<sup>nd</sup> June 2020

*To my Mother*

# Abstract

In Nature, self-assembly can be observed at various scales from microscopic ensembles up to large cosmic systems like galaxies. In particular, molecular self-assembly plays a key role in many pivotal microscopic processes of living organisms and is, therefore, seen as a crucial aspect in the field of biology. Furthermore, controlling molecular self-assembly on surfaces is regarded as a promising bottom-up approach for the fabrication of future nanodevices in the field of catalysis, sensor technology and microelectronics. One of the high aims for this next generation nanotechnology is to manipulate and store information on even smaller length scales, ultimately reaching the single molecular limit. However, achieving a satisfactory control over molecular structure formation still remains a great challenge.

In this work, an attempt is made to develop novel and generally applicable concepts to control and increase the variety of molecular structure formation on surfaces. Thermodynamics is used to describe the here examined model systems. This fundamental approach opens up the possibility to elucidate and understand the general design principles that govern the here examined systems.

As part of this effort, the impact of the nature of the substrate on the formation of molecular sub-monolayers is investigated. More specifically, substrates with different electronic structures, *i.e.*, both metallic as well as dielectric materials, are studied in detail. With the help of high-resolution scanning probe microscopy, the structure formation of adsorbates is examined and, combined with state-of-the-art density functional theory, insights on an atomic level are gained.

In the first part of this work, strategies to predict and control the thermodynamically most favorable molecular structure at constant temperature are discussed. Therefore, experiments were carried out at sufficiently high temperature, allowing the molecules to diffuse and reach their equilibrium position. Well-applicable concepts are presented to tailor the subtle balance between the molecule-molecule and molecule-surface interactions and, hence, to steer the mesoscopic structure. Moreover, the first successful demonstration of stable anchoring single molecules on a bulk insulator surface at room temperature is reported.

In the second part of this work, structural transitions of adsorbates as a function of well-defined temperature changes (heating and cooling) are observed. Examples for reversible as well as non-reversible two-dimensional structure transitions are illustrated. In this regard, the formation of kinetically trapped structures and strategies to overcome the activation barrier are addressed. Besides such a kinetically driven structural transition, a transition can also be induced by a change of the thermodynamically favored structure upon varying the temperature. The latter structural change is known as a thermally induced phase transition. The challenging interplay between kinetics and thermodynamics is analyzed to unravel the fundamental driving forces responsible for these two conceptually different structural transitions. Most interesting, a system of molecules adsorbed on a surface is presented that shows evidence of the rare and counterintuitive case of an inverse transition, the transition of an ordered phase into an unordered, mobile phase upon cooling.

As such, this work provides new insights regarding a microscopic description of molecular structure formation on surfaces and contributes towards developing general design strategies to control the formation of molecular nanostructures.

# Zusammenfassung

In der Natur kann das Prinzip von Selbstorganisation in verschiedenen Größenordnungen, von mikroskopischen Ensembles bis hin zu großen kosmischen Systemen wie Galaxien, beobachtet werden. Insbesondere die Selbstorganisation von Molekülen spielt eine Schlüsselrolle in vielen zentralen mikroskopischen Prozessen lebender Organismen und wird daher als ein entscheidender Aspekt auf dem Gebiet der Biologie angesehen. Darüber hinaus wird die Kontrolle von molekularer Selbstorganisation auf Oberflächen als vielversprechender *bottom-up* Ansatz für die Herstellung zukünftiger Nanobauelemente auf dem Gebiet der Katalyse, Sensortechnologie und Mikroelektronik angesehen. Informationen auf immer kleineren Längenskalen zu speichern und zu manipulieren, sodass die Größe elektronischer Bauelemente den Bestandteil einzelner Moleküle erreicht, entspricht dem primären Ziel im Bereich der Nanotechnologie. Die Verwirklichung einer zufriedenstellenden Kontrolle über die Bildung von Molekülstrukturen stellt die Wissenschaft weiterhin vor eine große Herausforderung.

Ziel dieser Dissertation war es, die Bildung molekularer Strukturen auf Oberflächen besser zu verstehen und allgemein anwendbare Konzepte zu entwickeln, um in Zukunft die Anzahl der Möglichkeiten zu erweitern und die Bildung der Strukturen voll umfänglich zu kontrollieren. Die Beobachtungen der in dieser Arbeit untersuchten Molekülsystemen konnten mithilfe von Konzepten der Thermodynamik beschrieben und erklärt werden. Dieser grundlegende Ansatz eröffnete die Möglichkeit, allgemeingültige Kontrollprinzipien von den hier untersuchten Modellsystemen abzuleiten.

Im Rahmen dieser Arbeit wurde der Einfluss des Substrates auf die Bildung molekularer Submonoschichten untersucht. Insbesondere wurde der Einfluss der elektronischen Struktur des Substrates anhand von metallischen und dielektrischen Modellsubstraten im Detail analysiert. Mithilfe hochauflösender Rastersondenmikroskopie wurde die Strukturbildung von Adsorbaten experimentell untersucht. Durch die hier erlangten experimentellen Resultate, kombiniert mit Modellrechnungen basierend auf der Dichtefunktionaltheorie, konnten die angestrebten neuen Erkenntnisse auf atomarer Skala gewonnen werden.

Im ersten Teil der Dissertation wurden Strategien zur Vorhersage und Steuerung der thermodynamisch günstigsten Molekülstruktur bei konstanter Temperatur entwickelt. Die Experimente wurden bei ausreichend hoher Temperatur durchgeführt, damit die Moleküle diffundieren und ihre Gleichgewichtsposition erreichen können. Geeignete Konzepte zur kontrollierten Manipulation der Molekül-Molekül und Molekül-Oberflächen Wechselwirkungen, und somit zur Steuerung der mesoskopischen Struktur, wurden vorgestellt. Darüber hinaus konnte erstmalig der Nachweis für eine erfolgreiche und stabile Verankerung einzelner Moleküle auf einer Bulk-Isolatoroberfläche bei Raumtemperatur erbracht werden.

Im zweiten Teil dieser Dissertation wurden strukturelle Transformationen von Adsorbaten in Abhängigkeit von fest definierten Temperaturänderungen (Heizen und Kühlen) betrachtet. Beispiele für reversible sowie irreversible zweidimensionale Strukturübergänge wurden detailliert beschrieben. In diesem Zusammenhang konnten die Bildung von kinetisch limitierten Strukturen, sowie Strategien zur Überwindung der Aktivierungsbarriere erläutert werden. Neben diesen kinetisch angetriebenen Strukturübergängen kann ein Übergang auch durch eine Änderung der thermodynamisch bevorzugten Struktur bei Variation der Temperatur induziert werden. Solch eine Strukturtransformation wird allgemein als thermisch induzierter Phasenübergang bezeichnet. Das komplexe Zusammenspiel von Kinetik und Thermodynamik wurde analysiert, um die grundlegenden Antriebskräfte für diese beiden konzeptionell unterschiedlichen Strukturübergänge aufdecken zu können. Als äußerst interessant erwies sich ein spezielles Molekül/Substrat System, das den seltenen und nicht intuitiven Fall der inversen Transformation, d.h. den Übergang einer geordneten Phase in eine ungeordnete mobile Phase durch Kühlen, vorweist.

Zusammengefasst wurden in dieser Arbeit eine Reihe von neuen Erkenntnissen für die mikroskopische Beschreibung von molekularen Strukturen auf Oberflächen gewonnen, die zur Entwicklung von allgemeingültigen Strategien zur kontrollierten Bildung von Nanostrukturen beitragen können.



# List of Publications

The present thesis is based on the following publications and manuscripts, which resulted from my work as a doctoral student at the Institute of Physical Chemistry, Johannes Gutenberg University Mainz, Germany. In addition, I am grateful to the *DFG fellowship* through the *Excellence Initiative by the Graduate School Materials Science in Mainz (GSC 266)* for funding the present work.

## Chapter 4:

**Simon Aeschlimann**, Lu Lyu, Benjamin Stadtmüller, Martin Aeschlimann and Angelika Kühnle, "Tailoring molecular island shapes: Influence of microscopic interaction on mesostructure", *Nano Research* **2020**, *13(3)*, 843–852

I performed the AFM experiments, analyzed the data, created the journal's back cover image and I took part in writing the first draft of the manuscript.

## Chapter 5:

**Simon Aeschlimann**, Sebastian V. Bauer, Maximilian Vogtland, Benjamin Stadtmüller, Martin Aeschlimann, Andrea Floris, Ralf Bechstein and Angelika Kühnle, "Anchoring of metal-complexing molecules on a bulk-insulator surface: Creating a regular metal array at room temperature", submitted, 2020

I performed the AFM experiments and analyzed the data. I wrote the first draft of the manuscript and created a journal cover suggestion.

## Chapter 6:

Chiara Paris, Andrea Floris, **Simon Aeschlimann**, Julia Neff, Felix Kling, Angelika Kühnle and Lev Kantorovich, "Kinetic control of molecular assembly on surfaces", *Communications Chemistry* **2018**, *1:66*

I took part in the AFM experiments, analyzed the experimental data and helped writing the first draft of the manuscript.

## Chapter 7:

**Simon Aeschlimann**, Julia Neff, Ralf Bechstein, Chiara Paris, Andrea Floris, Lev Kantorovich and Angelika Kühnle, "Focus on the Essential: Extracting the Decisive Energy Barrier of a Complex Process", *Advanced Materials Interfaces* **2019**, *1900795*

I took part in the AFM experiments. Moreover, I analyzed the experimental data, wrote a first draft of the manuscript and created the journal's inside cover image.

## **Chapter 8:**

**Simon Aeschlimann**, Lu Lyu, Sebastian Becker, Sina Mousavion, Thomas Speck, Hans-Joachim Elmers, Benjamin Stadtmüller, Martin Aeschlimann, Ralf Bechstein, Angelika Kühnle, "Mobilization upon Cooling", in preparation, 2020

I took part in the STM experiments. In addition, I performed the analysis and wrote the first draft of the manuscript.

# Contents

<b>1</b>	<b>Introduction</b>	<b>1</b>
<b>2</b>	<b>Assignment of Adsorbate/Substrate System to a Thermodynamic Ensemble</b>	<b>11</b>
<b>3</b>	<b>Methods and Experimental Set-up</b>	<b>15</b>
3.1	The Historical Path to Atomic Resolution . . . . .	15
3.2	Scanning Tunneling Microscopy (STM) . . . . .	20
3.3	Atomic Force Microscopy (AFM) . . . . .	24
3.4	Experimental Set-up . . . . .	26
<b>4</b>	<b>Tailoring molecular island shapes: Influence of microscopic interaction on mesostructure</b>	<b>29</b>
<b>5</b>	<b>Anchoring of metal-complexing molecules on a bulk-insulator surface: Creating a regular metal array at room temperature</b>	<b>41</b>
5.1	Abstract . . . . .	42
5.2	Introduction . . . . .	42
5.3	Results and Discussion . . . . .	44
5.4	Conclusion . . . . .	51
5.5	Methods . . . . .	51
5.6	Acknowledgement . . . . .	52
5.7	Supporting Information . . . . .	53
<b>6</b>	<b>Kinetic control of molecular assembly on surfaces</b>	<b>57</b>
<b>7</b>	<b>Focus on the Essential: Extracting the Decisive Energy Barrier of a Complex Process</b>	<b>87</b>
<b>8</b>	<b>Mobilization upon Cooling</b>	<b>107</b>
8.1	Abstract . . . . .	108
8.2	Main Text . . . . .	108
8.3	Acknowledgement . . . . .	116
8.4	Supporting Information . . . . .	117
<b>9</b>	<b>Conclusion and Outlook</b>	<b>119</b>

<b>Appendix</b>	<b>123</b>
<b>A Basics of Thermodynamics</b>	<b>125</b>
A.1 Introduction . . . . .	125
A.2 Macroscopic Experience of Temperature . . . . .	126
A.3 Boltzmann’s Microscopic Temperature Definition . . . . .	128
A.4 Clausius’ Entropy Concept . . . . .	132
A.5 Boltzmann’s Microscopic Entropy Definition . . . . .	134
A.6 Classification of Many-Particle Ensembles . . . . .	136
A.7 Thermodynamic Potentials . . . . .	138
A.8 Summary . . . . .	141
<b>Bibliography</b>	<b>145</b>

# Introduction

The properties of a material are governed by the structural arrangement of its atoms and molecules. A powerful method to create and control the formation of a desired structure is given by self-assembly: A process, which refers to an autonomous organization of components into patterns or structures without human intervention, only driven by thermodynamics, *i.e.*, following the goal to maximize entropy. Self-assembly can be observed in nature at various scales [1], guiding the formation of large-scale objects like galaxies, but also arranging microstructures made of molecules [2].

The concept of self-assembly has been used widely in various fields of natural and applied science from biology [3], chemistry [4], material science and physics. The possible future applications of self-assembly, including fabrication of tailored materials for optics [5], catalysis [6] and sensor technology, seem endless. Particularly, in the field of microelectronics [7, 8], molecular self-assembly is regarded as one of the most promising bottom-up approach to push the borders in miniaturization. In order to continue Moores' law and the rapid progress in information technology, there is a grand need for the fabrication of novel functional devices at molecular level. Therefore, developing new strategies to create molecular nanostructures on surfaces is of pivotal importance.

On the path to this goal, great achievements have been made in the last decades: Tremendous varieties of different nanostructures have been observed by investigating the molecular self-assembly of various atoms and organic molecules adsorbed on surfaces [9]. In the early studies, mostly adatoms and small molecules like carbon monoxide [10] have been examined. After establishing a fundamental understanding of single atoms interacting with a substrate, studies moved towards investigating the complex interactions of large molecular ensembles adsorbed on surfaces [11]. For such complex multi-particle systems, consisting of a large number of molecules adsorbed on a surface, molecular structure formation is governed by the subtle balance between molecule-molecule and molecule-substrate interactions [12–15].

The physical origin of the relevant forces for molecular structure formation is given by electromagnetic forces, mostly electrostatics [16]. Naturally, depending on the type of interaction, for example van der Waals, hydrogen, halogen and carbon

bonds, the properties of the interaction can vary a lot. While molecular bonds are by definition always attractive, electrostatic interaction as such can be either attractive or repulsive. Moreover, the different interaction types can be distinguished by their directionality and selectivity [17]. For example, metal coordination bonds and hydrogen bonds are highly directional and require a specific molecule geometry. This is in contrast to ion-ion interactions, which exhibit an isotropic character. The selectivity of an interaction type describes how compatible accessible binding partners are. Some bond types like  $\pi$ - $\pi$  interactions are mostly observed for aromatic molecules [18], while other interaction types, like van der Waals interaction, are rather unspecific.

A promising strategy to control molecular self-assembly is, thus, to use molecular building units by functionalizing the molecules with selective chemical groups or even organic precursors [19]. However, due to the large variety of different interaction mechanisms present for molecules adsorbed on surfaces [20], making reliable predictions about the adsorption structure remains a major challenge. Moreover, focusing on the use of molecular building blocks only neglects that the interactions guiding molecular self-assembly can be tuned by changing the substrate, coverage as well as temperature. These crucial aspects have been comparably rarely addressed, but bear great potential [21] for the creation of novel functional nanodevices. In view of that, the main aim of this work is to investigate the effects of varying the substrate, coverage and temperature on molecular self-assembly in order to gain a better understanding of the present microscopic interactions and to enable more realistic predictions in the future. Thus, the molecular adsorption structures on four conceptually different substrates - gold, copper, calcium fluoride and calcite - are here investigated.

The complexity of a thorough description of supramolecular self-assembly at surfaces stems from the high number of atoms and electrons involved in the formation of already small nanostructures. In equilibrium, the behavior of macroscopic physical quantities of such many-body systems is well described by thermodynamics. Therefore, in the **Appendix A**, the fundamental principles of thermodynamics, which are essential to understand the investigations discussed in this work, are summarized. The real power of thermodynamics is its universal applicability. Independent of the character of a system and its type of microscopic constituents, the laws of thermodynamics always apply. Hence, understanding thermodynamics is assumingly the major key to controlling molecular structure formation on surfaces. In **Chapter 2**, the specific adsorbate/substrate systems investigated in this work is generalized to a representative thermodynamic ensemble. The assigned ensemble forms the basis for the interpretations and discussions of the results presented in this work.

For experimentally observing the structure formation of molecules in real space

in the nanometer range, microscopes that surpass the Abbe limit of light microscopes, are needed. The invention of the scanning tunneling microscope (STM) by Binnig and Rohrer in 1981 allowed an easy access to direct topography recordings with atomic resolution for the first time in history. Five years later, the development of the atomic force microscope (AFM) enabled to examine even non-conductive substrates with high resolution. For this work, I used STM in the constant current mode and AFM in the frequency modulated mode as analyzing techniques to investigate the behavior of molecular submonolayers adsorbed on metal and bulk insulating substrates.

In **Chapter 3**, I present a short overview of the experimental set-up that was used in this work. I summarize the fundamental physical principles of scanning probe microscopy (SPM), which are necessary for understanding the here described experiments and discussions. This part is intentionally kept concise, because an extensive description of the set-up can be found elsewhere [22]. It is crucial to minimize any contaminations when observing the structure formation of submonolayers adsorbed on surfaces. Therefore, sample preparation as well as all measurements were performed under ultra-high vacuum (UHV) conditions. All UHV AFM measurements shown in this work were performed in the group at the Institute of Physical Chemistry, Johannes Gutenberg University Mainz. The here presented UHV STM measurements were carried out in collaboration with the group of Jun.-Prof. Dr. Benjamin Stadtmüller and Prof. Dr. Martin Aeschlimann at the department of Physics, TU Kaiserslautern.

This thesis is structured in the style of a cumulative work. The **Chapters 4-8** correspond to five publications written during my PhD work. These publications can be divided into two categories. The first part focuses on molecular structures on surfaces in equilibrium and the second part addresses structural transitions:

In the **first two publications** (Chapter 4 and Chapter 5), I analyze the molecular arrangement of self-assembled adsorbates at constant temperature and discuss the thermodynamically most favorable molecule adsorption structure. During the molecule sublimation process, the molecules might adsorb at various positions on the surface. Here, a sufficiently high substrate temperature is chosen so that the molecules are able to diffuse and reach their equilibrium position before starting the measurement. The focus of this part is centered on observing the effects of changing the properties of the substrate, *e.g.*, electronic structure and lattice constant, on the final structure, at various molecule coverage. For studying the impact of a systematic variation of substrate samples, I have selected dimolybdenum tetracetate (MoMo) to serve as a model adsorbate (see Fig. 1.1a). Historically seen, MoMo is of unique significance as it is regarded as a prime example for a quadruple bond between two transition metals [23].

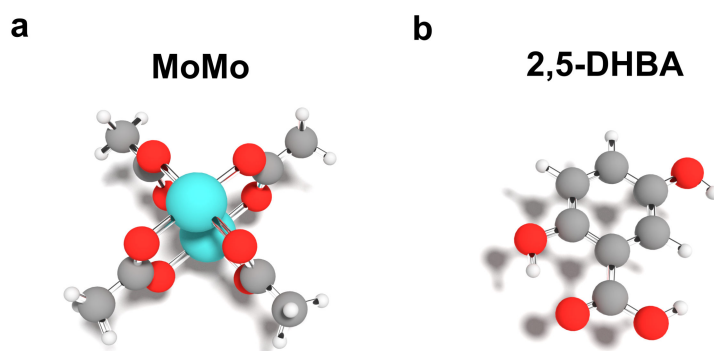


**Fig. 1.1.:** Ball-and-stick model of the two molecules studied in this work. Carbon (grey), oxygen (red), hydrogen (white) and molybdenum (cyan) atoms are indicated by their color. (a) Dimolybdenum tetraacetate (MoMo) exhibits a quadruple bond between the two molybdenum atoms. (b) The aromatic molecule 2,5-dihydroxybenzoic acid (2,5-DHBA) can interact by various ways via its benzene ring, carboxyl group (-COOH) and two hydroxyl groups (-OH).

Recently, the suitability of nanostructured surfaces as an ideal template to control molecular structure formation has been presented [24]. Motivated by this work, I demonstrate in **Chapter 4** how the mesoscopic structure can be tailored by controlling the interactions on the molecular level. More precisely, the potential to tune the molecular island shape by rationally changing the substrate lattice constant is explored. The versatility of this strategy is validated by using MoMo on three hexagonal surfaces, namely Cu(111), Au(111) and the electronically distinctively different CaF<sub>2</sub>(111) as model systems. Despite the complexity of the driving force determining the final adsorbates structure, it is shown that the mesoscopic island shape can be predicted by a simple comparison of the superstructure unit cell dimensions and the molecular bulk structure. This simple strategy can be used for tuning the mesostructure in a desired way.

In addition to the substrate crystal symmetry and lattice constant, also the electronic structure of the substrate has a decisive impact on the molecular arrangement. Metallic substrates typically exhibit a strong interaction with adsorbed molecules, due to charge transfer processes. In contrast, insulating (dielectric) substrates are typically characterized by weak molecule-surface interactions, as these systems are in general chemically poorly reactive [25]. This weak interaction hampers the simple transfer of molecular self-assembly principles developed for metal surfaces to insulators. On insulators, adsorbed molecules tend to desorb at comparatively low temperatures. Moreover, the diffusion barrier experienced by adsorbed molecules is often low, resulting in rapid movement and clustering mainly at step edges. Thus, the structure formation is often dominated by the intermolecular interactions with little possibilities to deliberately steer the structure formation by the interplay between



molecule-molecule and molecule-surface interactions. These obstacles need to be overcome as insulating substrates are beneficial for molecular nanodevices.

In the last years, first results have been presented demonstrating the formation of 1D [26–28], 2D [29, 30], 3D [31] and even more complex nanostructures [32] on insulators via self-assembly. The next step is to manipulate and store information on this nanoscale, ultimately on the single molecular limit. However, achieving this goal requires the realization of molecular assemblies of isolated molecules adsorbed in thermodynamically stable molecular configurations on surfaces at the typical device operation temperature, *i.e.*, at room temperature. So far, such assemblies were only observed on highly reactive metal surfaces for which the strong chemical molecule-surface bonding stabilizes molecular adsorption configurations as discussed above. However, the strong chemical molecule-surface bonding also severely alters the functionalities of the molecular complexes, thus, limiting their field of applications for molecular nanodevices. This unfavorable situation calls for the realization of isolated and thermodynamically stable adsorption configuration of molecular complexes on insulating surfaces at room temperature. Despite their huge potential for molecular applications, the realization of self-assembled molecular nanostructures on insulating surfaces at room temperature is still in its infancy.

In **Chapter 5**, I report the first successful demonstration of isolated and stable anchored molecules on a bulk insulator surface at room temperature. For this study, submonolayers of MoMo on calcite (10.4) were examined. Combining state-of-the-art atomic force microscopy and density functional theory calculations revealed that single molecules are thermodynamically favorable and neither diffuse nor rotate at 300 K. In conjunction with theoretical simulations, these observations are attributed to the energetically favorable adsorption position that is selected by a strong electrostatic molecule-surface interaction.

Besides the isolated molecular configuration at low coverages, the selected molecule MoMo offers the exciting opportunity to create ordered metal arrays at high coverage. Based on Boltzmann's statistical thermodynamic approach, as summarized in Appendix A, I demonstrate that this order is entropy driven. More specifically, the patterning is assigned to an interplay of surface templating and a hard-sphere repulsion of the molecules, which is conceptually different from attractive linkers as used in metal-organic frameworks [33].

As such, in Chapter 5, I demonstrate that by tailoring the molecule-surface bonding, anchoring of individual molecules on surfaces at room temperature is not limited to electric conductivity (metallic surfaces), but can be further extended towards the wide class of insulating materials. This enables new applications such as the here presented successful fabrication of an array of metal-complexing molecules at room

temperature.

In the **second part** (Chapters 6-8) of this work, I expand my investigations from static systems in equilibrium at constant temperature to structural transitions of molecules on surfaces upon well-defined changes in temperature. Using two distinctively different adsorbate model systems, the consequences of increasing the substrate temperature on the molecular adsorption arrangement are exemplarily analyzed and, subsequently, generic statements are deduced. Furthermore, these heating-induced two-dimensional structure transformations are tested on reversibility upon a subsequent cooling. Generally, a differentiation between *kinetically trapped structure transitions* and *phase transitions* are made, which are successively introduced in the following:

The driving force of kinetically trapped structure transitions cannot be described by thermodynamics in equilibrium only. A detailed understanding requires considering the interplay between thermodynamics and kinetics during the formation process. While thermodynamics describe which structure is adopted in equilibrium, kinetics characterize how quickly a transition takes place. In many cases, a simple relation discovered by Svante Arrhenius

$$\nu = \nu_0 \cdot e^{-\frac{E_a}{k_B \cdot T}} \quad (1.1)$$

is sufficient to describe the temperature dependence of a reaction rate  $\nu$ , where  $T$  is the temperature,  $k_B$  is the Boltzmann constant,  $E_a$  is the activation energy (also named energy barrier) and  $\nu_0$  is the pre-exponential factor. According to collision theory,  $\nu_0$  is the average frequency of collisions of two reacting particles [34].

When depositing molecules on metallic or insulating surfaces, sometimes, it is falsely assumed that the observed structure always equals the thermodynamically most favored structures. However, this may not always be the case as at certain conditions, less thermodynamically stable, *i.e.*, kinetically trapped structures, might be formed first. An energy barrier  $E_a$ , *e.g.*, a diffusion barrier, might prohibit a metastable state to reach the thermodynamically most favorable adsorption configuration in a typical time frame of experimental investigations. In order to distinguish both processes, the term self-organisation is generally used for describing the formation of kinetically trapped structures, and the term self-assembly defines the arrangement of structures representing the thermodynamic minimum. However, these terms are often used synonymously [17].

According to the Arrhenius equation, the transition rate  $\nu$  changes exponentially as a function of the temperature. Therefore, varying the temperature is a convenient and commonly used method in organic chemistry to control the time duration of

reactions and transitions. Upon increasing the temperature, the energy barrier of a kinetically trapped structure is overcome in a much shorter time frame, and so does the transition to a thermodynamically favorable structure occur. A kinetically trapped structure transition is considered to be an irreversible process upon changes in temperature. This is due to the fact that a subsequent cooling will not result in a reverse transition, because the system will remain in the thermodynamically favored structure (see Fig. 1.2a and b).

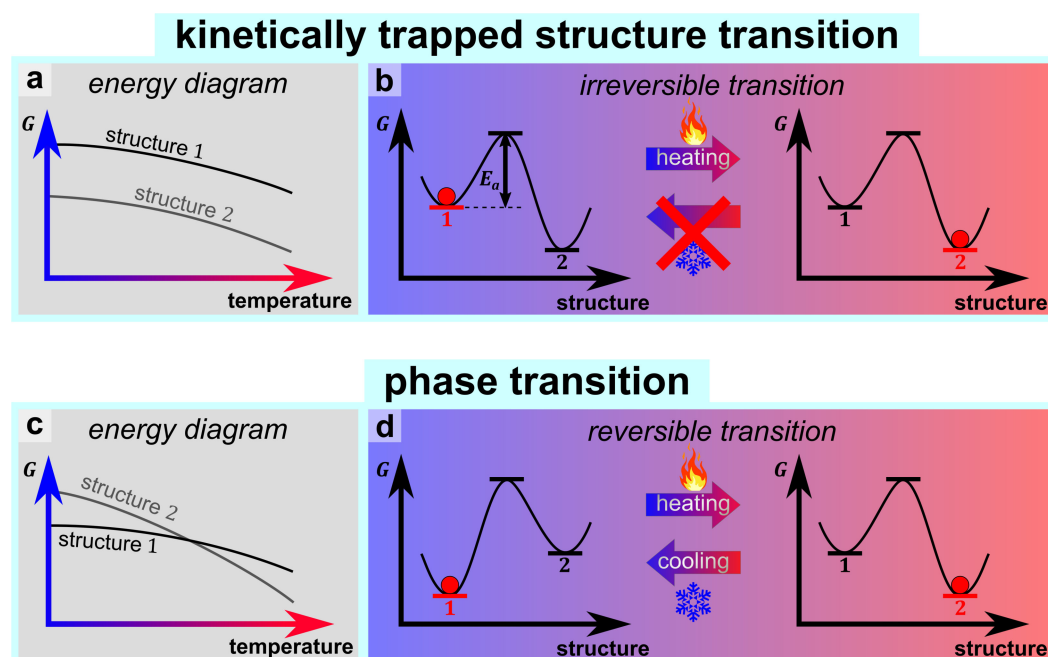


**Fig. 1.2.:** Classification of structural changes into *kinetically trapped structure transitions* and *phase transitions*. (a) Energy diagram for kinetically trapped structure transition showing a situation where structure 1 is thermodynamically unfavorable compared to structure 2. (b) At low temperature the molecules are kinetically trapped in structure 1. Upon increasing the temperature, the activation barrier  $E_a$  is overcome and a transition to the energetically favored structure 2 happens. The kinetically trapped structure transition is irreversible upon cooling, because the molecules will stay in thermodynamically favored structure 2. (c) The energy diagram for a phase transition, which exhibits a crossing point in the Gibbs energy of two different structures. At low temperature structure 1 is thermodynamically favored and at high temperature structure 2. (d) Illustration showing a reversible phase transition between structure 1 at low temperature and structure 2 at high temperature.

Using kinetics to control the formation of self-organized structures is an approach that may open up new avenues in designing functional nanomaterials. In **Chapter 6**, this general approach is transferred to on-surface molecular self-organization. A general route to create a set of metastable molecular structures on substrates is presented. Two key aspects characterize this approach: i) the preparation of an initial, metastable state of adsorbed molecules, realized immediately after the surface deposition; ii) the possibility of triggering, via a controlled heating procedure, a sequence

of structural transformations driven by kinetics rather than thermodynamics. The feasibility of this route is demonstrated using a model system of dihydroxybenzoic acid molecules (2,5-DHBA) on the (10.4) surface of calcite. 2,5-DHBA is an aromatic molecule as shown in Fig. 1.2b. The benzene ring, hydrogen groups and the carboxylic acid group of 2,5-DHBA allow for various binding possibilities with the substrate and neighboring molecules. This results in different adsorption geometries, which represent different local minima in the Gibbs energy landscape. The system was investigated by an interplay of AFM experiments and an in-depth theoretical analysis, based on Density Functional Theory (DFT). The DFT calculations were performed by Dr. Chiara Paris in the group of Prof. Dr. Andrea Floris and Prof. Dr. Lev Kantorovich at the King's College in London.

For this system, I observed a chain of structural transformations upon increasing the temperature. A major finding to understand this sequence is the system's initial state, which consists mostly of molecular dimers adsorbed on the surface. When increasing the temperature, the growth of a second network, consisting of monomers, was discovered (see Fig. 1.3). The ab-initio calculations shed light onto the atomistic details of this process, indicating that the dimer can only dissociate in the direct vicinity of a molecule network. A strategy is required for designing an experiment that allows for determining the barrier of this individual step solely. For complex processes, however, it can be very challenging to identify and unravel the individual process steps. Often, rather than addressing single steps individually, an effective barrier is obtained in the experiment, which does not allow for elucidating the atomistic mechanisms governing the process of interest.

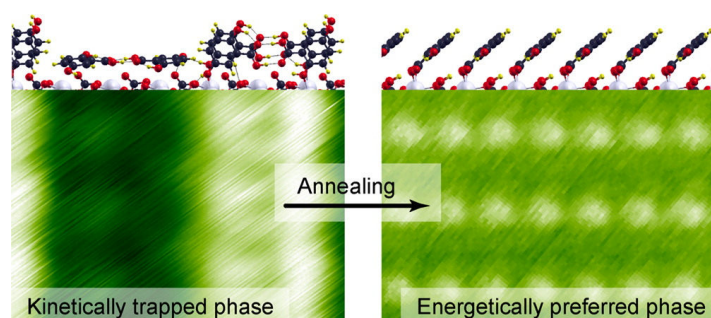


**Fig. 1.3.:** 2,5-DHBA adsorbed on calcite exhibits a kinetically trapped structure transition upon heating. When sublimating molecule dimers at low temperature, a kinetically trapped phase made up of dimers is formed. A dimer dissociation barrier prohibits the formation of monomers at low temperature. Upon increasing the temperature, a transition to an energetically preferred phase consisting of monomers happens. (Reprinted with permission from [35]. Copyright 2016 American Chemical Society.)

In **Chapter 7**, I demonstrate how the barrier of an individual step can be extracted by carefully analyzing the transition process by AFM and designing the experimental conditions such that the focus is on the dimer dissociation step solely. For

determining the barrier, I made sure to keep all factors constant that influence the reaction rate of interest. Based on this strategy, the temperature dependence of the reaction rate and, thus, the barrier of this individual transition step was obtained.

The next section of this thesis focuses on phase transitions. A phase transition describes a change of the structure representing the thermodynamic minimum upon varying the parameters like temperature and pressure. In this work, I concentrate on phase transitions induced by changes in temperature. As shown in the energy diagram in Fig. 1.2c, the Gibbs free energy  $G(T) = H - TS$  with the enthalpy  $H(T)$  and entropy  $S(T)$  of a structure is generally a function of temperature (see Appendix A). In order to observe a phase transition upon heating, the two lines, representing two different structures, have to cross in the Gibbs energy diagram. At low temperature, structure 1 is thermodynamically favored, and at high temperature a second structure 2. Hence, upon heating and passing the crossing point as shown in Fig. 1.2d, a transition to the new thermodynamically favored structure 2 will occur. Upon a subsequent cooling, the first structure is re-established, unless the second structure is kinetically trapped at low temperature. Therefore, such phase transitions may or may not be reversible.

Phase transitions are omnipresent both in nature and technology. They govern crucial processes in biology and influence our everyday life. In a conventional phase diagram, a crystalline phase melts upon increasing the temperature and upon further heating the liquid evaporates and, thus, transforms into the gas phase. In Figure 1.4, a simplified graph, indicating the Gibbs free energy for the different aggregate states, is shown. The slope of the graph,  $\partial G/\partial T$ , is given by the negative entropy,  $-S$ , of the respective phase. In many cases, it is safe to assume that the entropy of the solid is smaller than the entropy of the liquid, which is smaller than the entropy of the gas phase. This order in entropy dictates the conventional order at which different aggregate states are formed upon changing the temperature. This is why a liquid is expected to freeze into a solid upon cooling and a solid to melt into a liquid upon heating.

Already in 1903, Gustav Tammann [36] speculated about the opposite processes, namely melting upon decreasing the temperature, which is referred to „inverse melting“. So far, inverse melting has been observed for specific systems only, *e.g.* polymers and high-pressure phases [37]. In **Chapter 8**, I present an inverse transition for molecules adsorbed on a surface. When depositing MoMo onto Cu(111), a static and ordered phase forms at room temperature. Most surprising, this ordered phase dissolves upon cooling, and the molecules become mobile on the surface. In this chapter, I quantitatively analyze this unexpected phase transition and provide a possible microscopic explanation for the uncommon order of structural changes.

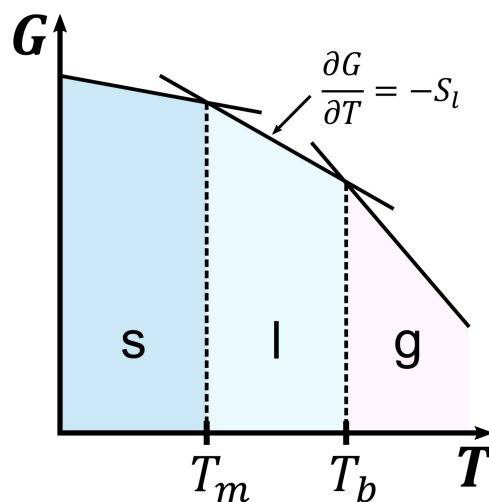


**Fig. 1.4.:** Gibbs free energy  $G$  as a function of temperature for various aggregate states. The conventional order of observed phases upon heating is solid (s), liquid (l) and gas phase (g).  $T_m$  and  $T_b$  indicate the melting and boiling temperature, respectively. Normally, the solid phase has the lowest enthalpy and accordingly lowest Gibbs free energy at low temperature. The slope of the graph  $\partial G/\partial T$ , is given by the negative entropy,  $-S$ , of the respective phase. Generally, mobile and disordered structures have a higher entropy, explaining that the gas phase is favourable at high temperatures.

Overall, in this work, I elucidate the thermodynamics and kinetics of molecular structures on surfaces as a function of changing the substrate, coverage and temperature. The here acquired findings contribute towards developing general design strategies to control the formation of molecular nanostructures. A summary of my experimental results and generic conclusions can be found in **Chapter 9**. In the **Acknowledgements**, I thank all contributors and fellow people who were involved in the making of this work.

## Assignment of Adsorbate/Substrate System to a Thermodynamic Ensemble

In this chapter, I will assign the specific heterogeneous adsorbate/substrate systems studied in this work to a representative thermodynamic ensemble. A general introduction about the classification of many-particle systems can be found in the Appendix A.6.

The focus of this thesis is centered on the investigation of molecular self-assembly on various substrates. As described in more detail in Section 3.4, all here discussed experiments were performed under ultra-high vacuum (UHV) conditions with a nearly constant base pressure of  $p_0 \leq 10^{-10}$  mbar. Molecules are sublimated onto a crystal, which serves as a substrate. Subsequently, the molecular structure formation is observed. In order to change and control the temperature, the substrate is thermally connected with a heat reservoir (see Fig. 2.1). Assuming that no molecules adsorb or desorb after the sublimation process, such a system can be described in first approximation by a canonical ensemble with movable walls. For such an ensemble the Gibbs free energy  $G$  is minimized (Appendix A.7). Considering that the pressure  $p_0$  is very small in UHV, we will show in the following that only a negligible amount of work  $W = p_0 \cdot \Delta V$  is necessary to increase the volume  $V$ .

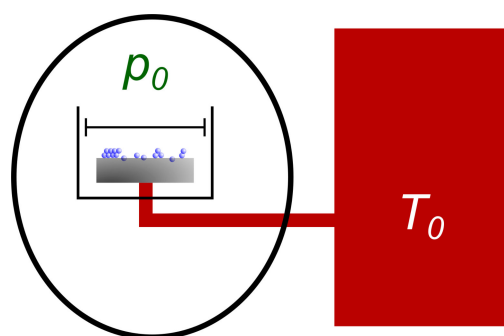


**Fig. 2.1.:** Illustration of the in this work examined adsorbate/substrate system. Molecules (blue balls) are adsorbed onto a crystal (grey rectangle) surface. This subsystem can exchange volume and entropy with a pressure and heat reservoir, respectively. The here displayed subsystem can be described by a canonical ensemble with movable walls.

From a two-dimensional point of view, the available surface for molecules adsorbed on a crystal is constrained by the substrate's borders. For this case, a two-dimensional canonical ensemble with fixed walls is sufficient to describe the experiment. Consequently, the structure with the minimal free energy  $F$  is observed in equilibrium. In the Appendix A.7, I demonstrate that the resulting physics is independent whether a two- or three-dimensional approach is considered.

It may be highly discussable to which extent the here used "canonical ensemble" model system represents a meaningful approximation of the studied adsorbate/substrate systems in this work. Next to the here considered heat exchange between the ensemble and the temperature reservoir, the adsorbate/substrate system will interact with the environment in various additional ways. For example, the ensemble might interact with local electric and magnetic fields, and even the earth's gravity may become important.

A comparison between the internal interactions present in the adsorbate/substrate system and the possible interactions with the environment of the system enables to provide a rough estimate of the interactions' influence onto the structure formation in the ensemble. In Chapter 4 and Chapter 8, I investigate molecular self-assembly on a copper crystal. The surface energy per area  $\gamma_{Cu} = 2 \text{ J/m}^2$  [38] of Cu(111) gives a first estimate of the molecule-substrate interactions present in the experiment and will be used for comparison.

For some interactions between the adsorbate/substrate system and its environment, it is simple to show that the influence can be neglected. For example, in good approximation, the influence of gravity can be neglected. This becomes obvious when comparing the Cu(111) surface energy  $\gamma_{Cu} = 2 \text{ J/m}^2$  with the energy  $W_G = m \cdot g \cdot \Delta s \approx 10^{-15} \text{ J}$ , which is needed to increase the height of one square meter of a copper monolayer ( $m \approx 10^{-7} \text{ kg}$ ) by one nanometer ( $\Delta s \approx 10^{-9} \text{ m}$ ). In an analogous way, it can be shown that further present interactions, *e.g.*, the interaction with electrical fields (UHV chamber can be regarded as a Faraday cage), are generally negligible. Since the here examined molecules MoMo and 2,5-DHBA possess no magnetic moment, the ensemble interaction with the earth's magnetic field doesn't need to be considered. Furthermore, in my experiments, surface-sensitive scanning-probe microscopy measurements ensured that during the experiments only a small number of molecules and atoms adsorb or desorb, *i.e.*, there is no noticeable particle exchange.

On the other hand, there are some substrate-environment interactions, whose influence is not immediately apparent. In this section, I have already mentioned that under UHV conditions, the work to change the volume can be neglected. Let us take a second, closer look on the work needed to expand a volume against a pressure of



$p_{Vacuum} \approx 10^{-10}$  mbar. In my experiments, a molecule monolayer adsorbed on a crystal has roughly a thickness of one nanometer,  $\Delta s \approx 10^{-9}$  m. Moreover, let us assume that due to some kind of structure transition the volume of this monolayer doubles. For a crystal with a surface area of one square meter,  $A = 1 \text{ m}^2$ , this correspond under UHV conditions to a work of  $W_{Vacuum} = p_{Vacuum} \cdot \Delta V = p_{Vacuum} \cdot A \cdot \Delta s \approx 10^{-17}$  J and is, hence, also neglectable compared to the Cu(111) surface energy  $\gamma_{Cu} = 2 \text{ J/m}^2$ . However, at standard pressure of  $p_{standard} = 1 \text{ bar}$ , the same volume expansion requires a work of  $W_{standard} \approx 10^{-4}$  J, which might has to be taken into account for an ensemble with weak intermolecular interactions.

Furthermore, in this work experiments at temperatures below room temperature are performed. As described above, for cooling, the adsorbates/substrate ensemble is in thermal contact with a reservoir at temperature  $T_0$ . In addition, the cooled sample is embedded into a UHV-chamber held at room temperature  $T_R$ . The UHV chamber interacts by thermal radiation with the sample. In our model system the UHV-chamber can be described by a second (infinite) temperature reservoir, which constantly heats the cooled sample (see Fig. 2.2a). This heating results in a temperature gradient between the sample and the cold reservoir at  $T_0$ . Consequently, this temperature gradient leads to a heat flow from the sample to the cold reservoir. Assuming that both temperature reservoirs are of infinite size, the heat flow from the warmer reservoir to the colder reservoir via the sample will continuously go on. Since the thermal radiation remains almost constant, an equilibrium between the radiant heat adsorbed by the sample and the heat flowing from the sample to the cold temperature reservoir is formed. At this equilibrium temperature  $T_S$ , there will be no net temperature change for the sample anymore. Such a steady (see Fig. 2.2b) state is named dynamic equilibrium. During the measurement, a thermometer was used to control that the temperature of the substrate remained constant during the experiment, *i.e.*, the dynamic temperature equilibrium of the sample had already been established. Following Stefan-Boltzmann's radiation law, the power radiated from a black body is directly proportional to the fourth power of the temperature  $\sim T^4$ . Therefore, the here described effect that thermal radiation builds up a temperature gradient between sample and its reservoir is accordingly largest for reservoir temperatures that deviate greatly from room temperature.

Based on these considerations, it is of no surprise that in the field of chemistry the canonic ensembles and macrocanonical ensembles (see Appendix Fig. A.4) are generally used to model the nature. For standard conditions the interaction between two systems is normally dominated by the exchange of heat, volume and particles. The influence of other interactions, *e.g.*, with the earth's gravity and external electric and magnetic field, can often be neglected. Since all here presented experiments were performed under UHV conditions, it is sufficient to focus on the exchange of heat as described by a canonical ensemble.

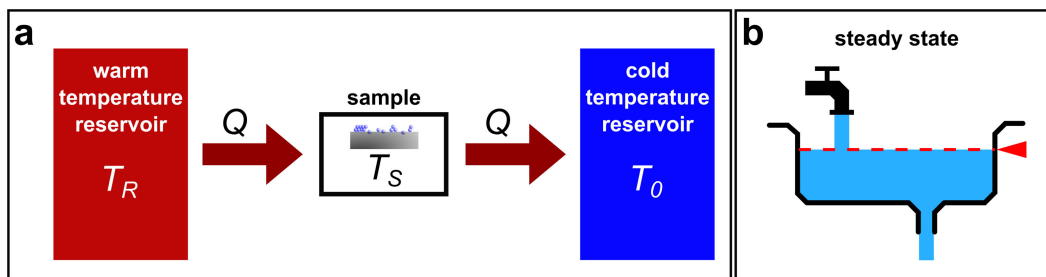


**Fig. 2.2.:** (a) A sample in thermal contact with two infinite temperature reservoirs. The left reservoir is at room temperature  $T_R$  and the right reservoir at lower temperature  $T_0$ . Heat  $Q$  flows from the warm reservoir to the sample and from the sample to the cold reservoir. The sample temperature  $T_S$  is balanced until the sample heat adsorption and output is equal (b) Steady state illustrated by a water-tap. For an equal water inflow and outflow, the water level (marked by red line) remains constant.

However, one question that not yet been fully clarified is what exactly does the term reservoir refer to in an actual experiment? In the model system canonical ensemble, the ensemble is thermally connected to a heat reservoir of comparatively large size and constant temperature  $T_0$ . However, in my actual experiment, I cool the substrate by a constant flow of liquid nitrogen or liquid helium, which is taken from a cryogenic storage dewar hold at ca. 77 K and 5 K, respectively. More precisely, the cryogen liquid cools a metallic heater. Gold wires thermally connect the heater and the sample. Applying a voltage to the metallic heater, the heater can be annealed and kept to the desired temperature  $T_0$ . So, what exactly is the reservoir? Is it only the gold wire and heater, which are actually at the desired temperature  $T_0$ ? Or does the reservoir also include the cryogenic liquid, which is probably at a much lower temperature than  $T_0$  or does the reservoir even include the power station creating the necessary electric current for the heater? As far as I know, these are still open questions. Stierstadt tries to circumvent this problem by referring to the environment of a non-isolated system as the part of the universe, which the non-isolated system exchanges a noteworthy amount of energy in a given time [39].

# Methods and Experimental Set-up

## Contents

3.1	The Historical Path to Atomic Resolution . . . . .	15
3.2	Scanning Tunneling Microscopy (STM) . . . . .	20
3.3	Atomic Force Microscopy (AFM) . . . . .	24
3.4	Experimental Set-up . . . . .	26

## 3.1 The Historical Path to Atomic Resolution

Humankind has always been interested in the structure and microscopic components of matter. In the last century, various methods to analyze the surface structure of solids have been developed. However, the path towards achieving atomic resolution of individual atoms has been long and imaging individual atoms at room temperature still remains a challenge. In the following, the milestones on this path are summarized in chronological order.

The first microscopes have been optical imaging systems. Ernst Karl Abbe noticed that with these optical methods it is nearly impossible to observe sub-wavelength structures. In 1873, he stated the well-known *Abbe limit*: Light traveling with wavelength  $\lambda$  in a medium with a refractive index  $n$  and converging to a spot with half-angle  $\theta$  will have a minimum resolvable distance of

$$d = \frac{\lambda}{2n \sin \theta} = \frac{\lambda}{2NA} \quad (3.1)$$

where the denominator  $2n \sin \theta$  is defined as the numerical aperture (NA). The human eye can roughly see in the wavelength range of 400 nm - 700 nm. Assuming an ideal numerical aperture of  $NA=1$ , no structures smaller than 200 nm can be distinguished in classical light microscopes. Compared to small molecules ( $\sim 1$  nm) or even atoms ( $\sim 0.1$  nm), this is by a factor of  $10^3$  too large. Next to the microscopes that image in real space, diffraction methods have been developed that image in reciprocal space and, thus, are subjected to another limit, the so-called Bragg condition. With the use of ultraviolet (UV) light ( $\sim 10$  nm - 400 nm) and X-rays ( $\sim 10^{-3}$  nm - 10 nm), and the invention of detectors sensitive to these light waves, atomic resolution of periodic structures was finally made possible. Nowadays,

*X*-ray diffraction [40] is commonly used to characterize the arrangement and unit cell dimensions of ordered atoms in crystals. Also, surface-sensitive methods like low-energy electron diffraction (LEED) [41–43] have been well established.

However, despite these revolutionary developments and achievements in analysis technology, examining individual molecules or atoms was still unreachable with these techniques. By means of these diffraction methods like *X*-ray diffraction and LEED, a collective signal of a large number of atoms is detected. Therefore, these analysis methods provide a very high resolution of periodic structures, but information about individual objects like defects and non-equally distributed properties are lost in the 'averaging' procedure. Methods working in real-space and not momentum-space were needed to study individual objects on the nanoscale. A major breakthrough was the invention of the transmission electron microscope (TEM) by Max Knoll and Ernst Ruska in 1931. The latter one was awarded with the Nobel prize in Physics in 1986 [44]. One of the first TEM systems is shown in Fig. 3.1a. TEM constitutes a real-space imaging method. Its mode of operation is similar to the one of light microscopes, but instead of a photon beam an electron beam is used. The electron beam is transmitted through a very thin sample, also called specimen. While passing through the specimen, the electrons can interact with the sample. Subsequently, the electron beam is projected onto an imaging device such as a fluorescent screen. Due to the small de Broglie wavelength of electrons, images with significantly higher resolution are achieved with TEM than with light microscopes. In the last decades, the set-up of TEM systems has been continuously improved and new modes like scanning TEM were developed. Nowadays, the current resolution limit of TEM is below 0.05 nm, as exemplarily shown in Fig. 3.1b for a silicon crystalline specimen observed from the [114] direction. As indicated by an image simulation displayed at the bottom of Fig. 3.1b, the shape of Si-Si dumbbells of a size of 45 pm has been resolved in the TEM image [45]. Due to the high resolution, TEM has been established to be an extremely valuable analysis method in various fields like chemistry, physics and biology. Recently, TEM images of the SARS-CoV-2 virus (see Fig. 3.1c) became well known world-wide. However, high-resolution TEM systems are expensive and therefore not easily available in common laboratories. Moreover, only very thin specimen can be investigated, limiting the applicability of TEM.

Another breakthrough was the first demonstration of the field ion microscope (FIM) by Erwin W. Müller in 1951 [48, 49]. In FIM, a sharp metal needle, named tip, is placed into a chamber and cooled to cryogenic temperatures ( $\sim 10 - 100$  K). The chamber is filled with an inert gas like helium or neon. When applying a voltage of approximately 10 kV between the tip and a cathode, gas atoms in the vicinity of the tip are ionized and, thus, repelled from the surface by the strong electric field. Collecting these repelled ions with a detector, a projection image of the surface is achieved. Already four years after the invention of the first FIM prototype, Müller

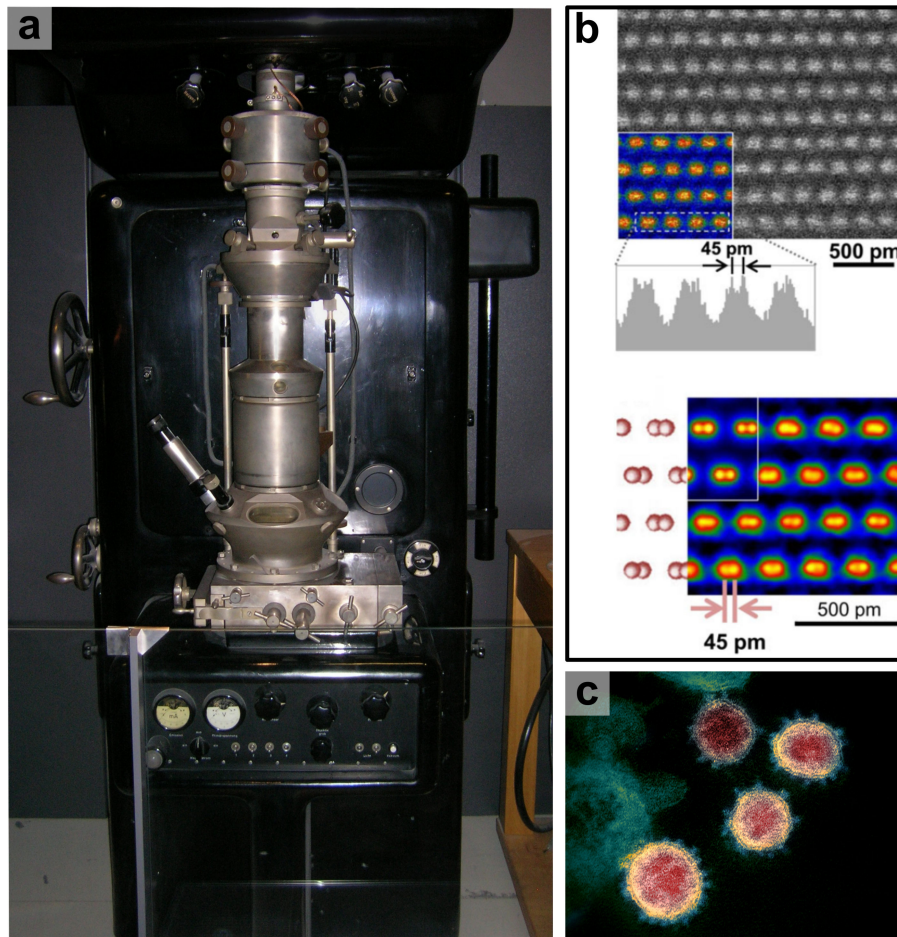


**Fig. 3.1.:** a) One of the first transmission electron microscopes (TEM) built by Ernst Ruska, originally installed at IG Farben-Werke and now on display at the Deutsches Museum in Munich, Germany (reprinted with permission from [46]). b) On the top, a scanning TEM image of a silicon specimen is shown. The specimen is observed from the [114] direction. An intensity profile of four averaged raw images is displayed in grey, indicating a double peak separated by 45 pm. These double peaks are ascribed to Si-Si dumbbells as illustrated at the bottom (adapted from [45]). c) Colorized TEM image of isolated SARS-CoV-2 virus. The crown-like spikes on the surface of the coronavirus give this virus family its name (adapted from [47]).

and his Ph.D. student, Kamnwar Bahadur have been able to resolve individual atoms on a sharp tungsten tip [49]. Intriguingly, Müller and Bahadur have been the first humans to observe individual atoms. This opened the door for a completely novel field of research [50] and led to a large amount of further FIM investigations, especially for studying surface diffusion of adatoms [51]. As described above, FIM relies on an electric-field induced ionization of inert gas atoms in the vicinity of a charged and very sharp needle. Therefore, FIM is limited to studying specific metallic materials, which can tolerate the applied high electrostatic fields, *e.g.*, tungsten or platinum.

A third milestone in depicting individual atoms was the development of the scanning tunneling microscope (STM) by Gerd Binnig and Heinrich Rohrer at IBM Zürich,

Switzerland, in 1981 [52]. An image of the first STM is shown in Fig. 3.2a. Already five years later, both inventors were awarded with the Nobel prize [53]. STM is a real-space imaging method based on the quantum effect of tunneling. A sharp metal tip (see Fig. 3.2b) is brought into the very close vicinity of a to be examined surface of a conductive sample. In the ideal case, the tip is mono-atomically sharp, *i.e.*, it has a single atom at the apex. A schematic drawing of the functionality of a STM is displayed in Fig. 3.2c. Applying a bias voltage between the tip and substrate enables electrons to tunnel through the vacuum from the tip to the surface and vice versa. The resulting electron current is the basic quantity measured in STM. As shown in the next section, the tunneling current strongly depends on the local density of electronic states (LDOS) of the substrate and the distance between the tip and sample.

Using piezo-electric crystals allows to move the tip with a precision of about 0.001 nm in all three dimensions. Monitoring the tunneling current as a function of position, while scanning with the tip across the surface, offers the possibility to display two-dimensional or even three-dimensional images of conductive surfaces with so far unprecedented space and energy resolution. Besides being a device for visualizing the local electronic topography, STM has quickly developed into being a multifunctional tool. For example, in the early 90's STM was successfully applied to manipulate single atoms, and hence, the first human-made nano-objects [58–61] were created. Moreover, using magnetic probe tips has led to spin-polarized scanning tunneling microscopy (SP-STM), which allows to study the local magnetic properties down to the atomic level [62, 63]. Consequently, the invention of the scanning tunneling microscopy is regarded to have one of the most profound influence in the field of nanoscience. C. Julian Chen has commented on this point in his introduction about STM [64]:

*"It was often said that STM is to nanotechnology what the telescope was to astronomy. Yet STM is capable of manipulating the objects it observes, to build nanoscale structures never existed in Nature. No telescope is capable of bringing Mars and Venus together."*

In order to expand these analysis techniques to the large and important field of insulating materials, in 1985, Gerd Binnig, Calvin Quate and Christoph Gerber have developed another scanning method, atomic force microscopy (AFM) [65]. This new method was inspired by the principles of STM and a stylus profilometer<sup>1</sup>. Similar to the functionality of an STM, the surface is scanned with a sharp tip, but instead of measuring an electron current, the force between surface and tip is determined. More precisely, the force between tip and sample is typically measured by monitoring the deformation of a spring, also called cantilever (see Fig. 3.2d). Therefore, AFM

<sup>1</sup>Contrary to what the younger generation might think, the stylus profilometer is not an algorithm for determining the 'coolness' and 'style' of a profile on Facebook, Twitter, Instagram, *etc.*

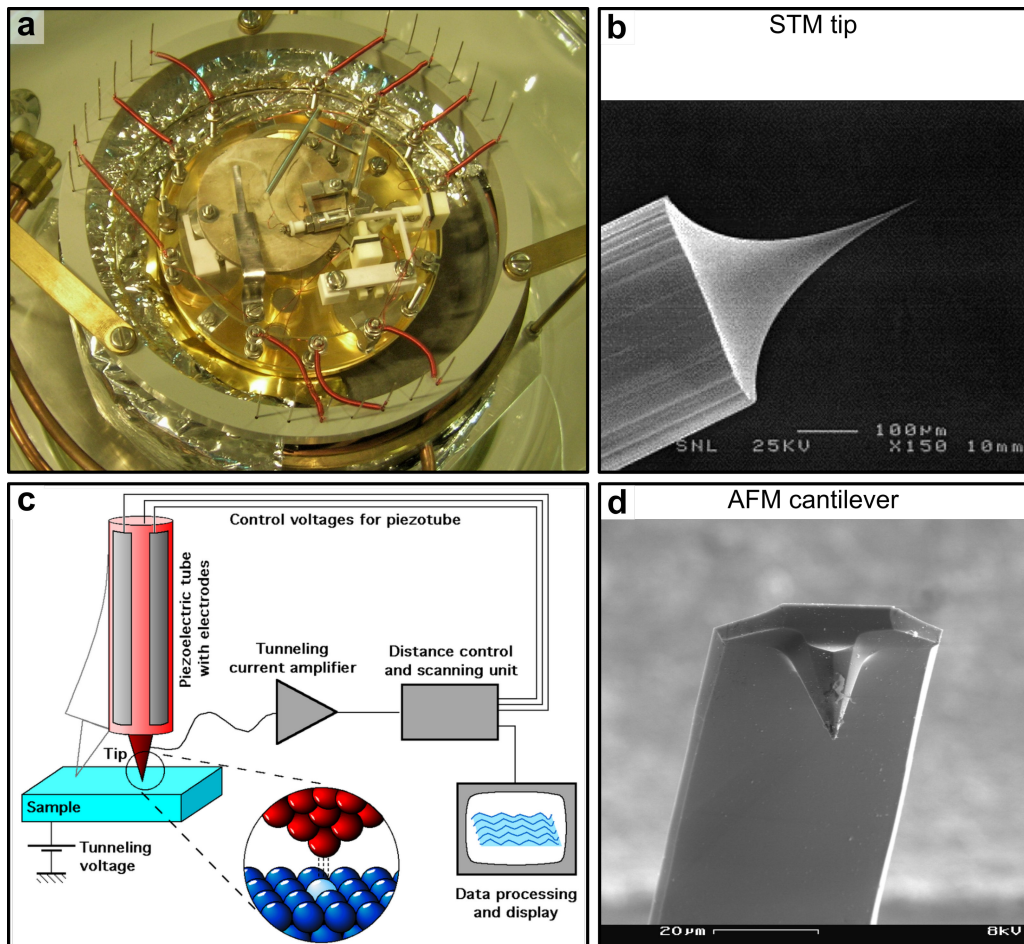


**Fig. 3.2.:** a) The first scanning tunneling microscope (STM) built by Binnig and Rohrer in 1981 at IBM Zürich and now on display at the Deutsches Museum in Munich, Germany (adapted from [54]) b) Scanning electron microscope image of an etched tungsten tip for STM measurements (adapted from [55]). c) Schematic drawing of a typical STM set-up. A voltage is applied between sample and tip. The resulting electron tunneling current provides information about the electronic structure of the sample and tip (reprinted with permission from [56]). d) Scanning electron microscope image of an AFM cantilever (adapted from [57]).

does not only allow to acquire 'force maps' with extremely high local resolution on insulating materials, but also contains different information about surface topography and structure compared to STM. While STM probes the electronic structure, AFM probes the force between tip and sample.

In this work, I present STM and AFM measurements. In the following, I will shortly explain the basic principles of STM and AFM, and introduce the experimental set-up used for my investigations.

## 3.2 Scanning Tunneling Microscopy (STM)

The basic principle of STM is the quantum-mechanical tunneling effect. In order to grasp the elementary concept, I will start by briefly discussing the fundamental theories of electrons tunneling through a potential barrier. The following description is based on the references [64, 66, 67].

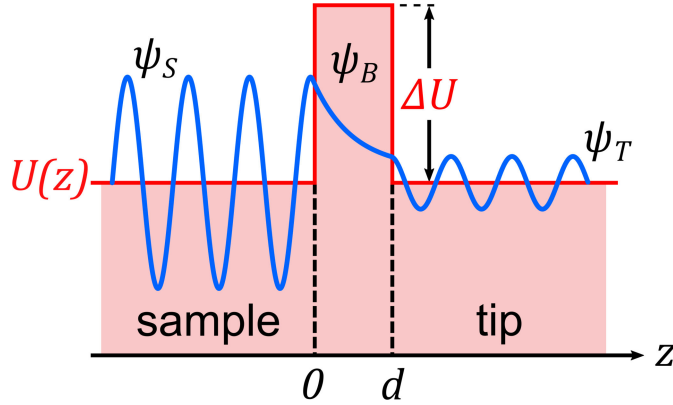


**Fig. 3.3.:** Illustration of the one-dimensional tunneling effect. In quantum physics, there is a non-zero probability of an excited electron with an energy  $E < U(0 < z \leq d)$  tunneling through a classically insuperable potential barrier  $\Delta U$ . The wave function (blue line) decays exponentially within the barrier.

A very simplified one-dimensional model of the STM set-up is displayed in Fig. 3.3. The potential barrier  $\Delta U$  represents the vacuum gap with the distance  $d$  between surface and tip. The sample and tip are positioned at the left and right side of the barrier, respectively. In classical physics, an approaching electron with an energy  $E < U(0 < z \leq d)$  is unable to overcome the 'higher' energy barrier and, therefore, is reflected. However, in quantum physics a finite probability exists that the electron is transmitted through the barrier. At each position  $z$  the electron's wave function  $\psi(z)$  has to satisfy the time-independent one-dimensional Schrödinger equation:

$$\frac{-\hbar^2}{2m} \frac{d^2}{dz^2} \psi(z) + U(z)\psi(z) = E\psi(z) \quad (3.2)$$

The solution of the wave function within each region of the sample, barrier and tip (see Fig. 3.3) can be written as:

$$\psi_S(z) = e^{ikz} + Ae^{-ikz} \quad , z \leq 0 \quad (3.3)$$

$$\psi_B(z) = Be^{\kappa z} + Ce^{-\kappa z} \quad , 0 < z \leq d \quad (3.4)$$

$$\psi_T(z) = De^{ikz} \quad , d < z \quad (3.5)$$

where  $k = \frac{\sqrt{2m(E-U)}}{\hbar}$  is the wave vector and  $\kappa = \frac{\sqrt{2m(U-E)}}{\hbar}$  is the decay constant. The coefficients  $A$ ,  $B$ ,  $C$  and  $D$  represent the amplitude of the reflected and trans-



mitted wave function, respectively. These coefficients can be obtained by considering the boundary conditions. More specifically, the wave function and their derivatives  $\frac{d\psi(z)}{dz}$  are continuous at the sample-barrier and barrier-tip interfaces. The barrier transmission coefficient  $T$  describes the ratio between the incoming current density  $I_i$  and the transmitted current  $I_t$

$$T = \frac{I_t}{I_i} = |D|^2 = \left( 1 + \frac{(k^2 + \kappa^2)^2}{4k^2\kappa^2} \cdot \sinh^2(\kappa d) \right)^{-1}. \quad (3.6)$$

In the common case that  $U \gg E$ , one has a strongly attenuating barrier (large  $\kappa$ ) and the transmission coefficient simplifies to

$$T \sim \frac{16\kappa^2 k^2}{(k^2 + \kappa^2)^2} \cdot e^{-2\kappa d}. \quad (3.7)$$

Even so this is a very simplified model, some basic features of STM can be readily explained. The height of the energy barrier  $U$  represents the energy to remove an electron from the sample or tip to the vacuum level. Primarily, electrons lying close to the Fermi energy  $E_F$  are involved in the tunneling process. Therefore, the energy barrier is basically given by the work function of the tip  $\Phi_T$  and the sample  $\Phi_S$ . The work function itself is material dependent. The values of typical metals used in STM experiments are summarized in Table 3.1. According to Equation 3.7, a common work function of 5 eV approximately results in a decrease of the tunneling current by one order of magnitude per 0.1 nm. This demonstrates the high sensitivity of STM to height changes  $\Delta d$  of the substrate's topography. It also indicates that the atom at the apex of the tip, closest to the substrate, is mostly involved in the tunneling process. This is an essential point, because the sharpness of the tip reflects the high lateral resolution of STM.

**Table 3.1.:** Work function and the corresponding decay constant for bulk crystals of elements typically used in STM experiments (adapted from [64]).

Element	Al	Au	Cu	Ir	Ni	Pt	Si	W
$\Phi$ (eV)	4.1	5.4	4.6	5.6	5.2	5.7	4.8	4.8
$\kappa$ (nm)	0.103	0.119	0.109	0.121	0.116	0.122	0.112	0.112

Using a perturbation theory ansatz, Bardeen has been able to develop a model to describe the tunneling junction between a conductive tip and a sample as present in STM experiments [67]. About 20 years later, his approach was extended by the Tersoff-Hamann-Model [68, 69] and by the work of Chen [70, 71]. In his approach, Bardeen considered the time-evolution of an electron state in the sample, perturbed by the potential of an approaching tip. Several further approximations are made in his model. First of all, only single-electron processes are considered. All multi-

electron tunneling effects like electron-electron scattering or variation in the barrier potential caused by neighboring tunneling electrons are neglected. However, these approximations are reasonable considering the small currents generally used in STM. Moreover, only elastic tunneling is taken into account, *i.e.*, electron energy loss due to interaction with quasi particles is neglected.

First order time-dependent perturbation theory results in the tunneling probability per unit time,  $P_{\mu\nu}(t)$ , of an individual electron tunneling from a single state  $\mu$  to a single state  $\nu$ :

$$P_{\mu\nu}(t) = \frac{2\pi}{\hbar} \delta(E_\nu^T - E_\mu^S) |M_{\mu\nu}|^2 \quad (3.8)$$

This formula is also known as Fermi's Golden rule.  $E_\mu^S$  and  $E_\nu^T$  are the energy of the state  $\mu$  in the sample and the energy of the state  $\nu$  in the tip, respectively. The delta function  $\delta(E_\nu^T - E_\mu^S)$  guarantees elastic tunneling. The matrix element  $|M_{\mu\nu}| = \langle \psi_\nu^T | U_T | \psi_\mu^S \rangle$  is defined as the projection of the initial state  $\psi_\mu^S$  perturbed by the potential  $U_T$  onto the final state  $\psi_\nu^T$ . More details can, *e.g.*, be found in the lecture notes of S. Lounis [66].

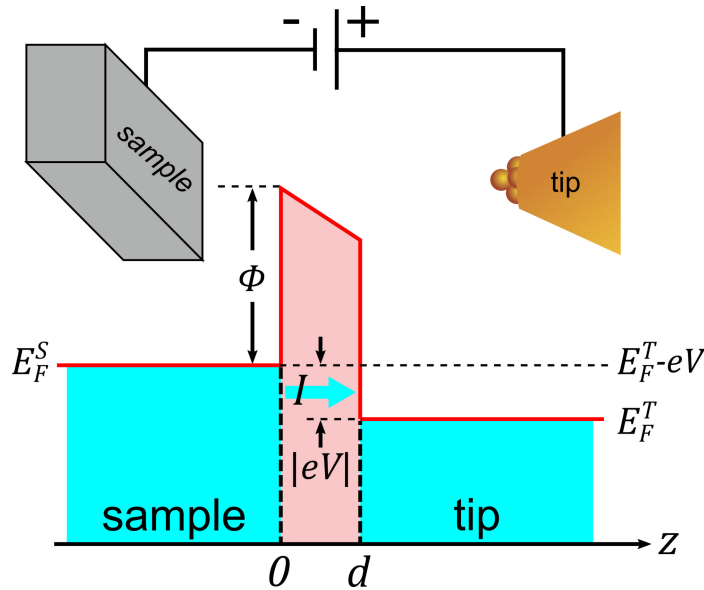


**Fig. 3.4.:** Applying a bias voltage  $V$  results in an energy shift  $eV$  of the Fermi level of the sample with respect to the Fermi level of the tip. The cyan color represents the occupied electron states. Due to the energy shift, more electrons can tunnel from the occupied states in the sample to the unoccupied states in the tip. The net tunneling direction is indicated with the cyan arrow. Note that by changing the sign of the bias voltage, the energy shift of the Fermi level is inverted and the net electron tunneling direction is flipped.

So far tunneling of electrons in a single state only is considered, but naturally, the tip and sample possess a complete spectrum of electron states. Therefore, for

determining the net current, all electron states of tip and sample involved in the tunneling process have to be considered. Obviously, electrons can only tunnel from an occupied state to an unoccupied state. At finite temperature, the electron state occupation probability at energy  $E$  is described by the Fermi-Dirac distribution:

$$f(E - E_F) = \left(1 + e^{\frac{E - E_F}{k_B T}}\right)^{-1} \quad (3.9)$$

with  $k_B$  being the Boltzmann constant. Consequently, the probability of the unoccupied states is described by  $1 - f(E - E_F)$ . Both, the sample and the tip have occupied and unoccupied states. Accordingly, the electrons can tunnel from the tip to the sample and vice versa. Applying a bias voltage  $V$  between the tip and the sample, the Fermi levels are shifted in respect to each other as shown in Fig. 3.4. For a sufficient high bias voltage, most electrons tunnel from the negatively charged electrode to the positively charged electrode (net current direction marked with a cyan arrow in Fig. 3.4). The electrons of the sample, lying below the Fermi energy of the tip, cannot reach the energetically higher lying unoccupied states of the tip. Therefore, by varying the sign of the applied bias voltage, the electron net flow direction can be controlled. Assuming a bias voltage  $V$  and accounting the electron state occupation probability, the tunneling current from sample to tip,  $I_{S \rightarrow T}$ , and from tip to sample,  $I_{T \rightarrow S}$ , is given by:

$$I_{S \rightarrow T} = \frac{4\pi e}{\hbar} \sum_{\mu\nu} f(E_\mu^S - E_F^S) \left[1 - f(E_\nu^T - E_F^T)\right] |M_{\mu\nu}|^2 \delta(E_\nu^T - E_\mu^S - eV) \quad (3.10)$$

$$I_{T \rightarrow S} = \frac{4\pi e}{\hbar} \sum_{\mu\nu} f(E_\nu^T - E_F^T) \left[1 - f(E_\mu^S - E_F^S)\right] |M_{\mu\nu}|^2 \delta(E_\nu^T - E_\mu^S - eV) \quad (3.11)$$

A factor of two has been added to account for the two possible spin states of each electron. The net total current  $I = I_{S \rightarrow T} - I_{T \rightarrow S}$  can be written as:

$$I = \frac{4\pi e}{\hbar} \sum_{\mu\nu} f(E_\mu^S - E_F^S) (E_\nu^T - E_F^T) |M_{\mu\nu}|^2 \delta(E_\nu^T - E_\mu^S - eV) \quad (3.12)$$

Introducing the electron density of state (DOS),  $n(E)$ , the sum of the discrete states can be replaced by an integral  $\sum_\mu \rightarrow \int dE n(E)$ . Considering a corresponding change of variables gives

$$I = \frac{4\pi e}{\hbar} \int d\epsilon \left[ f(E_F^T - eV + \epsilon) - f(E_F^S + \epsilon) \right] \times n^T(E_F^T - eV + \epsilon) n^S(E_F^S + \epsilon) \left| M(E_F^S + \epsilon, E_F^T - eV + \epsilon) \right|^2. \quad (3.13)$$

For a small bias voltage  $V$  and low temperature, the electron current simplifies to

$$I = \frac{4\pi e}{\hbar} V n^T(E_F^T) n^S(E_F^S) |M|^2. \quad (3.14)$$

Noteworthy, the tunneling current is a function of the joint electron DOS of the sample and the tip. A second important conclusion is that in STM, by changing the sign of the bias voltage  $V$ , the occupied as well as the unoccupied electronic states of the substrate can be accessed as discussed above. Combined with its high local resolution, these conclusions reflect the unique and powerful applicability of STM.

### 3.3 Atomic Force Microscopy (AFM)

Atomic force microscopy (AFM), being a specific type of scanning probe microscopy (SPM), is a powerful and surface-sensitive imaging method to analyze the structure of metallic and insulating substrates at the nanometer scale. While scanning the surface with a sharp tip attached to a cantilever, the force between the sample and tip is determined. AFM enables the possibility to acquire high-resolution real-space images.

The basic principles of AFM have been already sufficiently described in various PhD thesis from former members in our group [22, 72, 73]. In the following, I will give a short introduction of AFM operated in the frequency modulated (FM) mode, as used in all AFM measurements presented in this work. For advanced readers, I recommend to have a look on the more comprehensive and general description of AFM by H. Söngen *et al.* [74].

In Fig. 3.5, a schematic drawing illustrating the functionality of an AFM operated in the FM-mode is shown. The cantilever is excited to oscillate at its resonance frequency  $\nu_r$ . More specifically, the cantilever is driven by a shaking piezo vibrating at the cantilever's resonance frequency  $\nu_r$  with a constant phase shift of usually  $\phi = -\pi/2$  between the piezo and the cantilever. A common method to monitor the deflection  $q$  of the cantilever's tip is given by a laser beam and a position sensitive detector (PSD). The laser is focused onto the back of the cantilever and then reflected onto the PSD.

In FM-AFM, in total three feedback loops are utilized: the *amplitude controller*, the *phase-locked loop* (PLL) and the *z-feedback loop* (see Fig. 3.5). The deflection signal  $q$  of the oscillating cantilever is forwarded to the PLL and the amplitude loop. In the latter feedback loop, the determined amplitude of the oscillating tip  $q_0$  is compared with an externally, pre-given reference value. The force applied to excite the cantilever is adjusted to match the cantilevers deflection amplitude  $q_0$  with the

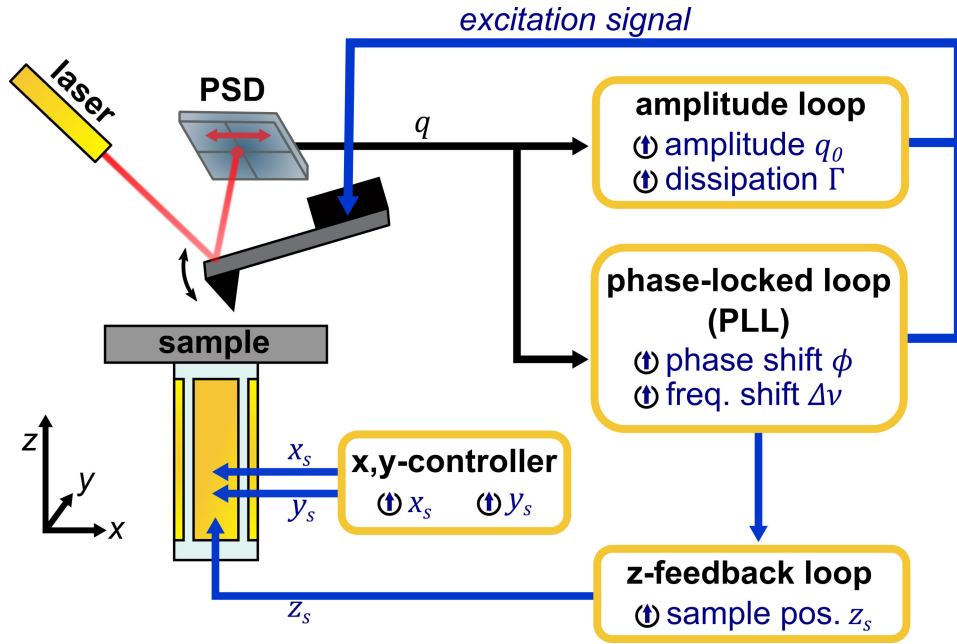


**Fig. 3.5.:** Schematic drawing of an AFM operated in the frequency modulated (FM) mode. A cantilever is excited to oscillate. Its deflection  $q$  is detected by a position sensitive device (PSD). The sample position  $\vec{p}_s = (x_s, y_s, z_s)$  with respect to the cantilever's can be regulated by piezo elements. In total, three feedback loops are used in FM-AFM. The *amplitude loop* keeps the maximum deflection of the oscillating cantilever constant. The *phase-locked loop* (PLL) keeps the phase  $\phi$  between the vibrating cantilever and the excitation signal constant. The so-called *z-feedback loop* keeps the frequency shift  $\Delta\nu$  between the cantilever's resonance frequency  $\nu_r$  and its eigenfrequency  $\nu_e$  constant by adjusting the sample position  $z_s$ .

reference value. The dissipation  $\Gamma$  defines the oscillator's loss in kinetic energy per time, mainly caused by friction. For measurements in ultra-high vacuum (UHV) the dissipation of the cantilever is generally very low.

A change in the tip-sample interaction, *e.g.*, when approaching the tip to the sample, will affect the resonance frequency of the cantilever. The PLL adjusts the frequency of the excitation signal to keep the phase shift  $\phi$  between the oscillating cantilever and the excitation piezo element constant. Furthermore, the PLL determines the resonance frequency  $\nu_r$  of the cantilever, which is then further passed to the z-feedback loop. The difference between the cantilever's resonance frequency  $\nu_r$  and its eigenfrequency  $\nu_e$  is described by the frequency shift:

$$\Delta\nu = \nu_e - \nu_r \quad (3.15)$$

The z-feedback loop keeps the frequency shift  $\Delta\nu$  constant by regulating the samples height  $z_s$  with the help of piezo elements. Consequently, by changing the z-feedback loop's reference value for the frequency shift  $\Delta\nu$ , the AFM controller can adjust the tip-sample distance. Therefore, this mode is called frequency modulated AFM.

With the help of an  $x,y$ -controller and further piezo elements, the sample position can be adjusted along the lateral directions. This enables to measure at different spots of the sample and, hence, scan across the surface. The collected height signal  $z_s$  as a function of lateral position is called *topography image*. In this work, mostly topography images are presented. For an ideal working  $z$ -feedback loop, the corrugation in the frequency shift signal  $\Delta\nu$  is zero, and all the information is stored in the topography channel. However, in practice a perfect feedback loop is not feasible, and it can make sense to also pay attention to the frequency shift image.

## 3.4 Experimental Set-up

In order to study molecular self-assembly of submonolayers on substrates, it is of utmost importance to keep the surface free from contaminations. Therefore, the sample preparation and all scanning probe microscopy (SPM) measurements presented in this work were performed under ultra-high vacuum (UHV) conditions with a base pressure generally below  $1 \cdot 10^{-10}$  mbar.

All AFM experiments on calcite ( $\text{CaCO}_3$ ) and calcium fluoride ( $\text{CaF}_2$ ) crystals shown in this work were carried out with a system built up by the group of Prof. Dr. Angelika Kühnle. The experimental set-up is displayed in Fig. 3.6. The UHV pressure is achieved by a multi-stage pump system. A rotary vane pump from *Edwards* serves as a pre-pump for a *Pfeiffer* turbo pump. Moreover, a titanium sublimation pump (TSP) and an ion-getter pump from Varian further improve the chamber pressure. During measurement, the pressure is only maintained by the ion-getter pump, because the vibration of the rotary vane pump and turbo pump, and a possible electrical interference coupling of the TSP might affect or even falsify the result of the experiment.

Measurements with atomic resolution are extremely sensitive to external vibrations. Therefore, the laboratory is located in the basement to absorb building vibrations. Furthermore, the complete UHV system is placed on four damping legs, and, in addition, the AFM is equipped with an eddy current brake.

As shown in Fig. 3.6, the UHV system consists of two large chambers, separated by a valve. The left chamber is for preparation only (marked with A in Fig. 3.6). Samples and cantilevers can be passed through a load lock into the preparation chamber. N-doped cantilevers with a nominal force constant of  $40 \text{ Nm}^{-1}$  and a resonance frequency of around 300 kHz were purchased from *Nanosensors*. Before usage, cantilevers were sputtered with  $\text{Ar}^+$  for 10 min. The calcite and calcium fluoride crystals were degassed in situ for two hours at about 650 K and for one hour at about 420 K, respectively. Subsequently, the  $\text{CaCO}_3 / \text{CaF}_2$  crystals were cleaved with a

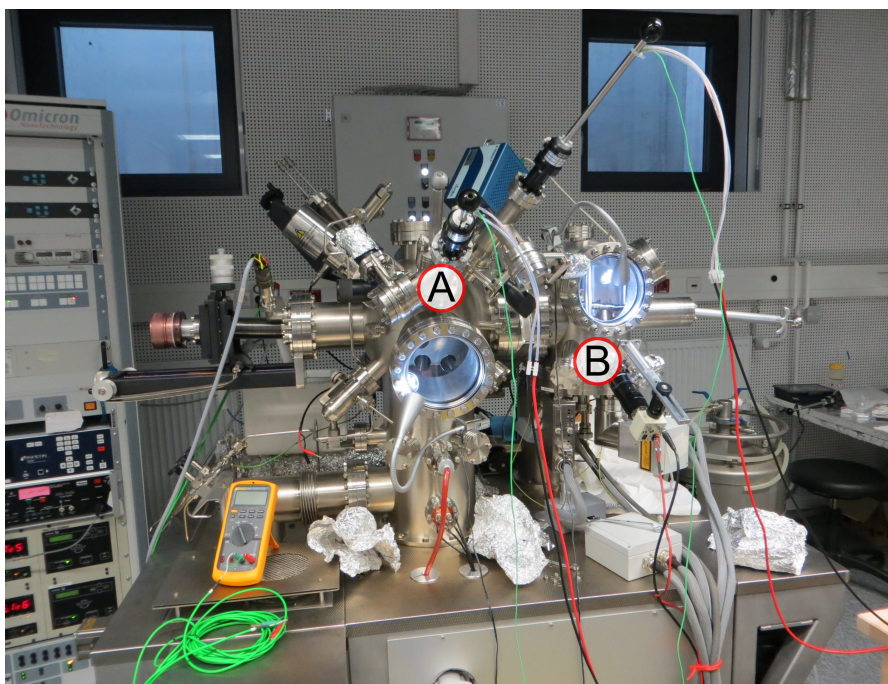


**Fig. 3.6.:** Photography of the UHV system and attached equipment used for AFM measurements. The preparation chamber labeled with (A) is separated by a valve from the microscope chamber labeled with (B) (adapted from [75]).

scalpel and annealed to about 580 K / 390 K for one hour to remove surface charges. The crystals were purchased from *Korth Kristalle*, Altenholz, Germany and cut into 2 mm x 4 mm blocks by *Vario Kristallbearbeitung*, Königs Wusterhausen, Germany. Dimolybdenum tetraacetate (MoMo) and 2,5-dihydroxybenzoic acid (2,5-DHBA) molecules, purchased from *Sigma Aldrich*, were evaporated using a home-built Knudsen cell based on the design of M. Schunack [76]. Before molecule deposition in UHV, the Knudsen cell is thoroughly outgassed in advance.

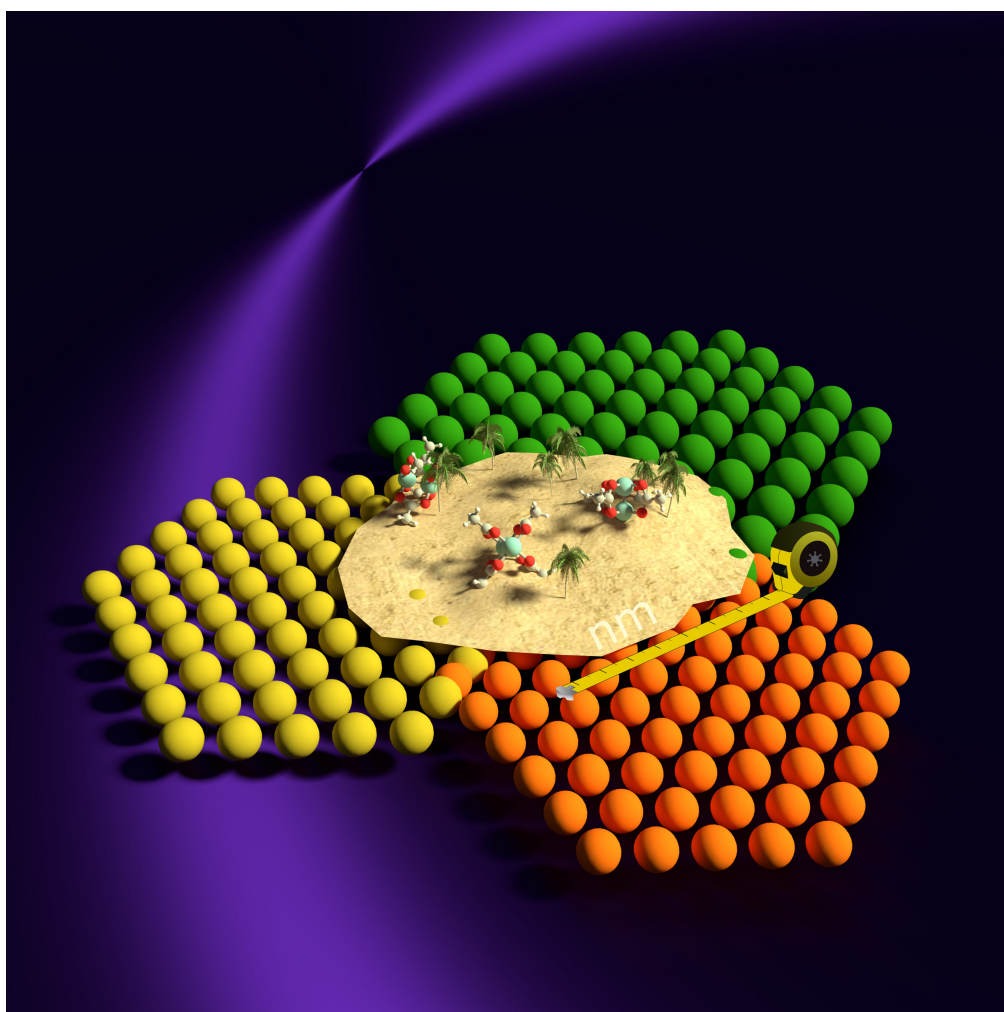
The AFM and a carousel for storing samples and cantilevers are located in the second main chamber to the right (marked with B in Fig. 3.6). Measurements were conducted using a *VT AFM XA* and a control unit from *Scienta Omicron*, Taunusstein, Germany. The systems temperature can be varied by a built-in heater and a flow cryostat. Using liquid nitrogen and liquid helium, a minimum substrate temperature of *ca.* 100 K and *ca.* 30 K was reached, respectively. Note that the sample temperatures stated in this work were measured at the sample holder stage using a *Pt-100 sensor* with an accuracy of  $\pm 1$  K and not at the sample surface. However, the manufacturer estimates the unknown temperature difference between the sample holder stage and the crystals surface to be less than 10 K.





## Tailoring molecular island shapes: Influence of microscopic interaction on mesostructure

Reprinted with permission from 'Simon Aeschlimann, Lu Lyu, Benjamin Stadtmüller, Martin Aeschlimann and Angelika Kühnle, "Tailoring molecular island shapes: Influence of microscopic interaction on mesostructure", *Nano Research* 2020, 13(3), 843–852'



Back cover image from *Nano Research*, Volume 13, Number 3



## Tailoring molecular island shapes: Influence of microscopic interaction on mesostructure

Simon Aeschlimann<sup>1,2</sup>, Lu Lyu<sup>3</sup>, Benjamin Stadtmüller<sup>3,4</sup>, Martin Aeschlimann<sup>3,4</sup>, and Angelika Kühnle<sup>5</sup> (✉)

<sup>1</sup> Institute of Physical Chemistry, Johannes Gutenberg University Mainz, Duesbergweg 10-14, Mainz 55099, Germany

<sup>2</sup> Graduate School Materials Science in Mainz, Staudingerweg 9, Mainz 55128, Germany

<sup>3</sup> Department of Physics and Research Center OPTIMAS, University of Kaiserslautern, Erwin-Schrödinger-Straße 46, Kaiserslautern 67663, Germany

<sup>4</sup> Graduate School Materials Science in Mainz, Erwin-Schrödinger-Straße 46, Kaiserslautern 67663, Germany

<sup>5</sup> Physical Chemistry I, Faculty of Chemistry, Bielefeld University, Universitätsstraße 25, Bielefeld 33615, Germany

© The Author(s) 2020

Received: 15 November 2019 / Revised: 7 February 2020 / Accepted: 9 February 2020

### ABSTRACT

Controlling the structure formation of molecules on surfaces is fundamental for creating molecular nanostructures with tailored properties and functionalities and relies on tuning the subtle balance between intermolecular and molecule-surface interactions. So far, however, reliable rules of design are largely lacking, preventing the controlled fabrication of self-assembled functional structures on surfaces. In addition, while so far many studies focused on varying the molecular building blocks, the impact of systematically adjusting the underlying substrate has been less frequently addressed. Here, we elucidate the potential of tailoring the mesoscopic island shape by tuning the interactions at the molecular level. As a model system, we have selected the molecule dimolybdenum tetraacetate on three prototypical surfaces, Cu(111), Au(111) and CaF<sub>2</sub>(111). While providing the same hexagonal geometry, compared to Cu(111), the lattice constants of Au(111) and CaF<sub>2</sub>(111) differ by a factor of 1.1 and 1.5, respectively. Our high-resolution scanning probe microscopy images reveal molecular-level information on the resulting islands and elucidate the molecular-level design principles for the observed mesoscopic island shapes. Our study demonstrates the capability to tailor the mesoscopic island shape by exclusively tuning the substrate lattice constant, in spite of the very different electronic structure of the substrates involved. This work provides insights for developing general design strategies for controlling molecular mesostructures on surfaces.

### KEYWORDS

scanning tunneling microscopy (STM), self-assembly, island shape, mesostructure, scanning probe microscopy (SPM), two-dimensional structures

### 1 Introduction

One of the crucial challenges in the miniaturization of device structures for further information technology and photonic applications is to devise novel concepts to fabricate active functional units on surfaces with atomic or molecular precision at the nanoscale. In this context, molecular self-assembly processes on surfaces have emerged as a powerful tool for creating functional molecular nanostructures on surfaces [1–6]. Making use of the tremendous variability of the molecular building blocks, the intermolecular and the molecule-surface interactions can be controlled to arrive at a specific surface structure that is encoded in the involved constituents [7, 8]. In many cases, the molecule-substrate interaction has been recognized to be governed by the electronic structure of the substrate, which, in turn, impacts the structural properties of self-assembled nano-materials on various substrates; e.g., bulk metals [9–15], two-dimensional materials [16, 17], and polar oxide surfaces [18–20]. Tuning the subtle balance between molecule-molecule and molecule-surface interactions [21] has opened up new pathways for creating an impressive variety of molecular structures on

surfaces [22–26]. For example, structures ranging from perfectly ordered two-dimensional layers [27], unidirectional rows [28, 29], porous networks [30, 31] to complex structures have been presented as a function of the specific molecular design [27, 32, 33]. Even richer structures have been demonstrated in multi-component systems, i.e., upon co-deposition of two types of molecules [34–39].

Despite these impressive results, a reliable structure prediction and rational control of the resulting structures is still largely lacking. In particular, the focus of intense research has been on exploring the variability of the molecular building blocks [24], while the influence of systematically varying the underlying substrate is rarely addressed. This is unfortunate as the substrate can act as a template [40, 41], directing molecular structure formation and providing a further dimension in rationally controlling molecular self-assembly on surfaces [42]. Moreover, to successfully employ molecular self-assembly in nano-structuring processes, it is also of utmost importance to control the structure formation on a mesoscopic scale. Here, we focus on this aspect and show that the mesoscopic shape of self-assembled molecular islands can be controlled by tuning the involved interactions

Address correspondence to angelika.kuehnle@uni-bielefeld.de

at the molecular scale. In particular, we demonstrate that the shape of molecular islands can be tuned by adjusting the lattice constant of the underlying surface.

In the bulk of a molecular crystal, the molecular order is solely determined by the intermolecular interactions. In contrast, adsorbed on a surface, the spacing between neighboring molecules within an island can be tuned by using different substrates with different lattice constants due to the additional molecule-substrate interaction. For this surface templating effect, a sufficiently high and site-specific molecule-substrate interaction is necessary. Otherwise, the shape of the molecular island cannot be influenced in a controlled manner by the substrate periodicity.

To be more specific, as illustrated in Fig. 1(a), molecules on a surface can interact with the underlying substrate (I) and neighboring molecules (II). In a simple first approximation, the interactions governing molecular structure formation on surfaces may be considered to be independent of each other. In general, adsorbates are not rotational invariant, which can lead to anisotropic interactions. Thus, the intermolecular interaction can strongly depend on the direction as demonstrated in Fig. 1(a), showing an example for an island stabilized by two different intermolecular interactions (IIa and IIb).

The resulting mesoscopic island shape reflects the mismatch of the bulk crystal unit cell dimensions and the surface lattice constant. Even though, in this simple approximation, the intermolecular interaction is assumed to be independent of the strength of the molecule-substrate interaction, it remains being a function of the molecule-molecule distance. If the surface lattice constant equals to an integer multiple of the molecular crystal unit cell dimensions, the molecules can adopt their ideal spacing along this direction. As a consequence, an island elongated along this direction is thermodynamically favorable. This is why the thermodynamically most stable mesoscopic island shape is a direct consequence of the subtle balance of the involved direction-dependent intermolecular interactions and the molecule-surface interaction. This provides the opportunity to rationally design the molecular island shape by tuning the lattice constant of the underlying crystal.

In this work, we explore this particular opportunity of tuning the mesoscopic island shape by acting on the microscopic interactions in the system at the molecular scale. An ideal molecule for this purpose is the binuclear neutral complex dimolybdenum tetracetate ( $\text{Mo}_2(\text{O}_2\text{CMe})_4$ ); in the following referred to as MoMo shown in Fig. 1(b). Despite its rotational symmetry, adsorbed on a surface, MoMo exhibits a strong anisotropy in the intermolecular interactions as illustrated in Fig. 1(a).

As model substrates, we have selected three hexagonal surfaces Cu(111), Au(111) and  $\text{CaF}_2(111)$  with different lattice constants. The lattice constant of Au(111) is slightly larger (1.1 times) and the lattice constant of  $\text{CaF}_2(111)$  is clearly larger (1.5 times) than the one of Cu(111). All surfaces form sufficiently strong, site-specific bonds to MoMo, making them highly suited for our surface templating study. Using scanning probe techniques, we study the self-assembly of submonolayer coverages of MoMo on these three surfaces. In all cases, the MoMo molecules adsorbed on these substrates form islands composed of molecules arranged in chains with a superstructure that is commensurate to the underlying lattice. Due to the different surface lattice constants, the commensurability results in different molecule-molecule distances and, hence, different molecule-molecule interaction strengths. This change at the molecular level has a profound influence on the mesoscopic island shape.

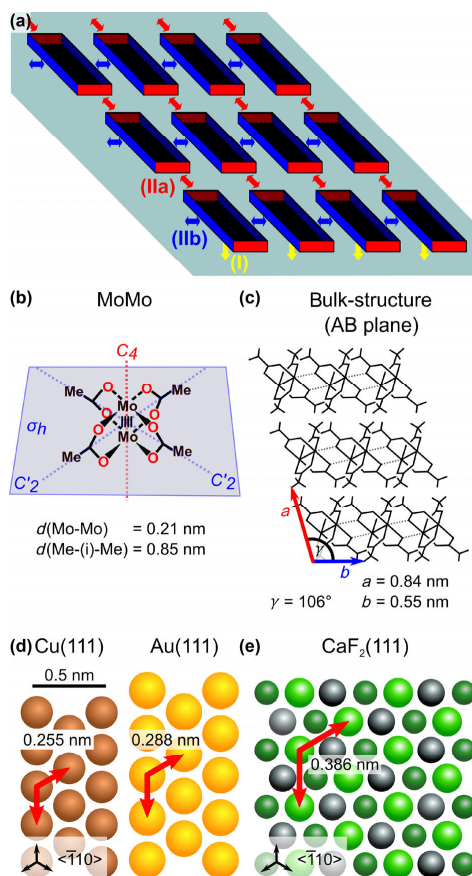


**Figure 1** (a) Sketch of anisotropic interactions in a molecular island adsorbed on a surface. The yellow arrows indicate the molecule-substrate interaction (I). The two-fold rotational symmetry of the molecules results in two different intermolecular interactions marked with a blue arrow (IIa) and a red arrow (IIb). In a simple first approximation, all interactions are considered to be independent of each other. Changing the molecule spacing along one direction will only affect the strength of the corresponding interaction and, thereby, change the subtle balance between the intermolecular interactions (IIa and IIb). Model of (b) the MoMo molecule and (c) top view of its crystal AB-plane consisting of stacked molecular chains. The MoMo molecules interact electrostatically between the positively charged molybdenum atoms and the oxygen atoms of the neighboring molecules, indicated by the grey dotted line. (d) Model of the hexagonal copper/gold (111) structure with a lattice constant of  $a_{\text{Cu}} = 0.255$  nm and  $a_{\text{Au}} = 0.288$  nm, respectively. (e) Model of the calcium fluoride (111) surface. Both, fluorine (green) and calcium (grey) ions are arranged in a hexagonal manner with a periodicity of  $a_{\text{CaF}_2} = 0.386$  nm, leading to a three-fold symmetry. Protruding fluorine ions are highlighted with a brighter green color. The 0.5 nm scale bar applies to (d) and (e).

Our work demonstrates that, in spite of the distinctly different nature of these surfaces (ionic surface versus noble metal surface), the driving force determining the island shape can be sufficiently described by a simple comparison of the superstructure unit cell dimensions and the molecular bulk structure. As long as site-specific adsorption is present, the driving force can even be reduced to the aspect of surface geometry (symmetry and periodicity). As a result, in this case, the microscopic electronic structure of the substrate does not

need to be considered for explaining the mesoscopic structure. Therefore, our work illustrates a way to control the mesoscopic island shape of molecules on surfaces by tuning the substrate lattice constants.

## 2 Materials and methods

Dimolybdenum tetraacetate ( $\text{Mo}_2(\text{O}_2\text{CMe})_4$ ), in this work referred to as MoMo) is a binuclear neutral complex of the transition metal molybdenum. It belongs to the  $D_{4h}$  symmetry point group (see Fig. 1(b)). Historically seen, MoMo is of unique significance, because it is a prime example for an intramolecular quadruple bond between two transition metals; and it generally serves as a precursor for the synthesis of other known compounds containing molybdenum quadruple bonds [43]. For the MoMo molecule, the quadruple bond manifests itself in an intramolecular Mo-Mo bonding distance of approximately 0.21 nm [44]. This is significantly shorter than the distance of 0.27 nm in a molybdenum single crystal [45].

The MoMo crystal has a triclinic superstructure as firstly reported by D. Lawton and R. Mason in 1965 [46]. Later, the triclinic crystal structure has been confirmed and corresponding lattice constants have been redetermined in higher accuracy in extensive diffraction measurements by F. A. Cotton et al. [47] and K. Hino et al. [48]. The molybdenum crystal AB plane, defined by the lattice constants  $a$  and  $b$ , is characterized by upright standing molecules being arranged next to each other along the  $b$ -direction (Fig. 1(c)). In the following, we will refer to this arrangement as molecular chains. The chains are stabilized by an intermolecular interaction between a molybdenum atom and an oxygen atom of the neighboring molecule (marked by a grey, dotted line in Fig. 1(c)). In the crystal structure, the molecules are slightly tilted with respect to the chain direction in order to optimize the configuration of the metal-metal axial position for the bridging Mo-O interaction [49]. Ultraviolet photoelectron spectroscopy (UPS) measurements indicate a  $\sigma$ - $\pi$  orbital splitting, presumably caused by this axial intermolecular interaction [50]. The lattice constant, i.e., the periodicity of the MoMo molecules along the chains in the bulk structure is  $b = 0.550 \text{ nm}^{\text{①}}$  (indicated by a blue arrow in Fig. 1(c)). In the AB plane of the MoMo crystal, the molecular chains are stacked up next to each other. This leads to a lattice constant of  $a = 0.842 \text{ nm}$  (indicated by a red arrow in Fig. 1(c)), which represents the distance of two molecules in neighboring chains. In the following, we will refer to the stacking direction  $a$  (red arrows) and the chain direction  $b$  (blue arrows). In the bulk structure, the two directions are enclosing an angle of  $\gamma = 106^\circ$ <sup>②</sup>.

The (111) surfaces of the metallic Cu and Au crystals exhibit a hexagonal surface structure (see Fig. 1(d)). The  $\text{CaF}_2$  crystal is a bulk insulator consisting of fluorine and calcium triple layers stacked in the order of  $(\text{F}^- - \text{Ca}^{2+} - \text{F}^-)_n$  along the [111] direction. Even so the layers are charged, there exists no net dipole moment perpendicular to the surface [51]. Figure 1(e) illustrates the  $\text{CaF}_2(111)$  surface. The positively charged  $\text{Ca}^{2+}$  ions (grey) and the negatively charged fluorine  $\text{F}^-$  ions (green) are arranged in a hexagonal manner with a surface lattice constant of  $a_{\text{CaF}_2} = 0.386 \text{ nm}$ . Thus, all substrates studied in this work, Cu(111), Au(111) and  $\text{CaF}_2(111)$ , possess a three-fold rotational symmetry. However, the lattice constant of Cu(111) is  $a_{\text{Cu}} = 0.255 \text{ nm}$  and, hence, slightly smaller compared to  $a_{\text{Au}} =$

0.288 nm, and roughly 1.5 times smaller compared to the insulator. Thus, Cu(111), Au(111) and  $\text{CaF}_2(111)$  share the same hexagonal lattice, but exhibit different lattice constants. Therefore, these substrates constitute an ideal model system to examine how the molecular island shape is affected by tuning the substrate lattice.

All experiments shown in this work were carried out with scanning probe microscopes from Scienta Omicron (VT AFM XA) under ultrahigh vacuum (UHV) conditions. Dynamic AFM (atomic force microscopy) experiments of MoMo on calcium fluoride were performed in frequency modulation mode [52]. We used n-doped silicon cantilevers from Nanosensors with a nominal force constant of  $40 \text{ N}\cdot\text{m}^{-1}$  and an eigenfrequency of 300 kHz in UHV. For the scanning tunneling microscopy (STM) measurements on Cu(111) and Au(111), another system from Scienta Omicron (VT AFM XA) was operated in constant current mode with the tunneling current  $I_t$  usually in the range of 70–90 pA. Positive and negative values correspond to tunneling from the occupied and into the unoccupied states of the sample, respectively.

The preparation of the bare surfaces as well as the molecule deposition were performed *in situ* with a chamber base pressure typically better than  $10^{-10}$  mbar. Optical quality calcium fluoride ( $\text{CaF}_2$ ) crystals were purchased from Korth Kristalle GmbH, Kiel, Germany. Prior to molecule sublimation, the  $\text{CaF}_2$  crystal was annealed to 400 K for 1 h. The Cu(111) and Au(111) single crystals from MaTeck, Jülich, Germany were cleaned by repeated cycles of  $\text{Ar}^+$  sputtering (1.5 keV, 20 min) and a subsequent annealing to about 850 K. The cleanliness and the surface morphology were inspected by recording large-scale STM images and low-energy electron diffraction (LEED).

The MoMo molecules were bought from Sigma-Aldrich, Germany, with a purity of 98%, and the powder was further purified in advance by long-time out-gassing at 400 K in a UHV molecular beam evaporator system. Subsequently, MoMo molecules were deposited using a home-built Knudsen cell that is heated for molecule sublimation. For the experiments shown here, molecules were sublimated for 10–50 min at a typical temperature of 440 K onto the sample at a distance of approximately 9 cm.

## 3 Results

In the first part of the result section, STM measurements of submonolayers of MoMo on Cu(111) are presented, which revealed a nearly perfect fit to the bulk periodicity along the chain direction. The self-assembly of this system has first been reported by Kollamana et al. [53]. Here, we therefore only summarize the most important conclusions concerning the molecule adsorption position. In addition, new, large overview STM images were taken in the present study to determine the island mesoscopic structure.

After submonolayer deposition of MoMo on Cu(111) at about 110 K, the co-existence of two different island structures is revealed (see Fig. 2(a)). Beside a chain phase (marked with blue lines), being similar to the AB plane of the molecular bulk, a second structure referred to as mesh phase (marked in cyan) is present [53]. The co-existence of the structures suggests that both structures are energetically similar. Here, the mesh phase, which is formed by flat-lying molecules, is not considered any further, because in this work we will focus on the chain phase solely, which is composed of upright-standing molecules.

An overview STM image (Fig. 2(a)) indicates that the islands of the chain phase on Cu(111) are elongated along the chain

<sup>①</sup> Following the notation of D. Lawton et al. (1965).

<sup>②</sup> Please note, the lattice constant  $a$  along the stacking direction is not the distance between two chains, because this distance would be measured perpendicular to the chains.

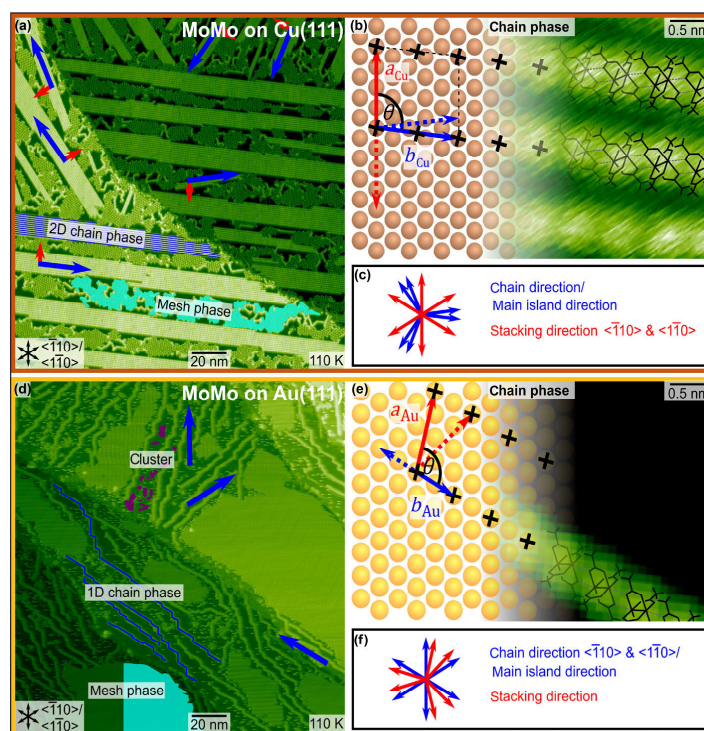


**Figure 2** (a) and (d) STM image of MoMo on Cu(111) and Au(111) at a coverage of  $\theta = 0.70$  ML at about 110 K. For illustration, one 2D chain phase island on Cu(111) and a few 1D chain phase islands on Au(111) are exemplary marked with dark blue lines. In both images part of a mesh phase island is marked in cyan. On Au(111), some molecule clusters are exemplary marked in purple. Blue arrows indicate main island growth directions of the chain phase. (b) and (e) Schematic representation of the chain phase superstructure superimposed onto a high-resolution STM image. The black crosses mark possible molecule adsorption position with respect to the Cu(111)/Au(111) lattice. The unit cell parameters on Cu(111) are  $a_{Cu} = 1.020$  nm,  $b_{Cu} = 1.110$  nm and  $\theta_{Cu} = 96.6^\circ$  [53]. On Au(111) the islands are only elongated along the chain direction. However, a virtual unit cell is given by  $a_{Au} = 1.036$  nm,  $b_{Au} = 0.576$  nm and  $\theta_{Au} = 106^\circ$ . A mirrored island structure is illustrated with dotted arrows. (c) and (f) The observed molecule stacking directions are indicated with red arrows and the chain directions are indicated with blue arrows. For both surfaces, there exist six energetically equal, but different oriented island structures. For Cu(111), the stacking directions are oriented along the  $\langle\bar{1}10\rangle$  and  $\langle 1\bar{1}0\rangle$  directions and for Au(111) the chain directions.

directions (blue arrows) and are rather limited in the stacking direction (red arrows). The islands can be over 300 nm long along the chain direction. The chain length is limited by a step edge or another chain phase island. In contrast to that, the islands width seems to be limited to roughly 30 nm, consisting of about 30 chains. In total six different chain directions (indicated by blue arrows) have been observed [53].

Figure 2(b) shows an illustration of MoMo adsorbed on the Cu(111) surface, superimposed onto a zoom image of the chain phase. The exact adsorption position on the surface is unknown, but also irrelevant for the following discussion. However, the black crosses in Fig. 2(a) indicate the relevant periodicity of the superstructure determined by STM. The unit cell along the chain direction is marked with a blue arrow ( $b_{Cu} = 1.110$  nm) and along the stacking direction with a red arrow ( $a_{Cu} = 1.020$  nm), enclosing an angle of  $\theta = 96.6^\circ$ . This adsorbates unit cell is commensurate to the underlying substrate. Each unit cell contains two molecules, with two different molecule adsorption positions within the unit cell. The molecules are separated by 0.530 and 0.580 nm along the chain direction [53]. Hence, on Cu(111) a second, probably energetically less favorable, adsorption position is accepted to enable a nearly optimal molecule-molecule distance along the

chain direction.

All stacking directions point along the high-symmetry  $\langle\bar{1}10\rangle$  and  $\langle 1\bar{1}0\rangle$  surface directions. For each stacking direction, one chain direction is favorable. The two opposite directions,  $\langle\bar{1}10\rangle$  and  $\langle 1\bar{1}0\rangle$ , therefore result in two mirrored island structures. In Fig. 2(b), the mirrored adsorption structure is marked with the dotted arrows. As expected from the surface symmetry, on Cu(111) this leads in total to six energetically equivalent island structures (see Fig. 2(c)), composed of six different island stacking directions (indicated by red arrows) and six different chain directions (indicated with blue arrows).

With the experiments presented here, we cannot determine the absolute microscopic adsorption position. However, the unit cell of the molecular adsorbates can be measured precisely, which is the key indicator for predicting the shape of the molecular islands at the mesoscale. With this knowledge, we now tune the mesoscopic molecular island shape by changing the underlying lattice periodicity. Upon increasing the lattice constant by changing from Cu(111) to Au(111), we induce a slightly larger molecule distance along the stacking direction (red) as compared to on Cu(111). Therefore, the lattice constant on Au(111) constitutes a nearly perfect fit to the bulk periodicity along the chain direction.

Figure 2(d) shows an overview STM image of MoMo on Au(111). The image again reveals a coexistence of two different island types. Based on a comparison with what we have found on Cu(111), we again find a phase of flat lying molecules (marked in cyan) and a phase that is composed of upright standing molecules (marked in blue). Therefore, we assign the structure of flat-lying molecules to the mesh phase and the structure of upright-standing molecules to the chain phase. In addition, some unordered molecular clusters are visible (marked in purple). For comparison, we again focus only on the chain phase. On Au(111), the chain phase consists solely of single, one-dimensional rows along the main symmetry directions  $\langle \bar{1}10 \rangle$  and  $\langle 1\bar{1}0 \rangle$ . On Au(111), a row length of up to about 200 nm is observed in the STM images. Similar to the two-dimensional chain phase on Cu(111), the one-dimensional chains on Au(111) end at step edge or other islands.

An illustration of MoMo adsorbed on the Au(111) surface, superimposed onto a zoom image of the chain phase is shown in Fig. 2(e). The chain phase islands solely form one-dimensional rows along the chain direction, extension along the stacking direction is not observed. In order to exclude a kinetically trapped structure, we have performed STM images at different temperatures in the range from 110 K up to 300 K. Even at elevated temperature, no change in the island shape is observed. Therefore, the extension along the stacking direction must be energetically unfavorable. The periodic molecule distance along the chain direction is marked with a blue arrow and black crosses ( $b_{Au} = 0.576$  nm). Following the substrate periodicity, a virtual two-dimensional unit cell is spanned up with a red arrow ( $a_{Cu} = 1.04$  nm) along the stacking direction, enclosing an angle of  $\theta = 106^\circ$ . This commensurable, virtual unit cell is identified by considering the next identical adsorption position upon keeping the unit cell dimension and angle as close to the molecular bulk unit cell as possible. However, such a hypothetical two-dimensional structure seems to be energetically unfavorable, because only single rows are observed. A mirrored adsorption structure is illustrated with dotted arrows. In total, six different chain directions along the  $\langle \bar{1}10 \rangle$  and  $\langle 1\bar{1}0 \rangle$  directions are observed, leading to six corresponding virtual stacking directions

as illustrated in Fig. 2(f).

In the third part of the result section, the self-assembly of submonolayers of MoMo on  $\text{CaF}_2(111)$  is discussed. Prior to molecule sublimation, high-resolution AFM images of the freshly cleaved  $\text{CaF}_2$  crystal (see Fig. 3(a)) are performed in order to determine the crystals orientation. Depending on the tip termination, different contrasts have been observed for  $\text{CaF}_2(111)$  with either the  $\text{Ca}^{2+}$  or  $\text{F}^-$  ions appearing brighter in the image [54, 55]. Therefore, the grey circles in Fig. 3(a) indicate the substrate periodicity and do not indicate specific ion positions. The high-symmetry directions  $\langle \bar{1}10 \rangle$  and  $\langle 1\bar{1}0 \rangle$ , and the lattice vectors are marked with blue arrows in Fig. 3(a).

At 130 K, dynamic AFM measurements are performed to determine the island structure as a function of the coverage (see Figs. 3(b)–3(d)). At a low coverage of 15% of a monolayer ( $\theta = 0.15$  ML) several islands, pointing in various directions, are visible. However, all islands exhibit a similar shape of lacerated rectangles, being elongated in specific directions (exemplary marked with a red arrow). We define the direction along the longest island side as the main axis and the island extension perpendicular to it as the island width. When increasing the coverage to half of a monolayer (see Fig. 3(c)) the number of islands per area and the island length along the main island axis direction increase, while the island width remains rather constant. A further increase of the coverage to nearly one monolayer (see Fig. 3(d)) leads to further elongation of the islands, but the island width still remains nearly unchanged. In total, six different directions for the main island axis are identified as illustrated with the red arrows in Fig. 3(d). The directions of the main island axes are independent of the temperature and coverage. The histograms in Fig. 3(e) display the average island width and length as a function of coverage. As mentioned above, a clear trend is visible. The island width remains rather constant, while the length increases with higher coverage.

In order to elucidate the inner island structure, high-resolution images are performed as shown in Fig. 4(a). Every island is made up of molecular chains lined up next to each other, similar to the arrangement in the bulk (see Fig. 1(c)). As

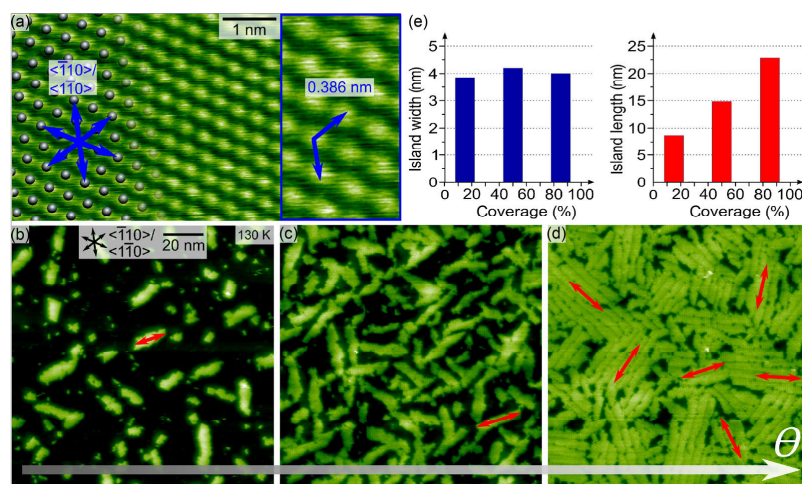


**Figure 3** (a) AFM image of freshly cleaved  $\text{CaF}_2(111)$ . High-symmetry directions  $\langle \bar{1}10 \rangle$  and  $\langle 1\bar{1}0 \rangle$  are marked with blue arrows. The lattice constant is indicated in the zoom image. (b)–(d) AFM images of MoMo on  $\text{CaF}_2(111)$  as a function of molecule coverage (b)  $\theta = 0.15$  ML, (c)  $\theta = 0.50$  ML and (d)  $\theta = 0.85$  ML at a fixed substrate temperature of about 130 K. At high coverage, several islands with the same direction of the main island axis are arranged next to each other. Red arrows indicate six different directions for the island main axis. The scale bar in (b) also applies to the images (c) and (d). (e) Average island width and length as a function of coverage. The average width remains nearly constant, while the average length increases.

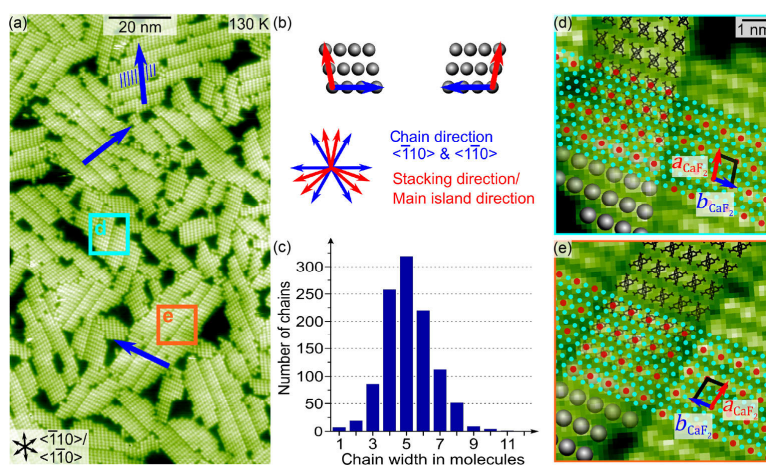


**Figure 4** (a) High-resolution AFM image of MoMo on  $\text{CaF}_2(111)$  with an island coverage of  $\theta = 0.85$  ML at about 130 K. Each island is made up of chains of molecules (indicated by blue arrows) oriented along the main surface symmetry directions  $\langle 110 \rangle$  and  $\langle 1\bar{1}0 \rangle$ . (b) For each of the chain directions along  $\langle 110 \rangle$  a mirrored island structure with the chain direction along  $\langle 1\bar{1}0 \rangle$  exist (indicated with blue arrows), leading to six different directions for the main island axis (indicated with red arrows). (c) Histogram of frequency of counted chains in image (a) as a function of the chain width in molecules. The average island width is five molecules. (d) and (e) Zoom onto two island structures that are mirror images of each other. The cyan blue circles indicate the substrate periodicity. The red circles mark the molecule positions. The superstructure with a unit cell dimension of  $b_{\text{CaF}_2} = 0.772$  nm (blue arrow),  $a_{\text{CaF}_2} = 1.021$  nm (red arrow) and angle of  $\gamma = 100.9^\circ$  are marked with the red and blue arrow, respectively.

indicated with blue arrows in Fig. 4(a), the molecular chains follow the main surface symmetry directions  $\langle 110 \rangle$  and  $\langle 1\bar{1}0 \rangle$ . For each chain direction along  $\langle 110 \rangle$  an energetically equivalent mirrored structure exists, with the chains pointing in the opposite  $\langle 1\bar{1}0 \rangle$  direction (see Fig. 4(b)). In total, this leads to six energetically equivalent island structures, composed of six chain directions (indicated with blue arrows) and one corresponding island stacking direction each (indicated by red arrows).

Quite contrary to the  $\text{Cu}(111)$  and  $\text{Au}(111)$  surface, the MoMo islands are mostly elongated (up to 50 nm) along the six stacking directions and are rather short (around 4 nm) in the six chain directions. Figure 4(c) displays a histogram of the chain widths frequency of occurrence. The histogram is obtained by counting the width of over 1,000 chains in the acquired AFM image shown in Fig. 4(a). The most frequent and also average chain width is five molecules. Approximately 7% of the chains have a width from four to six molecules and over 90% from three to seven molecules. For larger chain widths, the frequency of occurrence drastically decreases. The largest island width observed is eleven molecules. Therefore, a large island width must be energetically unfavorable. This might be a consequence of a slight offset of the molecule periodicity compared to the commensurability with the substrate.

Figures 4(d) and 4(e) show two mirrored MoMo islands on  $\text{CaF}_2(111)$  with the chain direction marked in blue and the stacking direction marked in red. Zooming onto the islands reveals the inner structure. The red circles highlight the molecule positions, which are commensurate with the periodicity of the substrate indicated by the cyan blue circles.<sup>①</sup> The surface unit cell of the superstructure is marked with a parallelogram spanned by a blue vector  $b_{\text{CaF}_2} = 0.772$  nm along the chain direction and a red vector  $a_{\text{CaF}_2} = 1.021$  nm along the stacking

direction enclosing an angle of  $\gamma = 100.9^\circ$ . Inspired by the molecular bulk structure (see Fig. 1(c)), a proposed molecule geometry of nearly up-right standing molecules is superimposed on the islands in the image.

#### 4 Discussion

In the following, the above described adsorption structure of submonolayers of MoMo on  $\text{Cu}(111)$ ,  $\text{Au}(111)$  and  $\text{CaF}_2(111)$  are critically discussed and compared to the known bulk structure. This analysis reveals the impact of the substrate on the molecular self-assembly and elucidates how to take advantage of this knowledge to direct the molecules to automatically arrange in a desired mesoscopic island shape.

As described above, the AB plane of the bulk consists of molecular chains stabilized by an intermolecular interaction between the positively charged ( $+1.17$  e) molybdenum atoms and the negatively charged ( $-0.29$  e) oxygen atoms of the neighboring molecules [48]. In the bulk, this leads to an optimized molecule-molecule spacing of 0.550 nm along the chains (chain direction) and a distance of 0.842 nm between the chains, referred to as stacking direction (see Table 1).

First, we will compare and elucidate the mesoscopic island structure between the two similar metallic substrates  $\text{Cu}(111)$  and  $\text{Au}(111)$ . In a second step, we will discuss in what manner the here described method of tuning the lattice constant can be applied to bulk insulators like  $\text{CaF}_2(111)$ , which exhibit a completely different electronic structure.

Our study reveals that similar chain phase islands form after deposition of MoMo molecules on both,  $\text{Cu}(111)$  and on  $\text{Au}(111)$  [53]. On both surfaces, the molecule-substrate interaction leads to a commensurate superstructure.

For  $\text{Cu}(111)$ , the lattice constant of 0.255 nm and its multiples do not fit well to the periodicity of 0.550 nm along the chain direction found in the MoMo bulk structure. However, on  $\text{Cu}(111)$  two different adsorption sites are occupied within one unit cell, resulting in a nearly ideal molecule-molecule distance of 0.530 and 0.580 nm (see Table 1). Consequently,

<sup>①</sup> As described above, the periodicity and orientation of the substrate is known, but not the absolute ion position. Thus, the cyan circles only represent the periodicity and not the absolute position.



**Table 1** Unit cell dimensions for the bulk AB plane and for the chain phase on Cu(111), Au(111) and CaF<sub>2</sub>(111). Lattice constants similar to the bulk structure are marked in green (< 10%) and major deviating lattice constants are marked in red. The deviation relative to the corresponding bulk lattice is given in percentage

MoMo ...	In bulk structure	On Cu (111)	On Au (111)	On CaF <sub>2</sub> (111)
Periodicity <i>b</i> along chain direction in nm	0.550	0.530/0.580 (+5%)	0.576 (+5%)	0.772 (+40%)
Periodicity <i>a</i> along stacking direction in nm	0.842	1.020 (+21%)	1.036 (+23%)	1.021 (+21%)
Angle $\gamma$ in °	106	96 (−9%)	106 (±0%)	101 (−5%)

along the chain direction MoMo prefers to have a nearly ideal molecule-molecule distance on the cost of a second, maybe energetically less favorable, adsorption position. However, along the stacking direction the molecule-molecule distance of 1.02 nm is approximately 20% larger than the ideal configuration in the MoMo bulk crystal. Presumably, the increased distance along the stacking direction weakens the interaction between neighboring chains, while the interaction of the molecules in the chains remains similar as in the bulk. Therefore, the substrate-induced change in the intermolecular interactions

offers a straightforward explanation as to why the resulting island shape is elongated in the chain direction, as the intermolecular-interactions are stronger along this direction. Our large-scale STM measurements confirm this assumption (see Figs. 4 and 5): On Cu (111), the chain phase islands are strongly elongated along the chain direction (indicated by a blue arrow) for more than 300 nm, but much shorter in the stacking direction (indicated by a red arrow).

In contrast to the structure on Cu(111), a different overall island shape is found for the self-assembly of MoMo on Au(111). The lattice constant of Au(111) is 0.288 nm, and hence, slightly larger than of Cu(111). Along the chain direction, two times the lattice constants of Au(111) results in a molecule-molecule distance of 0.576 nm (see Table 1), which already fits well to the ideal configuration in the bulk; allowing a strong molecule-molecule interaction along the chain direction. Therefore, on Au(111) the adsorbates can sit at the optimal adsorption position and still have a nearly perfect molecule-molecule distance along the chain direction. However, along the stacking direction the conceptual molecule-molecule distance of 1.036 nm is approximately 23% larger compared to the periodicity along the stacking direction in the bulk structure. The larger molecule periodicity weakens the molecule-molecule interactions between two neighboring chains to a negligible value, which explains the observed single chains (see Figs. 4 and 5).

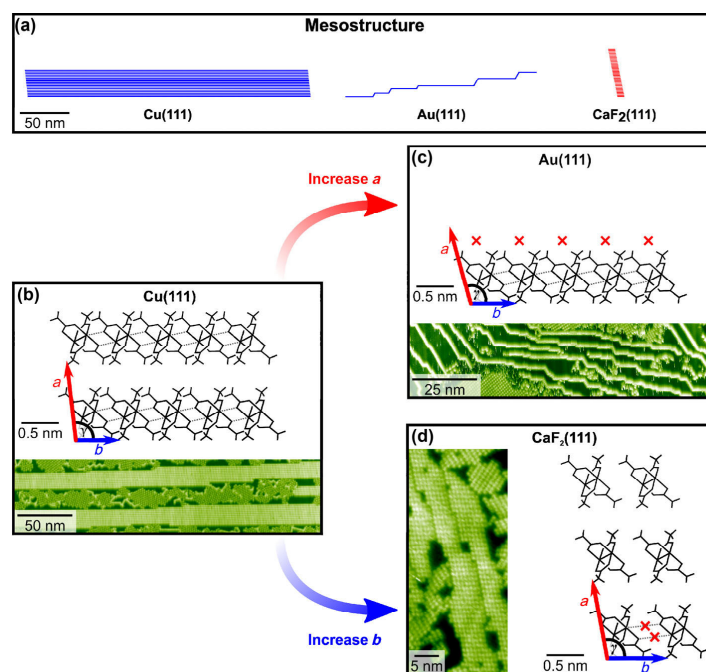


**Figure 5** Illustration of mesoscopic structure as a function of the substrates' lattices constant. (a) Comparison of MoMo island shapes on the substrates Cu(111), Au(111) and CaF<sub>2</sub>(111) at low temperature (110 K and 130 K, respectively). (b) The Cu (111) lattice allows a favorable molecule-molecule distance along the chain direction (indicated by a blue arrow), but induces a larger molecule distance along the stacking direction (indicated by a red arrow) as compared to the molecular bulk. Consequently, the islands are strongly elongated along the chain direction and short along the stacking direction. Next to the chain islands, there exists a mesh phase, which is not considered here. (c) The slightly larger lattice constant on Au(111) results in a large molecule-molecule distance along the stacking direction. Therefore, only one-dimensional rows, elongated along the chain direction are observed. (d) The periodicity of the CaF<sub>2</sub>(111) substrate and site specific adsorption leads to a similar molecule-molecule distance along the stacking direction as compared to Cu(111), but forces the molecules to increase the distance along the chain direction. In contrast to the island shape on Cu(111), the islands on CaF<sub>2</sub>(111) are, thus, elongated in the stacking direction and have a short chain length. The red crosses in (c) and (d) indicate a weakened molecule-molecule interaction compared to on Cu(111), caused by a larger molecule spacing along this direction.

By shedding light on the origin of the observed mesostructure of MoMo on Cu(111) and Au(111), we successfully demonstrated the presented strategy to control the self-assembled mesostructure by tuning the lattice constant. Changing the substrates from Cu(111) to Au(111) transforms two-dimensional islands into one-dimensional rows (see Figs. 5(a)–5(c)). Furthermore, we gain insights into the range of influence of the molecule-molecule interactions. While a molecule distance of 1.020 nm on Cu(111)—being equal to a mismatch of 0.178 nm compared to the ideal bulk configuration—still allows a weak interaction between neighboring chains, a slightly larger mismatch of 0.194 nm on Au(111) already results in a negligible molecule-molecule interaction.

As shown above, the described method to control the mesostructure by varying the lattice constant has worked well for the metallic substrates Cu(111) and Au(111), which exhibit a similar electronic structure. In the following, we will critically discuss to which extent this method can be transferred to bulk insulators like CaF<sub>2</sub>(111) and compare our prediction to the observed self-assembled MoMo island structures.

Interestingly, MoMo on CaF<sub>2</sub>(111) exhibits site specific adsorption and, hence, a commensurate superstructure as on the noble metal surfaces and a similar molecule orientation of nearly upright standing molecules in the chain phase. However, it reveals a completely different mesoscopic island shape. On the insulator, the distance between two chains along the stacking direction is equal to the one on Cu(111), about 20% larger than the bulk value. However, the molecule spacing along the chain direction is approximately 40% larger as compared to the bulk structure (see Table 1). Therefore, on CaF<sub>2</sub>(111), the molecule-molecule interaction along the chains is expected to be greatly reduced. Consequently, on CaF<sub>2</sub>(111) one expects the island growth to be suppressed along the chain direction. As predicted, the islands on CaF<sub>2</sub>(111) are predominately elongated along the stacking direction, but with a modest length (~ 40 nm) as compared to the island length on Cu(111) (~ 300 nm) as illustrated in Fig. 5(d). Furthermore, at low temperature, the islands are considerably larger on Cu(111) as compared to CaF<sub>2</sub>(111) (see Fig. 5(b)).

Regardless of the substrates microscopic electronic differences, the commensurate superstructure and the similar molecule-molecule interaction mechanism of MoMo on Cu(111), Au(111) and CaF<sub>2</sub>(111) enables the possibility to successfully control the islands mesostructure by changing the substrates' lattice constant. For explaining the resulting mesoscopic island structure, we make use of strong simplifications. Therefore, we understand that systems can exist where this simple model will break down. However, for the three examples tested here, our simple model provides a reasonable explanation for the resulting mesoscopic island shapes.

## 5 Conclusion

A strategy is presented for tuning the mesoscopic island shape by rationally changing the underlying substrates' lattice constant. As a model system, MoMo molecules are deposited on three different surfaces, Cu(111), Au(111) and CaF<sub>2</sub>(111). The used substrates are similar as they exhibit hexagonal symmetry, but, compared to Cu(111), Au(111) and CaF<sub>2</sub>(111) offer by a factor of 1.1 and 1.5 larger lattice constants, respectively. Our scanning probe microscopy results reveal elongated islands in all cases, however, the internal molecule stacking and the directions with respect to the orientation of the substrate differ significantly. For Cu(111), two-dimensional islands are elongated along the chain direction while for CaF<sub>2</sub>(111), two-dimensional islands

are elongated along the stacking direction. For Au(111), in contrast to the other surfaces, only one-dimensional single rows along the chain direction are formed. These differences in the mesoscopic shape can be rationalized by the subtle balance between molecule-surface and intermolecular interactions at the molecular level. The commensurability of the structures dictates the intermolecular spacing in the islands and, thus, the thermodynamically most favorable island shape is a direct consequence of the lattice mismatch. For Cu(111), we conclude that the lattice dimension fits perfectly to the chain direction of the molecular bulk structure, while in the stacking direction the substrate induces a 20% increased molecule-molecule distance. As predicted, we found for Au(111) a slightly larger mismatch of 23% along the stacking direction, weakening the interaction between neighboring chains even further to a negligible value. Hence, for Au(111) only single rows form along the chain direction. For CaF<sub>2</sub>(111), the molecule-molecule distance is extended in both directions, however, in this case the stacking direction is more favorable as it exhibits the smaller deviation (both absolute and percentagewise). Interestingly, for site specific adsorption the mesoscopic island shape can be rationalized from the surface geometry alone, without considering microscopic electronic details. This work contributes to a comprehensive understanding of tuning mesoscopic island shapes by controlling the interactions at the molecular scale, which is mandatory for understanding the performance of future molecular devices.

## Author contributions

The manuscript was written through contributions of all authors. All authors have given approval to the final version of the manuscript.

## Acknowledgements

S. A. is a recipient of a DFG-fellowship through the Excellence Initiative by the Graduate School Materials Science in Mainz (GSC 266). L. L., B. S., and M. A. thank the Deutsche Forschungsgemeinschaft (DFG, SFB/TRR 88 "Cooperative Effects in Homo- and Heterometallic Complexes (3MET)" Project C5) for financial support and Markus Gerhards (University of Kaiserslautern) for stimulating discussions.

**Funding note** Open access funding provided by Projekt DEAL.

**Open Access** This article is licensed under a Creative Commons Attribution 4.0 International License, which permits use, sharing, adaptation, distribution and reproduction in any medium or format, as long as you give appropriate credit to the original author(s) and the source, provide a link to the Creative Commons licence, and indicate if changes were made.

The images or other third party material in this article are included in the article's Creative Commons licence, unless indicated otherwise in a credit line to the material. If material is not included in the article's Creative Commons licence and your intended use is not permitted by statutory regulation or exceeds the permitted use, you will need to obtain permission directly from the copyright holder.

To view a copy of this licence, visit <http://creativecommons.org/licenses/by/4.0/>.

## References

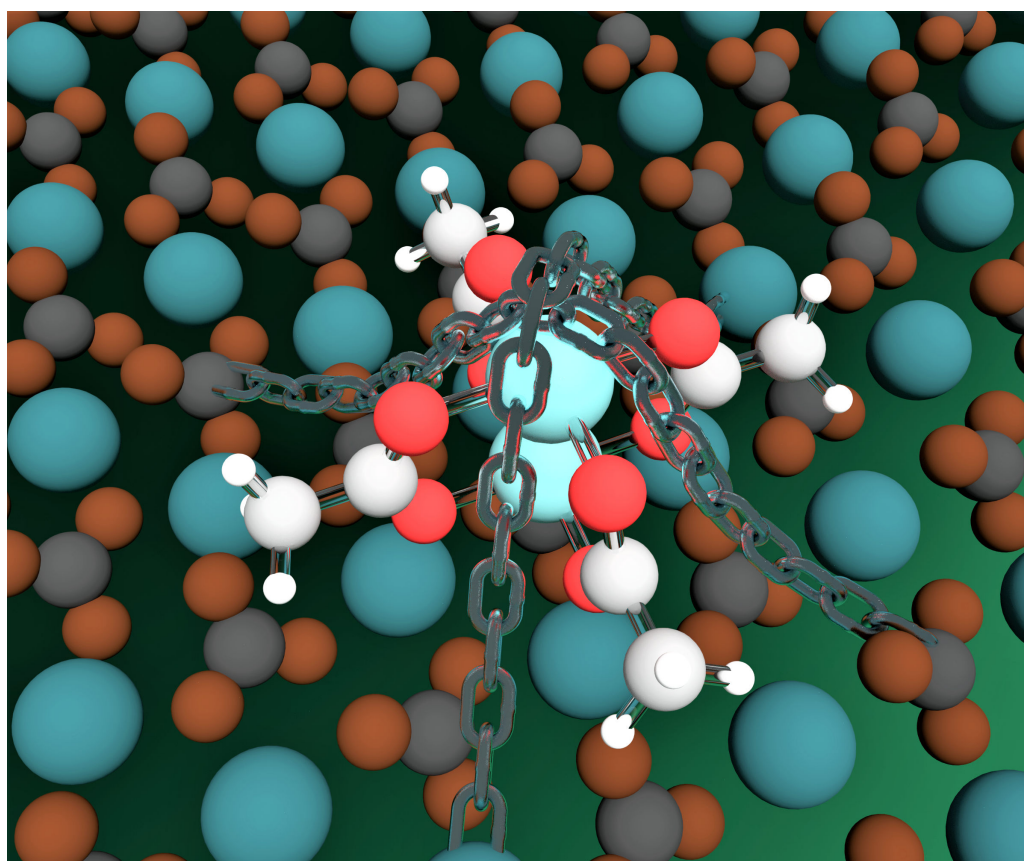
- [1] Lehn, J. M. Supramolecular chemistry—scope and perspectives molecules, supermolecules, and molecular devices (Nobel Lecture). *Angew. Chem., Int. Ed.* **1988**, *27*, 89–112.

- [2] Barth, J. V.; Costantini, G.; Kern, K. Engineering atomic and molecular nanostructures at surfaces. *Nature* **2005**, *437*, 671–679.
- [3] Barth, J. V. Molecular architecture on metal surfaces. *Annu. Rev. Phys. Chem.* **2007**, *58*, 375–407.
- [4] Erler, P.; Schmitt, P.; Barth, N.; Irmiler, A.; Bouvron, S.; Huhn, T.; Groth, U.; Pauly, F.; Gragnaniello, L.; Foni, M. Highly ordered surface self-assembly of Fe<sub>4</sub> single molecule magnets. *Nano Lett.* **2015**, *15*, 4546–4552.
- [5] Leonhardt, E. J.; Van Raden, J. M.; Miller, D.; Zakharov, L. N.; Alemán, B.; Jasti, R. A bottom-up approach to solution-processed, atomically precise graphitic cylinders on graphite. *Nano Lett.* **2018**, *18*, 7991–7997.
- [6] Timmer, A.; Mönig, H.; Uphoff, M.; Diaz Arado, O.; Amirjalayer, S.; Fuchs, H. Site-specific adsorption of aromatic molecules on a metal/metal oxide phase boundary. *Nano Lett.* **2018**, *18*, 4123–4129.
- [7] Whitesides, G. M.; Mathias, J. P.; Seto, C. T. Molecular self-assembly and nanochemistry: A chemical strategy for the synthesis of nanostructures. *Science* **1991**, *254*, 1312–1319.
- [8] Nieckarz, D.; Rzyzko, W.; Szabelski, P. On-surface self-assembly of tetrapotic molecular building blocks. *Phys. Chem. Chem. Phys.* **2018**, *20*, 23363–23377.
- [9] De Feyter, S.; De Schryver, F. C. Two-dimensional supramolecular self-assembly probed by scanning tunneling microscopy. *Chem. Soc. Rev.* **2003**, *32*, 139–150.
- [10] Bauer, O.; Mercurio, G.; Willenbockel, M.; Reckien, W.; Schmitz, C. H.; Fiedler, B.; Soubatch, S.; Bredow, T.; Tautz, F. S.; Sokolowski, M. Role of functional groups in surface bonding of planar  $\pi$ -conjugated molecules. *Phys. Rev. B* **2012**, *86*, 235431.
- [11] Willenbockel, M.; Lüftner, D.; Stadtmüller, B.; Koller, G.; Kumpf, C.; Soubatch, S.; Puschnig, P.; Ramsey, M. G.; Tautz, F. S. The interplay between interface structure, energy level alignment and chemical bonding strength at organic-metal interfaces. *Phys. Chem. Chem. Phys.* **2015**, *17*, 1530–1548.
- [12] Stepanow, S.; Ohmann, R.; Leroy, F.; Lin, N.; Strunskus, T.; Wöll, C.; Kern, K. Rational design of two-dimensional nanoscale networks by electrostatic interactions at surfaces. *ACS Nano* **2010**, *4*, 1813–1820.
- [13] Zhao, W. H.; Zhu, H.; Song, H. J.; Liu, J.; Chen, Q. W.; Wang, Y.; Wu, K. Adsorption and assembly of photoelectronic TioPc molecules on coinage metal surfaces. *J. Phys. Chem. C* **2018**, *122*, 7695–7701.
- [14] Huempfer, T.; Sojka, F.; Forker, R.; Fritz, T. Growth of coronene on (100)- and (111)-surfaces of fcc-crystals. *Surf. Sci.* **2015**, *639*, 80–88.
- [15] Mannsfeld, S. C. B.; Fritz, T. Understanding organic-inorganic heteroepitaxial growth of molecules on crystalline substrates: Experiment and theory. *Phys. Rev. B* **2005**, *71*, 235405.
- [16] Kumar, A.; Banerjee, K.; Liljeroth, P. Molecular assembly on two-dimensional materials. *Nanotechnology* **2017**, *28*, 082001.
- [17] He, X. Y.; Zhang, L.; Chua, R.; Wong, P. K. J.; Arramel, A.; Feng, Y. P.; Wang, S. J.; Chi, D. Z.; Yang, M.; Huang, Y. L. et al. Selective self-assembly of 2,3-diaminophenazine molecules on MoSe<sub>2</sub> mirror twin boundaries. *Nat. Comm.* **2019**, *10*, 2847.
- [18] Lazarov, V. K.; Cai, Z. H.; Yoshida, K.; Zhang, K. H. L.; Weinert, M.; Ziemer, K. S.; Hasnip, P. J. Dynamically stabilized growth of polar oxides: The case of MgO(111). *Phys. Rev. Lett.* **2011**, *107*, 056101.
- [19] Goniakowski, J.; Finocchi, F.; Noguera, C. Polarity of oxide surfaces and nanostructures. *Rep. Prog. Phys.* **2008**, *71*, 016501.
- [20] Noguera, C. Polar oxide surfaces. *J. Phys.: Condens. Matter* **2000**, *12*, R367–R410.
- [21] White, T. W.; Martinsovich, N.; Troisi, A.; Costantini, G. Quantifying the “subtle interplay” between intermolecular and molecule-substrate interactions in molecular assembly on surfaces. *J. Phys. Chem. C* **2018**, *122*, 17954–17962.
- [22] Otero, R.; Gallego, J. M.; De Parga, A. L. V.; Martín, N.; Miranda, R. Molecular self-assembly at solid surfaces. *Adv. Mater.* **2011**, *23*, 5148–5176.
- [23] Slater, A. G.; Beton, P. H.; Champness, N. R. Two-dimensional supramolecular chemistry on surfaces. *Chem. Sci.* **2011**, *2*, 1440–1448.
- [24] Goronzy, D. P.; Ebrahimi, M.; Rosei, F.; Arramel, A.; Fang, Y.; De Feyter, S.; Tait, S. L.; Wang, C.; Beton, P. H.; Wee, A. T. S. et al. Supramolecular assemblies on surfaces: Nanopatterning, functionality, and reactivity. *ACS Nano* **2018**, *12*, 7445–7481.
- [25] Cun, H. Y.; Wang, Y. L.; Du, S. X.; Zhang, L.; Zhang, L. Z.; Yang, B.; He, X. B.; Wang, Y.; Zhu, X. Y.; Yuan, Q. Z. et al. Tuning structural and mechanical properties of two-dimensional molecular crystals: The roles of carbon side chains. *Nano Lett.* **2012**, *12*, 1229–1234.
- [26] Gesquière, A.; Jonkheijm, P.; Hoeben, F. J. M.; Schenning, A. P. H. J.; De Feyter, S.; De Schryver, F. C.; Meijer, E. W. 2D-structures of quadruple hydrogen bonded oligo(p-phenylenevinylene)s on graphite: Self-assembly behavior and expression of chirality. *Nano Lett.* **2004**, *4*, 1175–1179.
- [27] Mukherjee, A.; Sanz-Matias, A.; Velpula, G.; Waghay, D.; Ivasenko, O.; Bilbao, N.; Harvey, J. N.; Mali, K. S.; De Feyter, S. Halogenated building blocks for 2D crystal engineering on solid surfaces: Lessons from hydrogen bonding. *Chem. Sci.* **2019**, *10*, 3881–3891.
- [28] Kühnle, A.; Molina, L. M.; Linderth, T. R.; Hammer, B.; Besenbacher, F. Growth of unidirectional molecular rows of cysteine on Au(110)-(1×2) driven by adsorbate-induced surface rearrangements. *Phys. Rev. Lett.* **2004**, *93*, 086101.
- [29] Rahe, P.; Nimmrich, M.; Greuling, A.; Schütte, J.; Stará, I. G.; Rybáček, J.; Huerta-Angel, G.; Starý, I.; Rohlfing, M.; Kühnle, A. Toward molecular nanowires self-assembled on an insulating substrate: Heptahelicene-2-carboxylic acid on calcite (1014). *J. Phys. Chem. C* **2010**, *114*, 1547–1552.
- [30] Pawin, G.; Wong, K. L.; Kwon, K. Y.; Bartels, L. A homomolecular porous network at a Cu(111) surface. *Science* **2006**, *313*, 961–962.
- [31] Li, J.; Wiegold, S.; Öner, M. A.; Simon, P.; Hauf, M. V.; Margapoti, E.; Garrido, J. A.; Esch, F.; Palma, C. A.; Barth, J. V. Three-dimensional bicomponent supramolecular nanoporous self-assembly on a hybrid all-carbon atomically flat and transparent platform. *Nano Lett.* **2014**, *14*, 4486–4492.
- [32] Kim, H. W.; Jung, J.; Han, M.; Ku, J.; Kuk, Y.; Kim, Y. Dimensionality control of self-assembled azobenzene derivatives on a gold surface. *J. Phys. Chem. C* **2019**, *123*, 8859–8864.
- [33] Kezilebieke, S.; Amokrane, A.; Boero, M.; Clair, S.; Abel, M.; Bucher, J. P. Steric and electronic selectivity in the synthesis of Fe-1,2,4,5-tetracyanobenzene (TCNB) complexes on Au(111): From topological confinement to bond formation. *Nano Res.* **2014**, *7*, 888–897.
- [34] Keeling, D. L.; Oxtoby, N. S.; Wilson, C.; Humphry, M. J.; Champness, N. R.; Beton, P. H. Assembly and processing of hydrogen bond induced supramolecular nanostructures. *Nano Lett.* **2003**, *3*, 9–12.
- [35] Theobald, J. A.; Oxtoby, N. S.; Phillips, M. A.; Champness, N. R.; Beton, P. H. Controlling molecular deposition and layer structure with supramolecular surface assemblies. *Nature* **2003**, *424*, 1029–1031.
- [36] Blunt, M. O.; Hu, Y.; Toft, C. W.; Slater, A. G.; Lewis, W.; Champness, N. R. Controlling the two-dimensional self-assembly of functionalized porphyrins via adenine–thymine quartet formation. *J. Phys. Chem. C* **2018**, *122*, 26070–26079.
- [37] Pfeiffer, C. R.; Pearce, N.; Champness, N. R. Complexity of two-dimensional self-assembled arrays at surfaces. *Chem. Commun.* **2017**, *53*, 11528–11539.
- [38] Goiri, E.; Matena, M.; El-Sayed, A.; Lobo-Checa, J.; Borghetti, P.; Rogero, C.; Detlefs, B.; Duvemay, J.; Ortega, J. E.; De Oteyza, D. G. Self-assembly of bicomponent molecular monolayers: Adsorption height changes and their consequences. *Phys. Rev. Lett.* **2014**, *112*, 117602.
- [39] Stadtmüller, B.; Lüftner, D.; Willenbockel, M.; Reinisch, E. M.; Sueyoshi, T.; Koller, G.; Soubatch, S.; Ramsey, M. G.; Puschnig, P.; Tautz, F. S. et al. Unexpected interplay of bonding height and energy level alignment at heteromolecular hybrid interfaces. *Nat. Commun.* **2014**, *5*, 3685.
- [40] Hooks, D. E.; Fritz, T.; Ward, M. D. Epitaxy and molecular organization on solid substrates. *Adv. Mater.* **2001**, *13*, 227–241.
- [41] Zhou, H. T.; Zhang, L. Z.; Mao, J. H.; Li, G.; Zhang, Y.; Wang, Y. L.; Du, S. X.; Hofer, W. A.; Gao, H. J. Template-directed assembly of pentacene molecules on epitaxial graphene on Ru(0001). *Nano Res.* **2013**, *6*, 131–137.
- [42] Kalashnyk, N.; Ledieu, J.; Gaudry, É.; Cui, C.; Tsai, A. P.; Fournée, V. Building 2D quasicrystals from 5-fold symmetric corannulene molecules. *Nano Res.* **2018**, *11*, 2129–2138.
- [43] Cotton, F. A.; Daniels, L. M.; Hillard, E. A.; Murillo, C. A. The lengths of molybdenum to molybdenum quadruple bonds: Correlations, explanations, and corrections. *Inorg. Chem.* **2002**, *41*, 2466–2470.

- [44] Kelley, M. H.; Fink, M. The molecular structure of dimolybdenum tetra-acetate. *J. Chem. Phys.* **1982**, *76*, 1407–1416.
- [45] Ross, R. G.; Hume-Rothery, W. High temperature X-ray metallography: I. A new debye-scherrer camera for use at very high temperatures II. A new para-focusing camera III. Applications to the study of chromium, hafnium, molybdenum, rhodium, ruthenium and tungsten. *J. Less Common Met.* **1963**, *5*, 258–270.
- [46] Lawton, D.; Mason, R. The molecular structure of molybdenum(II) acetate. *J. Am. Chem. Soc.* **1965**, *87*, 921–922.
- [47] Cotton, F. A.; Mester, Z. C.; Webb, T. R. Dimolybdenum tetraacetate. *Acta Crystallogr. Sect. B: Struct. Sci., Cryst. Eng. Mater.* **1974**, *30*, 2768–2770.
- [48] Hino, K.; Saito, Y.; Benard, M. Electron-density distribution in crystals of tetra- $\mu$ -acetato-dimolybdenum(Mo-Mo). *Acta Crystallogr. Sect. B: Struct. Sci., Cryst. Eng. Mater.* **1981**, *37*, 2164–2170.
- [49] Lichtenberger, D. L.; Ray, C. D.; Stepniak, F.; Chen, Y.; Weaver, J. H. The electronic nature of the metal-metal quadruple bond: Variable photon energy photoelectron spectroscopy of  $\text{Mo}_2(\text{O}_2\text{CCH}_3)_4$ . *J. Am. Chem. Soc.* **1992**, *114*, 10492–10497.
- [50] Lichtenberger, D. L.; Kristofzski, J. G. Intermolecular influences on M–M multiple bonds from thin-film UPS studies of group VI  $\text{M}_2(\text{O}_2\text{CCH}_3)_4$  complexes. *J. Am. Chem. Soc.* **1987**, *109*, 3458–3459.
- [51] Engelhardt, J. B.; Dabringhaus, H.; Wandelt, K. Atomic force microscopy study of the  $\text{CaF}_2(111)$  surface: From cleavage via island to evaporation topographies. *Surf. Sci.* **2000**, *448*, 187–200.
- [52] Albrecht, T. R.; Grütter, P.; Horne, D.; Rugar, D. Frequency modulation detection using high- $Q$  cantilevers for enhanced force microscope sensitivity. *J. Appl. Phys.* **1991**, *69*, 668–673.
- [53] Kollamana, J.; Wei, Z.; Lyu, L.; Zimmer, M.; Dietrich, F.; Eul, T.; Stöckl, J.; Maniraj, M.; Ponzoni, S.; Cinchetti, M. et al. Control of cooperativity through a reversible structural phase transition in momo-methyl/Cu(111). *Adv. Funct. Mater.* **2018**, *28*, 1703544.
- [54] Foster, A. S.; Barth, C.; Shluger, A. L.; Reichling, M. Unambiguous interpretation of atomically resolved force microscopy images of an insulator. *Phys. Rev. Lett.* **2001**, *86*, 2373–2376.
- [55] Foster, A. S.; Barth, C.; Shluger, A. L.; Nieminen, R. M.; Reichling, M. Role of tip structure and surface relaxation in atomic resolution dynamic force microscopy:  $\text{CaF}_2(111)$  as a reference surface. *Phys. Rev. B* **2002**, *66*, 235417.

## Anchoring of metal-complexing molecules on a bulk-insulator surface: Creating a regular metal array at room temperature

This paper manuscript from Simon Aeschlimann, Sebastian V. Bauer, Maximilian Vogtland, Benjamin Stadtmüller, Martin Aeschlimann, Andrea Floris, Ralf Bechstein and Angelika Kühnle is currently under review.



## 5.1 Abstract

Controlling self-assembled nanostructures on bulk insulators at room temperature is crucial towards the fabrication of future molecular devices, *e.g.*, in the field of nanoelectronics, catalysis and sensor applications. However, at temperatures realistic for operation anchoring individual molecules on electrically insulating support surfaces remains a big challenge, due to the inertness of the substrate. Here, we present the formation of an ordered array of single anchored molecules, namely dimolybdenum tetraacetate, on the (10.4) cleavage plane of calcite ( $\text{CaCO}_3$ ). Based on our combined study of atomic force microscopy measurements and density functional theory calculations, we show that the molecules neither diffuse nor rotate at room temperature. The strong anchoring is explained by electrostatic interaction of an ideally size-matched molecule. When increasing the coverage, entropy drives the molecules to form locally ordered arrays. More specifically, the patterning is assigned to the strong molecule-surface interaction and a hard-sphere repulsion of the molecules, which is conceptually different from attractive linkers as used in metal-organic frameworks. Our work demonstrates that tailoring the molecule-surface interaction opens up the possibility for anchoring individual metal-complexing molecules into ordered arrays.

## 5.2 Introduction

Molecules on surfaces [77, 78] offer a great variability of creating functional structures for future technologies [79–81], including molecular electronics [82, 83], data storage [84, 85], sensing [86] and catalysis [87, 88]. This is particularly true when considering molecules that carry or coordinate metal atoms, *e.g.*, in structures formed from metalated molecules such as metaloporphyrins [89] and metalocyanines [90] as well as surface-supported metal-organic frameworks [91, 92] or metal-organic coordination networks [93]. All these structures offer additional interesting magnetic and superior catalytic [87] activities [91, 94–96]. Creating functional molecular structures on surfaces is based on the capability to anchor molecules to specific adsorption sites under operation condition, *i.e.*, ideally at room temperature. For many applications, in particular molecular electronics, data storage, sensing and catalysis, it is highly desirable to decouple the electronic structure of the molecules - and especially coordinated metal atoms - from the underlying substrate surface [97], which can be achieved by using a bulk insulator as substrate. Many insulator surfaces, however, are rather inert [25, 98], which is why organic molecules often exhibit weak binding and high diffusivity on bulk insulator surfaces. In recent years, several strategies have been developed for anchoring organic molecules to insulator surfaces, including molecule functionalization for specific binding or increasing electrostatic

interactions [13, 99–104]. However, stabilizing single molecules on an electrically insulating support sample at room temperature remains a great challenge, and examples are limited to clusters [105] rather than single molecules. As stabilizing single molecules on bulk insulators bear great potential for future applications, it is highly desired to develop strategies to prevent the molecules from clustering, but still exhibiting a sufficient molecule-substrate interaction for anchoring. So far, it has been demonstrated that single molecules can be trapped at defects on rutile titanium dioxide (110) [106]. However, in presence of the defects, the band gap of  $\text{TiO}_2$  is strongly reduced, and hence, the insulating properties vanish [107]. As far as we know, cytosine trimers on the calcium fluoride (111) cleavage plane have been identified to be the smallest observed stable configuration at room temperature on a bulk insulator [105]. For cytosine monomers, a diffusion barrier of 0.5 eV has been determined [105], which corresponds to a high mobility at room temperature. Until now, only larger monomers, like 4,4'-di(4-carboxyphenyl)-6,6'-dimethyl-2,2'-bipyridine on NiO (001), are found to have a reduced mobility on insulators [108]. But in the latter case, due to a strong molecule-molecule interaction, cluster or even larger molecular islands are formed at increased coverage. Thus, to the best of our knowledge, at room temperature no immobile and stable monomers on bulk insulators have been observed so far.

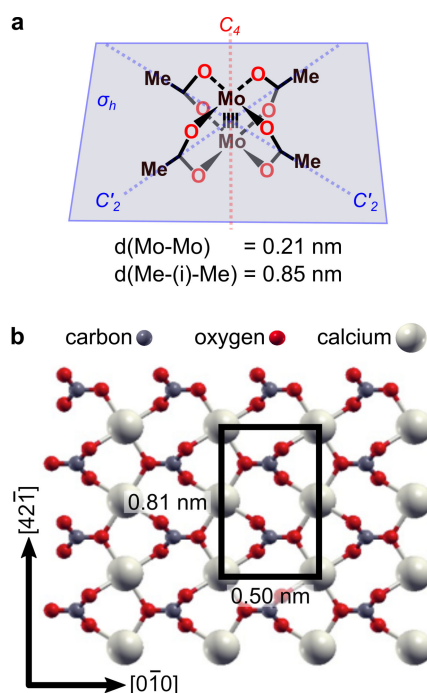


**Fig. 5.1.:** Model of the system studied here. (a) The MoMo molecule adsorbed on (b) the calcite (10.4) surface. The surface unit cell is marked with a black rectangle.

Here, we present the formation of an ordered array of individual dimolybdenum tetraacetate ( $\text{Mo}_2(\text{O}_2\text{CMe})_4$ , in this work referred to as MoMo, Fig. 5.1a) molecules

on the natural (10.4) cleavage plane of the bulk insulator calcite, the most stable modification of calcium carbonate (for a surface structure see Fig. 5.1b). Based on our atomic force microscopy (AFM) images carried out in the frequency modulation mode under ultra-high vacuum conditions, we provide experimental evidence of the fact that the MoMo molecules neither diffuse nor rotate on the surface held at room temperature. Our results indicate that the molecules adopt a specific adsorption position that is governed by a perfect match between the charge distribution within the molecule and at the surface. The resulting electrostatic interaction leads to a strong anchoring of single molecules in a well-defined, arrested geometry with apparently high diffusion and rotation barriers.

When increasing the molecule coverage on the surface, the molecules arrange in an ordered array. As MoMo contains metal atoms, our work constitutes an example for creating an ordered array of metal atoms on a bulk insulator material. Thus, we arrive at a structure similar to the situation in surface-supported metal-organic frameworks. Interestingly, the observed order is not induced by intermolecular attraction, but a strong, side-specific surface interaction and a hard-sphere repulsion between the molecules. Thus, in contrast to the attractive linkers employed in surface-supported metal-organic frameworks, in our system the order is based on a combination of intermolecular repulsion and substrate specific adsorption positions. Therefore, this work describes a prime example of single, metal-coordinating molecules strongly anchored onto an insulator surface at room temperature and, hence, elucidates an alternative route for creating an ordered metal array.

### 5.3 Results and Discussion

Upon submonolayer deposition of MoMo onto calcite (10.4) held at room temperature, individual features can be recognized in AFM images as shown in Fig. 5.2. From the size of these bright features and the high-resolution images presented below, we can clearly assign the bright features to single molecules. In Fig. 5.2a, a representative image is given after low-coverage deposition (approximately 0.07 molecules per  $\text{nm}^2$ ). Here, a calcite terrace is seen with individual molecules that are randomly scattered over the surface. Each molecule is imaged as a protrusion with radial symmetry. No inner structure can be recognized in this image. When increasing the coverage to approximately 0.41 molecules per  $\text{nm}^2$ , areas with higher molecule density can be seen as in Fig. 5.2b. At this coverage, no obvious order can be observed in the areas with higher density. The latter finding is changed when further increasing the coverage to 0.65 molecules per  $\text{nm}^2$  as in Fig. 5.2c. Now, some short-range order becomes apparent in small domains in the areas with high molecule density (marked with white circles in Fig. 5.2d), *e.g.*, in the upper right



area of the image. In Fig. 5.2d, height profiles are taken along the main symmetry directions  $[42\bar{1}]$  (see yellow arrow) and  $[0\bar{1}0]$  (see blue arrow) of the calcite substrate. The maxima in these height profiles are commensurate with the periodicity of the underlying substrate, which is indicated by white calcium ions. Consequently, MoMo molecules seem to adopt a favorite adsorption site on the surface.

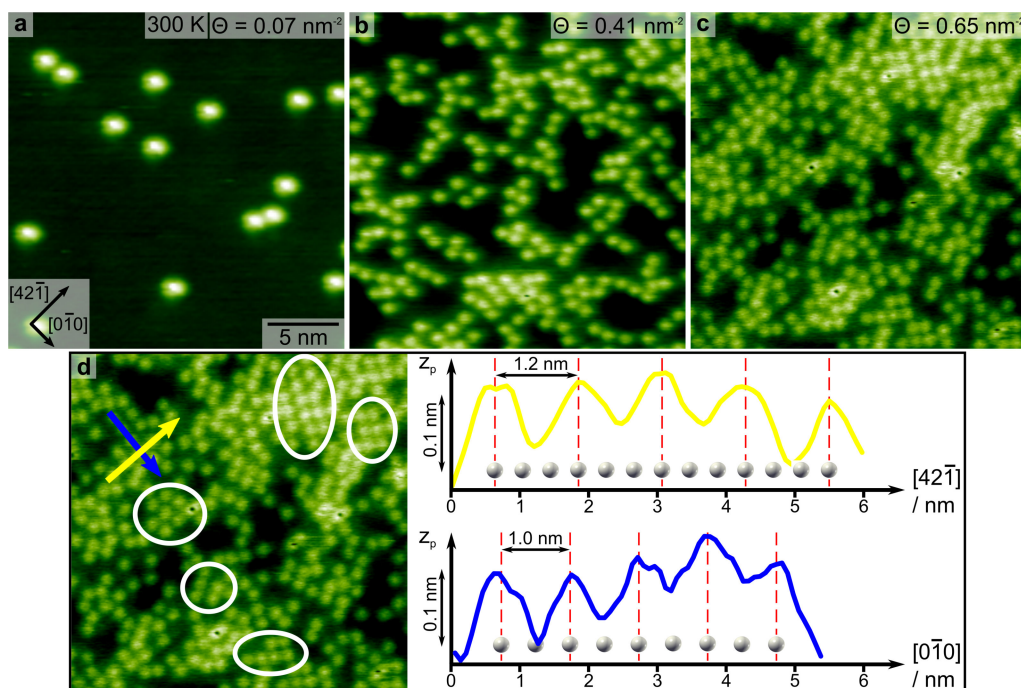


**Fig. 5.2.:** AFM image of MoMo molecules on calcite (10.4) as a function of coverage. (a) At a low coverage of 0.07 molecules per  $\text{nm}^2$ , single molecules are obtained. (b) Upon increasing the coverage to 0.41 molecules per  $\text{nm}^2$ , areas with higher molecule density are seen, however, no ordered inner structure is visible. (c) At a high coverage of 0.65 molecules per  $\text{nm}^2$ , partly ordered domains can be observed. (d) Some ordered domains are marked with a white circle. Height profiles along the  $[42\bar{1}]$  (yellow arrow) and  $[0\bar{1}0]$  (blue arrow) direction are displayed. The white calcium ions indicate the substrate lattice. MoMo adsorbs exclusively on identical adsorption sites.

To shed light onto the adsorption geometry of the MoMo molecule on calcite (10.4), we next perform high-resolution images with the tip close to the surface (*i.e.*, large excitation frequency shift values) as given in Fig. 5.3. As can be seen in Fig. 5.3a, the molecules now appear as features with a bright rim and a dark cross-like structure in the center. The here observed change in contrast of the molecules from bright dots to dark cross-like objects upon decreasing the tip-sample distance can be explained as contrast inversion upon entering into the repulsive regime [109, 110]. Interestingly, the appearance of the dark cross in the inner part of the molecule sheds light onto important details about the molecule adsorption geometry. First, the  $C_4$  symmetric shape of the inner cross indicates that the molecules lie flat on the surface rather than standing upright. Second, all crosses show the same orientation with respect

to the  $[0\bar{1}0]$  crystal direction as evidenced by the reproduction of the crosses in Fig. 5.3b. Therefore, we conclude that MoMo cannot rotate freely at its adsorption spot on the calcite surface. Still, a possibility exists for a stepwise rotation of  $\pm 90^\circ$ , however, since MoMo possesses a  $C_4$  symmetry this rotation would not change the adsorption configuration. Hence, MoMo is effectively locked in one adsorption configuration on the calcite surface (see zoom images in Fig. 5.3c). Third, as the molecules are imaged intact in our AFM measurements, jumps from one to the other adsorption site are very rare. The latter finding already provides a first indication for a high diffusion barrier experienced by MoMo on calcite (10.4).

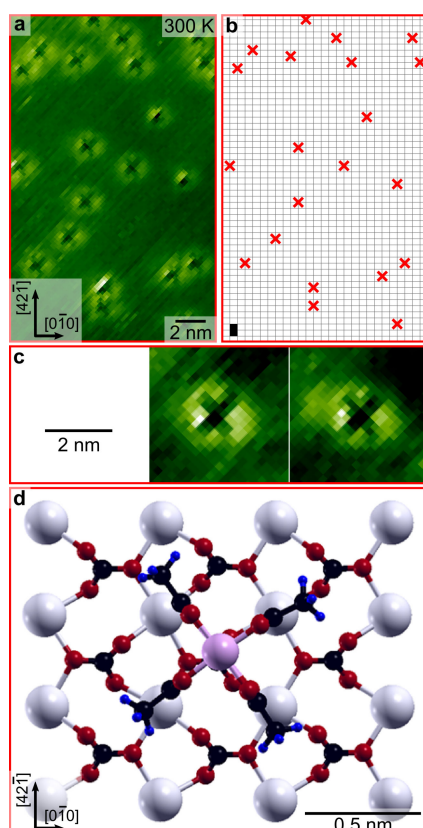


**Fig. 5.3.:** MoMo adsorption geometry on calcite (10.4). (a) High-resolution AFM image of MoMo molecules on calcite (10.4) held at room temperature. The molecules are imaged as dark, cross-like structure surrounded by a bright rim. All crosses are oriented in the same direction. (b) Sketch of the position of the crosses to illustrate the uniform orientation and adsorption site. A calcite (10.4) unit cell is marked with a black rectangle in the bottom left corner. Due to non-linear thermal drift, a slight deviation between (a) and (b) is visible. (c) Zoom onto two molecules highlighting the cross-like structure. (d) Top view of the thermodynamically most stable MoMo adsorption geometry on calcite (10.4) determined by DFT calculations.

To elucidate the adsorption geometry, we performed density functional theory (DFT) calculations of a single MoMo molecule on calcite (10.4). Fig. 5.3d shows the most favorable adsorption geometry out of 64 tested molecule configurations (see Sup-

porting Information, I. Section, Fig. 5.6). Our calculations clearly indicate that the adsorption geometry is governed by electrostatics: The positive molecule core composed of the two molybdenum atoms is centered on top of a negatively charged carbonate group. Moreover, the molecule aligns in a way that four of the oxygen atoms of the molecule can interact with the positively charged calcium ions of the surface. This adsorption geometry readily explains the experimentally observed cross-like features in our AFM images.

Next, we further elucidate the mobility of the molecules on the surface and the above-mentioned locally ordered domains. When comparing consecutive images taken with a time lapse of 16 min, only few molecules change position along the  $[4\bar{2}1]$  and  $[\bar{4}21]$  directions (Fig. 5.4), corresponding to a diffusion rate of about  $3.5 \cdot 10^{-5} \text{ s}^{-1}$ . This demonstrates the low diffusivity of the molecules at room temperature. In order to obtain an estimate for the diffusion barrier we have performed experiments up to approximately 330 K and observed in a series of images the average percentage of molecules, which have moved between two images. At 300 K, about 3 % and at 330 K about 20 % of the molecules have moved between 16 min. Therefore, at elevated temperatures above 400 K, we assume the molecules to overcome the diffusion barrier in a reasonable time frame.

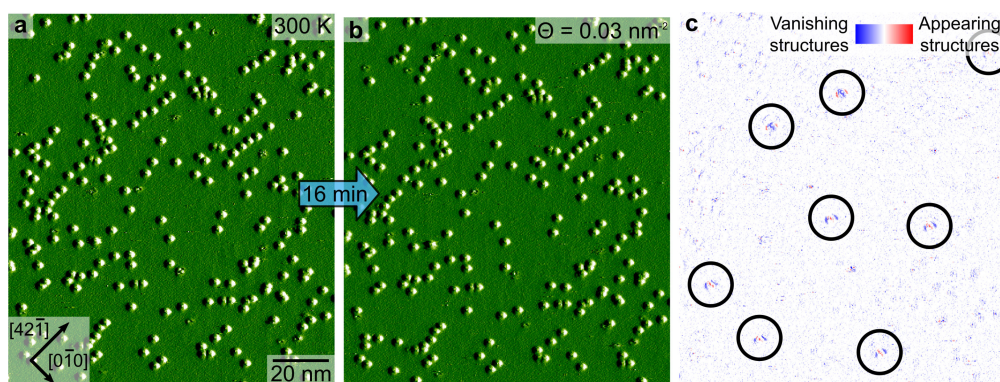


**Fig. 5.4.:** Diffusion study of MoMo on calcite (10.4). (a and b) Two consecutive AFM images with a time lapse of 16 min of the same area. (c) Difference image of the images shown in (a) and (b), illustrating that 8 (marked by black circles) out of 241 molecules change position. Blue and red colors label disappearing and appearing features, respectively.

As the molecules cannot diffuse at room temperature, the absence of islands at low coverage might be simply prohibited by the fact that arriving molecules are kinetically trapped at their positions. To investigate whether island formation can be induced when the diffusion barrier can be overcome, we perform annealing experiments. In this experiment, we anneal the sample at a given temperature for one hour, let it cool down to room temperature and image the surface. This experiment is repeated with increasing annealing temperature to observe the re-

sulting structural changes in the molecular pattern on the surface (see Supporting Information, II. Section, Fig. S5.7). Although the molecules start to move at elevated temperatures, the qualitative arrangement in a randomly scattered fashion remains basically unchanged up to a temperature of approximately 740 K, at which we had difficulties to regain stable imaging conditions as irregular clusters start to form. We tentatively ascribe the latter finding to the fact that the molecules start to decompose and the fragments tend to cluster. We note that MoMo is known to desorb from the metal surface Cu(111) at a temperature below 500 K [111], indicating the strong anchoring on a bulk insulator that is achieved in this study. For MoMo on calcite (10.4) an adsorption energy of 2.25 eV is obtained in our DFT calculations, which readily explains the high desorption temperature. In particular, although the molecules start to move at elevated temperatures, they do not assemble to form dense islands. This is an interesting finding as it provides evidence for the fact that there is no detectable attractive interaction between the molecules.

With this observation, we return to our above finding of local order in small domains when the molecule surface density is high. Assuming an identical adsorption position for all molecules and a simple hard-sphere repulsion between the molecules, we can draw unit cells for arrangements in which the molecules are densely packed, yet assuming no attractive interaction between the spheres.

In the following, we will examine how well such a simple hard-sphere repulsion model coincides with our observation of locally ordered domains. First, we determine the diameter of the hard-sphere, which is supposed to represent an adsorbed MoMo molecule in our model. Fig. 5.5a indicates the periodicity of the calcite (10.4) surface. Each crossing point of the grey grid designates a possible molecule adsorption position, *i.e.*, a possible center of an adsorbed molecule. A MoMo molecule adsorbed on the surface (molecule center marked by a red dot in Fig. 5.5a) will block some of the neighboring adsorption positions for other molecules. In our measurements, we found a minimal molecule-molecule distance of 0.95 nm. Hence, the adsorption positions marked black in Fig. 5.5a cannot be occupied. Only the next adsorption positions marked in blue are still available. The most distant blocked adsorption position is 0.81 nm away from the molecule center. Therefore, for our hard-sphere model, the diameter is in the range of by  $0.81 \text{ nm} < d \leq 0.95 \text{ nm}$ .

This experimentally determined diameter agrees well with the DFT calculations of two MoMo molecules at varying distances, *i.e.*, when moving away from each other along the  $[42\bar{1}]$  direction (see Supporting Information, III. Section, Fig. S5.8): The calculations show that an intermolecular repulsion vanishes at center to center distances larger than about  $d_{DFT} = 0.91 \text{ nm}$ . The intermolecular repulsion at smaller distances originates from an electrostatic interaction between two methyl groups of the interacting molecules and continuously decreases with increasing

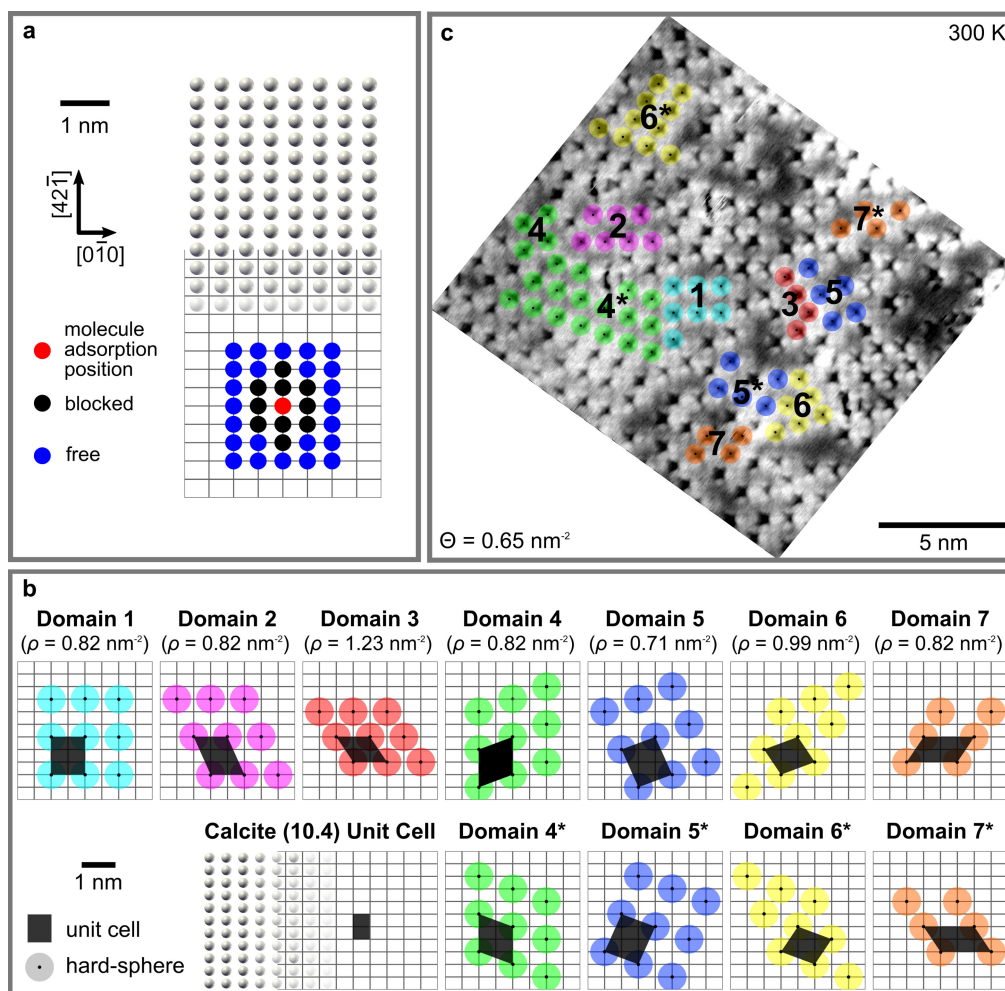


**Fig. 5.5.:** Ordered molecular arrays at high coverage (a) Spheres representing carbon atoms and the grey grid illustrate the periodicity of the calcite (10.4) surface. Each crossing point of the grid indicates a possible MoMo center adsorption position. A molecule centered at the red dot blocks direct neighbor adsorption positions (marked with black dots) for other molecules. Blue dots indicate nearby free adsorption positions. A diameter of  $0.81 \text{ nm} > d \geq 0.95$  is determined for the hard-sphere model. (b) Structure of possible domains based on the assumption that the molecules (i) adopt at identical adsorption sites and (ii) experience hard-sphere repulsion. The quantity  $\rho$  states the molecule density within the domain. (c) AFM image with high molecule coverage of  $\Theta = 0.65 \text{ nm}^{-2}$ . The molecules arrange in locally ordered domains. All unit cells envisioned in (b) can be identified in the image.

molecule-molecule distance. Based on these DFT calculations, we can recognize that the molecules slightly differ from ideal hard-spheres. In fact, the molecule density can be increased to some extent under pressure, because the short-range repulsion increases continuously and not abruptly when two molecules are brought together (see Fig. S5.8). Therefore, MoMo molecules might be rather described as slightly compressible rubber balls instead of rigid spheres. However, the lack of any noticeable intermolecular attraction and the determined short-range repulsion of two MoMo molecules still strongly motivates to use a hard-sphere approximation.

Such a hard-sphere approach results in various periodic structures. In Fig. 5.5b, seven densely packed unit cells, labelled Domain 1 to Domain 7, are illustrated. Four of these domains exist in an identical, mirror imaged configuration, labelled with an asterisk. Domain 1, 2, 4 and 7 all have an equal molecule coverage of  $\Theta = 0.82 \text{ nm}^{-2}$ , while domain 5 is less densely packed ( $\Theta = 0.71 \text{ nm}^{-2}$ ) and Domain 6 is more densely packed ( $\Theta = 0.99 \text{ nm}^{-2}$ ). The most densely packed structure is Domain 3 with  $\Theta = 1.23 \text{ nm}^{-2}$ . In principle, other less densely packed unit cells are also possible. However, at low coverage, a hard-sphere interaction does not lead to a noticeable order.

If the assumptions of a single adsorption position and hard-sphere repulsion are correct, we should be able to find some or all of the above-mentioned domains in the locally ordered areas in our images. To inspect whether this simple picture might be useful to explain the experimental findings, we analyze an AFM image taken at high molecular coverage and close tip-sample distance in order to benefit from contrast inversion for imaging the precise molecule position and orientation. As shown in Fig. 5.5c, the molecule coverage is very high ( $0.65 \text{ molecules per nm}^{-2}$ ), resulting in many areas exhibiting local order. When marking the center position of the molecules, we can, indeed, identify the above envisioned densely packed configurations on the surface. This finding corroborates our interpretation of hard-sphere repulsion. In the absence of intermolecular attraction, the internal energy does not depend on the specific molecular arrangement on the surface, given that the molecules always occupy the same adsorption position. Therefore, the here observed ordered arrangement at high coverage is fully entropy driven [112]. This assignment is motivated by the fact that for hard-spheres the local dense packing of some of the spheres increases the number of possibilities of the others to arrange [113].

For a further comparison between experiment and our model, we have performed a Metropolis-Monte-Carlo simulation of ideal hard spheres. A link to the interactive simulation can be found here:

<http://wwwhomes.uni-bielefeld.de/rbechstein/MMC/user/MoMo.html> (username: *akk*, password: *akkbkkckk*, see Supporting Information, IV. Section for details about the hard-sphere simulation). Comparing simulations with experimental results at the same coverage reveals similar structures. At high coverage (see Fig. 5.5), the same locally ordered domains are observed in both cases. However, in the simulation for ideal hard-sphere repulsion, the most dense domain, Domain 3, is observed more often compared to the domains with lower density. In contrast to the simulation, in Fig. 5.5c, large areas are covered by low-density domains, e.g., Domain 4 and Domain 6, and Domain 3 is comparably rare. This deviation between experiment

and model can be readily explained by the slight deviation of the MoMo molecules from the idealized model of incompressible spheres.

## 5.4 Conclusion

In this work, we provide experimental and theoretical evidence for anchoring individual MoMo molecules onto the (10.4) surface of the bulk insulator calcite held at room temperature. Our AFM results indicate that the molecules neither diffuse nor rotate at room temperature, illustrating the strong molecule-surface interaction. High-resolution images taken at close tip-sample distances reveal a cross-like inner structure of the molecules. From these high-resolution images we deduce that the molecules lie flat on the surface and adopt an identical adsorption position and orientation. The strong molecule-substrate interaction and the observed orientation can be readily explained by a simple electrostatic picture, illustrating the very close match between the charge distribution within the molecule and on the surface. Annealing experiments show that the molecules do not form islands even if they have enough energy to overcome the diffusion barrier. This finding can be explained by the absence of a notable intermolecular attraction. In fact, when assuming identical adsorption positions and a hard-sphere repulsion between the molecules, ordered molecular domains can be envisioned, which we indeed find in high-coverage structures. Our results, thus, demonstrate that the formation of ordered arrays of this metal-complexing molecule is entropy driven, rather than by intermolecular attraction. This study contributes to exploring alternative strategies for creating ordered metal arrays on electrically insulating support surfaces.

## 5.5 Methods

### Experimental Section

All AFM measurements shown in this work were carried out with a Scienta Omicron VT AFM XA operated in the frequency modulation mode [114]. Sample preparation as well as molecule deposition were performed *in situ* with a chamber base pressure typically better than  $10^{-10}$  mbar. All temperatures stated in this work were measured with a Pt-100 sensor located at the sample holder stage with an accuracy of  $\pm 1$  K. Note that the temperature at the sample surface will differ from this read-out. Optical quality calcite ( $\text{CaCO}_3$ ) crystals were purchased from Korth Kristalle GmbH, Kiel, Germany. After insertion into the UHV chamber, the crystals were annealed at 700 K to remove air-borne contaminants before *in-situ* cleavage. Prior to molecule deposition, the crystal was annealed at 650 K for 1 h. The dimolybdenum tetraacetate (MoMo) molecules were bought from Aldrich, Munich, Germany, and were

used after thorough degassing. Molecule deposition was done using a home-built Knudsen cell that is heated to approximately 440 K for molecule sublimation. The coverages shown in this work were achieved by sublimation times ranging from 10 to 50 min with the cell being positioned approximately 9 cm away from the sample.

### Computational Methods

DFT calculations were performed with the planewave-pseudopotential package Quantum ESPRESSO [115], using Ultrasoft pseudopotentials [116] with a wave function (charge) kinetic energy cutoff of 408 eV (4080 eV) and a GGA-PBE [117] exchange-correlation functional. The Grimme-D2 van der Waals interaction [118] was included. The Brillouin-zone was sampled with the  $\mathbf{k} = \Gamma$  point. Calcite (10.4) was modeled with a periodically repeated slab of three layers, with a vacuum gap between the adsorbed molecule and the bottom layer of the slab replica of  $\sim 15$  Å. Only forces on molecule atoms and surface atoms belonging to the first two layers were allowed to relax, up to 0.026 eV/Å. A smearing of 0.16 eV was used to improve convergence in the electronic iterations.

## 5.6 Acknowledgement

Financial support from the German Research Foundation through grant DFG Project KU 1980/10-1 is gratefully acknowledged. S.A. is a recipient of a DFG-fellowship through the Excellence Initiative by the Graduate School Materials Science in Mainz (GSC 266). B.S., and M.A. thank the Deutsche Forschungsgemeinschaft (DFG, SFB/TRR 88 "Cooperative Effects in Homo- and Heterometallic Complexes (3MET)" Project C9). We sincerely appreciate Hagen Söngen's help writing the hard-sphere simulation code. Via a membership (A.F.) of the UK's HEC Materials Chemistry Consortium, funded by EPSRC (EP/L000202, EP/R029431), this work used the ARCHER UK National Supercomputing Service (<http://www.archer.ac.uk>).



## 5.7 Supporting Information

### I. DFT Calculations of Single MoMo on Calcite (10.4)

DFT atomic relaxations were performed to identify the most stable adsorption geometry of a single MoMo molecule on calcite (10.4). The molecule was relaxed on the surface starting from 64 non-equivalent initial configurations (see Fig. S5.6). The energy of the most stable configuration (shown in Fig. 5.3d of the main text) is set to  $E = 0$  eV. The first group of geometries corresponds to  $E < 0.2$  eV. Note that some different initial configurations relax in the same final geometry. For instance, 40, 41, 56 ( $E = 0$  eV) or 16, 48 ( $E = 30$  meV) or 14, 62 ( $E = 10$  meV). These configurations have the Mo atom on top of a carbonate group and four MoMo oxygens bind with the neighbouring Ca atoms. Some configurations are very close in energy. This stems from two facts: *i*) the molecule is slightly tilted as it aligns to one of the two diagonals connecting two Ca atoms (this gives rise to two slightly different orientations and energies); *ii*) the molecule can adsorb in two non-equivalent  $[0\bar{1}0]$  rows. At higher energies ( $0.2 < E < 0.5$  eV), the molecule is not on top of the carbonate group (not shown) but keeps a similar orientation as for more stable geometries. At even larger energies ( $E > 0.5$  eV), the molecule can be rotated by  $45^\circ$  (with respect to its stable geometry, with only two MoMo oxygens bound with the Ca atoms) or can be in bridge position between two Ca atoms.

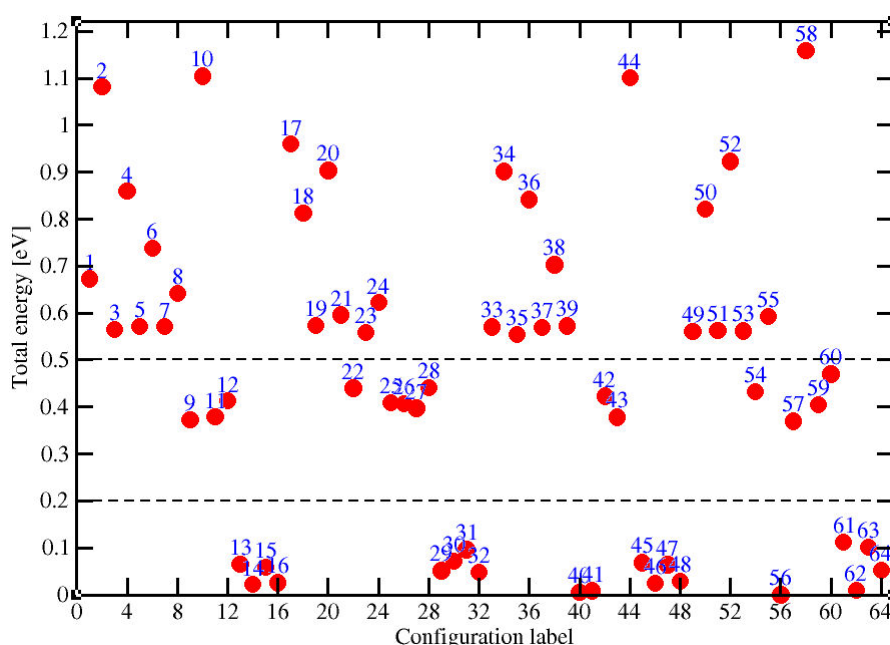


**Fig. S5.6.:** DFT total energies of optimized geometries of a single MoMo molecule on calcite (10.4) calculated from 64 non-equivalent initial configurations. Configurations are labelled from 1 to 64. The energies are referred to the most stable configurations (40, 41, 56), where we set  $E = 0$  eV.

## II. Annealing Experiments

Annealing experiments of MoMo on calcite (10.4) are performed to investigate whether island formation can be induced upon heating. In these experiments, we anneal the sample at a given temperature for one hour, let it cool down to room temperature and image the surface. This procedure is repeated with increasing annealing temperatures to observe the resulting structural changes in the molecular pattern on the surface. As shown in Fig. S5.7, AFM images are obtained at room temperature subsequent to annealing to 300 K, 356 K, 492 K, 628 K, 698 K and 738 K. Basically, no change in the random molecule distribution is observed up to an annealing temperature of approximately 700 K. However, above 700 K large clusters are formed, which we tentatively ascribe to a decomposition of the molecules and a clustering of the arising fragments.

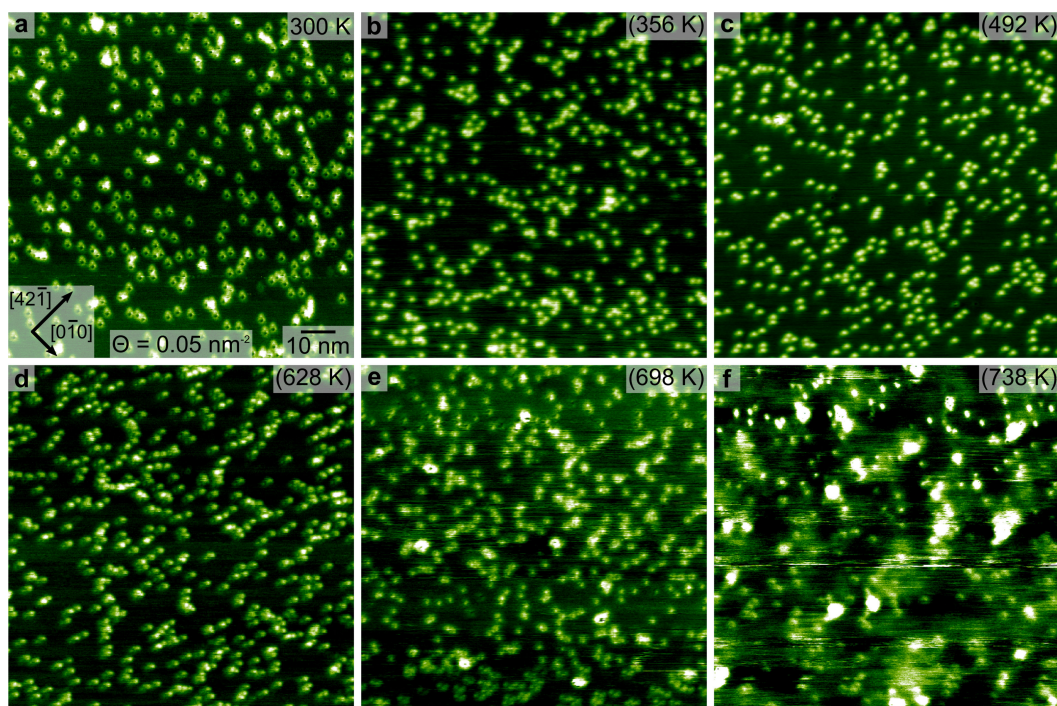


**Fig. S5.7.:** AFM images of MoMo on calcite (10.4) at room temperature subsequent to annealing for one hour at a) 300 K, b) 356 K, c) 492 K, d) 628 K, e) 698 K and f) 738 K. a)-e) The qualitative molecule arrangement in a randomly scattered fashion remains basically unchanged up to a temperature of approximately 700 K. f) Above 700 K, large clusters are formed, for that reason we had difficulties to regain stable imaging conditions.

## III. DFT Calculations of Intermolecular Interaction

In this Section, we evaluate via DFT the repulsive energy between two MoMo molecules. Our aim is to ascertain the validity of the hard-sphere repulsive model illustrated in the main text and detailed in the IV. Section. In Fig. S5.8 we plot the total energy of the two interacting molecules in gas phase with a fixed orientation, as a function of the distance between their centres along the  $[42\bar{1}]$  direction. We adopt the orientation of the most stable adsorption geometry found on the surface (see Fig. 5.3d of the main text). We keep the orientation fixed (the molecule atoms can only move along  $[42\bar{1}]$ ) to reproduce the constraints imposed by the surface. We start from a short distance (0.81 nm, experimentally not observed) and compute the total energy until no further change in energy can be detected. The repulsion, vanishing at  $d_{DFT} = 0.91$  nm, is related to the electrostatic interaction between the  $\text{CH}_3$  groups. Note that when the molecules are allowed to rotate in gas phase (not shown) they manage to relax by keeping a short distance (0.855 nm). However, on the surface this would be energetically unfavourable, as the change in orientation would make the MoMo interaction with the surface Ca atoms far less optimal. As shown in Fig. 5.3d, the short-range repulsion increases continuously when two MoMo molecules are brought together and not as abruptly as for a rigid sphere. Therefore, in contrast to ideal hard-spheres, MoMo molecules can be slightly compressed under sufficient pressure. However, in a first approximation it remains justified to use a hard-sphere model, because a short-range repulsion only and no intermolecular attraction is recognized.

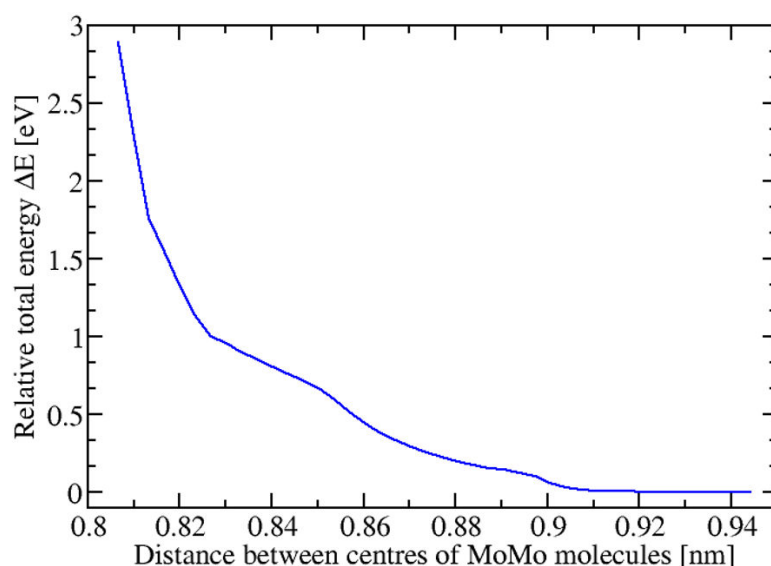


**Fig. S5.8.:** AFM images of MoMo on calcite (10.4) at room temperature subsequent to annealing for one hour at a) 300 K, b) 356 K, c) 492 K, d) 628 K, e) 698 K and f) 738 K. a)-e) The qualitative molecule arrangement in a randomly scattered fashion remains basically unchanged up to a temperature of approximately 700 K. f) Above 700 K, large clusters are formed, for that reason we had difficulties to regain stable imaging conditions.

### III. DFT Calculations of Intermolecular Interaction

Metropolis Monte Carlo simulations of MoMo adsorbed on calcite (10.4) were performed. In this simulation MoMo molecules were modelled as hard spheres with a diameter of  $d = 0.90$  nm. According to our experimental observations, in the simulation the molecules were constrained to exclusively adsorb on specific positions on top of a carbonate group of the calcite surface. A link to the interactive simulation can be found here <http://wwwhomes.uni-bielefeld.de/rbechstein/MMC/user/MoMo.html> (username: *akk*, password: *akkbkkckk*). Fig. S5.9 displays three snapshots from this simulation, showing an equilibrated situation for various coverage. The crossing points of the grey grid indicate possible molecule adsorption positions. For comparison between experiment and simulation the same coverages of (a)  $\Theta = 0.07$  nm<sup>-2</sup>, (b)  $\Theta = 0.41$  nm<sup>-2</sup> and (c)  $\Theta = 0.65$  nm<sup>-2</sup> as in Fig. 5.2 are chosen. Similar to the experiment, at low coverage (see Fig. S5.94a) only single molecules are obtained, exhibiting no ordered structure. Upon increasing the coverage (see Fig. S5.94b and c), various periodic domains are formed in the dense areas, both in the experiment as well as in the hard-sphere simulation. However, the dense domains, Domain 3 and Domain 6, occur much more frequently in the simulation than observed in the experiment. A possible explanation for this deviation could be that the repulsion between two MoMo molecules does not decrease as isotropically and abruptly as for a perfect hard sphere.

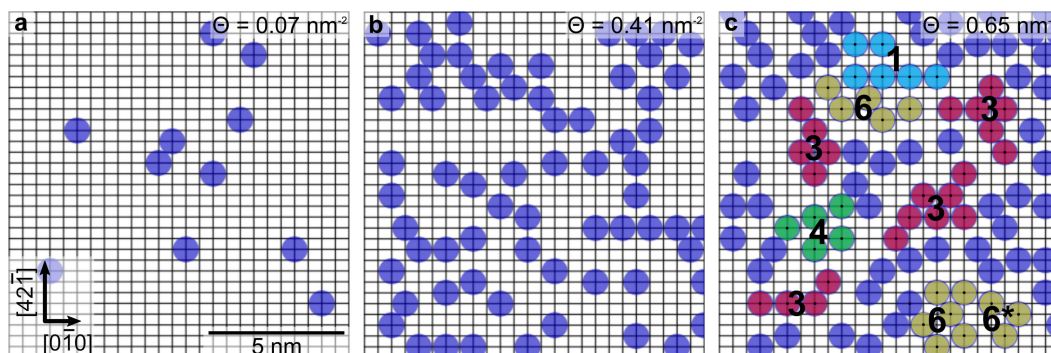


**Fig. S5.9.:** Snapshots of Metropolis Monte Carlo hard-sphere simulation of MoMo adsorbed on calcite (10.4) surface at various coverage. MoMo molecules are illustrated as blue spheres with a radius of 0.90 nm. The grey grid illustrates the periodicity of the calcium ions of the calcite sample. (a) At low coverage of  $\Theta = 0.07$  nm<sup>-2</sup>, single molecules are obtained and no order is recognizable. (b) Upon increasing the coverage to  $\Theta = 0.41$  nm<sup>-2</sup>, a few denser areas, indicating first periodicity, are formed. (c) At high coverage of  $\Theta = 0.65$  nm<sup>-2</sup>, ordered areas are visible and marked with the corresponding domain. The most dense Domain 3 occurs most frequently.

## Kinetic control of molecular assembly on surfaces

Reprinted with permission from 'Chiara Paris, Andrea Floris, Simon Aeschlimann, Julia Neff, Felix Kling, Angelika Kühnle and Lev Kantorovich, "Kinetic control of molecular assembly on surfaces", *Communications Chemistry* **2018**, 1:66'



ARTICLE

DOI: 10.1038/s42004-018-0069-0

OPEN

# Kinetic control of molecular assembly on surfaces

Chiara Paris<sup>1</sup>, Andrea Floris<sup>1,2</sup>, Simon Aeschlimann<sup>3,4</sup>, Julia Neff<sup>3</sup>, Felix Kling<sup>3</sup>, Angelika Kühnle<sup>3</sup> & Lev Kantorovich<sup>1</sup>

It is usually assumed that molecules deposited on surfaces assume the most thermodynamically stable structure. Here we show, by considering a model system of dihydroxybenzoic acid molecules on the (10.4) surface of calcite, that metastable molecular architectures may also be accessed by choosing a suitable initial state of the molecules which defines the observed transformation path. Moreover, we demonstrate that the latter is entirely controlled by kinetics rather than thermodynamics. We argue that molecules are deposited as dimers that undergo, upon increase of temperature, a series of structural transitions from clusters to ordered striped and then dense networks, and finally to a disordered structure. Combining high-resolution dynamic atomic force microscopy experiments and density-functional theory calculations, we provide a comprehensive analysis of the fundamental principles driving this sequence of transitions. Our study may open new avenues based on kinetic control as a promising strategy for achieving tailored molecular architectures on surfaces.

<sup>1</sup>Department of Physics, King's College London, London WC2R 2LS, UK. <sup>2</sup>School of Mathematics and Physics, University of Lincoln, Brayford Pool, Lincoln LN6 7TS, UK. <sup>3</sup>Institute of Physical Chemistry, Johannes Gutenberg-University Mainz, Duesbergweg 10-14, 55099 Mainz, Germany. <sup>4</sup>Graduate School Materials Science in Mainz, Staudingerweg 9, 55128 Mainz, Germany. Correspondence and requests for materials should be addressed to A. F. (email: [afloris@lincoln.ac.uk](mailto:afloris@lincoln.ac.uk)) or to L. K. (email: [lev.kantorovitch@kcl.ac.uk](mailto:lev.kantorovitch@kcl.ac.uk))

When depositing molecules on metallic and insulating surfaces, it is often assumed<sup>1–14</sup> that the self-assembled structures observed are the most thermodynamically stable. However, this may not always be the case as at certain conditions, less thermodynamically stable, i.e., kinetically trapped structures, might be formed first. Therefore, using kinetics to control the formation of self-assembled structures is an approach that may open up new avenues in designing novel 2D materials. In particular, insulating substrates are of special importance for future molecular electronics, since metallic substrates cause substantial difficulties due to the appearance of leakage currents adversely affecting the devices performance. The calcite (10.4) surface represents a promising example of an insulating system, as it contains localized positively charged Ca ions and negatively charged carbonate groups CO<sub>3</sub>, able to anchor small organic molecules strongly<sup>14–17</sup>.

One of the most interesting examples demonstrating the potential of this new approach is provided<sup>17</sup> by a system of 2,5-dihydroxybenzoic acid (DHBA) organic molecules, deposited on the calcite (10.4) surface (Fig. 1a). The molecules undergo a number of structural transitions when increasing the substrate temperature. Initially, a disordered structure consisting of clusters is formed; next, an ordered so-called striped network appears, which, upon heating the sample, is replaced by another ordered network denoted as dense<sup>17</sup> (see Fig. 1b–e). The dense network is finally transformed into a set of disordered clusters upon further heating<sup>17</sup>. At the same time, understanding of the actual mechanisms at play, which drive the structural transformations of DHBA molecules after their deposition on the calcite surface, is missing so far. However, elucidating the role played by the thermodynamics and kinetics in determining the specific sequence of the observed networks is highly promising as it provides a route towards tailoring molecular structure formation on surfaces by kinetic control.

Here, using a combination of high-resolution dynamic atomic force microscopy (AFM) and ab initio density-functional theory (DFT) calculations, we provide a comprehensive explanation of the mechanisms driving the structural transformations of DHBA molecules after their deposition on the calcite surface. First, we present evidence that, under existing experimental conditions, the molecules are deposited on the surface mostly as dimers. We find that this specific molecular initial state is crucial in triggering the particular sequence and variety of the structures realized, whose relative stability is analyzed in a wide range of temperatures via thermodynamic arguments (DFT-based free energies). Second, within a fully ab initio approach, we calculate energy barriers associated with all evident transitions connecting the various molecular structures, allowing us to comprehensively rationalize the transition path. To the best of our knowledge, this level of theoretical analysis of the kinetics of structural transitions is unprecedented. This enables us to suggest (i) the atomistic mechanisms of dissolution and growth of each network; (ii) the composition of disordered structures along the transformation path; (iii) the rate-limiting steps in the formation of the dense network and, finally, (iv) some peculiar catalytic phenomena at play during its growth. The role played by the thermodynamics and kinetics in this complex molecular process is fully elucidated, enabling us to demonstrate that the path observed is controlled by kinetics rather than thermodynamics. Indeed, if thermodynamics establishes the most stable structure under given external conditions (e.g., coverage and temperature), kinetics provides the particular path towards this structure via a sequence of metastable states that require the highest transition rates to reach. This is highly relevant as it provides a route towards tailoring molecular structure formation on surfaces by kinetic control.

## Results

**Experimental results.** Temperature-dependent high-resolution dynamic AFM experiments were performed to image the self-organization process of DHBA molecules sublimated on the calcite (10.4) surface.

DHBA molecules were deposited onto calcite held at 100 K and, upon stepwise heating up to 400 K, four different structural arrangements have been identified<sup>17</sup>. At low temperatures, a disordered arrangement of clusters is observed. Above 220 K, the disordered clusters start to transform into islands of a striped network, Fig. 1b. The striped network is the predominant structure in the temperature window of about 240 to 260 K, and, as illustrated in Fig. 1d, is composed of DHBA dimers formed by double hydrogen bonding of their carboxylic groups. Above a temperature of about 260 K, a continuous transition from islands of the ordered striped network to the ordered dense network islands occurs on the surface, Fig. 1c. At variance with the striped network, in the dense network the molecules are anchored to the surface through their carboxylic groups and form a monolayer consisting of upright monomers, Fig. 1e. The dense network is the dominating structure<sup>17</sup> in the temperature range from 290 to 350 K, before it is replaced by yet another structure, formed by unordered clusters. Here, we focus on the formation of the striped network islands and the transition of the striped into the dense network. The transition process is visualized via taking a sequence of high-resolution images of the same area at room temperature over a long period of time (see Fig. 1b, c and the Supplementary Movie 1 for a complete movie of the transition). Notably, over time the dense network islands grow at locations that are different from the ones occupied by the striped network islands prior to their disappearance. Therefore, there must be a mass transfer between the two different locations, corresponding to species that appear due to dissolving striped islands and which must serve as the building material for the forming dense structures. As detailed below, the transfer is realized via mobile molecular dimers, which typically (at room temperature) move faster than the AFM scanning frequency. Hence, these species cannot be imaged at these conditions unless their diffusion rate is sufficiently decreased upon cooling the sample. AFM images of the mobile species are acquired by preparing the sample at room temperature and subsequently cooling the substrate to 185 K, as shown in Fig. 2.

As scattered individual species are clearly visible in Fig. 2 (in addition to the striped and dense islands), this suggests the co-existence of at least three structures at room temperature: striped, dense and mobile. According to the size of the scattered species being about 1 nm in diameter (measured as full width at half maximum in height profiles), we expect them to be either monomers or dimers.

As described above a series of images at room temperature (295 K) were acquired to gain a deeper insight into the striped-to-dense transformation process (see Supplementary Movie 1). In Fig. 3a–f the changes between consecutive images of the series are displayed. Striped islands dissolve and dense islands grow. After four hours, most of the striped islands vanished (over a longer period of time we expect all striped islands to dissolve). While the number of striped islands clearly decreases, the number of dense islands remains nearly constant during the observation, each increasing in size. The total area of coverage (striped plus dense islands) does not change noticeably over time ( $27 \pm 5\%$ ). Thus, assuming that no molecules adsorb or desorb, the density of the mobile species remains also constant.

As for the dense islands, only growth is observed, indicating a larger attachment over detachment rate. Due to the glide reflection symmetry of the calcite (10.4) surface, two chiral dense



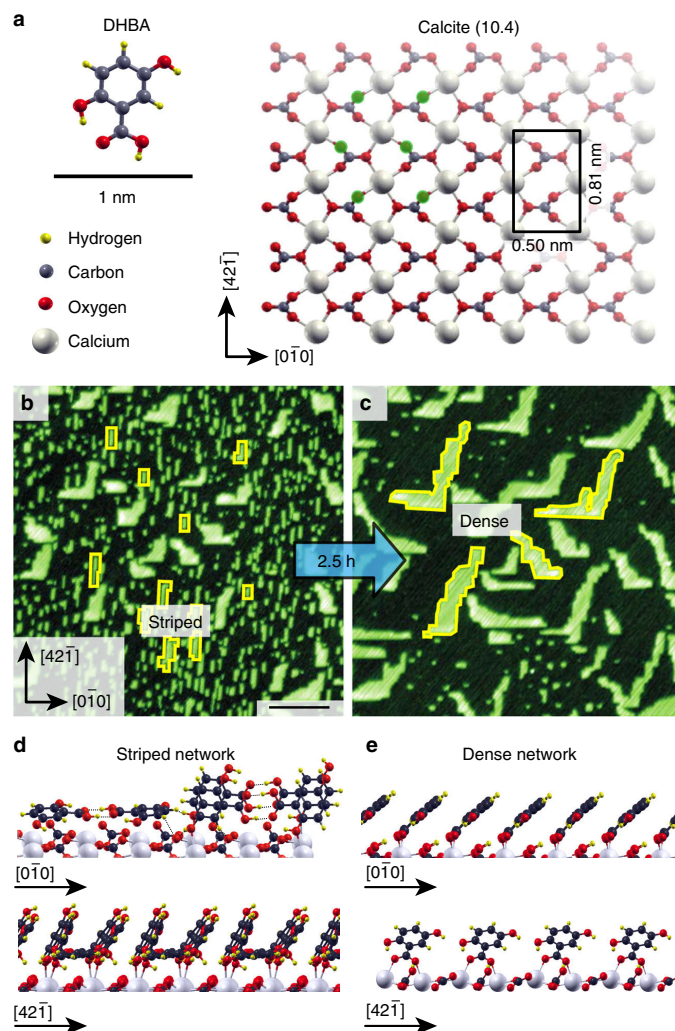


**Fig. 1** Ordered networks formed by DHBA molecules on calcite. **a** DHBA molecule and top view of the (10.4) calcite surface. Green circles on some of the carbonate groups indicate the protruding oxygen atoms of the surface. **b, c** Room temperature dynamic AFM images illustrating the striped-to-dense transition. Scale bar is 100 nm. In **b** the striped network is mostly present, while in **(c)** mainly dense network islands are visible. The latter image was taken 2.5 h after the former. **d, e** Side views of the two networks obtained via DFT simulations<sup>17</sup>. **d** The striped network is formed by DHBA dimers strengthened by double hydrogen bonding of their carboxylic groups; the unit cell of this network consists of one flat and two nearly vertical dimers arranged in parallel rows. The primitive ( $6 \times 1$ ) unit cell of  $3.0 \times 0.8 \text{ nm}^2$  contains six molecules. **e** In the dense network molecules are anchored to the surface through their carboxylic groups and form a monolayer of upright monomers with one molecule occupying the area of the ( $1 \times 1$ ) calcite unit cell, i.e., the molecule surface density is identical in both network structures ( $2.5/\text{nm}^2$ ). (Images of structures used were adopted from ref. <sup>17</sup>)

island domains exist. Dense islands growth often results in a checkmark-like form of the islands (see Fig. 3d, islands A and B).

As discussed above, a striped network island is not converted directly into a dense one at the same spot. However, the growth of the dense network islands coincides with a decrease of the striped network islands: the dense network islands “consume” the striped network. This results in a preferred dissociation of the striped islands, over their growth. In other words, the disappearance of the striped network “feeds” the mobile structure while the latter

is, in turn, “consumed” at the same rate by the growing dense network.

For a detailed analysis of the growth and dissolution of the striped network, a second image series was run with the substrate kept at the somewhat lower temperature of 286 K (see Supplementary Movie 2). In Fig. 4 the changes between two consecutive images in this series are displayed. Here, we can follow the growth and dissociation of the striped network islands.

In Fig. 4b, c, an enlarged image of a nucleation and, respectively, a complete decay of a small striped island are

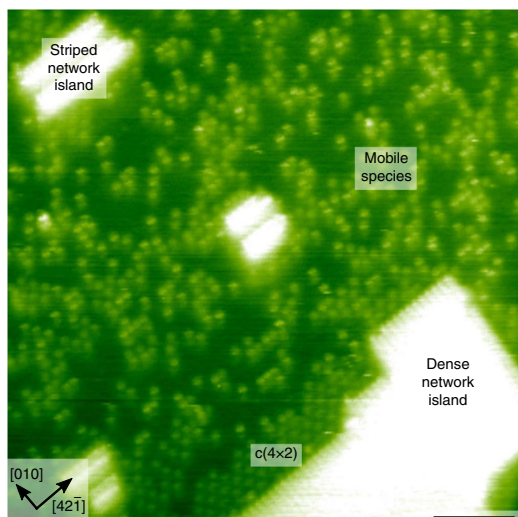


**Fig. 2** Drift-corrected AFM image of DHBA on calcite. The image reveals mobile particles next to the striped and dense networks. The sample is prepared at room temperature and cooled down to 185 K. As can be seen, the area between the striped and the dense networks is occupied by species that are not observed at room temperature. Thus, these species are mobile at room temperature. Close to the dense network island, another molecule arrangement with a  $c(4 \times 2)$  superstructure is visible (see Supplementary Note 7 and Supplementary Figure 19 for more information). Scale bar is 10 nm

evident. Molecules mostly attach along the  $[42\bar{1}]$  direction (Fig. 4d) and detach (Fig. 4e) at similar rate along the  $[421]$  and  $[4\bar{2}1]$  directions.

**Thermodynamic consideration.** The observed order in which DHBA networks appear after deposition with subsequent heating—first the striped and only then the dense network—can only be understood if we assume that initially the molecules are deposited on the surface predominantly as dimers rather than monomers. To understand this argument, let us first compare the free energies of the 2D on-surface gases of monomers and dimers with the free energies of the striped and dense networks, all calculated per molecule. In computing these free energies, vibrational and configurational entropic contributions were included in all cases (see Supplementary Note 1 for details).

The results of our calculations, Fig. 5, show that in the temperature interval of interest the 2D on-surface gas of dimers is the least stable, followed by the striped and then the dense networks, with the 2D on-surface gas of monomers being the most energetically favorable (similar results are obtained at other coverages, see Supplementary Figure 1). This analysis shows that the striped network is less favorable than the dense one, and hence its appearance before the dense network must be due to kinetic reasons (to be considered below). Moreover, it follows that if DHBA molecules were deposited as monomers, they, being the most stable, would clearly have remained as such, without forming any of the ordered structures experimentally observed. The crucial implication is that immediately after the deposition there must be a 2D gas of dimers on the surface, serving as the necessary ingredient for the subsequent formation of the striped network.

Therefore, the relevant question that one has to ask is this: why the DHBA dimers are expected to be the initial dominant species on the surface, immediately after the deposition. Several arguments justify this statement. In the gas phase, a single DHBA dimer is by 0.8 eV more stable than two separate monomers<sup>17</sup>, due to the formation of a double hydrogen bond between their carboxylic groups and to the absence of any stabilizing monomer–surface interaction. We corroborate this finding by a simple kinetic analysis (see also Supplementary Note 2 and Supplementary Figures 2 and 3), showing that in the gas phase at equilibrium dimers would significantly dominate over monomers in a very wide range of temperatures ( $T = 300$ – $1000$  K), which extends far above the experimental DHBA sublimation temperature ( $T \sim 338$  K). There is yet another argument to support dimers as initial dominant molecular units. The molecules deposition is done by heating a DHBA powder, which is known<sup>18</sup> to consist of DHBA dimers. Hence, it is natural to suggest that during the sublimation mostly dimers would be desorbed from the powder and form a vapor of dimers, since in the solid the intradimer interaction is stronger than the interaction between dimers. Therefore, mostly dimers must be adsorbed on calcite prior to formation of the ordered networks, and the very first disordered structure observed immediately after the evaporation on the surface ( $T = 100$ – $\sim 220$  K), must be a random arrangement of mostly individual dimers and their clusters. In fact, below the striped network formation temperature (220 K), the dimers mobility must be strongly suppressed.

The metastable character of the dimer structure highlighted in Fig. 5 is crucial, as it represents a necessary condition for triggering the variety of structures observed at higher temperatures.

As the temperature is increased above 220 K and dimers become sufficiently mobile, the striped network, also composed of dimers, is formed. Interestingly, even if Fig. 5 shows that this network is more favorable than the 2D on-surface gas of dimers, the dense network and the on-surface 2D monomer gas are even more stable. Why then the latter two networks are not formed directly after deposition, and instead, a much more complex sequence of structures is observed?

**Kinetic consideration of structural transitions.** To address the question above, it is necessary to look at the kinetics of the network formation. Three possibilities can be envisaged, with the one having the lowest overall energy barrier to be the most probable: (i) dimers dissociate into monomers, thus a 2D on-surface gas of monomers is formed; (ii) mobile dimers form striped islands, and (iii) mobile dimers form dense islands. Option (i) requires overcoming an energy barrier of 1.35 eV<sup>17</sup>, which is not feasible unless the temperature is increased significantly above room temperature. To investigate options (ii) and (iii), we need to consider the dimer mobility on the surface and the dimer attachment barriers to striped and dense islands. However, since the mobility barriers are required in both cases, they can be disregarded as we are only interested in comparing the growth rates of the two ordered networks. Also, in the DHBA attachment simulations we assumed that islands of either networks already exist, hence ignoring the associated nucleation processes. This assumption seems reasonable when comparing the growth of the two networks. In fact, even assuming that their nucleation barriers are quite diverse, the rate of the nuclei enlargement would eventually depend on how easy it is to attach a further molecule or a dimer to them. Note that one may ignore the attachment of monomers to both ordered

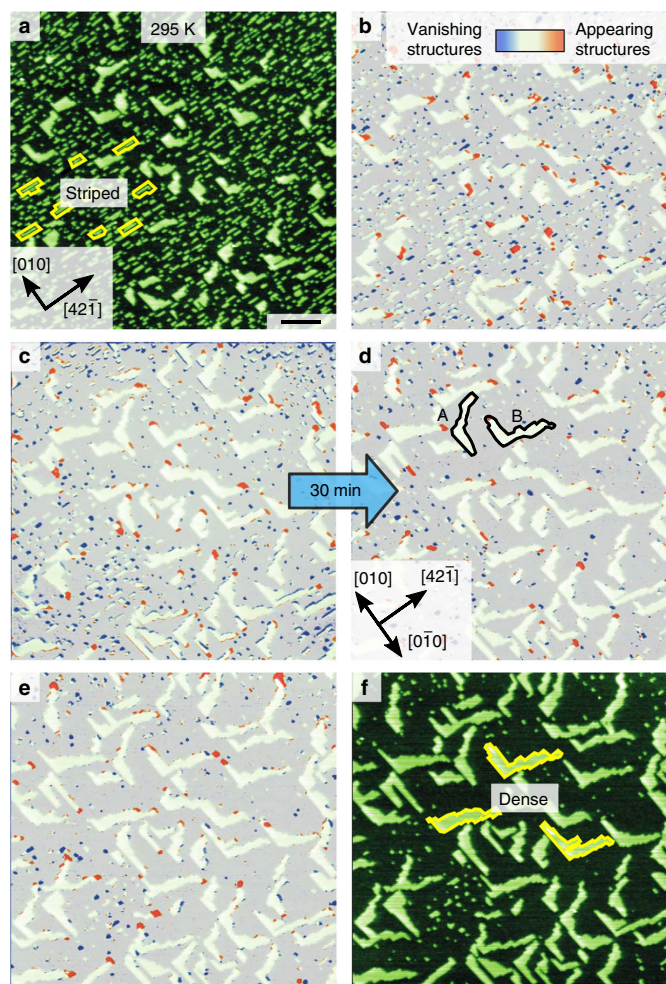


**Fig. 3** An ordered selection of difference images. The AFM images were obtained during a 2.5 h series performed on a calcite surface area partially covered with DHBA molecules (see Supplementary Movie 1 for a movie of the complete series). Scale bar is 100 nm. The sample temperature is 295 K. The striped islands (some marked in **(a)**) dissolve in time, while dense islands grow (some marked in **(f)**). **b–e** Difference images are calculated by subtracting the previous image from the current one. Vanishing structures are shown with blue color, while appearing ones are in red. In **d** two chiral dense islands A and B are highlighted. Both island types grow mainly along the  $[42\bar{1}]$  direction, while, in addition, islands of type A grow along  $[0\bar{1}0]$  and islands of type B grow in  $[010]$  direction

networks, as prior to their formation mostly dimers populate the surface.

**Attachment processes to the striped network.** Many attachment processes to an existing striped island are possible: a dimer can attach to an island edge, corner or kink; it can attach from various directions; the attached dimer final configuration can be either flat or upright (and in the latter case, there are two upright “sites” in the striped network unit cell). Using Nudged Elastic Band (NEB) calculations, we considered mostly attachments along the  $[42\bar{1}]$  direction, as this was observed to be the main striped island growth direction in our experiments (see Fig. 4). Several monomer attachment processes were also considered.

In the very large space of possibilities analyzed, some of which are shown in Fig. 6 (see Supplementary Note 3, Supplementary Tables 1 and 2, as well as Supplementary Figures 4–9 for other processes, their barriers and molecular images), five most relevant processes  $c1(d)$ ,  $k1(d)$ ,  $k2(d)$ ,  $k3(d)$ , and  $k4(d)$  were found. In  $c1(d)$ , a flat dimer is attached to a flat-lying position at a corner with a 0.49 eV energy barrier. At the kink site the full unit cell (three dimers) can be attached in various ways, e.g., by first attaching the first ( $k2(d)$ , the attachment barrier 0.59 eV) and then the second ( $k3(d)$ , 0.85 eV) dimers into their appropriate vertical positions, and then adding a flat dimer ( $k1(d)$ , 0.67 eV), with the process  $k3(d)$  being rate limiting. Alternatively, after attaching the first vertical dimer ( $k2(d)$ ), a flat dimer can be attached next ( $k4(d)$ ), this is similar to  $k1(d)$  but would likely require a lower barrier

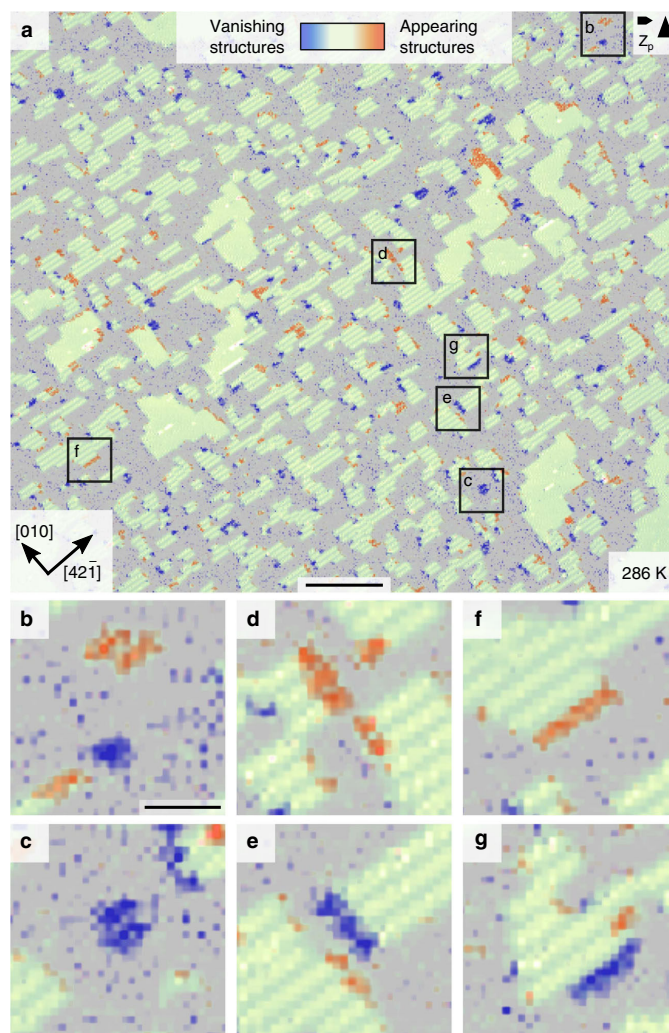


**Fig. 4** Difference images from a series taken at 286 K. **a** The time difference between the two consecutive images is  $\Delta t = 32$  min (see Supplementary Movie 2 corresponding to this series). Vanishing structures are marked blue and appearing structures red. Selected areas are shown in more detail underneath the main panel (**a**). They display the evolution of the striped islands in time: nucleation (**b**) and decay (**c**) of a striped island, growth (**d**) mainly along the  $[42\bar{1}]$  direction and dissolution (**e**) along the  $[42\bar{1}]$  and  $[421]$  directions, growth (**f**) and dissolution (**g**) along the perpendicular  $[010]$  and  $[0\bar{1}0]$  directions. Scale bars are 50 nm in (**a**) and 10 nm in (**b**)

since the second vertical dimer on one side is missing), followed by the attachment of the second vertical dimer (an edge process e4(d), see Supplementary Note 3 and specifically Supplementary Figure 4), with the barrier of 0.74 eV. Both attachment routes are compared in Supplementary Figure 10; note that the second route is overall more favorable having the largest barrier by 0.11 eV lower. The attachment barriers in other processes, including those involving upright dimers at the corner sites as final states, were found to be within 0.8–1.25 eV, i.e., considerably higher.

These results indicate that the growth of the striped islands happens by moving kinks, with the two upright and a single flat dimers positions filled up in a certain order.

Finally, in all favorable processes, the final total energies are lower than the initial ones and the detachment barriers are higher than the attachment ones, ensuring stability of the striped phase over the on-surface gas of dimers.

**Attachment processes to the dense network.** As was mentioned, there exists a competing process after the disordered dimer network is formed upon DHBA deposition, which is associated with dimers attaching to the dense islands. Analyzing this will allow a comparison with the attachment barriers to the striped network from the on-surface gas of dimers. We will establish that the

growth (i) mainly happens at the kinks, and (ii) mostly occurs along the experimentally observed directions. In Supplementary Figure 12, we show schematically the possible attachment directions to edges and kinks of a dense island along the two main surface directions (twelve mechanisms in total, see Supplementary Figures 13–18), which we considered.

In each case we first calculated the energy difference between an initial state (a dimer placed nearby an island), and a final state (the two dimer molecules are attached to the dense island, which is made of monomers), see Supplementary Notes 5 and 6. As for edge attachments, we considered four processes. With the exception of processes k1(d) and k7(d), shown in Fig. 7, which are thermodynamically favorable, the final state in most processes was higher in energy than the initial one by 0.2–0.4 eV. This preliminary analysis allows excluding thermodynamically unfavorable processes of dense islands growth, as they would have no influence on kinetics as one would expect relatively high energy barriers. For instance, the barrier for e3(d) (see Supplementary Table 3) was found to be very high, 1.92 eV. Hence, only the two NEB kink paths k1(d) and k7(d) are meaningful, with calculated energy barriers of 0.91 and 0.71 eV, respectively, much lower than

for the edge attachment. Therefore, we can conclude that the growth of the dense islands must occur mostly by the kink mechanism.

In k1(d) and k7(d) processes, a dimer first approaches the dense network, then it dissociates, and finally the two monomers attach to the island one after another, next to each other (see Supplementary Figure 15). The monomers change their orientation on the surface as required when attaching. Importantly, the growth mechanisms associated with k1(d) and k7(d) correspond to the experimentally observed dense island growth along the  $[42\bar{1}]$  and  $[010]$  directions, respectively (see Fig. 3d, where the shape of island B assumes precisely these main growth directions). Due to the glide symmetry of calcite, there will be domains growing along the  $[42\bar{1}]$  and  $[0\bar{1}0]$  directions as well, also in agreement with experimental observations (Fig. 3d, island A).

Interestingly, the dissociation barrier of the dimer in proximity to the dense network (between 0.71 and 0.91 eV) is much lower than the one for a free dimer on the surface (1.35 eV). This “network-assisted” dimer dissociation is explained by the formation of inter-molecular interactions inside the dense network structure<sup>17</sup>, which strongly reduce the cost of breaking two intradimer hydrogen bonds. Thus, we conclude, a specific catalytic mechanism is at work for dissociating the dimers in the presence of the dense network.

In conclusion, we are now able to answer the question posed above, related to the three possible paths for the system of the on-surface gas of dimers to take. The energy barriers for the dimer dissociation (1.35 eV), the dimer attachment to the dense network (0.71–0.91 eV) and to the striped network (0.49–0.74 eV) enable us to understand that the striped network is the first to form: this route requires overall the smallest energy barriers. Therefore, the appearance of the striped network is governed by kinetics rather than thermodynamics of the system: this metastable network is formed before a more stable dense network, because it is easier to reach at the given experimental conditions.

**Striped-to-dense network transition.** Next, in order to understand the formation of the second, dense network, we analyze the attachment mechanisms to the dense islands (attachment of dimers have already been considered above). We first have to understand whether monomers or dimers, serving as the building material for the dense network, are mostly become available on the surface after the striped islands dissolution. Hence, we compare the barriers required for both dimers and monomers to detach from the striped islands.

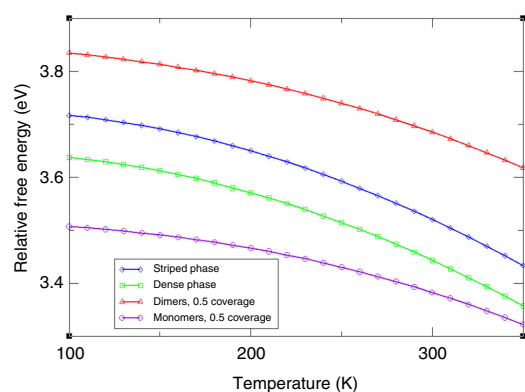


**Fig. 5** Calculated free energies of different structures of DHBA molecules on calcite. Shown are the free energies (per molecule) of the 2D on-surface gases of DHBA monomers and dimers ( $\theta_{A1} = 0.5$  monomer coverage, corresponding to a molecular density of  $1.25$  monomers/nm<sup>2</sup>), and of the ordered striped and dense networks

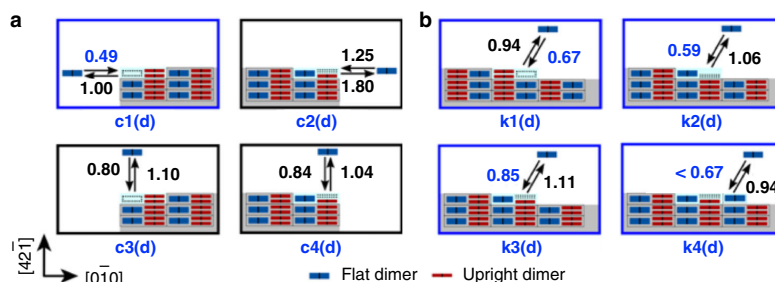


**Fig. 6** Dimer attachment and detachment processes at a striped island. Schematics show a selection of such processes (a) at a corner and (b) at a kink of the island. Red and blue boxes correspond to upright and flat dimers, respectively. The calculated energy barriers (in eV) are also indicated next to the arrows associated with them, with the most favorable ones highlighted in blue. The labeling is such that, e.g., c2(d) process corresponds to the attachment at a corner (marked “c”), where the moving unit is a dimer (“d”); edge and kink are labeled with “e” and “k”, respectively. Attaching a dimer at a vacant site (not shown, see Supplementary Note 3) at a step edge requires very small energy barriers, as anticipated

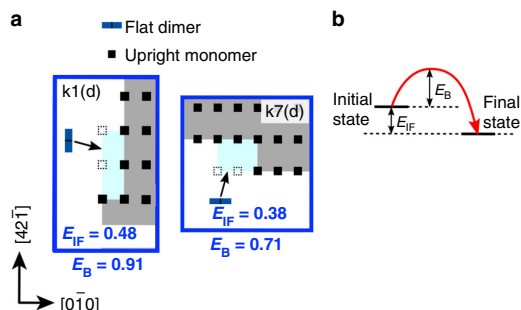


**Fig. 7** Selected dimer attachment processes at a kink of the dense island. **a** Two energetically favorable processes are shown for two surface step directions, k1(d) and k7(d); **b** energy diagram defining the energies given in **a**,  $E_B$  (energy barrier) and  $E_{IF}$ . The latter corresponds to the difference between the initial (a dimer is placed next to the island) and final (the two molecules from the dimer are attached to the island) states of each process (the larger the more favorable). The arrows point out the directions of attachment of the species to the network

Of all processes considered (see Supplementary Note 3), the reverse paths in processes c1(d), k1(d) and k4(d) of Fig. 6 has the lowest detachment barriers (1.00 and 0.94 eV). The higher detachment than attachment barriers can be ascribed to breaking  $\pi$ -stacking interactions of the removed dimer with the neighboring upright dimers. At the same time, it is much more difficult to remove a monomer from the striped islands (energy barriers are 1.10–1.57 eV), since the intradimer hydrogen bonds must break for releasing the first monomer of each dimer. Moreover, when comparing with the dimer detachment process, two consecutive detachments of monomers from the striped islands need to happen, leading to an even lower overall rate (see Supplementary Note 4 and Supplementary Figure 11). Hence, the mobile species introduced in Section Results, which supply the material for building the dense network, are to be mostly dimers. Therefore, the attachments of dimers to the dense islands, already considered in Section Experimental methods, are entirely sufficient for understanding the growth of the dense network.

Finally, we note that attachments of dimers to the dense network have a larger rate (lower barriers, 0.71–0.91 eV) than their dissociation on the surface (1.35 eV), i.e., one can safely assume that dimers, after leaving the striped islands, may diffuse to dense islands without dissociation.

## Discussion

The energy barriers considered above enable us to understand the underlying mechanisms of the observed transitions. Figure 8 summarizes our findings from two perspectives: (a) temperature and (b) free energy.

The initial preparation of the system (process 1  $\rightarrow$  2  $\rightarrow$  3), whereby the surface becomes mostly populated by DHBA dimers and their clusters, appears to be crucial. At temperatures below 224 K, when the mobility of dimers is limited, a dimer-based disordered structure is formed (state 3). As the temperature is elevated, the dimers' mobility becomes sufficient to form the striped network (state 4B), as this requires the lowest energy barriers corresponding to the dimer attachment to striped islands; the on-surface gas of monomers (state 4A) and the dense network (state 4C) are less accessible at these temperatures, even though

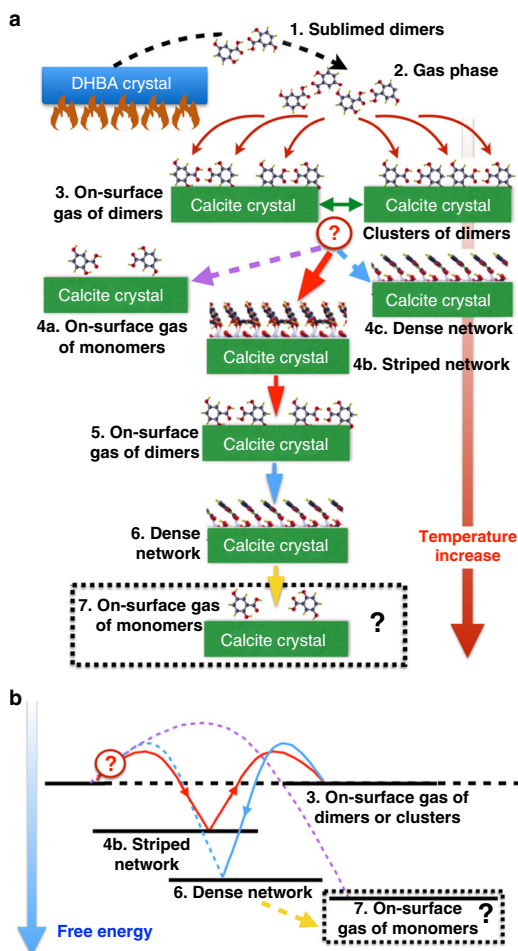


**Fig. 8** Schematic summary diagrams illustrating all considered processes. The processes available to the system and the path taken are shown as a function of **a** temperature and **b** free energy. In **b** only on-surface states and processes as well as the minimum energy paths are shown schematically. In both panels solid arrowed lines correspond to the favorable transition paths, while dashed lines represent other possible processes, which are unlikely. Dimers sublimed from a DHBA powder are deposited on the calcite surface, held at a relatively low temperature, forming a structure composed of free dimers and their clusters, transitions 1  $\rightarrow$  2  $\rightarrow$  3. Next, the system chooses to form the striped islands (3  $\rightarrow$  4b) over other two paths available (on-surface monomers and dense islands) since the selected route corresponds to a higher effective rate (a lower energy barrier). Dissolution of the striped islands at higher temperature leads to mobile dimers, which diffuse towards existing dense islands and attach to them, contributing to their growth (4b  $\rightarrow$  5  $\rightarrow$  6). We speculate that eventually, at even higher temperatures, the dense islands may decompose leading to the on-surface gas of monomers (6  $\rightarrow$  7), the most energetically favorable structure. Hence, over the whole transition path the free energy of the system decreases. (Images of structures used were adopted from ref. 17)

both structures have a lower free energy (Fig. 8b). The specific initial state 3 created in our experiments, an on-surface gas of dimers, triggered the specific evolution path for the DHBA molecules along the different networks, including the formation of metastable striped islands. As the temperature is increased further, dimers are able to detach from the striped islands, (transition 4B  $\rightarrow$  5). The dimers leave the striped network, diffuse, and attach to existing dense islands (5  $\rightarrow$  6), as this requires even smaller barriers than for the detachment from the striped network. These low values stem from a “network-assisted” dimer dissociation, an effect induced by the proximity of the dense island to the approaching dimer. Thus, the island catalyzes the breaking of the dimer—another important ingredient for the specific sequence of structures observed. In this respect, we speculate that if the dimer dissociation was not assisted, the scenario would have been completely different, with the dense network not forming at all. Indeed, the required energy barrier to form this network would be comparable to the one necessary to dissociate dimers into monomers (1.35 eV), leading directly to the thermodynamically most stable phase of on-surface monomers (see Figs. 5 and 8b).

As the temperature is increased even further, the dense islands would decompose, and the on-surface gas of monomers would finally prevail (Fig. 8). However, the fact that monomers are not observed experimentally in the temperature range studied, indicates a rather high barrier for their formation on the surface.

Note that, as the barriers for all processes are relatively close, the striped-to-dense transition may even happen at a not-too-elevated (e.g., room) temperature, although in this case the process requires a considerable time (many hours, see Supplementary Movie 1)<sup>16</sup>.

Concluding, in this work we propose a novel route for creating a set of metastable molecular architectures on crystal surfaces. This is achieved by triggering a sequence of structural transformations entirely controlled by kinetics rather than thermodynamics. The first key feature of our approach is a judicious choice of the initial molecular state of the system, immediately after the deposition on the surface. The second is a controlled, stepwise heating procedure necessary to make the metastable networks accessible from the initial state first, and from one another in subsequent stages.

The feasibility of this route is demonstrated by an example of DHBA organic molecules deposited on an insulating calcite surface. Here, the initial state of the system is an on-surface gas of mostly DHBA dimers. Via a comprehensive theoretical analysis, we show that dimers (rather than monomers) trigger the specific structural transformation observed, due to the hierarchy of energy barriers connecting different molecular arrangements. The sequence of structures (disordered  $\rightarrow$  ordered striped  $\rightarrow$  ordered dense  $\rightarrow$  disordered), is controlled by kinetics: at each relevant temperature interval, the kinetically most accessible structure is formed, selected on the basis of the lowest energy barriers, rather than of its thermodynamic stability. The observed structural path is associated with an increased thermodynamic stability of the whole system.

We believe that this study has a wide appeal since it demonstrates, by providing a detailed insight into the mechanisms of growth of molecular assemblies, the importance of the initial molecular state on the surface and the crucial role of kinetics. Accessing specific structural paths via kinetic control could significantly expand our abilities of realizing a wider variety of molecular motifs on metallic and insulating surfaces. This could represent an important step in designing molecular architectures on substrates, with a potential in the area of growth and structural transformations of organic molecular self-assemblies and in surface functionalization.

## Methods

**Computational methods.** DFT calculations were mainly performed with the Quickstep code<sup>19</sup> (within the CP2K package, <http://www.cp2k.org/>), that uses a mixed Gaussian and plane waves basis set, the Goedecker, Teter and Hutter (GTH) pseudopotentials<sup>20</sup> and a GGA-PBE<sup>21</sup> exchange-correlation functional including a Grimme-D2 van der Waals interaction.<sup>22</sup> We used a plane-wave basis energy cut-off of 600 Ry and the  $\Gamma$  point to sample the Brillouin-zone. In all calculations large enough supercells were considered to justify the latter approximation, e.g.,  $6 \times 2$  cell (in terms of the primitive calcite unit cell) measuring  $3.03 \times 1.62 \text{ nm}^2$  was used to model the striped and dense networks. The calcite substrate was modeled with a periodically repeated slab of three layers, allowing a vacuum gap between the adsorbed ad-layer and the bottom layer of the slab above it of  $\sim 30 \text{ \AA}$ . Relaxations were considered completed when atomic forces were  $< 0.02 \text{ eV/\AA}$ . Only atoms belonging to the two uppermost top layers and all atoms of the molecules were allowed to relax. Atomic vibrations were calculated using the frozen-phonon method with the free energy obtained within the quasi-harmonic approximation.<sup>23</sup> Climbing image nudged elastic band (CI-NEB)<sup>24, 25</sup> calculations were performed using overall between 9 and 14 replicas, including the initial and final states. Note that the appropriate vibrational analysis at the saddle points was not performed due to enormous cost and complexity of such calculations. Pre and postprocessing were done using the TETR/LEV00 package (<http://www.nms.kcl.ac.uk/lev.kantorovitch/codes/lev00/index.html>).

**Experimental methods.** Sample preparations and AFM measurements were carried out under ultrahigh vacuum conditions with a base pressure  $< 10^{-10}$  mbar. Temperature-dependent high-resolution images were performed with a Scienta Omicron VT AFM XA operated in the frequency modulation mode following the procedure reported previously<sup>17</sup>. A Pt-100 sensor with an accuracy of  $\pm K$  located at the sample holder stage was used to determine the temperatures stated in this article. The unknown temperature difference between sample holder stage and sample surface is estimated by the manufacturer to be less than 10 K. Optical quality calcite (CaCO<sub>3</sub>) crystals were purchased from Korth Kristalle GmbH, Kiel, Germany and cleaved in situ to obtain less contaminated (10.4) surfaces. Sub-monolayers of DHBA molecules from Aldrich, Munich, Germany were deposited on the surface by heating a prior thoroughly outgassed home-built Knudsen cell to 67 °C.

## Data and code availability

The data that support the findings of this study are available from the corresponding author upon reasonable request.

Received: 3 January 2018 Accepted: 26 September 2018  
Published online: 22 October 2018

## References

1. Barth, J. V. Molecular architectonic on metal surfaces. *Annu. Rev. Phys. Chem.* **58**, 375–407 (2007).
2. Rosei, F. et al. Properties of large organic molecules on metal surfaces. *Prog. Surf. Sci.* **71**, 95–146 (2003).
3. Pawin, G., Wong, K. L., Kwon, K. Y. & Bartels, L. A homomolecular porous network at a Cu(111). *Surf. Sci.* **313**, 961–962 (2006).
4. Pawin, G. et al. A surface coordination network based on substrate-derived metal adatoms with local charge excess. *Angew. Chem. Int. Ed.* **47**, 8442–8445 (2008).
5. Phillips, A. G., Perdigo, L. M. A., Beton, P. H. & Champness, N. R. Tailoring pores for guest entrapment in a unimolecular surface self-assembled hydrogen bonded network. *Chem. Commun.* **46**, 2775–2777 (2010).
6. Böhringer, M. et al. Two-dimensional self-assembly of supramolecular clusters and chains. *Phys. Rev. Lett.* **83**, 324–327 (1999).
7. Abdurakhmanova, N. et al. Stereoselectivity and electrostatics in charge-transfer Mn- and Cs-TCNQ4 networks on Ag(100). *Nat. Commun.* **3**, 940 (2012).
8. Floris, A., Comiso, A. & De Vita, A. Fine-tuning the electrostatic properties of an alkali-linked organic adlayer on a metal substrate. *ACS Nano* **7**, 8059–8065 (2013).
9. Della Pia, A. et al. Anomalous coarsening driven by reversible charge transfer at metal–organic interfaces. *ACS Nano* **8**, 12356–12364 (2014).
10. Rahe, P. et al. Tuning molecular self-assembly on bulk insulator surfaces by anchoring of the organic building blocks. *Adv. Mater.* **25**, 3948–3956 (2013).
11. Kunstmann, T. et al. Dynamic force microscopy study of 3,4,9,10-perylenetetracarboxylic dianhydride on KBr(001). *Phys. Rev. B* **71**, 121403(R) (2005).
12. Nony, L. et al. Cu-TBPP and PTCDA molecules on insulating surfaces studied by ultra-high-vacuum non-contact AFM. *Nanotechnology* **15**, S91–S96 (2004).

13. Hauke, C. M. et al. Controlling molecular self-assembly on an insulating surface by rationally designing an efficient anchor functionality that maintains structural flexibility. *ACS Nano* **7**, 5491–5498 (2013).
14. Rahe, P., Lindner, R., Kittelmann, M., Nimmrich, M. & Kühnle, A. From dewetting to wetting molecular layers: C60 on CaCO<sub>3</sub>(104) as a case study. *Phys. Chem. Chem. Phys.* **14**, 6544–6548 (2012).
15. Kittelmann, M. et al. Controlled activation of substrate templating in molecular self-assembly by deprotonation. *J. Phys. Chem. C* **117**, 23868–23874 (2013).
16. Kittelmann, M., Rahe, P., Gourdon, A. & Kühnle, A. Direct visualization of molecule deprotonation on an insulating surface. *ACS Nano* **6**, 7406–7411 (2012).
17. Paris, C. et al. Increasing the templating effect on a bulk insulator surface: from a kinetically trapped to a thermodynamically more stable structure. *J. Phys. Chem. C* **120**, 17546–17554 (2016).
18. Adam, M. S. et al. Stability and cooperativity of hydrogen bonds in dihydroxybenzoic acids. *New J. Chem.* **34**, 85–91 (2010).
19. VandeVondele, J. et al. Quickstep: fast and accurate density functional calculations using a mixed gaussian and plane waves approach. *Comput. Phys. Commun.* **167**, 103–128 (2005).
20. Goedecker, S., Teter, M. & Hutter, J. Separable dual-space Gaussian pseudopotentials. *Phys. Rev. B* **54**, 1703–1710 (1996).
21. Perdew, J. P., Burke, K. & Ernzerhof, M. Generalized gradient approximation made simple. *Phys. Rev. Lett.* **77**, 3865–3868 (1996).
22. Grimme, S. Semiempirical GGA-type density functional constructed with a long-range dispersion correction. *J. Comp. Chem.* **27**, 1787–1799 (2006).
23. Kantorovich, L. *Quantum Theory of the Solid State: An Introduction*. (Kluwer, London, 2004).
24. Jónsson, H., Mills, G. & Jacobsen, K. W. Nudged elastic band method for finding minimum energy paths of transitions, in *Classical and Quantum Dynamics in Condensed Phase Simulations*. (eds Berne, B. J., Ciccotti, G., & Coker, D. F.) Vol. 385 (World Scientific, Singapore, New Jersey, London, Hong Kong, 1998).
25. Henkelman, G. & Jónsson, H. A climbing image nudged elastic band method finding saddle points and minimum energy paths. *J. Chem. Phys.* **113**, 9901–9904 (2000).

### Acknowledgments

C.P. would like to thank the ACRITAS Marie Curie Initial Training Network (ITN) project for funding. Via our membership of the UK's HEC Materials Chemistry Consortium, which is funded by EPSRC (EP/L000202), this work used the ARCHER UK National Supercomputing Service (<http://www.archer.ac.uk>). Financial support from the EU through grant PAMS (seventh framework program GA 610446) is gratefully

acknowledged. S.A. is a recipient of a DFG-fellowship through the Excellence Initiative by the Graduate School Materials Science in Mainz (GSC 266). A.K. gratefully acknowledges funding from the Germany Research Foundation via grant KU1980/10-1.

### Author contributions

C.P. performed all calculations; L.K., A.F., and C.P. planned and discussed the calculations strategy; S.A., J.N., and F.K. designed and performed the experiments; L.K., A.K., and A.F. wrote the manuscript with contributions from all authors, and all the authors discussed the results.

### Additional information

**Supplementary information** accompanies this paper at <https://doi.org/10.1038/s42004-018-0069-0>.

**Competing interests:** The authors declare no competing interests.

**Reprints and permission** information is available online at <http://npg.nature.com/reprintsandpermissions/>

**Publisher's note:** Springer Nature remains neutral with regard to jurisdictional claims in published maps and institutional affiliations.



**Open Access** This article is licensed under a Creative Commons Attribution 4.0 International License, which permits use, sharing, adaptation, distribution and reproduction in any medium or format, as long as you give appropriate credit to the original author(s) and the source, provide a link to the Creative Commons license, and indicate if changes were made. The images or other third party material in this article are included in the article's Creative Commons license, unless indicated otherwise in a credit line to the material. If material is not included in the article's Creative Commons license and your intended use is not permitted by statutory regulation or exceeds the permitted use, you will need to obtain permission directly from the copyright holder. To view a copy of this license, visit <http://creativecommons.org/licenses/by/4.0/>.

© The Author(s) 2018



## Supplementary Note 1 Free energy calculations of 2D gas of on-surface monomers and dimers

When calculating the free energy of the 2D gas of monomers or dimers, one has to add the entropic contribution due to the fact that the species can occupy various lattice sites.

Let  $M$  be the total number of lattice sites and  $N$  the number of species (either monomers or dimers). Then, the relative (with respect to the surface) free energy of the 2D gas of our species is

$$F_N = N (\Delta E_{DFT} + \Delta F_{vibr}) - TS_N \quad (1)$$

where  $\Delta E_{DFT}$  is the difference of DFT energies of a single species placed on the surface and that of the surface itself,  $\Delta F_{vibr}$  is the analogous difference between the vibrational contributions of the two systems (which is already temperature dependent),  $S_N$  is the corresponding structural entropy due to all possible distributions of  $N$  species on  $M$  lattice sites, and  $T$  absolute temperature. Considering the fact that monomers and dimers may be in two chiral states on every lattice site, we can write:

$$S_N = k_B \ln \left[ 2^N \frac{M!}{N!(M-N)!} \right] \quad (2)$$

where  $k_B$  is the Boltzmann's constant. Using the Simpson's formula,  $\ln n! \cong n \ln n - n$ , where  $n$  is either  $M$ ,  $N$  or  $M - N$ , we obtain for the free energy, calculated per species, the following expression:

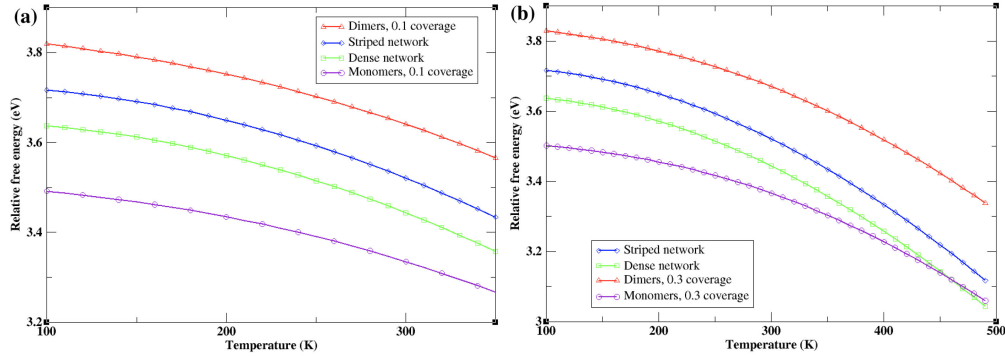
$$\frac{F_N}{N} = \Delta E_{DFT} + \Delta F_{vibr} - k_B T \left[ \ln \frac{1-\theta}{\theta} - \frac{1}{\theta} \ln(1-\theta) + \ln 2 \right] \quad (3)$$

where  $\theta = N/M$  is the coverage.

The obtained expression allows calculating the free energy as a function of temperature for various coverages of dimers and monomers. When comparing the free energies of monomers and dimers, we used for dimers an expression for the coverage corresponding to the same number of monomers, i.e. the coverage of dimers,  $\theta_D = \theta_M/2$ , where  $\theta_M$  is the monomer coverage.

Note that for the striped and dense networks the structural entropy contribution comes only due to presence of two chiral possibilities [1]; its contribution to the free energy per molecule is negligible.

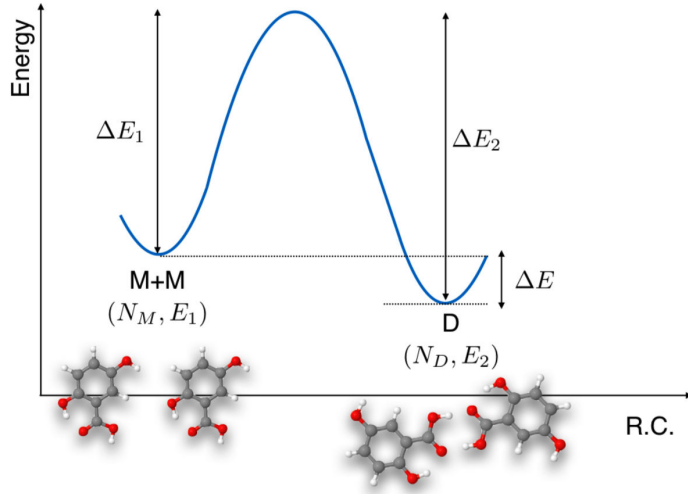
Free energies of dimers, monomers, striped and dense networks were compared in the main text for the value of  $\theta_M = 0.5$ . In **Supplementary Figure 1** we show the results of the calculations for two other values of the monomer coverage  $\theta_M = 0.1$  and  $\theta_M = 0.3$ . One can see that the results remain qualitatively the same.



**Supplementary Figure 1:** Free energies comparison of the on-surface 2D gases of monomers and dimers. Two coverages (a)  $\theta_M = 0.1$  and (b)  $\theta_M = 0.3$  are shown, with the free energies of the striped and dense networks.

## Supplementary Note 2 Gas phase simulations: DHBA molecules vs. dimers

As has already been discussed in the main text, at room temperature DHBAs form solid crystals [2] where molecules are arranged into pairs of dimers connected *via* H-bonds at the carboxylic groups. Prior to the deposition onto the surface, DHBAs solid crystals are heated to  $\sim 338$  K and sublime. It seems natural that the most likely outcome of sublimation are dimers rather than monomers.



**Supplementary Figure 2:** A schematic energy profile of the DHBA dimer (D) formation in the gas phase. Schematics of two monomers (left) and a dimer (right) are shown at the bottom.

Another, a somewhat independent argument, is based on the consideration of a gas phase of dimers and monomers at equilibrium. To understand whether this kind of gas will mostly be populated by dimers or monomers, we shall perform here a simple kinetic analysis. We shall consider a gas of a fixed number of molecules,  $N_0$ , some of which may form dimers, in a fixed volume and at a particular temperature  $T$ . The relative concentrations of molecules

and dimers,  $n_D = N_D/N_0$  and  $n_M = N_M/N_0$ , respectively, satisfy the obvious conservation identity,  $1 = n_M + 2n_D$ , where  $N_M$  is the number of single molecules and the number of dimers is  $N_D$ . Note that it follows from this equation that  $n_D$  cannot be larger than  $1/2$ .

The energy profile for the reaction between dimers and single molecules is shown schematically in **Supplementary Figure 2**. The change of  $n_M$  as a function of time can be written as

$$\frac{\partial n_M}{\partial t} = -2k_{2M \rightarrow D}n_M^2 + 2k_{D \rightarrow 2M}n_D \quad (4)$$

where  $k_{2M \rightarrow D} = \nu \exp(-\beta\Delta E_1)$  is the rate constant for the dimer formation and  $k_{D \rightarrow 2M} = \nu \exp(-\beta\Delta E_2)$  is the rate constant for the reverse process, while  $\Delta E_1$  and  $\Delta E_2$  are the corresponding energy barriers (see **Supplementary Figure 2**),  $\beta = 1/k_B T$ , and we assumed the same prefactors  $\nu$  for both transition processes.

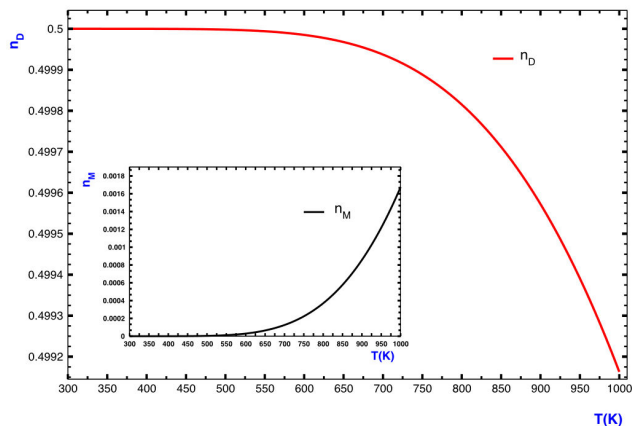
Using the above equations, one obtains in the steady state, when  $\partial n_M/\partial t = 0$ , a quadratic equation for  $n_D$ ,

$$n_D^2 - \left(1 + \frac{1}{4}e^{-\beta\Delta E}\right)n_D + \frac{1}{4} = 0,$$

where  $\Delta E = \Delta E_2 - \Delta E_1$ , which only solution satisfying the necessary condition  $n_D \leq 1/2$  is

$$n_D = \frac{1}{2} \left[ 1 + \frac{1}{4}e^{-\beta\Delta E} - \frac{1}{\sqrt{2}}e^{-\beta\Delta E/2} \sqrt{1 + \frac{1}{8}e^{-\beta\Delta E}} \right] \quad (5)$$

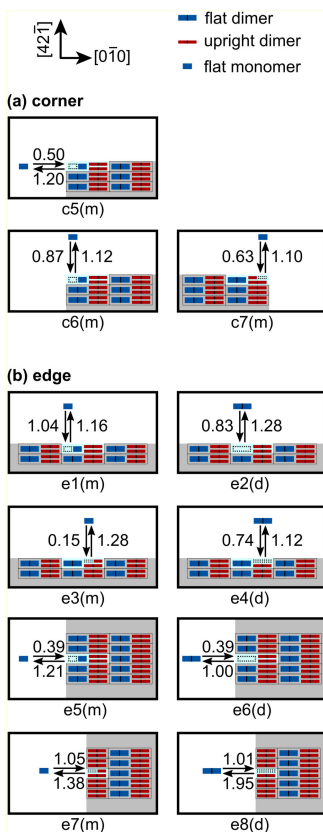
Therefore, using Supplementary Equation (5) and  $n_M = 1 - 2n_D$ , we can evaluate how the relative concentrations of single molecules and dimers change in the gas phase as a function of temperature. In Supplementary Equation (5),  $\Delta E = 0.8$  eV is the DFT calculated energy difference between two single molecules and the dimer in the gas phase [1]. The results are shown in **Supplementary Figure 3**.



**Supplementary Figure 3:** Concentrations of dimers and single molecules as functions of temperature  $T$ . Here  $n_D$  and  $n_M$  are relative concentrations of dimers and monomers, respectively.

In the range of temperatures  $T=300$  K-1000 K, the gas phase results are that  $n_D \simeq 1/2$ , *i.e.* such a gas will be mostly populated by dimers ( $n_D \gg n_M$ ). This means that any monomers escaping the surface of the DHBA sample upon heating will most likely form dimers after sublimation.

Hence, we conclude that at the experimental temperature of sublimation ( $T \approx 338$  K), the gas phase composition is strongly dominated by the presence of dimers. Therefore, DHBA will most probably adsorb onto the surface in the form of dimers. Note, however, that the actual temperature of the molecules in the gas phase after sublimation is lower since the molecules will lose their energy in order to escape from the crystal during the sublimation process. This however will not affect the conclusion made.



**Supplementary Figure 4:** Calculated attachment/detachment monomer and dimer processes to/from the striped island. Schematic representations of the processes at (a) a corner and (b) an edge vacancy site. The corresponding energy barriers (in eV) are also indicated.

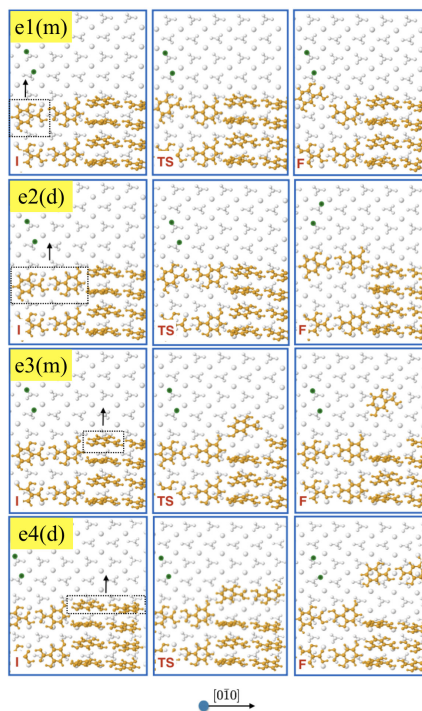
### Supplementary Note 3 Attachment/detachment transitions to/from a striped network island

In the following, we report detailed descriptions of several attachment/detachment mechanisms of both monomers and dimers to/from the corners, kinks and edge vacancies of a striped island. The most relevant processes (for dimers at the corners and kinks) were shown schematically in Fig. 6 of the main text. In **Supplementary Figure 4** we show schematically other processes considered: (a) attachment/detachment of monomers at a corner of an island, and (b) of monomers and dimers at an edge vacant site.

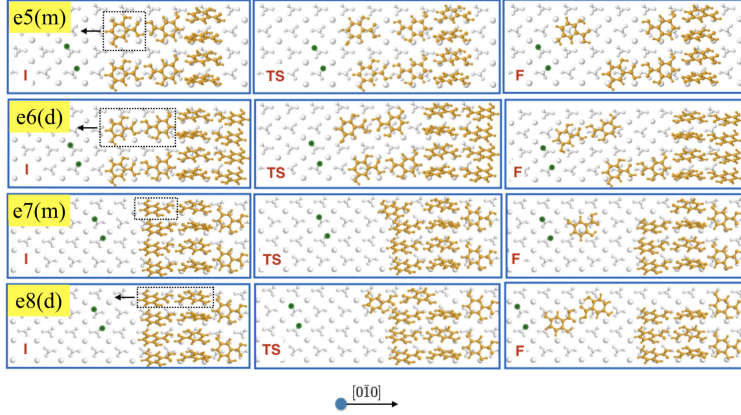
Detailed molecular models for all considered transitions are shown in the following figures. For definiteness, in all cases the initial state (I) corresponds to a monomer (dimer) attached to the striped island, while in the final state (F) the monomer (dimer) is located some distance away from the island. TS corresponds to the transition state with the highest energy along the transition path. Thus, I to F paths correspond to detachment transitions, while reverse F to I paths - to attachment transitions. However, not in all cases the reverse transitions are of interest, as explained in the main text.

Detachment/attachment mechanisms at edge vacancies of a striped island are presented in **Supplementary Figure 5** and **Supplementary Figure 6**; the corresponding energy barriers are given in **Supplementary Table 1**. In **Supplementary Figure 5** edges are periodically repeated along the [010] direction of calcite surface, while an

empty space is created along the  $[4\bar{2}\bar{1}]$  direction of the surface to allocate molecules or dimers after the detachment (before the attachment). The opposite applies to the edges shown in **Supplementary Figure 6**, which are now periodic along the  $[42\bar{1}]$  direction while the empty space between stripes of molecules runs along the  $[0\bar{1}0]$  direction. Although reverse transitions correspond to attachment processes with a dimer attaching to an edge containing an empty spot, these are of less interest due to a low probability of these events. Naturally, many of such processes are associated with very small energy barriers and lead to a considerable gain in the energy.



**Supplementary Figure 5:** Detachment/attachment mechanisms of molecules and dimers from/to the edge vacancies of the striped network. Structures are periodic along the  $[0\bar{1}0]$  direction and for the detachment transition molecules and dimers are moved away from the network into an empty space of the on-surface structure along the  $[4\bar{2}\bar{1}]$  direction. For each mechanism, the initial (I), final (F) and transition states (TS) are shown. Green dots highlight the alternating protruding oxygen atoms of the surface along the  $[4\bar{2}\bar{1}]$  direction for better visualisation.

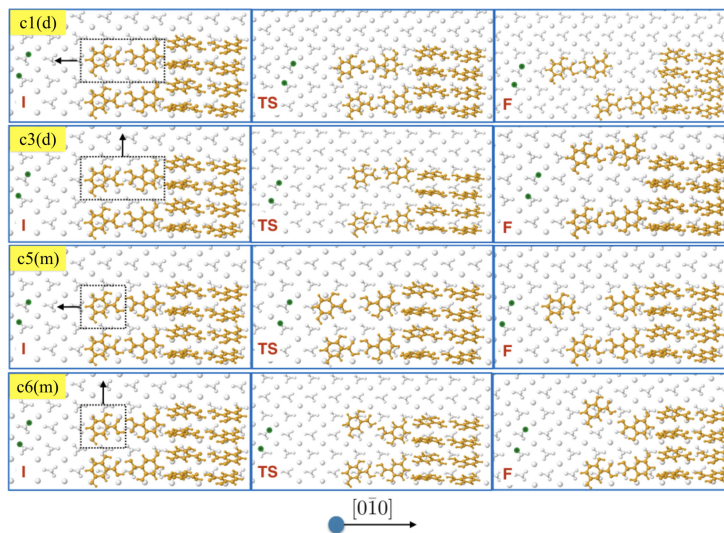


**Supplementary Figure 6:** Detachment/attachment mechanisms of molecules and dimers from/to the edge vacancies of the striped network. Structures are periodic along the  $[42\bar{1}]$  direction and for the detachment transition molecules and dimers are moved away from the network into an empty space of the on-surface structure along the  $[0\bar{1}0]$  direction. Notations are as in **Supplementary Figure 5**.

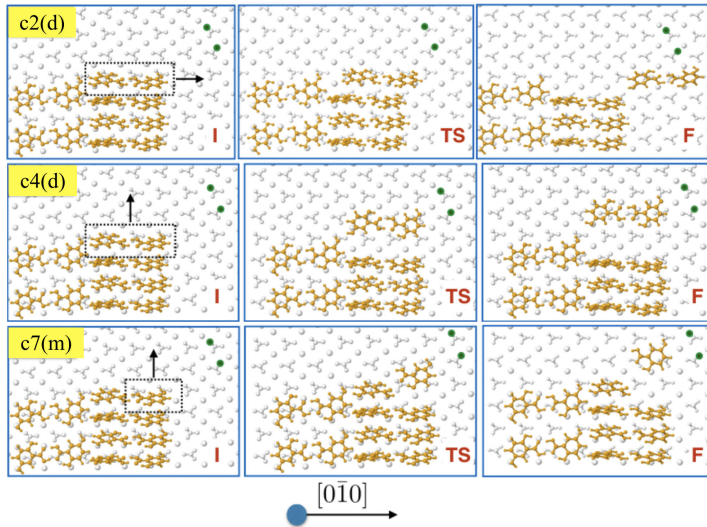
Edge ( $0\bar{1}0$ )	I	F	$E_{det}$	$E_{att}$	Edge ( $42\bar{1}$ )	I	F	$E_{det}$	$E_{att}$
e1(m)	0.00	0.12	1.16	1.04	e5(m)	0.00	0.82	1.21	0.39
e2(d)	0.00	0.45	1.28	0.83	e6(d)	0.00	0.61	1.00	0.39
e3(m)	0.00	1.13	1.28	0.15	e7(m)	0.00	0.33	1.38	1.05
e4(d)	0.00	0.38	1.12	0.74	e8(d)	0.00	0.94	1.95	1.01

**Supplementary Table 1:** Energetics of the attachment/detachment mechanisms at the edge vacancies of the striped network. The considered processes are depicted in **Supplementary Figure 5** and **Supplementary Figure 6**. For each path, we report the energy difference between the initial (I) (dimer/molecule attached to the network) and final (F) (dimer/molecule detached from the network) states and the corresponding detachment,  $E_{det}$ , and attachment,  $E_{att}$ , energy barriers, calculated with the NEB method. Energies are given in eV.

In **Supplementary Figure 7** and **Supplementary Figure 8** several mechanisms depicting a detachment of molecules and dimers from a corner of a striped island are shown; the corresponding energy barriers are collected in **Supplementary Table 1**. Although reverse processes do describe the corresponding attachment processes, not all of them are of interest. For instance, processes associated with attachment of molecules can be ignored as dimers are in abundance on the surface upon deposition. However, processes reverse to C4(D2), C6(D1) and C8(D2) (the path C2(D1) are discussed in the main text) correspond to the attachment of a dimer to a corner of a striped island, and hence are of interest. For these cases we also report in **Supplementary Table 2** the calculated attachment barriers.



**Supplementary Figure 7:** Calculated detachment/attachment mechanisms of flat dimers and molecules at corners of the striped network. Shown processes are for a *molecule* (c5(m) and c6(m)) and dimer (c1(d) and c3(d)). For a detachment transition, in c1(d) and c5(m) the dimer and the molecule, respectively, are moved away from the island along the  $[0\bar{1}0]$  direction, while in c3(d) and c6(m) along the  $[4\bar{2}\bar{1}]$  direction. Path c1(d) is discussed in detail in the main paper as it corresponds to the one with the lowest energy barrier. Notations are as in **Supplementary Figure 5**.



**Supplementary Figure 8:** Calculated detachment/attachment mechanisms of vertical dimers and molecules at corners of the striped network. Shown are processes for an upright dimer (c2(d) and c4(d)) and molecule, c7(m). The reverse processes correspond to an attachment into the corresponding upright position in the island. For a detachment transition, in c4(d) and c7(m), the dimer and the molecule, respectively, are moved away from the island along the  $[42\bar{1}]$  direction, while in c2(d) along the  $[0\bar{1}0]$  direction. Notations are as in **Supplementary Figure 5**.

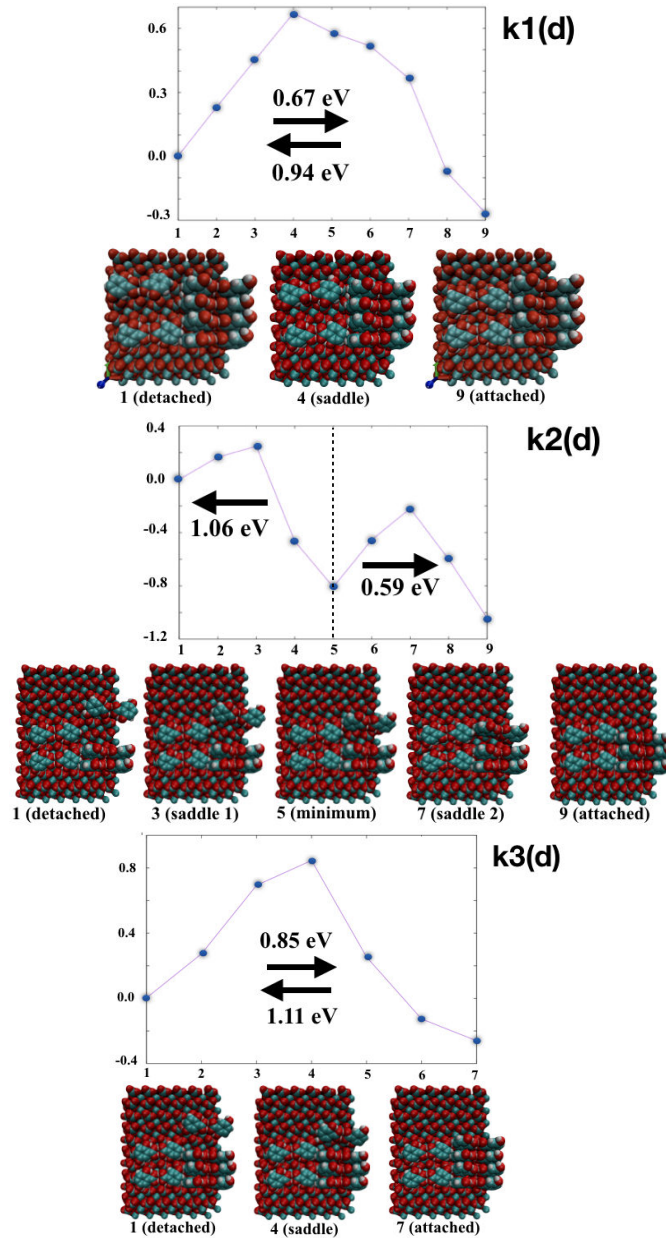
Corner	I	F	$E_{det}$	$E_{att}$	Corner	I	F	$E_{det}$	$E_{att}$
<b>c1(d)</b>	0.00	0.51	1.00	0.49	<b>c5(m)</b>	0.00	0.70	1.20	0.50
<b>c2(d)</b>	0.00	0.55	1.80	1.25	<b>c6(m)</b>	0.00	0.25	1.12	0.87
<b>c3(d)</b>	0.00	0.30	1.10	0.80	<b>c7(m)</b>	0.00	0.47	1.10	0.63
<b>c4(d)</b>	0.00	0.20	1.04	0.84					

**Supplementary Table 2:** Energetics of the detachment/attachment mechanisms at the corners of a striped island. The considered processes are depicted in **Supplementary Figure 7** and **Supplementary Figure 8**. For each path, we report the energy difference between the initial (I) (dimer/molecule attached to the island) and final (F) (dimer/molecule detached from the island) state and the corresponding detachment,  $E_{det}$ , and attachment,  $E_{att}$ , energy barriers, calculated with the NEB method. Energies are given in eV.

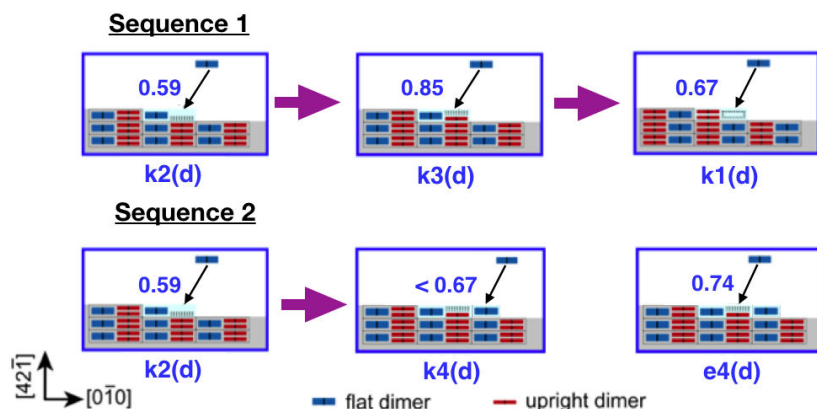
In **Supplementary Figure 9** three processes of attaching/detaching a dimer from/to a kink site are shown. The attachment process k2(d) consists of two peaks with the barriers of 0.25 eV and 0.59 eV, respectively, the latter one being rate-limiting. Therefore, if the whole unit cell (3 dimers) are attached one after another via the following sequence: (i) the first vertical dimer [k2(d)], (ii) the second vertical dimer [k3(d)] and finally (iii) the flat dimer [k1(d)], then the barrier determining the overall rate of the striped network growth will be determined by the 0.85 eV barrier of the k3(d) process. However, this particular sequence (i.e. the growth mechanism) at the kink does not need to be the only one possible. One can also envisage (amongst others also possible), e.g., the following sequence: (i) the first vertical dimer [k2(d)], (ii) the flat dimer [k4(d)], and then (iii) the second vertical dimer [e4(d), **Supplementary Figure 4**]. In this latter sequence a lower overall attachment barrier is required. Indeed, the process k4(d) is similar to k1(d). However, since when the flat dimer is attached there is only one vertical dimer at the kink side, a barrier even lower than the one for the k1(d) process (0.67 eV) is expected here. Concerning the process e4(d) for the edge attachment, considered above, the barrier is 0.74 eV, which appears to be rate-determining in this case (0.59 eV, < 0.67 eV and 0.74 eV), leading overall to a kinetically more favourable process than the former sequence. The two sequences are compared in **Supplementary Figure 10**.

Note that in all cases other possibilities of the dimer attachment differing by the location of the dimer away





**Supplementary Figure 9:** Attachment (detachment) of a flat and upright dimer at the striped island kink site. In k1(d) a dimer is attached at a flat kink position; k2(d) and k3(d) - at the first and then second upright kink positions. The dimers in question are highlighted by red boxes, while the corresponding arrows indicate the process direction and the corresponding energy barrier. Energies in the left upper corner in boxes enable comparison of the total energies of the initial and final states in each case. The k2(d) calculation was split into two B simulations as indicated by the vertical dashed line.



**Supplementary Figure 10:** Two possible sequences (amongst many others possible) for the kink growth mechanism of a striped network.

from the kink in the initial state were also considered; however, these processes led to larger energy barriers and hence are not presented here.

#### Supplementary Note 4 Consecutive detachment of monomers from a striped network island

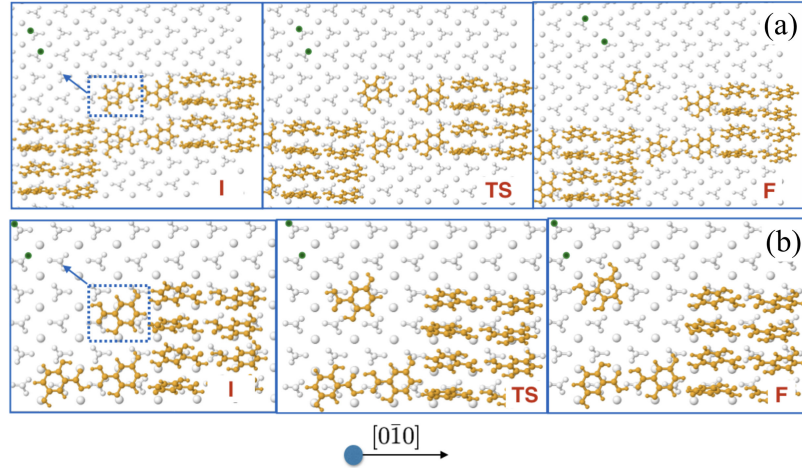
In **Supplementary Figure 11a** a consecutive detachment of two monomers from a kink site of a striped island, in which the molecules are released one after another, is shown.

For the first molecule [path (a)], a large barrier of 1.57 eV is required which is mostly due to breaking of the H-bonds inside the dimer. The second barrier [path (b)] is much lower, 0.92 eV, and is due to breaking of a weaker  $\pi$ -stacking interactions with the nearby upright dimers. Note that once single molecules are released from the striped island, it is energetically unfavorable for them to form dimers on the surface as a dimer on the surface is less favorable by 0.5 eV [1]. Hence, the detached molecules will most likely remain as monomers. The first detachment with the highest barrier is the rate limiting process leading to a rather low likelihood of the separate detachments of monomers from striped islands at experimental observation temperatures, as compared to the detachment of a dimer in one step.

#### Supplementary Note 5 Attachment of dimers to a dense network island

All possible processes we considered are shown schematically in **Supplementary Figure 12**. In the following, we report a detailed description of several attachment mechanisms of dimers to the edges (**Supplementary Figure 13** and **Supplementary Figure 14**) and kinks (**Supplementary Figure 15** - **Supplementary Figure 18**) of a dense island; the energetics of each process is collected in **Supplementary Table 3**. In the two important kink cases, the processes k1(d) and k7(d), the dimers first dissociate close to the kink and then one molecule attaches after the other. In doing so, the molecules change their orientation to match the one required in the dense island. If the NEB band of the k1(d) process basically contains a single well-defined peak, the band for the k7(d) process consists of two peaks with the close barriers of 0.66 eV and 0.71 eV, respectively, with the larger one defining the kinetics.

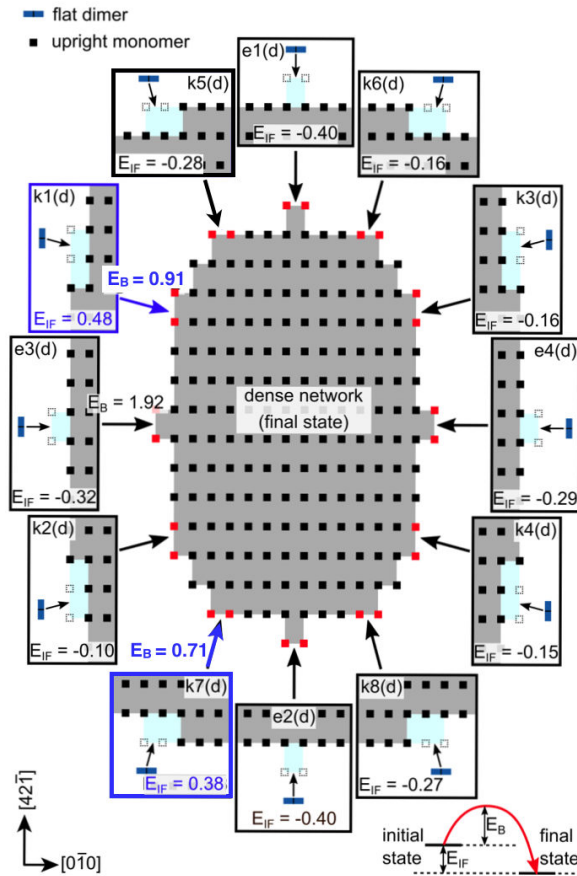
Note that in most cases, apart from the three cases indicated in the Table and discussed in the main text, only initial and final states were calculated.



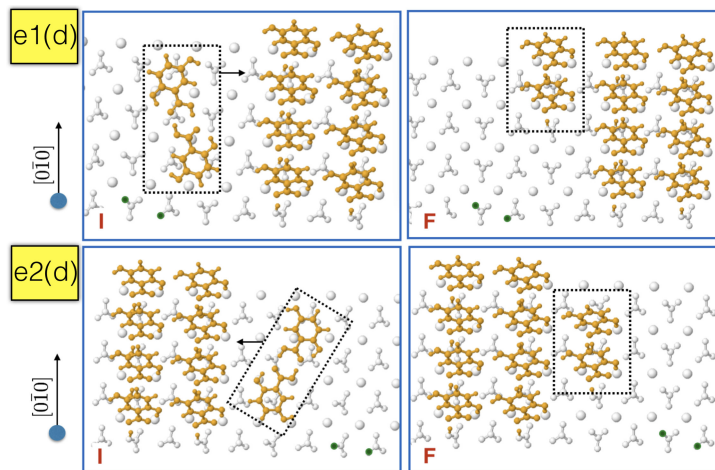
**Supplementary Figure 11:** Two consecutive detachment paths of a monomer from a kink site at the striped island. Overall, this leads to the detachment of a single dimer: (a) the first monomer is detached, (b) the second. Notations are as in **Supplementary Figure 5**.

Edge	I	F	$E_{att}$	Kink	I	F	$E_{att}$
<b>e1(d)</b>	0.00	0.40	-	<b>k1(d)</b>	0.48	0.00	0.82
<b>e2(d)</b>	0.00	0.20	-	<b>k2(d)</b>	0.00	0.10	-
<b>e3(d)</b>	0.00	0.32	1.92	<b>k3(d)</b>	0.00	0.16	-
<b>e4(d)</b>	0.00	0.29	-	<b>k4(d)</b>	0.00	0.15	-
				<b>k5(d)</b>	0.00	0.27	-
				<b>k6(d)</b>	0.00	0.16	-
				<b>k7(d)</b>	0.38	0.00	-0.71
				<b>k8(d)</b>	0.00	0.28	-

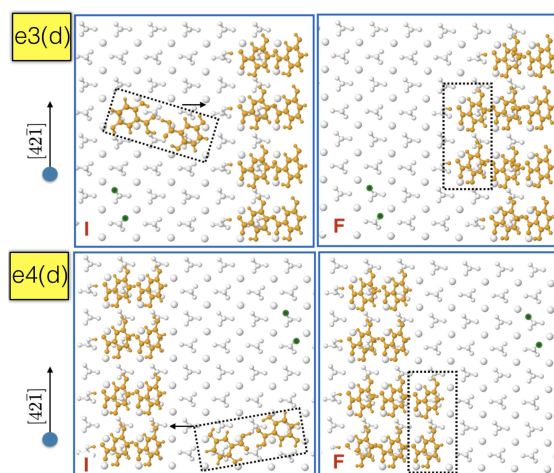
**Supplementary Table 3:** Energetics of the dense network attachment mechanisms. Energies are given in eV. For each type of edge and kink structures we report the energy difference between the initial (I, the dimer is adsorbed near the dense network island) and final states (F, the dimer is attached to the island). For three transitions also the calculated barriers  $E_{att}$  between the initial and final states are also shown.



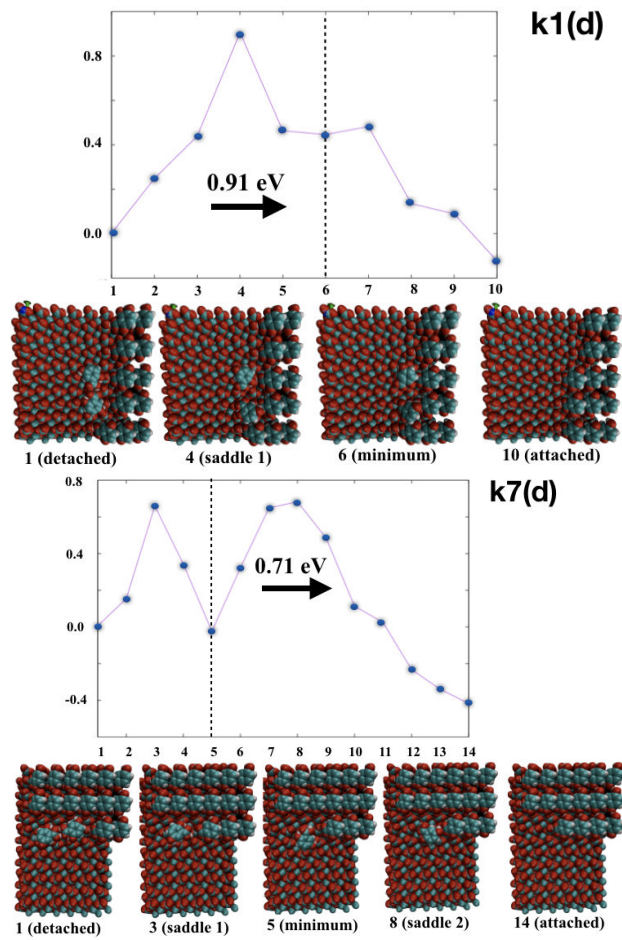
**Supplementary Figure 12:** Schematics of different types of edges and kinks at the dense network structure. Edge and kink processes are indicated by letters “e” and “k” followed by a number. Only processes associated with the attachment of dimers are shown. The arrows point out the directions of attachment of species to the network with the energy barrier  $E_B$  (where available) indicated. The difference between the initial (a dimer is placed next to the island) and final (the two molecules from the dimer are attached to the island) states of each process,  $E_{IF}$ , are also indicated in all cases. The processes k1(d) and k7(d), for which the attachment is energetically favourable, are highlighted by a blue box.



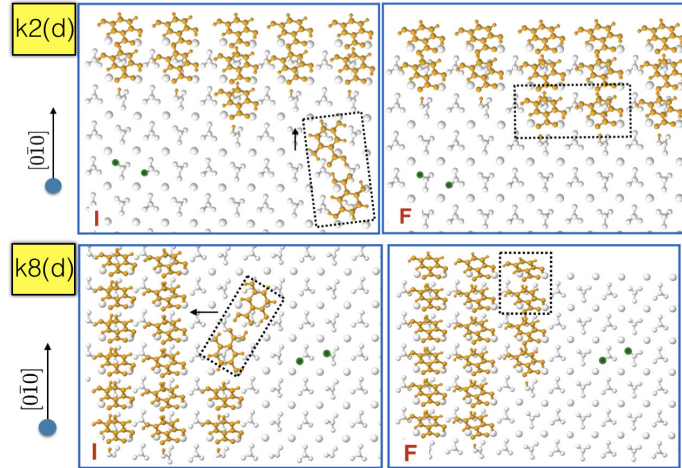
**Supplementary Figure 13:** Two processes of attachment of a dimer at the  $[0\bar{1}0]$  edge of the dense network structure. The direction of attachment to the edge corresponds also to its direction of growth. Notations are as in **Supplementary Figure 5**.



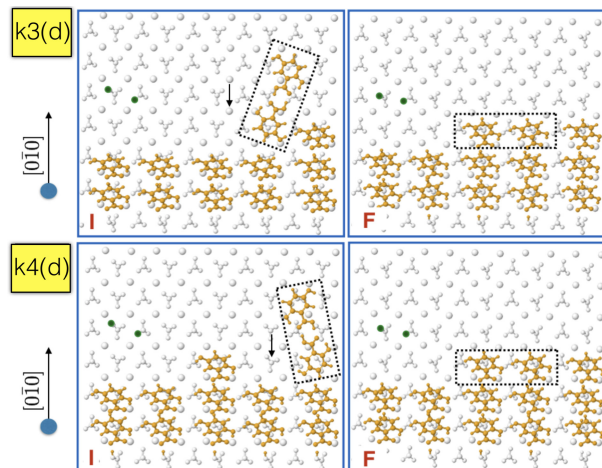
**Supplementary Figure 14:** Two processes of attachment of a dimer at the  $[42\bar{1}]$  edge of the dense network structure. The direction of attachment to the edge corresponds also to its direction of growth. Notations are as in **Supplementary Figure 5**.



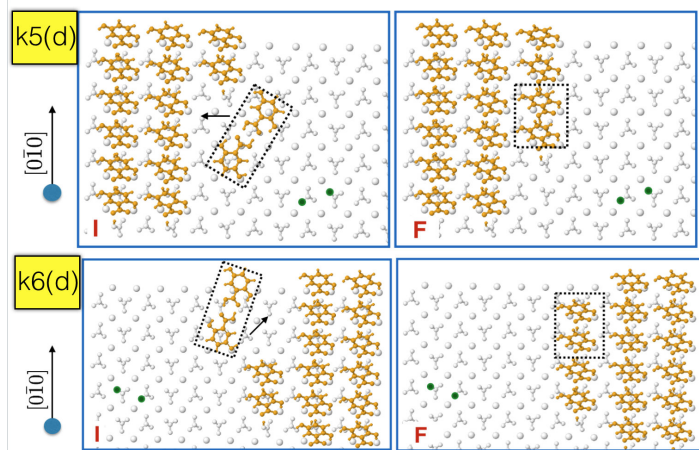
**Supplementary Figure 15:** Two attachment processes at the  $[\bar{4}21]$  kink of the dense island. In k1(d) the kink grows along the  $[42\bar{1}]$  direction, while in k7(d) along the  $[010]$  direction. Notations are as in **Supplementary Figure 5**.



**Supplementary Figure 16:** Attachment mechanisms of a dimer at the  $[\bar{4}21]$  kink of the dense network structure. In k2(d) the kink grows along the  $[\bar{4}21]$  direction, while in k8(d) along the  $[0\bar{1}0]$ . Notations are as in **Supplementary Figure 5**



**Supplementary Figure 17:** Attachment mechanisms of a dimer at the  $[\bar{4}21]$  kink of the dense network structure. In k3(d) the kink grows along the  $[\bar{4}21]$  direction, while in k4(d) along the  $[\bar{4}21]$  direction. Notations are as in **Supplementary Figure 5**.



**Supplementary Figure 18:** Attachment mechanisms of a dimer at the  $[0\bar{1}0]$  kink of the dense network structure. In k5(d) the kink grows along the  $[010]$  direction, while in k6(d) along the  $[0\bar{1}0]$ . Notations are as in **Supplementary Figure 5**.

## Supplementary Note 6 Attachment of monomers to a dense network island

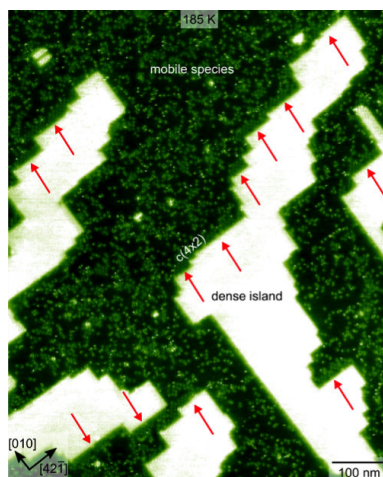
Although we have established, both on thermodynamic and kinetics grounds, that the dimers would mostly attach to the dense network, for completeness we have also considered an attachment of a monomer at a kink site. We find that (i) the initial state corresponding to a single molecule adsorbed nearby the dense network is slightly more stable than the final state where the molecule is attached to the island, and (ii) the attachment barrier is higher (1.15 eV) compared to the ones for the dimer attachment. Hence, we conclude that if single molecules do populate the mobile phase, they would rather lie alone on the surface or sit next to the dense network island.

Note that the detachment barrier (corresponding to the reverse process) is significant (around 1.1 eV), ensuring stability of the dense network at temperatures at which the network is formed.

## Supplementary Note 7 $c(4 \times 2)$ structure

For DHBA on calcite (10.4) only the striped and dense network islands can be imaged via AFM measurements at room temperature [1]. Upon a subsequent cooling of the substrate to 185 K the mobile species become immobilized and, therefore, become visible in the AFM images (see **Supplementary Figure 19**) taken at a low temperature. One can see that close to the dense network islands another molecule arrangement with a  $c(4 \times 2)$  superstructure is evident. We expect the mobile species arrange into the  $c(4 \times 2)$  arrangement as a consequence of the cooling procedure. The  $c(4 \times 2)$  superstructure is only observed in the direction of dense islands growth. Two chiral domains of the dense islands lead to the  $c(4 \times 2)$  molecule arrangement at the side of the dense islands either along the  $[010]$  and  $[0\bar{1}0]$  directions, respectively. It is unclear at the moment if and how the formation of this  $c(4 \times 2)$  structure influences the dense islands growth. However, since the  $c(4 \times 2)$  structure has not been detected at room temperature, it is likely that this structure is not stable at elevated temperatures and only forms upon cooling the sample.





**Supplementary Figure 19:** An AFM image of DHBA on calcite (10.4) revealing a  $c(4 \times 2)$  superstructure next to the dense islands. The sample is prepared at room temperature and cooled down to 185 K. The  $c(4 \times 2)$  structure is only found at the direction of growth along  $[010]$  and  $[0\bar{1}0]$  directions, respectively (indicated by red arrows).

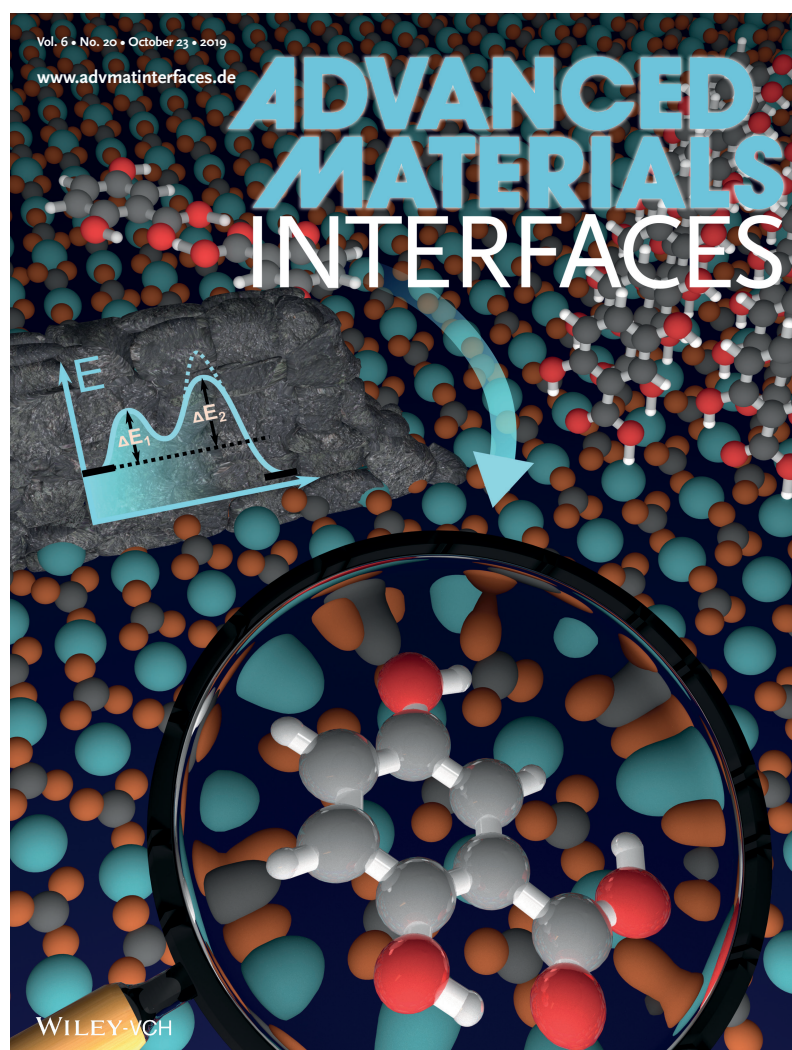
## References

- [1] Paris, C. et al. Increasing the templating effect on a bulk insulator surface: From a kinetically trapped to a thermodynamically more stable structure. *The Journal of Physical Chemistry C* **120**, 17546-17554 (2016).
- [2] Adam, M.-S. et al. Stability and cooperativity of hydrogen bonds in dihydroxybenzoic acids. *New J. Chem.* **34**, 85-91 (2010).



## Focus on the Essential: Extracting the Decisive Energy Barrier of a Complex Process

Reprinted with permission from 'Simon Aeschlimann, Julia Neff, Ralf Bechstein, Chiara Paris, Andrea Floris, Lev Kantorovich and Angelika Kühnle, "Focus on the Essential: Extracting the Decisive Energy Barrier of a Complex Process", *Advanced Materials Interfaces* 2019, 1900795'



Inside cover from *Advanced Materials Interfaces*, Volume 6, Number 20



## Focus on the Essential: Extracting the Decisive Energy Barrier of a Complex Process

Simon Aeschlimann, Julia Neff, Ralf Bechstein, Chiara Paris, Andrea Floris, Lev Kantorovich, and Angelika Kühnle\*


Molecular processes at surfaces can be composed of a rather complex sequence of steps. The kinetics of even seemingly simple steps are demonstrated to depend on a multitude of factors, which prohibits applying a simple Arrhenius law. This complexity can make it challenging to experimentally determine the kinetic parameters of a single step. However, a molecular-level understanding of molecular processes such as structural transitions requires elucidating the atomistic details of the individual steps. Here, a strategy is presented to extract the energy barrier of a decisive step in a very complex structural transition by systematically addressing all factors that impact the transition kinetics. Only by eliminating these factors in the measurement the experimental data will follow an Arrhenius law and the barrier can be extracted for the single step. Using the system of 2,5-dihydroxybenzoic acid on calcite (10.4) as an example, the energy barrier is determined for the attachment-assisted dissociation of molecular dimers in the structural transition from a striped to a dense molecular surface structure. This disentanglement approach is mandatory for a direct comparison with theoretical results and provides molecular-level insights into the transition mechanism.

The quantitative understanding of the kinetics of atomic and molecular processes at surfaces is pivotal to many fields, e.g., within epitaxy,<sup>[1–3]</sup> catalysis,<sup>[4–7]</sup> switches and sensor applications<sup>[8–10]</sup> or smart materials.<sup>[11]</sup>

Investigating the kinetics of molecular processes at surfaces allows determining the energy barriers of the steps involved.<sup>[12,13]</sup> When the process of interest can be directly followed by an experimental technique, the kinetics of the process might be accessible. As an example, scanning tunneling microscopy (STM) provides the capability to determine the barrier of a very fundamental surface process, namely diffusion of atoms<sup>[14,15]</sup> and molecules<sup>[16,17]</sup> on metal surfaces.<sup>[18]</sup> In many of these studies, the barrier of this single step can be deduced in an elegant and simple fashion from a direct measurement of the hopping events as a function of the temperature.

Microscopy techniques can also shed light on the kinetics in systems where the reaction is accompanied by a change in the relative surface coverage, e.g., for lipase enzymes that degrade surface-supported lipid bilayers,<sup>[19,20]</sup> photoinduced switching<sup>[21]</sup> or the growth of graphene flakes.<sup>[22]</sup> Another example focusses on the chemical exchange reaction kinetics between two different epoxy networks that has been determined by recording the temperature-dependent interfacial broadening.<sup>[23]</sup> Besides microscopy, other methods such as the quartz-crystal microbalance have been used to monitor the formation kinetics of lipid bilayers from vesicles bilayer<sup>[24,25]</sup> and the change in mass has been measured to follow the growth of nanowires on a copper surface.<sup>[26]</sup> These elegant examples do, however, require the process of interest to be directly reflected in a measurable quantity, e.g., the hopping frequency, the change of the surface coverage, or interfacial broadening, which allows applying a simple Arrhenius approach to determine the barrier. However, in many cases—as in the present work—the situation can be considerably more complex and the Arrhenius law fails to describe the kinetics of the complete process. Complex processes, in contrast to the simple examples presented above, depend on various factors.<sup>[27,28]</sup> As an example, it is well known that even simple adsorbate diffusion usually depends on the coverage.<sup>[14]</sup> Moreover, for many surface reactions complex pathways involving transition states have been revealed.<sup>[29]</sup> In the latter case, recording an

S. Aeschlimann, Prof. J. Neff  
Institute of Physical Chemistry  
Johannes Gutenberg University Mainz  
Duesbergweg 10-14, 55099 Mainz, Germany  
S. Aeschlimann  
Graduate School Materials Science in Mainz  
Staudingerweg 9, 55128 Mainz, Germany  
Dr. R. Bechstein, Prof. A. Kühnle  
Physical Chemistry I  
Department of Chemistry  
Bielefeld University  
Universitätsstraße 25, 33615 Bielefeld, Germany  
E-mail: kuehnle@uni-bielefeld.de  
Dr. C. Paris, Dr. A. Floris, Prof. L. Kantorovich  
Department of Physics  
King's College London  
London WC2R 2LS, UK  
Dr. A. Floris  
School of Chemistry  
University of Lincoln  
Brayford Pool, Lincoln LN6 7TS, UK

 The ORCID identification number(s) for the author(s) of this article can be found under <https://doi.org/10.1002/admi.201900795>.

© 2019 The Authors. Published by WILEY-VCH Verlag GmbH & Co. KGaA, Weinheim. This is an open access article under the terms of the Creative Commons Attribution-NonCommercial License, which permits use, distribution and reproduction in any medium, provided the original work is properly cited and is not used for commercial purposes.

DOI: 10.1002/admi.201900795

averaged observable results in monitoring an effective reaction rate due to several involved steps. This can make it challenging to disentangle the kinetics of the involved steps and, thus, determine the corresponding individual energy barriers. Therefore, the barrier of a single step of interest might not be experimentally accessible in a straightforward manner. In turn, this makes it difficult or even impossible to compare experimentally determined energy barriers with theoretical simulations. A possible approach is to greatly simplify the system under investigation, e.g., when studying catalytic processes at surfaces, a reaction in the gas phase is investigated instead.<sup>[5]</sup> However, this approach, as a matter of principle, cannot capture the mechanistic and kinetic details that govern the processes at the surface. In contrast, our disentanglement approach is to leave the system unchanged but design the experimental conditions in a way that information on individual steps can be disclosed.

In general, to determine the energy barrier of a process step, the temperature dependence of the respective rate constant has to be measured. Knowing the detailed process pathway, the experimental conditions can be adjusted to focus on the specific step of interest and to elucidate the molecular-scale mechanisms. A prime example to illustrate the complexity of structural transitions and corresponding rates is given by 2,5-dihydroxybenzoic acid (2,5-DHBA, model shown in Figure 1a) on the (10.4) cleavage plane of calcite (model shown in Figure 1b).<sup>[30]</sup> In this system, a temperature-driven structural transition has been experimentally observed from a so-called striped to a dense phase.<sup>[31]</sup> This transition has recently been elucidated in detail using density functional theory,<sup>[30]</sup> unraveling the individual transition steps. The striped phase is composed of hydrogen-bonded molecular dimers and the dense phase of molecular monomers. Therefore, the formation of the dense phase has been shown to be associated with the dissociation of the dimers. While the dissociation of an isolated hydrogen-bonded dimer on the surface is associated with a high energy barrier, the corresponding process has been shown to be facilitated by the presence of a dense island, reducing the barrier to only 0.7 eV.

This is why this decisive step is referred to as attachment-assisted dimer dissociation. Obviously, it is highly desirable to benchmark this theoretical result against an experimental validation, especially because many benzoic acid derivatives are known to form dimers in the bulk phase. Experimentally, however, the barrier of this decisive dissociation step is difficult to determine as many factors—such as space limitations and capture zone depletion—are known to influence or even suppress this process. Therefore, it is important to carefully exclude the effect of such factors when aiming for a meaningful measurement of the respective rates. The generic strategy presented here can be adopted to other systems where the kinetics depends on multiple factors.

Here we demonstrate that the experiment can be performed in a way that we eliminate the influence of all known factors on the transition rate except for the temperature dependence. This approach allows for extracting the barrier for this individual step exclusively. While we present the disentanglement for the specific system of 2,5-DHBA on calcite (10.4), the proposed approach is applicable to other systems as well and, therefore, is of more general nature. The disentanglement is mandatory for a direct comparison of experimental and theoretical results and constitutes the fundament for providing molecular-level insights into the transition mechanism.

In the gas phase, 2,5-DHBA is known to form dimers<sup>[30]</sup> like in the bulk. Therefore, upon sublimating the molecules onto the calcite (10.4) surface, dimers will be deposited. In this work, we sublimated the molecules onto calcite held at about 100 K and studied the structures that form as a function of substrate temperature. Dynamic atomic force microscopy (AFM) images taken after low-coverage deposition reveal streaky features, indicative of mobile dimers. Below 260 K these dimers form molecular islands on the surface (see Figure 2, left inset in a), which—due to their striped inner structure—are referred to as striped islands.<sup>[31]</sup> As detailed in the Supporting Information, the striped islands are in equilibrium with the mobile dimers. When increasing the substrate temperature above  $\approx 260$  K, mobile dimers start to form a further type of island, the so-called dense islands (see Figure 2, right inset in a). Thereby “consumed” mobile dimers are “refilled” by dimers detaching from the striped islands, keeping the concentration of mobile dimers constant at  $0.3 \text{ dimers nm}^{-2}$  (see Figure S2 in the Supporting Information). As a consequence, the area covered by striped islands shrinks, while the area covered by the dense islands grows.

Interestingly, the dense islands are built by molecular monomers rather than dimers. Therefore, the formation of the dense islands requires the dimers to dissociate, explaining why this transition is only observed for temperatures above  $\approx 260$  K.

The aim of the present study is to validate the theoretically obtained dissociation barrier of 0.7 eV<sup>[30,31]</sup> by obtaining an experimental counterpart of this barrier. However, simply monitoring the increase in dense island area would result in measuring a false dimer dissociation barrier, because the increase in the dense island area depends on various factors and, therefore, is not exclusively governed by temperature. Hence, we first need to identify the factors impacting the transition rate of the step of interest. Second, we then design the experiment in a way that these factors remain unchanged throughout the measurement. Finally, temperature-dependent

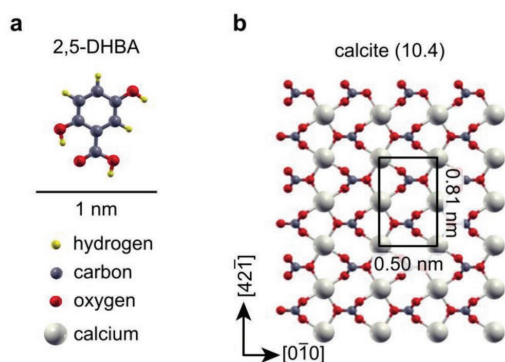


**Figure 1.** Model of a) the 2,5-DHBA molecule and b) the calcite (10.4) surface studied here. The scale bar applies to both panels.

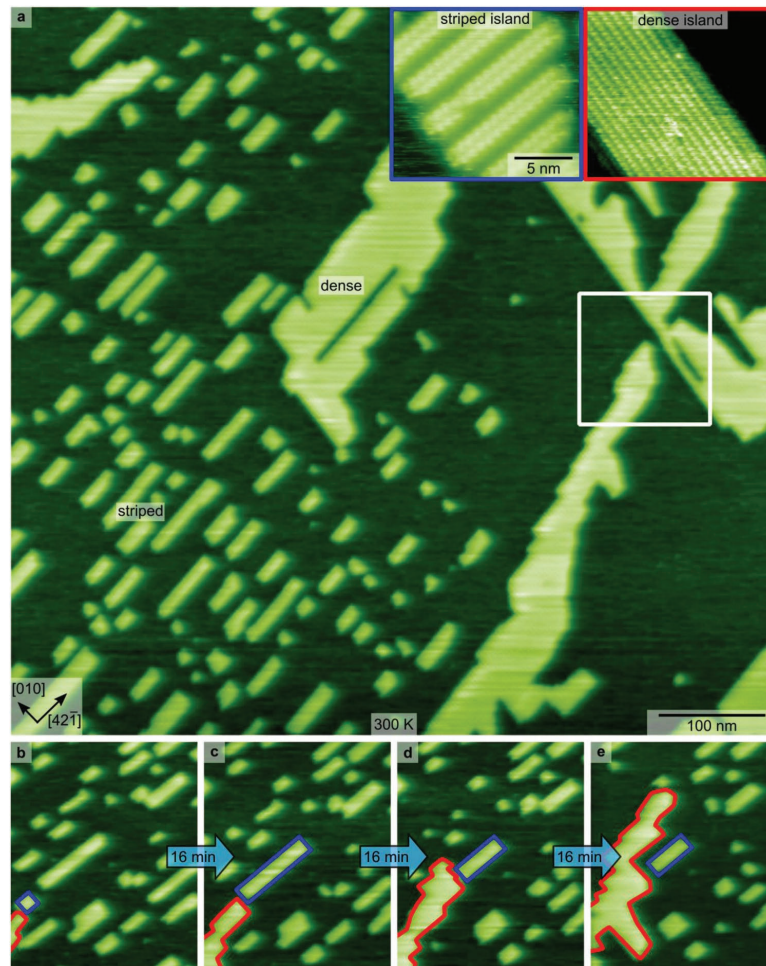


**Figure 2.** Dynamic AFM images that elucidate factors affecting the transition rates. In these images, both striped and dense islands are seen. Due to the large scan area, the two islands types appear rather similar. However, zooming onto the respective islands allows for unambiguous identification of striped (see left inset with blue frame in (a)) and dense (see right inset with red frame in (a)) islands. a) In an area where the growing edge of a dense island approaches an already existing dense island (marked by a white rectangle), the growth is ultimately stopped due to space limitation (# 2). Also note the depletion of the area around the dense island: The formation of dense islands apparently consumed the striped islands in the proximity, resulting in a capture zone depletion (#3). b–e) Image series revealing the growth of a dense island (marked by the red perimeter). When a striped island is approached (marked by the blue perimeters), the dense island partly circumvents the striped island. In the course of the process, the stripe island is gradually consumed.

measurements are taken and the temperature-dependent transition rates are obtained.

In the following, we discuss the relevant factors and present our strategies to rule out their influence on the rate determination.

First, the dimer dissociation rate should scale with the concentration of mobile dimers (#1). As discussed above, the concentration of mobile dimers is maintained at a constant value as long as striped islands are still present on the surface. Thus,

to ensure a constant mobile dimer concentration, a necessary yet not sufficient (see below #3) condition is an excess of striped islands.

Second, the inspection of image series revealed that the dense island growth occurs predominantly at a specific island edge, whose normal vector is aligned along the  $[42\bar{1}]$  surface direction. Consequently, the growth rate is affected by the accessibility of the mobile dimers to this specific edge. When other islands (striped or dense) are blocking this growing edge of the

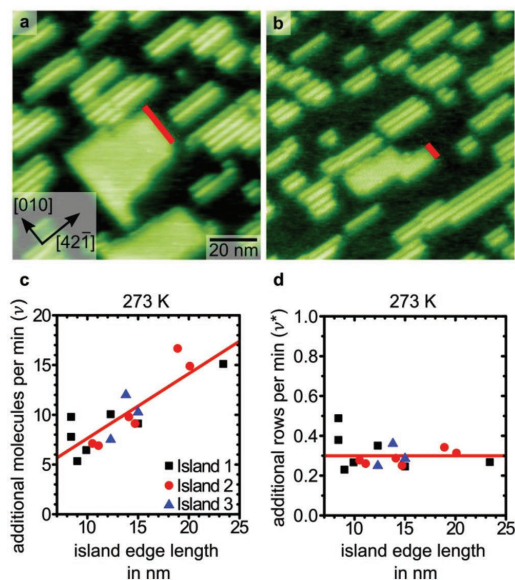


**Figure 3.** Dynamic AFM images to explain the dependence of the measured rates  $v$  on the island edge length (#4). From the experiments, we find that the dense islands grow predominantly from the edge (marked in red) with the normal vector oriented in the  $[42\bar{1}]$  direction. In a), a longer growing edge is seen as compared to b). c) The growth of three different islands is observed at 273 K. The experimentally obtained rates (in terms of additional molecules per time step) are found to be proportional to the island edge length. Therefore, we divide the number of additional molecules by the length of the island edge (i.e., we effectively count the number of newly formed rows per time step) to obtain the transition rate  $v'$  that is found to be independent of the island edge length d).

given island, its growth is effectively halted by a space limitation (#2, illustrated in Figure 2a). In the case of a dense island blocking, the growth is ultimately stopped (Figure 2a). In the case of a striped island blocking, the growth can be resumed as soon as the striped island has dissolved (Figure 2b–e). To avoid that space limitations affect the rate determination, we must ensure that exclusively islands with sufficient growth area are considered.

Third, the capture area in the vicinity of the growing edge might be depleted from mobile dimers (Figure 2a), when the constant equilibrium concentration of mobile dimers is not regained fast enough. This local capture area depletion (#3) can occur when equilibrium is not reached, e.g., when surrounding islands hinder mobile dimers from entering the capture area or when striped islands are far away as compared to the diffusivity. Therefore, when measuring transition rates, the islands that are monitored in time for the rate measurement were carefully chosen not to be affected by this effect.

Fourth, as the transition is known to be assisted by the presence of the dense phase, the size of the already existing dense islands must be considered. To be precise, the molecule attachment rate should scale with the growing edge length (#4). As shown in Figure 3a,b, the islands vary in their edge length. In

addition, time-dependent measurements indicate that the edge length of a single island can also change in time. The experimental observations indeed confirm that the molecule attachment rate is proportional to the growing edge length of the dense island (see Figure 3c). To take this effect into account and be able to compare the rate with the individual one that was calculated theoretically,<sup>[30]</sup> we divide the counted number of newly attached molecules by the growing edge length. This procedure eventually results in a transition rate  $v^*(T)$  that unravels the kinetics solely of the desired dimer dissociation step (Figure 3d); see the Supporting Information for the rigorous justification of this procedure.

Finally, we need to confirm that the above four factors cover all aspects that influence the transition rate. To this end, we validate that the measured growth rates are constant at constant temperature (see Figure S3 in the Supporting Information).

After having clarified the factors that impact the transition rate measurements, we performed temperature-dependent dynamic AFM image series following the growth of carefully chosen, individual dense islands. A typical representation is shown in Figure 4, which illustrates the data collection at a substrate temperature of 276 K. Two consecutive images with a time delay of 16 min (Figure 4a,b) are compared by generating a difference image (Figure 4c), that highlights vanishing (blue) and appearing (red) structures.

In the images, an abundance of striped, as compared to dense, islands can be seen, which are expected to effectively refill the concentration of mobile dimers (addressing #1). Thus, the concentration of mobile dimers is assumed to remain constant, which, in turn, means that the obtained rate is independent of the total molecular coverage. The striped islands are observed to both shrink and grow at both ends, indicating that the detachment from the striped islands is not the rate-limiting step. Mobile dimers are visible by the streaks that cover the otherwise bare surface areas. Near the center of the image, a single dense island exists, which is the island under investigation. We confirm that the growing edge in the upper right part of the island is not blocked by other islands (#2) and that the capture zone surrounding the growing edge is not fenced in by other islands (#3). From the difference image in Figure 4c we can clearly identify the growing edge of the dense island, which is the edge in the upper right part of the island. As outlined above, we finally divide the number of newly attached monomers by the length of the growing edge (#4) to arrive at a valid representation of the transition rate that is constant at the given temperature. Due to the careful design of the experiment, the determination of the rate is now reduced to the essential step, namely the attachment-assisted dimer dissociation barrier.

Following the route described here, we determined the transition rates at various temperatures. Each rate measurement was performed using image series composed of several images. For high rates (i.e., high temperatures), a measurement time of about 1 h was sufficient, while small rates (i.e., low temperatures) required measurement times of more than 4 h. As we have limited the process to the temperature dependence solely, we can now make use of a simple Arrhenius plot for extracting the energy barrier (see the Supporting Information for details on the procedure). The resulting plot is given in Figure 5.



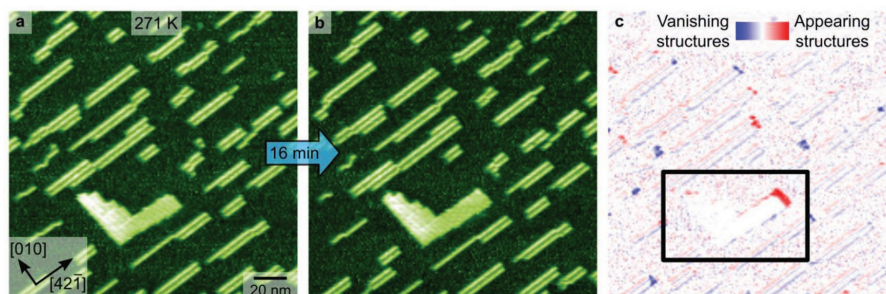


**Figure 4.** Illustration of the growth rate determination. a) Dynamic AFM image taken at a substrate temperature of 271 K. The surface is covered with striped islands, a single angle-shaped dense island near the center and mobile dimers. b) Image acquired 16 min after the image shown in (a) using the same imaging conditions. c) Difference image illustrating the growth of the dense island at the upper island edge, the growth in other directions is substantially smaller, indicating further constraints that are not considered here (the growing dense island is marked with rectangle). Striped islands are seen to shrink or grow at the ends of the stripes. Note that the images are corrected for linear drift to allow for taking a meaningful difference image. A minor nonlinear drift effect is still visible in the image, which is manifested in the faint blue regions to the lower right and the red regions to the upper left of all features. These faint regions are, therefore, artefacts from nonlinear drift.

From the Arrhenius plot in Figure 5, we are now able to extract the pre-exponential factor and the energy barrier for the single step of interest, namely the attachment-assisted dimer dissociation. The calculated pre-exponential factor is  $1.9 \pm 0.1 \times 10^{12}$  1/s, while the energy barrier was found to be  $(0.8 \pm 0.1)$  eV. This experimental value compares excellently with the calculated value of 0.7 eV for the attachment-assisted dimer dissociation as obtained from density-functional theory. This direct comparison is possible only because of the disentanglement approach presented here, allowing for extracting the barrier of an individual transition step within a rather complex sequence of steps. The excellent agreement between experiment and theory corroborates the picture drawn based on the calculations and the experimental observations. Our results contribute to an in-depth understanding of the process at the molecular level.

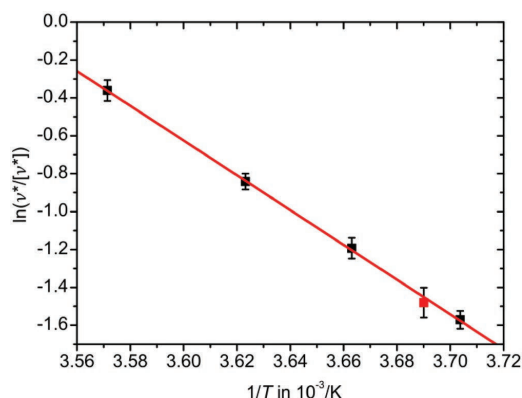


**Figure 5.** Arrhenius plot of the transition rate constant as a function of inverse substrate temperature. Except for the data point marked in red, all data points shown here are collected on the same sample. We reproduced the results with a new sample (271 K). The stated errors are the calculated standard errors of the mean.

The structural transition of 2,5-DHBA on calcite (10.4) from a so-called striped to a dense phase is composed of a sequence of individual transition steps. To obtain molecular-level insights into the underlying atomistic mechanism, we demonstrate our new disentanglement approach by precisely analyzing the transition process based on dynamic AFM image series. These experimental data disclose factors that impact the transition kinetics from mobile dimers to the dense phase, including space limitations, capture zone depletion and the length of the growing edge. By carefully excluding these factors, their impact on the measured rates is eliminated, hence exclusively the dependence of the transition rate on temperature is left. These experimental insights allow for exclusively extracting the temperature-dependent rates for a single step, namely the decisive attachment-assisted dimer dissociation. Our results reveal a transition barrier of 0.8 eV, which agrees well with the theoretical result of 0.7 eV. This study demonstrates how a complex process can be analyzed by limiting the investigation to a single, essential transition step and extracting detailed information exclusively for this individual transition.

### Experimental Section

All dynamic AFM measurements shown in this work were carried out with a Scienta Omicron VT AFM XA operated in the frequency modulation mode as described elsewhere.<sup>[31]</sup> N-doped silicon cantilevers were used from Nanosensors with a nominal force constant of  $40 \text{ N m}^{-1}$  and an eigenfrequency of 300 kHz in UHV. The images shown here were taken with a scan speed of 2 lines per second, which means that one image (trace and retrace) with  $500 \times 500$  pixel takes about 8 min. Sample preparation as well as molecule deposition were performed in situ with a chamber base pressure typically better than  $10^{-10}$  mbar. Optical quality calcite ( $\text{CaCO}_3$ ) crystals were purchased from Korth Kristalle GmbH, Kiel, Germany. The 2,5-DHBA molecules were bought from Aldrich, Munich, Germany. Molecule deposition was done using a home-built Knudsen cell that is heated to  $\approx 70$  °C for molecule sublimation. For the experiments shown here, a sublimation time of 10 min onto a sample at a distance of  $\approx 9$  cm was used. To ensure that the scanning process does not affect the observed kinetics, experiments were performed comparing

the situation after continuous scanning and after having paused the scanning process. Moreover, imaging at different setpoints, i.e., different tip-sample distances did not result in different kinetics, which further indicates that the scanning does not influence the transition process.

## Supporting Information

Supporting Information is available from the Wiley Online Library or from the author.

## Acknowledgements

The manuscript was written through contributions of all authors. All authors have given approval to the final version of the manuscript. Most stimulating discussions with Maximilian Vogtland and Martin Aeschlimann are gratefully acknowledged. S.A. is a recipient of a DFG-fellowship through the Excellence Initiative by the Graduate School Materials Science in Mainz (GSC 266).

## Conflict of Interest

The authors declare no conflict of interest.

## Keywords

Arrhenius, atomic force microscopy, energy barrier, nanoscience, surface science

Received: May 6, 2019

Revised: July 12, 2019

Published online:

- [1] D. I. Rogilo, L. I. Fedina, S. S. Kosolobov, B. S. Ranguelov, A. V. Latyshev, *Phys. Rev. Lett.* **2013**, *111*, 036105.
- [2] R. D. Smith, R. A. Bennett, M. Bowker, *Phys. Rev. B* **2002**, *66*, 7.
- [3] Y. Han, S. M. Russell, A. R. Layson, H. Walen, C. D. Yuen, P. A. Thiel, J. W. Evans, *Phys. Rev. B* **2013**, *87*, 155420.
- [4] S. Schauerhmann, H. J. Freund, *Acc. Chem. Res.* **2015**, *48*, 2775.
- [5] H. Schwarz, *Catal. Sci. Technol.* **2017**, *7*, 4302.
- [6] P. Z. Chen, T. P. Zhou, S. B. Wang, N. Zhang, Y. Tong, H. X. Ju, W. S. Chu, C. Z. Wu, Y. Xie, *Angew. Chem., Int. Ed.* **2018**, *57*, 15471.
- [7] A. Saywell, J. Schwarz, S. Hecht, L. Grill, *Angew. Chem., Int. Ed.* **2012**, *51*, 5096.
- [8] A. Johnson-Buck, J. Nangreave, S. Jiang, H. Yan, N. G. Walter, *Nano Lett.* **2013**, *13*, 2754.
- [9] P. Tegeder, *J. Phys.: Condens. Matter* **2012**, *24*, 394001.
- [10] C. Nacci, M. Baroncini, A. Credi, L. Grill, *Angew. Chem., Int. Ed.* **2018**, *57*, 15034.
- [11] D. Spitzer, V. Marichez, G. J. M. Formon, P. Besenius, T. M. Hermans, *Angew. Chem., Int. Ed.* **2018**, *57*, 11349.
- [12] S. Ditze, M. Stark, M. Drost, F. Buchner, H. P. Steinrück, H. Marbach, *Angew. Chem., Int. Ed.* **2012**, *51*, 10898.
- [13] M. Lepper, J. Köbl, L. Zhang, M. Meusel, H. Hölzel, D. Lungerich, N. Jux, A. de Siervo, B. Meyer, H. P. Steinrück, H. Marbach, *Angew. Chem., Int. Ed.* **2018**, *57*, 10074.
- [14] G. Ertl, *Angew. Chem., Int. Ed.* **2008**, *47*, 3524.
- [15] T. R. Linderroth, S. Horch, E. Lægsgaard, I. Stensgaard, F. Besenbacher, *Phys. Rev. Lett.* **1997**, *78*, 4978.
- [16] M. Schunack, T. R. Linderroth, F. Rosei, E. Lægsgaard, I. Stensgaard, F. Besenbacher, *Phys. Rev. Lett.* **2002**, *88*, 156102.
- [17] J. Weckesser, J. V. Barth, K. Kern, *J. Chem. Phys.* **1999**, *110*, 5351.
- [18] J. V. Barth, *Surf. Sci. Rep.* **2000**, *40*, 75.
- [19] K. Balashev, N. J. DiNardo, T. H. Callisen, A. Svendsen, T. Bjornholm, *Biochim. Biophys. Acta, Biomembr.* **2007**, *1768*, 90.
- [20] H. L. Wu, L. Yu, Y. J. Tong, A. M. Ge, S. Yau, M. Osawa, S. Ye, *Biochim. Biophys. Acta, Biomembr.* **2013**, *1828*, 642.
- [21] S. Jaekel, A. Richter, R. Lindner, R. Bechstein, C. Nacci, S. Hecht, A. Kühnle, L. Grill, *ACS Nano* **2018**, *12*, 1821.
- [22] K. Celebi, M. T. Cole, J. W. Choi, F. Wyczisk, P. Legagneux, N. Rupesinghe, J. Robertson, K. B. K. Teo, H. G. Park, *Nano Lett.* **2013**, *13*, 967.
- [23] C. F. He, S. W. Shi, X. F. Wu, T. P. Russell, D. Wang, *J. Am. Chem. Soc.* **2018**, *140*, 6793.
- [24] E. Reimhult, F. Höök, B. Kasemo, *Phys. Rev. E* **2002**, *66*, 051905.
- [25] S. R. Tabaei, J. A. Jackman, S.-O. Kim, V. P. Zhdanov, N.-J. Cho, *Langmuir* **2015**, *31*, 3125.
- [26] B. T. Richards, S. R. Schraer, E. J. McShane, J. Quintana, B. D. A. Levin, D. A. Muller, T. Hanrath, *Chem. Mater.* **2017**, *29*, 4792.
- [27] S. S. Chae, S. Jang, W. Lee, D. W. Jung, K. H. Lee, J. D. Kim, D. Jeong, H. Chang, J. Y. Hwang, J.-O. Lee, *Small* **2018**, *14*, 1801529.
- [28] J. Seo, J. Lee, G. Jeong, H. Park, *Small* **2019**, *15*, 1804133.
- [29] H. M. Zhang, J. H. Franke, D. Y. Zhong, Y. Li, A. Timmer, O. D. Arado, H. Monig, H. Wang, L. F. Chi, Z. H. Wang, K. Mullen, H. Fuchs, *Small* **2014**, *10*, 1361.
- [30] C. Paris, A. Floris, S. Aeschlimann, J. Neff, F. Kling, A. Kühnle, L. Kantorovich, *Commun. Chem.* **2018**, *1*, 66.
- [31] C. Paris, A. Floris, S. Aeschlimann, M. Kittelmann, F. Kling, R. Bechstein, L. Kantorovich, A. Kühnle, *J. Phys. Chem. C* **2016**, *120*, 17546.

Copyright WILEY-VCH Verlag GmbH & Co. KGaA, 69469 Weinheim, Germany, 2019.

**ADVANCED  
MATERIALS**  
INTERFACES

## Supporting Information

for *Adv. Mater. Interfaces*, DOI: 10.1002/admi.201900795

**Focus on the Essential: Extracting the Decisive Energy Barrier  
of a Complex Process**

*Simon Aeschlimann, Julia Neff, Ralf Bechstein, Chiara Paris,  
Andrea Floris, Lev Kantorovich, and Angelika Kühnle\**

Supporting Information to:

Focus on the Essential: Extracting the Decisive

Energy Barrier of a Complex Process

*Simon Aeschlimann,<sup>a,b</sup> Julia Neff,<sup>a</sup> Ralf Bechstein,<sup>c</sup> Chiara Paris,<sup>d</sup> Andrea Floris,<sup>d,e</sup> Lev Kantorovich,<sup>d</sup> Angelika Kühnle<sup>c\*</sup>*

<sup>a</sup> Institute of Physical Chemistry, Johannes Gutenberg University Mainz, Duesbergweg 10-14, 55099 Mainz, Germany

<sup>b</sup> Graduate School Materials Science in Mainz, Staudingerweg 9, 55128 Mainz, Germany

<sup>c</sup> Physical Chemistry I, Department of Chemistry, Bielefeld University, Universitätsstraße 25, 33615 Bielefeld

<sup>d</sup> Department of Physics, King's College London, London WC2R 2LS, UK

<sup>e</sup> School of Chemistry, University of Lincoln, Brayford Pool, Lincoln, LN6 7TS, UK

## Detailed Description of Structural Transition

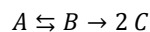
In the following, we provide a detailed description of the individual steps involved in the observed structural transition of 2,5-DHBA on calcite (10.4). This understanding of the transition pathway provides the basis for designing the experiment in a way that we are able to extract the barrier of the attachment-assisted dissociation step.

## Transition Mechanism

The molecules studied here are known to form dimers in the gas phase [1]. Therefore, upon sublimation of the molecules onto calcite (10.4) under ultrahigh vacuum conditions, dimers will arrive on the surface. The dimers have been observed to form islands with a striped inner pattern, referred to as *striped islands*. [2]. In the following, the letter *A* refers to a dimer within a striped island. The quantity  $[A]$  describes the corresponding “concentration” *i.e.*, the number of dimers (that are within striped islands) per observed surface area. The striped islands have been shown to be in equilibrium with mobile dimers that diffuse on the surface. The mobile dimers are labelled *B* and their corresponding concentration  $[B]$ . For temperatures above  $\sim 260$  K, a transition of the striped islands into another island type has been observed. The new islands are referred to as *dense islands*. However, the dense islands do not form directly from the striped islands, but rather *via* the mobile dimers as intermediates. Within the dense islands, the molecules do no longer form dimers but exist as monomers [1]. A monomer within a dense island is referred to as *C*, and the concentration  $[C]$  corresponds to the number of monomers (within the dense islands) per observed surface area. As the dense islands are built by monomers, the formation of the dense islands requires the mobile dimers to dissociate. Previous density-functional theory calculations have

shown that this dissociation is assisted by the attachment to the dense islands [1], greatly reducing the corresponding barrier from 1.4 eV for an isolated dimer to 0.7 eV upon dissociation at an already existing dense island. This is why this dissociation step has been referred to as *attachment-assisted dissociation*. The barriers of all other steps have been found to be significantly smaller than 0.7 eV. Obviously, it is interesting to benchmark the theoretical value of the rate-limiting step against an experimental determination of this barrier height. However, the dissociation barrier is experimentally not directly accessible but requires a well-controlled experiment to be conducted to reduce the measurement to the essential transition step.

For this analysis, we start by stating the reaction equation. Dimers in the striped islands are in equilibrium with dimers in the mobile phase. Dimers in the mobile phase can transform into dense islands. In our experiments, we exclusively observe growth of the dense islands. Therefore, the reverse reaction from the dense islands into the mobile dimer phase is not considered here:



For a simple reaction from an educt  $X$  to a product  $Y$ , the reaction rate might be described by  $v = \frac{d[Y]}{dt} = k [X]^\alpha$ , where  $k$  is the reaction rate constant and  $\alpha$  is the reaction order in  $[X]$ . However, the dependence of the reaction rate on the concentration of the educt is not known *a priori* and might be different from the simple relation given above. For example, in our system, the transition rate for dense island growth depends not only on the temperature and the concentration of mobile dimers but also on factors such as the area available for islands growth.

## Transition Rates

For the equilibrium between striped islands and mobile dimers, we can specify the transition rate by considering the change in concentration of  $A$ . The number of dimers in the striped islands shrinks by the detachment of dimers from the islands, which is associated with the transition rate  $v_{AB}(T, [A], \dots)$ , and it grows by attachment of mobile dimers to the striped islands with a transition rate of  $v_{BA}(T, [B], \dots)$ .

$$\frac{d[A]}{dt} = -v_{AB}(T, [A], \dots) + v_{BA}(T, [B], \dots)$$

Accordingly, as long as the temperature is kept below  $\sim 260$  K, the change in the concentration of  $B$  is given by:

$$\frac{d[B]}{dt} = +v_{AB}(T, [A], \dots) - v_{BA}(T, [B], \dots)$$

When the temperature is above  $\sim 260$  K, the mobile dimers can transform into dense islands. In this case, the change in the concentration of  $B$  reads:

$$\frac{d[B]}{dt} = +v_{AB}(T, [A], \dots) - v_{BA}(T, [B], \dots) - v_{BC}(T, [B], \dots)$$

Finally, the change in the concentration of  $C$  can be obtained from the rate of mobile dimers that dissociate to form the dense islands:

$$\frac{d[C]}{dt} = +2 v_{BC}(T, [B], \dots),$$

where the factor of 2 is introduced, because one dimer yields two monomers. Thus,  $v_{BC}(T, [B], \dots)$  is obviously related to a dimer dissociation rate, however, it reflects the growth of all observed islands. To arrive at the individual dimer dissociation rate,  $v_{BC}^*$ , we need to consider that the dissociation is assisted by the presence of dense islands. To be precise, the theoretical calculations have suggested the dissociation to take place at kink sites of the growing edges solely,

*i.e.*, the dimer dissociation rate is proportional to the number of kinks. Therefore, the above dimer dissociation rate  $v_{BC}(T, [B], \dots)$  must be proportional to the number of kink sites at the edges in question and to the individual dimer dissociation rate  $v_{BC}^*$ . The latter is the quantity we are interested in and that can be directly compared with the theory. The number of kinks, in turn, is proportional to the length of the growing edge,  $L$ , and we finally arrive at:

$$v_{BC}(T, [B], \dots) \propto G v_{BC}^* \propto L v_{BC}^* \quad (1)$$

### **First Step: Equilibrium between Striped Islands and Mobile Dimers**

Experiments performed with low molecular coverages at room temperature exhibit no island growth. Our experiments revealed that islands form only when a critical concentration of mobile dimers, referred to as  $[B]_0$ , is reached. For concentrations below  $[B]_0$ , all molecules exist as dimers in the mobile phase. For total concentrations above  $[B]_0$  and a substrate temperature below  $\sim 260$  K, striped islands exist on the surface. The islands are seen to shrink and grow, but the total area covered by striped islands remains constant in time as shown in the images given in Fig. S1. Thus, we can conclude that dimers in the striped islands are in equilibrium with mobile dimers. Long-time series showing the equilibrium of the striped islands and mobile dimers disclose no sign of dimer desorption. Thus, the concentration of mobile dimers as well as the concentration of dimers in the striped islands remain constant. When further molecules are deposited, the area of striped islands increases accordingly, while the concentration of mobile dimers stays constant at  $[B]_0$ . On the other hand, when the number of mobile dimers is reduced by the formation of dense islands in the second reaction step, the area of striped islands will shrink to ensure that the concentration of the mobile dimers remains constant. This is an important finding as it provides evidence of a



constant concentration of mobile dimers throughout the course of the transition, as long as striped islands are present on the surface.

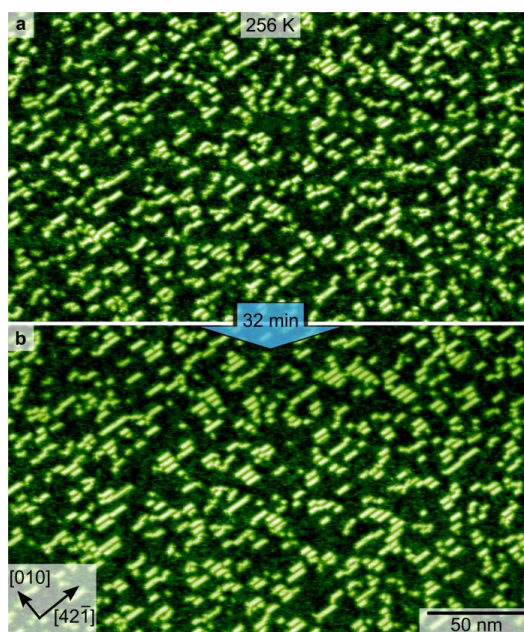


**Figure S1:** Two AFM images illustrating dissolution and growth of striped islands at a substrate temperature of 256 K.

### Second Step: Growth of Dense Islands

For a total concentration larger than  $[B]_0$  and a substrate temperature above  $\sim 260$  K, the dimers transform into dense islands, a process that has been shown to be kinetically hindered at temperatures below  $\sim 260$  K. The decisive step is the dissociation of the dimers into monomers, which has been found to be assisted by the attachment of the molecules to an existing dense island. The transformation of mobile dimers into the dense islands disturbs the equilibrium between the striped islands and the mobile phase. As a consequence, striped islands vanish to refill the mobile

phase. The detachment of dimers from the striped islands can be observed already at low temperatures, while the formation of dense islands only happens at temperatures above  $\sim 260$  K due to the comparably high barrier for the latter process. Thus, the dissolution of striped islands is fast as compared to the formation of dense islands. Therefore, the equilibrium between striped islands and mobile dimers is regained quickly (as long as  $[A] \gg [C]$ ), resulting in a constant concentration of mobile dimers,  $[B]_0$ , throughout the entire transition process until all striped islands are consumed and the process stops (see Fig. S2).

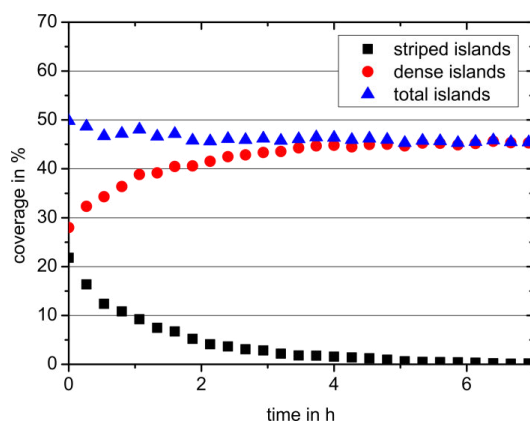


**Figure S2:** Experimentally obtained coverage of striped and dense islands as a function of time. The growth of the dense islands (red circles) leads to dissolution of the striped islands (black squares). The total coverage of islands (blue triangles) remains nearly constant during the experiment (7 h). Hence, assuming that no molecules desorb from the surface, the concentration of mobile dimers  $[B]_0$  remains also constant. The substrate was kept at 295 K and a  $500 \times 500 \text{ nm}^2$  image was taken every 16 min.

To determine the barrier of the attachment-assisted dimer dissociation, we concentrate on the second reaction step, namely the transformation of mobile dimers into dense islands. The corresponding transition rate,  $\nu_{BC}(T, [B], \dots)$ , is likely to depend on the concentration of the mobile dimers on the surface (#1). However, as this concentration remains constant in our

experiments, we can neglect this dependence. Furthermore, from our experiments we learn that the transition rate not only depends on the temperature, but also on factors such as area limitations (#2), capture zone depletion (#3) and the length of the growing edge (#4) at the dense island.

The key aspect of the main text is to demonstrate that the experiment can be performed in a manner such that the transition rate  $v_{BC}^*(T)$  is measured, which depends on the temperature only. As follows from Eq. (1), the transition rate is related to the rate of added molecules of carefully chosen island edges through division by the length  $L$  of the growing edge [3]:

$$v_{BC}^*(T) \propto \frac{1}{L} \frac{d[C]}{dt}$$

Thus, following this strategy, we remove the dependence of the transition rate on all other factors besides the temperature. Given that all factors affecting the reaction rate are captured in the above analysis, the quantity obtained in this way should now be constant for a fixed temperature. We have validated this statement by monitoring the number of newly created rows per time step to confirm that this number remains constant. An illustration for this procedure is given in Fig. S3.

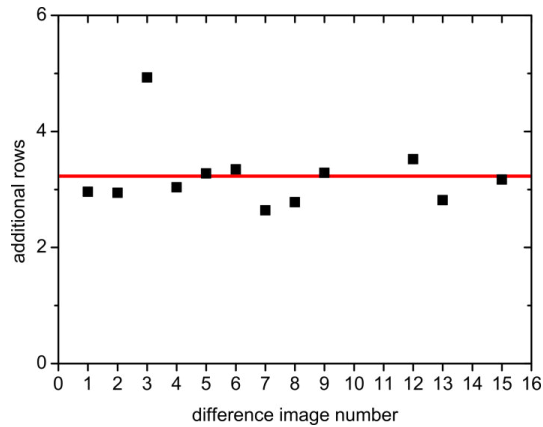


**Figure S3:** Number of newly formed rows at an island per image frame. The number remains more or less constant during the course of this experiment taken at a constant temperature of 271 K. An image is taken every 16 min. The total measurement time was four hours.

### Determination of the Barrier of the Attachment-Assisted Dimer Dissociation

In the section above, we have shown how the determination of the transition rate can be reduced to exclusively measuring the temperature dependence of the decisive reaction rate. Now, as we have narrowed down all factors to the temperature dependence solely, we can use a simple Arrhenius approach which follows from Transition State Theory [4] to obtain the energy barrier of the decisive step:

$$v^*(T) = v_0^* e^{-\frac{E_A}{k_B T}}$$

Here,  $v_0^*$  is the attempt frequency,  $k_B$  is the Boltzmann constant and  $E_A$  is the barrier of interest. Figure 5 of the main text is obtained by plotting the logarithm of the reaction rate against the inverse temperature [5]:

$$\ln(v^*(T)/[v^*]) = -\frac{E_A}{k_B} \frac{1}{T} + \ln(v_0^*/[v^*])$$

### References

- [1] C. Paris, A. Floris, S. Aeschlimann, J. Neff, F. Kling, A. Kühnle, L. Kantorovich, Kinetic control of molecular assembly on surfaces, *Communications Chemistry*, 1 (2018) 66.
- [2] C. Paris, A. Floris, S. Aeschlimann, M. Kittelmann, F. Kling, R. Bechstein, L. Kantorovich, A. Kühnle, Increasing the Templating Effect on a Bulk Insulator Surface: From a Kinetically Trapped to a Thermodynamically More Stable Structure, *J. Phys. Chem. C*, 120 (2016) 17546-17554.
- [3] As we are interested in the dissociation barrier, the proportionality constant can be neglected here. The latter does only affect the pre-factor.

[4] A. Nitzan, *Chemical Dynamics in Condensed Phases: Relaxation, Transfer, and Reactions in Condensed Molecular Systems*, Oxford University Press, Oxford, 2014.

[5] The square brackets are used to state the units in order to have a dimensionless quantity in the logarithm.



## Mobilization upon Cooling

This paper manuscript from Simon Aeschlimann, Lu Lyu, Sebastian Becker, Sina Mousavion, Thomas Speck, Hans-Joachim Elmers, Benjamin Stadtmüller, Martin Aeschlimann, Ralf Bechstein and Angelika Kühnle is currently under preparation.

## 8.1 Abstract

Phase transitions between different aggregate states are omnipresent in nature and technology. Conventionally, a crystalline phase melts upon heating. Already in 1903, Gustav Tammann speculated about the opposite processes, namely melting upon cooling. So far, evidence for such "inverse" transitions in real systems is rare and limited to exotic systems or specific conditions. Here, we demonstrate an inverse phase transition for molecules adsorbed on a surface. Molybdenum tetraacetate on copper (111) forms an ordered structure at room temperature. This phase dissolves upon cooling, and the molecules become mobile, *i.e.*, mobilization upon cooling is observed. This unexpected phase transition is ascribed to the fact that the molecules in the ordered phase have more internal degrees of freedom as compared to the mobile phase.

**One Sentence Summary:** Molecules that form a two-dimensional ordered phase on a surface kept at room temperature become mobile upon cooling to 220 K.

## 8.2 Main Text

A phase transition describes a reversible change in the state of matter upon varying external conditions, typically pressure or temperature. As an example, commonly a crystal melts upon heating and a liquid crystallizes upon cooling (Fig. 8.1A).

Already in 1903 Gustav Tammann, a chemist at the University of Göttingen, speculated about the inverse process, a rather counterintuitive phase transition termed "inverse melting" [36, 119]. In inverse melting, a crystalline phase melts upon cooling, in contrast to conventional melting where it would melt upon heating (Fig. 8.1B). While Tammann himself has never found evidence for such a peculiar phase transition to exist in nature, his ideas have later gained recognition when specific systems were identified that, indeed, show inverse melting behavior [37, 120, 121]. So far, however, the known instances where inverse melting has been reported are limited to extreme conditions such as low temperatures and high pressures, or rather exotic systems. For example, helium exhibits inverse melting at high pressures above 20 bar and temperatures lower than 1 K [120]. Metal alloys, the major research interest of Tammann, show a phase transition from a crystalline to an unordered state upon cooling; however, the unordered state is amorphous (immobile) rather than liquid (mobile) [121–126]. Likewise, evidence for an inverse transition from an ordered to an amorphous state has been presented for polymeric systems [127–130]. Most interestingly, a reversal of the expected transition direction should also be



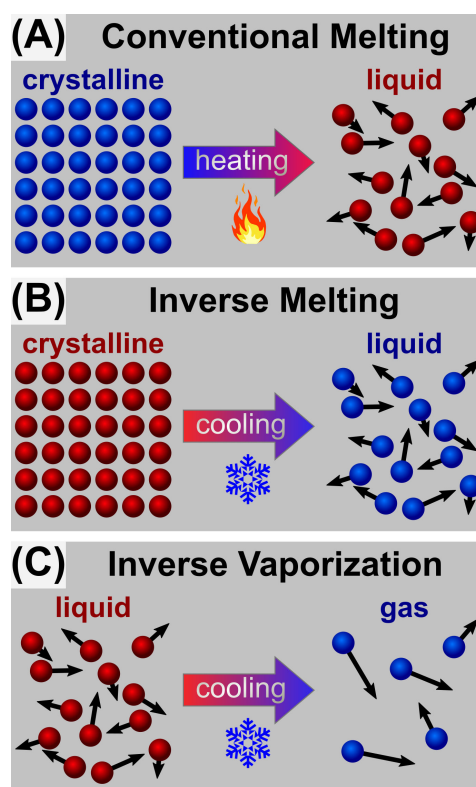


**Fig. 8.1.: Conventional and inverse phase transitions.** (A) In a conventional phase transition, a crystalline phase melts upon heating. (B) In inverse melting, the above order is reversed. An ordered crystalline phase melts upon cooling, forming an unordered mobile (liquid) phase. (C) Similarly, in inverse vaporization a liquid vaporizes upon cooling.

possible when going from liquid to gas at low pressures, *i.e.*, inverse vaporization (Fig. 8.1C), a phenomenon that, however, has not yet been reported.

For molecules adsorbed on a surface, phase transitions can be observed in a similar manner as for three-dimensional (3D) bulk material [131]. Molecules confined to a surface may form two-dimensional (2D) ordered arrangements. Such an ordered phase might be assigned to a crystalline-like phase or a liquid-like phase, depending on the strength of the molecule-molecule interactions. In the other extreme, molecules with little molecule-molecule interaction might be able to freely diffuse over the surface. Such a mobile phase corresponds to a gaseous-like state in 3D.

For such a 2D system, an inverse order-disorder transition has been presented for an organic overlayer adsorbed on a silver (111) surface [132]. Here, low-energy electron diffraction data have allowed for concluding that an ordered phase undergoes a transition to an unordered phase upon cooling. However, as diffraction data reveal reciprocal space information, it cannot be decided whether the unordered state corresponds to a surface-confined mobile phase or to an amorphous solid only.

Here, we present a system of adsorbed molecules on a surface that shows an inverse phase transition from a two-dimensional ordered to a mobile state. At room temperature, an ordered phase is formed. Upon cooling, a large fraction of the molecules becomes mobile on the surface. To the best of our knowledge, this is the first demonstration of mobilization upon cooling on a surface. Our scanning tunneling microscopy (STM) images allow for investigating the system in real space. This enables us to directly follow the transition by observing the change in relative surface coverage of the two phases. Moreover, the low-temperature phase can be unambiguously assigned to mobile species, *i.e.*, we provide a direct proof that the unordered state corresponds to mobile molecules rather than an amorphous solid state.

In this work, we investigate dimolybdenum tetraacetate  $\text{Mo}_2(\text{O}_2\text{CCH}_3)_4$  (MoMo) on the (111) plane of copper in ultrahigh vacuum using STM (materials and methods are available in the Supporting Information 8.4). For this system, it has previously been shown that different phases form depending on the copper substrate temperature [133]. When the copper substrate is held at room temperature (300 K), a so-called chain phase exists on the surface, which consists of upright-standing molecules that arrange in ordered chains aligned next to each other (Fig. 8.2, left-hand side). Upon cooling the substrate below a temperature of approximately 220 K, another ordered phase evolves, which is referred to as mesh phase (Fig. 8.2, right-hand side). In the mesh phase, the molecules are lying flat on the surface. While the phase transition from the chain to the mesh phase has been reported before [133], we here concentrate on the intermediate temperature regime, *i.e.*, cooling from 300 K to about 220 K. In this intermediate temperature regime, yet another phase is found, which is characterized by a fuzzy appearance (Fig. 8.2, middle panel). As shown in the following, the streaky features seen in this fuzzy phase can be ascribed to mobile molecules. Consequently, an ordered structure present at room temperature transforms into mobile molecules upon cooling, *i.e.*, mobilization upon cooling is observed. This transition could be related to the transition from the crystalline to the liquid state (inverse melting) or to the transition from the liquid to the gaseous state (inverse vaporization). As will be shown below, the inverse transition reported here can be assigned to inverse vaporization rather than inverse melting.

To elucidate this transition in more detail, in Fig. 8.3 representative STM images taken at different temperatures are presented. For these images, a molecular coverage of  $2/3$  ML was deposited onto the surface (1 ML corresponds to a full monolayer coverage of the chain phase). At a substrate temperature of 300 K, the only molecular phase present is the chain phase (Fig. 8.3A, a detailed view is given in the inset). When cooling the substrate to 220 K (Fig. 8.3B), the chain phase dissolves in some areas. In these areas, the fuzzy phase becomes apparent. The mobility of the structures at this temperature of 220 K is illustrated by an image series in Fig. 8.3C.

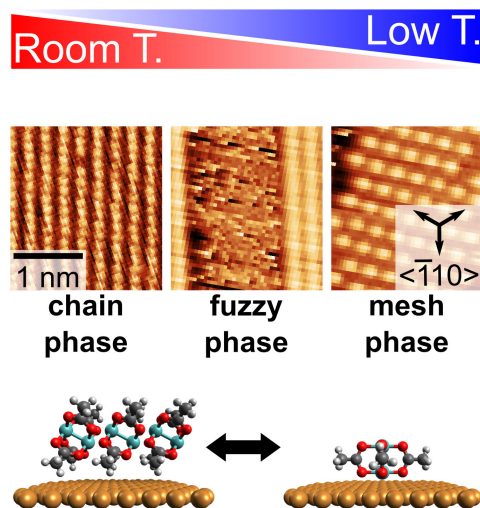


**Fig. 8.2.:** Phases adopted by MoMo adsorbed on Cu(111). At room temperature, an ordered chain phase is formed that is composed of upright standing molecules. Upon cooling, a coexisting fuzzy phase evolves on the surface, which is ascribed to flat-lying molecules that are mobile on the surface. Further cooling results in the formation of yet another phase, the mesh phase composed of ordered flat-lying molecules.

Here, consecutive images are shown with a time lapse of 3.5 min between two successive images. From this series it becomes evident that the chain phase dissolves and reforms at different positions over time. Moreover, we observe the formation of a further modification of the chain structure, which is composed of single chains that can have a curved shape (in the following referred to as single-chain phase). Further cooling to 150 K (Fig. 8.3D) results in the appearance of the above-mentioned mesh phase, which coexists with the chain phase. At this temperature of 150 K, few fuzzy features can still be recognized, indicative of the mobile molecules. When cooling down to 106 K (Fig. 8.3E), the fuzzy structures have vanished completely, and the surface is covered by the chain and mesh phase exclusively.

To confirm reversibility of the phase transition, experiments upon cooling and also upon heating the copper substrate were performed. The data shown in Fig. 8.3 are independent of the direction in which the temperature was changed, confirming the reversibility of the presented phase transition. Moreover, no desorption of MoMo molecules took place during the experiments. This can be reliably checked upon evaluating the coverage at low temperatures when all molecules become immobile.

The presented data is quantified by analyzing the surface coverage of the respective phases. With the knowledge of the molecular surface density in the chain and mesh phase, 1.79 and 0.71 molecule/nm<sup>2</sup> respectively [133], and of the fact that no desorption takes place, we can calculate the fraction of the molecules that constitute the chain, fuzzy and mesh phase at a given temperature (Fig. 8.4). As can be seen, at a temperature of 300 K, the majority of the molecules exist in the chain phase

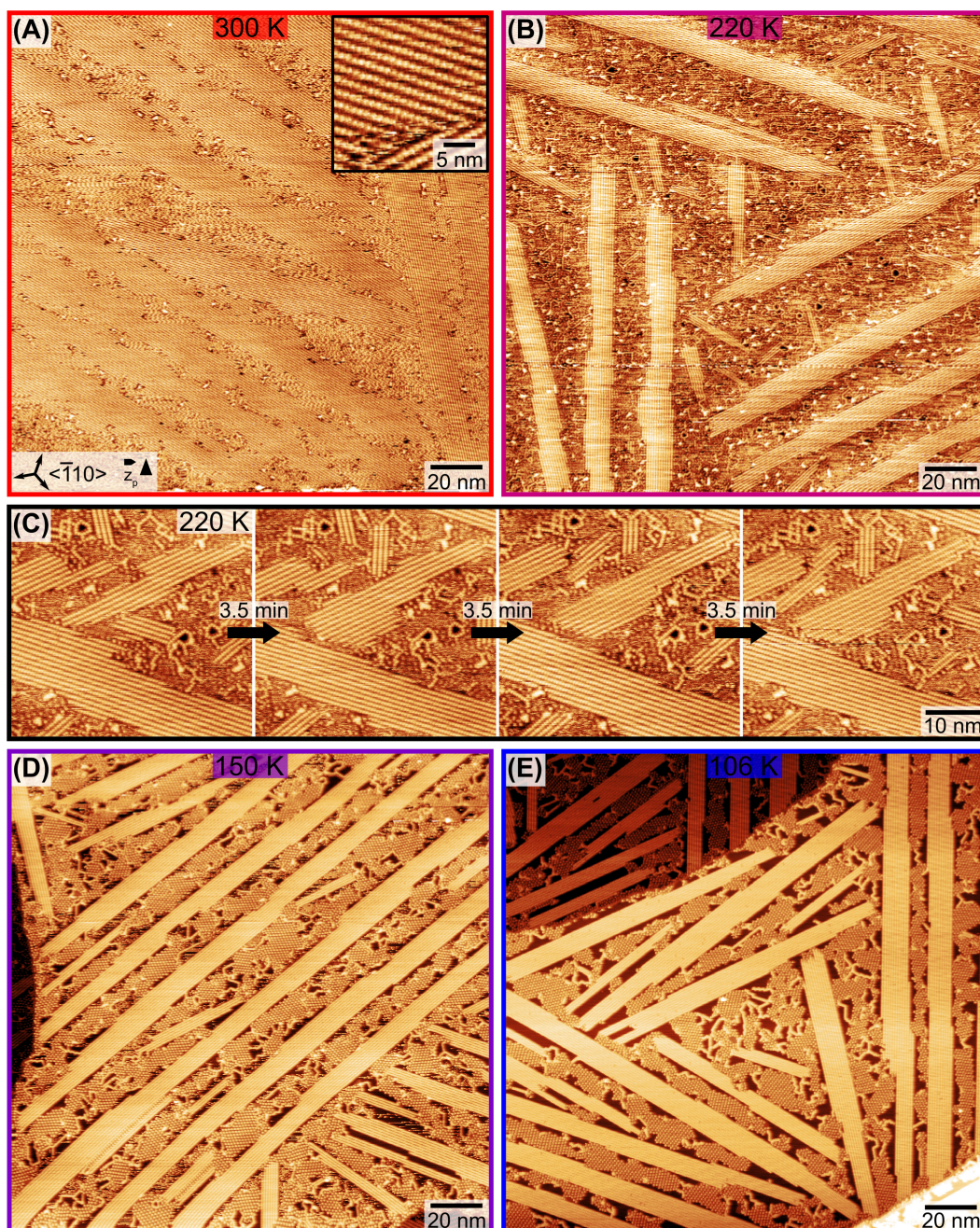


**Fig. 8.3.: Mobilization upon cooling.** Scanning tunneling microscopy images of MoMo adsorbed on Cu(111) held at different temperatures. (A) At room temperature, the only molecular structure present on the surface is the chain phase. The top-right inset provides a detailed view of the chain phase. (B) Upon cooling to 220 K, the chain phase dissolves and the fuzzy phase evolves. (C) Sequential images illustrating the mobility of the molecules at 220 K. (D) Further cooling to 150 K results in the appearance of the mesh phase. At this temperature, the fuzzy phase is nearly vanished. (E) At 106 K, only the chain and the mesh phase remain on the surface.

(nearly 100%), while the few remaining molecules are mobile (fuzzy phase). Upon decreasing the temperature to 220 K, the fraction of molecules in the chain phase decreases to about 70%, while the fraction of molecules that are mobile increases

to 30%. These numbers corroborate the above-reported finding of molecules in the ordered chain phase becoming mobile upon cooling, *i.e.*, mobilization upon cooling is observed in the temperature window from 300 to 220 K (marked in blue in Fig. 8.4). Upon further reduction of the temperature, the mesh phase forms, and the number of mobile molecules decreases again. We note that the formation of the mesh phase is a further interesting aspect of this system, however, the emphasis of this work is on the phase transition from the chain to the fuzzy phase.

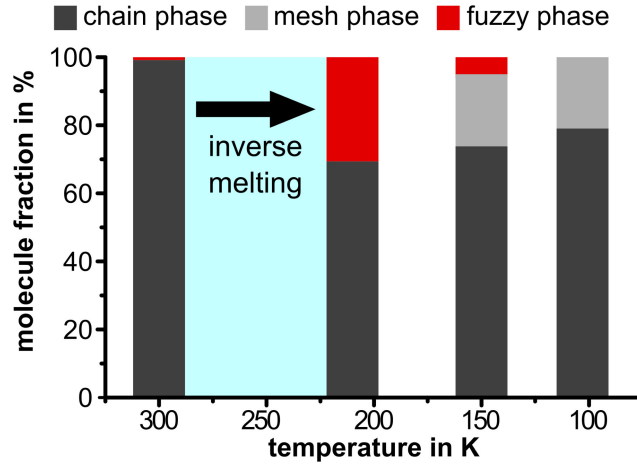


**Fig. 8.4.: Coexisting molecular phases for MoMo on Cu(111) at different temperatures.** At room temperature, exclusively the chain phase is present on the surface. When cooling to 220 K, the number of molecules in the chain phase decreases and mobile molecules evolve (fuzzy phase). The data in the temperature window from 300 to 220 K (shaded blue) give evidence for mobilization upon cooling. Upon further cooling, the mesh phase evolves. At 100 K, both the chain and the mesh phase coexist on the surface. The data shown in the figure are taken from about 40 independent images. We evaluated samples upon cooling as well as upon annealing to confirm the reversibility of the phase transition. Furthermore, by comparing room temperature and low temperature data after several cooling and annealing cycles, we concluded that the molecules do not desorb from the surface during the experiment.

Next, we will generally discuss inverse phase transitions to understand why mobilization upon cooling is present here. The phase behavior of a material is often depicted in a diagram showing the temperature  $T$  and pressure  $p$  (Fig. 8.5A). At the phase boundary, where two phases coexist, the difference in the chemical potential of the two states vanishes. From this equilibrium condition, the slope of any boundary in the phase diagram of a three-dimensional (3D) material can be calculated, which is known as Clapeyron equation. For a melting transition, the system transforms from a crystal (index  $c$ ) to a liquid (index  $l$ ):

$$\frac{dP}{dT} = \frac{S_{m,l} - S_{m,c}}{V_{m,l} - V_{m,c}} = \frac{\Delta S_m}{\Delta V_m} \quad (8.1)$$

Here,  $S_m$  and  $V_m$  denotes the molar entropy and molar volume, respectively. For a normal melting transition, the molar entropy,  $S_m$ , and the molar volume,  $V_m$ , *increase* upon melting. Hence, such a transition has a positive slope in the  $pT$ -diagram as present in region I in Fig. 8.5A. However, materials exist for which the molar volume decreases upon melting, with water being the most prominent example for such an anomalous melting transition that is associated with a negative slope in the  $pT$ -diagram (region II in Fig. 8.5). As already pointed out by Gustav Tammann [36], the melting curve might curl down again, which results in region III with an inverse melting transition. This transition is associated with a *decrease* in both, the molar volume and the molar entropy upon inverse melting, resulting again in a positive slope of the melting curve. Similarly, for the conventional vaporization transition, the slope of the curve is positive, *i.e.*, both the molar entropy and the molar volume *increase* upon vaporization. For inverse vaporization to occur, however, the slope of the curve has to be negative, which means that the molar entropy must *decrease* upon vaporization (assuming that the change in molar volume remains positive upon inverse vaporization).

In conclusion, both inverse transitions discussed above require the molar entropy to decrease, while for inverse melting the molar volume needs to decrease in addition. The fact that the entropy of the crystalline (or liquid) phase is larger than the entropy of the liquid (or gaseous) phase appears, on a first glance, counterintuitive [37, 119]. This is because the high positional order in a crystal is often associated with a low entropy. This view is, however, limited, as in molecular systems further degrees of freedom, *e.g.*, oscillations and rotations contribute to the heat capacity as well. Therefore, an ordered phase consisting of interacting building blocks might have a higher entropy than a liquid or gaseous phase consisting of individual building blocks.

Finally, we want to address the question why an inverse transition is seen for the specific two-dimensional (2D) system of adsorbed MoMo molecules on a copper (111) surface studied here. In the view of the general discussion presented above, two conditions need to be met for inverse melting to be observed (decrease in both molar entropy and molar volume). The molar volume discussed above for the 3D case corresponds in 2D to the average area per molecule in the respective phase on the surface. Thus, as a first condition for inverse melting to occur, the available area per molecule needs to be larger for the crystalline than for the liquid phase. This condition is not met here as the molecules in the ordered phase stand upright (Fig. 8.5B) while the molecules in the mobile phase lie flat on the surface and occupy a larger surface area (Fig. 8.5C), *i.e.*, the area per molecule *increases* upon cooling. We, therefore, now discuss inverse vaporization. In this case, the only condition to be met is the decrease in molar entropy. The fulfilment of this condition can be rationalized by the following consideration. If the molecules lie flat in the liquid

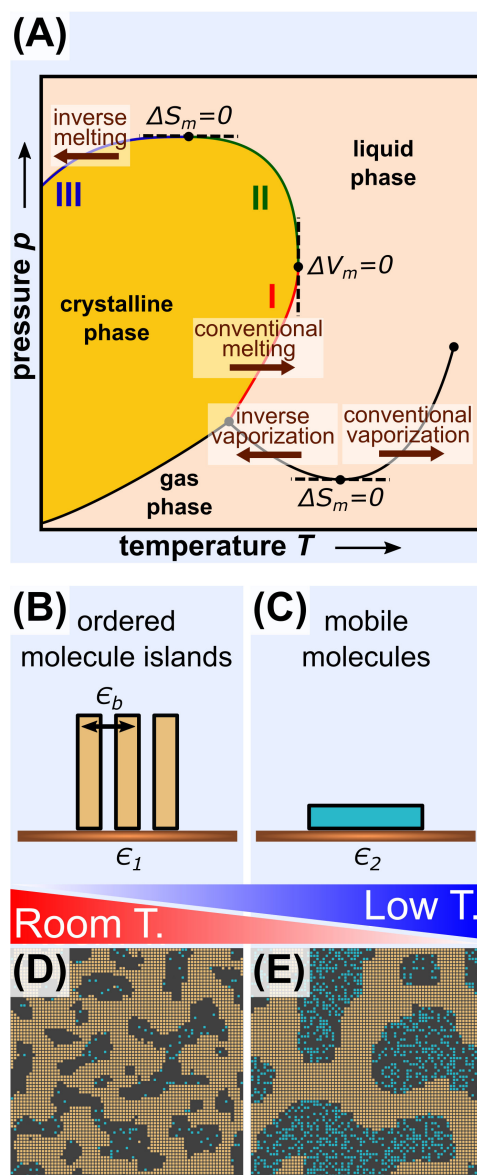


**Fig. 8.5.: Schematic phase diagram illustrating inverse melting and inverse vaporization.** (A) Phase diagram showing the phase boundary between a crystalline, a liquid and a gaseous phase; adapted and extended from Ref. [119]. In normal melting (region I), both the molar entropy and the molar volume increases upon a phase transition from the crystalline to the liquid phase, which results in a positive slope of the phase boundary. Substances, for which the molar volume decreases upon melting – such as water – show so-called anomalous melting with a negative slope (region II). When both, the molar volume and the molar entropy decrease upon melting, inverse melting takes place, which is again associated with a positive slope (region III). Similarly, inverse vaporization can take place when the slope of the vaporization curve becomes negative. (B, C) Conformational transition of MoMo molecules, from upright standing in an ordered phase (B) to flat-lying mobile in an unordered phase (C), which is accompanied by a loss of single-molecule entropy. The parameter  $\epsilon_b$  denotes the lateral binding energy between two standing molecules, while  $\epsilon_1$  and  $\epsilon_2$  denotes the binding energy of the molecules with the substrate in the standing and lying configuration, respectively. (D) Simulation snapshot of a lattice gas at reduced temperature  $T/\epsilon_b = 0.3$  and (E)  $T/\epsilon_b = 0.2$ , where  $\epsilon_b$  is the lateral binding energy of standing molecules. The upright-standing molecules are colored in light brown, while the flat-lying molecules are colored in blue.

phase, they need to have a stronger binding towards the surface [133]. Stronger binding results in an increase of the vibrational and rotational energy levels of the functional groups involved in the binding. As a consequence, these degrees of freedom cannot contribute to the heat capacity of the flat-lying molecules to the same extent as for the upright-standing molecules.

The latter picture is corroborated by Monte Carlo simulations of a lattice gas [37, 134], a minimal model in which molecules hop between discrete sites (materials and methods are available in the Supporting Information 8.4). In addition, molecules can transform between two conformations: lying or standing. While the binding energy with the substrate is larger for the lying molecules, standing molecules are attracted by other standing molecules. As argued above, each standing molecule gains entropy from molecular degrees of freedom (vibrations, librations, *etc.*) that are suppressed in the lying conformation. Figs. 8.5D and 8.5E show typical snapshots at two temperatures. At the higher temperature (Fig. 8.5D), extended domains of standing molecules (colored blue in Fig. 8.5D and E) form (here identified with the chain phase) and only few molecules have detached and lie (colored orange in Fig. 8.5D and E) on the substrate. Cooling to a lower temperature (Fig. 8.5E), a substantial fraction of molecules lies down. These molecules are highly mobile and move in the space left by the compact chain phase, thus forming a mobile phase that can be identified with the fuzzy phase.

Our work thus demonstrates that the conditions for an inverse transition such as mobilization upon cooling in 2D systems are met when the transition is associated with a distinct change in the molecular adsorption geometry that strengthens the binding towards the surface in a way that it quenches vibrational and rotational degrees of freedom. We propose that molecules with many internal degrees of freedom might more frequently show inverse transitions as compared to simple atomic systems, with the perspective to tune transition conditions and adsorption morphologies.

### 8.3 Acknowledgement

S.A. is a recipient of a DFG-fellowship through the Excellence Initiative by the Graduate School Materials Science in Mainz (GSC 266). B.S., and M.A. thank the Deutsche Forschungsgemeinschaft (DFG, SFB/TRR 88 "Cooperative Effects in Homo- and Heterometallic Complexes (3MET)" Project C9).



## 8.4 Supporting Information

### I. Materials and Methods

**Experimental Part.** The shown experiments of submonolayers of dimolybdenum tetraacetate (MoMo) on Cu(111) were carried out with a scanning tunnelling microscope (STM) from ScientaOmicron (VT AFM XA). The system was operated in constant current mode with the tunneling current  $I_t$  usually in the range of 70-90 pA. Positive and negative values correspond to tunneling from the occupied and into the unoccupied states of the sample, respectively. Electrochemically etched tungsten tips were used. All preparation steps and measurements were performed in situ with a chamber base pressure typically better than  $10^{-10}$  mbar. Prior to molecule sublimation, the Cu(111) crystals from MaTeck, Jülich, Germany were cleaned by repeated cycles of  $\text{Ar}^+$ -sputtering (1.5 keV, 20 min) and a subsequent annealing to about 800 K. The MoMo molecules were bought from Sigma-Aldrich, Germany, with a purity of 98%. Molecule deposition was done with a quartz crucible held at 440 K using a water cooled 3-cell evaporator TCE-BSC from Kentax. A molecule coverage of about 1.2 molecules per  $\text{nm}^2$  was used for all experiments.

**Theoretical Part.** Monte Carlo simulations on a square lattice with  $L \times L$  sites, whereby each site is either unoccupied or occupied by a molecule [135], were performed. Molecules can be in one of two conformations: lying or standing. The free energy as a function of lattice configuration reads

$$F(\{n\}; T) = -\epsilon_b \sum_{i,j} n_i n_j + (\epsilon - Ts) \sum_i n_i \quad (8.2)$$

where  $n_i = 1$  if the site is occupied by a standing molecule and zero otherwise. The first sum runs over pairs of adjacent lattice sites. The model parameters are: the lateral binding energy  $\epsilon_b$  between two standing molecules, the gain of binding energy  $\epsilon = \epsilon_2 - \epsilon_1$  with the substrate of a lying molecule, and the gain  $s$  of entropy of a single standing molecule when compared to a lying molecule. We implemented two types of trial moves: moving a molecule to an adjacent site and converting a molecule between standing and lying. Trial moves are accepted or rejected using the usual Metropolis criterion. Parameters for the snapshots shown in Figure 8.5 are  $\epsilon = 3\epsilon_b$  and  $s = 6k_B$ .



## Conclusion and Outlook

The complementary experimental and theoretical studies described in this work were dedicated to investigate general design principles that govern molecular structure formation on surfaces. High-resolution scanning probe microscopy (SPM) measurements provided a direct view on real-space images at the molecular level. By combining SPM with state-of-the-art density functional theory (DFT) calculations, insights about the fundamental mechanisms determining the molecular adsorption structure were gained.

In the first part of this thesis, general approaches to predict and control the thermodynamically most favorable molecular adsorption structure were discussed. The effects of changing the properties of the substrate, *e.g.*, electronic structure and lattice constant, on the arrangement of self-assembled adsorbates were studied in detail at constant temperature.

In **Chapter 4**, I demonstrated that a rational change of the substrate's lattice constant enables the tunability of the mesoscopic island shape of molecules adsorbed on surfaces. This systematic concept was validated for a metal-containing molecule, dimolybdenum tetraacetate (MoMo), on three prototypical surfaces, Cu(111), Au(111) and CaF<sub>2</sub>(111). All of these model samples exhibit the same hexagonal geometry but have different lattice constants. As a function of the substrate, molecular islands of various size, elongated along different directions, and even one-dimensional single rows were observed. The experimental results validate unambiguously that the thermodynamically most favorable mesoscopic islands shape can be actively controlled and guided by a proper choice of a lattice mismatch between the formed island structure and the molecular bulk structure.

A promising strategy to increase the variety of self-assembled arrangements on surfaces is the change from metallic to dielectric substrates. However, at temperatures realistic for operation of functional devices, *i.e.*, at room temperature, adsorbed molecules on insulators tend to be mobile, or cluster at step edges. Often, the molecules even desorb at comparatively low temperatures. In **Chapter 5**, a primary example for anchoring individual molecules on bulk insulators held at room temperature was presented. Experimental and theoretical evidence for a strong molecule-surface interaction between single MoMo molecules and the dielectric

substrate surface calcite (10.4) was provided. The results of this study revealed that the molecules neither diffuse nor desorb even at room temperature. This finding was explained by a strong electrostatic interaction, resulting from an ideal match of the charge distribution between the molecule and the sample. Moreover, due to the absence of a notable intermolecular attraction, the molecule-molecule interaction can be described by hard-sphere repulsion in this system. Taking advantage of the molecular short-range repulsion, the formation of an ordered array of metal-containing MoMo molecules was achieved at high coverage. Such kind of ordered metal arrays on insulators might open the possibility to manipulate and store information on the molecular level in the future.

In the second part of this work, transitions of molecular structures on surfaces, induced by well-defined temperature changes, were discussed. Examples for reversible as well as non-reversible structure transitions were presented and thoroughly investigated.

A kinetically trapped structure is in a metastable state with an associated energy barrier prohibiting the formation of the thermodynamically favorable arrangement. For a sufficient increase in temperature, this barrier can be overcome, and the thermodynamically favored structure is formed within a time scale comparable to the duration of the here presented experimental observations. In **Chapter 6**, a combined experimental and theoretical study was presented, demonstrating the applicability of kinetics to control the formation of self-organized structures of molecules on surfaces. The main idea of this approach was to prepare a kinetically trapped structure during the sublimation process and subsequently trigger a sequence of irreversible transitions to thermodynamically more favorable structures upon heating. This approach was exemplarily demonstrated for dihydroxybenzoic acid molecules (2,5-DHBA) on calcite (10.4): Various structures from clusters up to one-dimensional stripes and even two-dimensional islands were realized for this system by a successive increase of the temperature.

The key aspect of the above described structure transitions was found to be the dissociation of 2,5-DHBA dimers into monomers. In some cases, the energy barrier of a reaction rate can be determined by a simple Arrhenius fit. However, complex structural transformations, as present for 2,5-DHBA on calcite (10.4), are composed of a sequence of individual transitions, which made it difficult to investigate a single step exclusively. In **Chapter 7**, a strategy to disentangle these individual steps was presented, in order to carry out an Arrhenius fit of the transition step of interest: First, a detailed understanding of the complete transition needs to be gained to identify the individual steps. Second, the experiment has to be prepared in a way to eliminate all factors, except of the temperature, that impact the kinetics of the essential step. For 2,5-DHBA on calcite specifically this meant that any influence of

space limitations, capture zone depletion and the length of the growing edge had to be disclosed. Following this approach, a 2,5-DHBA dimer dissociation barrier of 0.8 eV was determined, which agrees well with the theoretical result of 0.7 eV.

In **Chapter 8**, reversible phase transitions for molecules adsorbed on surfaces were studied. Most astonishingly, for MoMo on Cu (111) the rare and counterintuitive case of an inverse transition, the transition from an ordered phase to an unordered phase upon cooling, was identified. The observed behavior can only be explained by a lower molar entropy of the mobile phase in comparison to the static ordered phase. One possible explanation could be given by a strong confinement of the flat-lying molecules to the surface in the mobile phase in comparison to weakly bonded up-right standing molecules in the ordered phase. Due to the possibility of such a substrate mediated confinement, we propose that molecules adsorbed on a surface exhibit more frequently an inverse transition as three-dimensional bulk systems. Further studies investigating the here described inverse transition as a function of coverage are highly desirable, because studying the effect of space limitation could be a further path for exploring the microscopic insights of such inverse transitions. While at high coverage only a part of the molecules take part in the phase transition upon cooling, a complete phase transition might be observed at low coverage, *i.e.*, all molecules being mobilized upon cooling. Furthermore, in future investigations, the variety of organic molecules bear great potential of tuning the systems internal degrees of freedom that can be switched on and off. This approach is generally known as molecule engineering and might lead to the discovery of new systems exhibiting inverse transitions or might even allow to control the transition temperature.

In conclusion, the thermodynamics and kinetics of molecular structure formation on surfaces were investigated in this thesis. The findings in this work contribute towards developing novel strategies for building and designing molecular structures used for future devices in nanotechnology.



# Appendix





# Basics of Thermodynamics

## A.1 Introduction

From our experience we know that a ball rolling down a hill is slowed down by friction. However, the inverse case, the ball spontaneously gaining kinetic energy by the heat of the ground and then moving up the hill is not observed. Furthermore, we know that heat will always flow from hot to cold. What is the cause of this "direction" in time? The conservation of energy and momentum does not provide an explanation for such kind of effects. The answer of this question is given by thermodynamics and the introduction of entropy as described in the following.

In contrast to mass or electronic charge, the thermodynamic state functions temperature and pressure are non-intrinsic properties of atoms, *i.e.* a single atom does not have a fixed temperature or pressure. Temperature and pressure are only defined for many-particle systems. Commonly, on a macroscopic level one has to deal with a huge magnitude of  $10^{23}$  particles. These large number often makes it easy to lose the overview. On the other hand, the true value of thermodynamics is reflected in its universal validity, independent of the particles' properties. Therefore, it is of no surprise that thermodynamics is used in various fields such as quantum physics [136], astrophysics [137], chemistry [138], information processing [139] and biology [140], to name a few. Especially in the field of molecular self-assembly, a profound understanding of the thermodynamics is necessary to create and functionalize nanostructures as shown in the main chapters of this work.

Due to its versatility and importance, one finds a large number of comprehensive articles and books about thermodynamics in literature [39, 141–143]. Here, I will summarize the basic concept of thermodynamics and focus on the definition of temperature  $T$  and entropy  $S$ , following the ideas of Ludwig Eduard Boltzmann (1844-1906). Probably, Boltzmann's greatest accomplishment is that his statistical approach was able to assign a microscopic description to temperature and entropy, which have been rather abstract macroscopic functions at that time.

The main goal of this chapter is to give a broad overview of the concepts of thermodynamics and persuade the reader of the versatility and power of this approach. I will focus on the part of thermodynamics, which is important for understanding the dis-

cussions in this work. However, this chapter is by far insufficient for a comprehensive understanding, which requires a much more detailed elaboration.

## A.2 Macroscopic Experience of Temperature

Even so the exact molecular mechanism is still under discussion, different thermoreceptors at the human skin have been found to have a sense of cold and warm in respect to the normal human body temperature. The human skin has about 250 000 temperature receptors in total and most of them are for cold. Nonetheless, our sense of temperature is rather inaccurate and is also affected by non-temperature dependent influences like personal feelings or wind *etc.* Therefore, in meteorology sometimes an *apparent temperature* as a function of air temperature, relative humidity and wind speed is used to describe the weather.

With the help of thermometers, we can determine the temperature of objects much more precisely. Different mechanism, for example thermal expansion, change in resistance or thermoelectric effect are utilized for thermometers. Nowadays, commercially available resistance thermometers have a relative accuracy of about  $\delta T/T = 10^{-6}$ .

For the measurement, the thermometer has to be brought into contact with the probe until a thermal equilibrium is formed.<sup>1</sup> The concept of equilibrium plays an important role in thermodynamics. In many textbooks, the authors distinct between equilibrium and non-equilibrium thermodynamics. Arnold Münster defines the thermodynamic equilibrium in his famous book "*Classical thermodynamics*" [144]:

*An isolated system is in thermodynamic equilibrium when, in the system, no changes of state are occurring at a measurable rate.*

Specifically, this means that when two systems, *i.e.*, probe and thermometer, are put into thermal contact and we wait long enough until a thermal equilibrium is formed, both systems will have the same temperature and in average, there is no net heat transfer between them.

Thermodynamics is based on universal main laws. These laws are not conclusions deduced from philosophical first principles. They are in fact an observation from several centuries of experiments. Ralph H. Fowler (1889-1944) stated the

---

<sup>1</sup>Pyrometers are an exception, which allow measuring the temperature from a distance. Pyrometers determine the temperature by analysing the thermal radiation emitted by the probe. The Stefan-Boltzmann law describes a proportional relation between the radiant emittance and the temperature  $P \sim T^4$ .

zeroth law of thermodynamics in 1930:

*If two systems are each in thermal equilibrium with a third, they are also in thermal equilibrium with each other.*

Fig. A.1 shows an illustration of the zeroth law. Even if the zeroth law sounds trivial, it is a very important finding, because it implies that temperature is worth measuring. Regardless of systems inner structure and their interaction, when two systems of equal temperature are brought in thermal contact, no net heat transfer takes place and the temperature remains the same. For example, when we measure the air temperature in a room, it is safe to assume that all objects in that room have the same temperature, as soon as thermal equilibrium is reached. Analogous principles have also been found for different kind of equilibriums in many-particle systems, for example in respect to pressure. However, due to their lesser fundamental importance it has not been ranked to one of the main clauses.

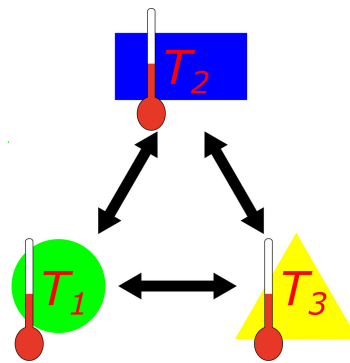


**Fig. A.1.:** Illustration of zeroth law of thermodynamics. If system 1 and system 2 are in thermodynamic equilibrium  $T_1 = T_2$ , and system 3 and 2 in equilibrium  $T_3 = T_2$ , then all systems have the same temperature  $T_1 = T_2 = T_3$

Summarized, we can measure the macroscopic state function called temperature  $T$  and, with the help of experiments, we are able to observe the effects of a change in temperature to a system. An increase in temperature results for example in an increase of the length of a piece of metal or in an increase of the pressure of a gas stored in a fixed volume. However, a microscopic explanation for these effects was missing for long time. Boltzmann was able to ascribe the temperature of a macroscopic body to the properties of its microscopic components. His approach is based on a statistical interpretation, which we shortly discuss in the next section. Mainly, we follow the concept of Boltzmann's textbook "*Vorlesungen über Gastheorie*" [145].

## A.3 Boltzmann's Microscopic Temperature Definition

From our experience, we know that the temperature of a body increases when we add energy in form of heat. We also noticed that many chemical reactions conduct faster in warm systems than in cold systems. Therefore, it seems reasonable that temperature is somehow connected with the inner energy  $U$  of the system. Boltzmann's consideration let him to the assumption that the temperature of a many-particle system is a result of the distribution of energy among its microscopic constituents.

Here, we discuss and illustrate Boltzmann's considerations in a very simplified model system. Assuming we have a single particle, and energy can only be absorbed by a momentum transfer along the  $x$ ,  $y$  and  $z$  direction. Consequently, there is an infinite amount of possibilities to distribute a fixed amount of energy. For example, one possible option is to store all energy in momentum along  $x$  direction, an alternative is to share the energy in an arbitrary proportion between momentum in  $x$  and  $y$  directions. However, Boltzmann suggested that energy can only be received in fixed proportions. Nowadays, we would call that "*quantization of energy*". This is quite impressing, considering that at Boltzmann's time neither experimental evidence of atoms has been found nor has quantum physics been established. Boltzmann's assumption states that there is only a finite number of various configurations to distribute the energy.

Let us assume we only have two energy quanta  $\Delta\varepsilon$  and we have to distribute this energy in the above described model system with one particle. Then, there exist six different configurations  $\omega$  to distribute these two energy quanta  $\Delta\varepsilon$ , as illustrated in Fig. A.2a. For  $n$  energy quanta  $\Delta\varepsilon$ , there are  $\omega = (2 + n)!/(2 \cdot n!)$  different configurations possible. As shown in Fig. A.2b, the number of microscopically different configurations  $\omega$  rises monotonously with the total inner energy  $U = n \cdot \Delta\varepsilon$ . In physics, various names exist for the number  $\omega(U)$ : multiplicity, degeneracy, permutability, *etc.* In thermodynamics  $\omega(U)$  is called the number of microstates.

We will now enlarge our simplified model by a second particle. What will happen, when we bring two particles into contact, such that the two particles can exchange their momentum and energy? In this regard the **first law of thermodynamic** has been stated by Rudolf Clausius (1822-1888):

*In a thermodynamic process involving a system, the change in the internal energy*

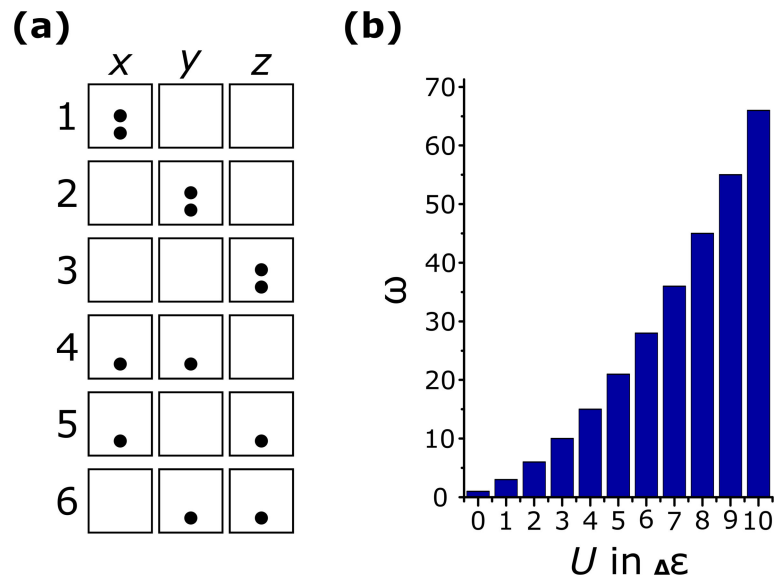


**Fig. A.2.:** a) Six different configurations to distribute two energy quanta  $\Delta\varepsilon$  (•) on a particles momentum in  $x$ ,  $y$  and  $z$  direction. (b) The number of possible microstates  $\omega$  as a function inner energy  $U = n \cdot \Delta\varepsilon$  (adapted from [39])

$U$  is equal to the sum of the heat transfer  $Q$  into the system and the work  $W$  done on it.

$$dU = dQ + dW \quad (\text{A.1})$$

On the right side of Equation A.1, a dashed d was us for the differential quantities to indicate that heat and work are process functions and do not represent state functions of energy. The first law allows to draw a balance of energy between interacting systems and leads to the **conservation of energy**. Particularly, in our example, this means that when particle 1 loses energy, the energy of particle 2 increases of the same amount and *vice versa*. Hence, the total energy  $U^* = U_1 + U_2$  of system 1 and system 2 stays constant. However, the first law of thermodynamics does not state anything about the distribution of energy. Here, the question rises, what is the most likely distribution? Concerning this problem, Boltzmann made a **basic assumption in statistical mechanics**:

*An isolated system in equilibrium is with equal probability in each of its accessible microstates.*

Accordingly, a system does not favor any specific microstates and if we measure often and long enough, we would find the system at least once in each of it allowed states, which follow the basic rules of physics. Hence, in our model of two particles, the system can be found equally likely in all of its different microstates, as long as the total energy criteria  $U^* = U_1 + U_2$  from the first law of thermodynamic is fulfilled.

A macrostate describes a many-particle system with a few state functions like energy or temperature. Various microstates can lead to the same macrostate. However, some macrostates, for example a specific energy distributions between the two particles  $U_1$  and  $U_2$  are more likely, because a larger number of microstates corresponds to them. The total number of different microstates  $\omega^*(U_1, U_2)$  of both particles with an energy  $U_1$  and  $U_2$  is given by

$$\omega^*(U_1, U_2) = \omega_1(U_1) \cdot \omega_2(U_2), \quad (\text{A.2})$$

where  $\omega_1(U_1)$  and  $\omega_2(U_2)$  is the number of microstates for particle 1 and 2, respectively. For six energy quanta, a total number of  $\sum \omega^* = 462$  different microstates exist in our two particle model (see Table A.1). As shown in Table A.1, the system is most likely to be found in  $U_1 = U_2 = 3\Delta\varepsilon$ , because 100 different microstates correspond to this energy distribution. Against our intuition, there is still a chance of 28/462 that particle 1 contains all the energy and particle 2 none. One might believe that this is against nature. However, in our simplified model we have considered only two particles and six energy quanta. As described above, thermodynamics is a description of macroscopic systems with a large number of particles and one energy quanta can be very small in comparison to the inner energy of macroscopic objects. Therefore, in macroscopic objects the number of possible microstates  $\omega$  is inconceivable large.

**Table A.1.:** Number of microstates  $\omega^*(U_1, U_2)$  for six energy quanta  $\Delta\varepsilon$  as a function of the energy distribution between two particles.  $\omega_1(U_1)$  and  $\omega_2(U_2)$  refers to the number of microstates for particle 1 and particle 2 at a given energy  $U_1$  and  $U_2$ , respectively. The system is most likely to be found in  $U_1 = U_2 = 3\Delta\varepsilon$ .

$U_1 (\Delta\varepsilon)$	0	1	2	3	4	5	6	
$U_2 (\Delta\varepsilon)$	6	5	4	3	2	1	0	
$\omega_1$	1	3	6	10	15	21	28	
$\omega_2$	28	21	15	10	6	3	1	
$\omega^* =$	28	63	90	100	90	63	28	$\sum \omega^*$
$\omega_1 \cdot \omega_2$				$= \omega_{max}^*$				$= 462$

In chapter 2 of the text book *Thermodynamik Von der Mikrophysik zur Makrophysik* [39], Klaus Stierstadt visualizes the high number of the state function  $\omega$  for macroscopic objects by discussing the ideal gas. In one liter of gas, there are over  $10^{(10^{23})}$  different microstates possible in an energy interval  $U = 152 \text{ J}$  and  $U + \delta U = 152.00152 \text{ J}$ . About every  $10^{-10} \text{ s}$ , each of the  $10^{22}$  atoms in the gas collides with another one, which allows an energy transfer and in principle a change of the microstate. Therefore, since the big bang about  $10^{10}$  years ago, the system has

roughly passed about  $10^{50}$  different microstates. A neglectable amount compared to  $10^{(10^{23})}$  possible microstates for one liter of gas.

Consequently, the extreme case described above - two systems in thermal equilibrium, but the entire energy stored in only one system - is highly unlikely that probably no one will ever be able to observe it in a macroscopic system. In other words, it can be shown that the standard deviation from the expectation value is going to zero for such a macroscopic system. Furthermore, with a sufficiently large total energy<sup>2</sup>  $U$ , the discrete function  $\omega(U)$  can be replaced in good approximation by a continuously differentiable function  $\Omega(U)$ . The differentiable function  $\Omega(U)$  allows a much simpler mathematical treatment. Thus, a criterion can be found, determining which macrostate possess the most possible microstates.

For two systems 1 and 2 in equilibrium, the total number of microstates  $\Omega^*(U_1 = U^* - U_2) = \Omega_1(U_1) \cdot \Omega_2(U_2)$  is maximal for:

$$\frac{\partial \Omega^*(U_1)}{\partial U_1} = \frac{\partial \Omega_1(U_1)}{\partial U_1} \cdot \Omega_2(U_2) + \frac{\partial \Omega_2(U_2)}{\partial U_1} \cdot \Omega_1(U_1) = 0 \quad (\text{A.3})$$

and

$$\frac{\partial^2 \Omega^*(U_1)}{\partial U_1^2} < 0. \quad (\text{A.4})$$

From  $U_2 = U^* - U_1$  it follows:

$$\frac{\partial \Omega_2(U_2)}{\partial U_1} = \frac{\partial \Omega_2(U_2)}{\partial U_2} \cdot \frac{\partial U_2}{\partial U_1} = -\frac{\partial \Omega_2(U_2)}{\partial U_2} \quad (\text{A.5})$$

Equation A.5 in A.3 gives:

$$\frac{\partial \Omega_1(U_1)}{\partial U_1} \cdot \Omega_2(U_2) = \frac{\partial \Omega_2(U_2)}{\partial U_2} \cdot \Omega_1(U_1) \quad (\text{A.6})$$

We separate the variables:

$$\frac{\partial \Omega_1(U_1)}{\partial U_1} \cdot \frac{1}{\Omega_1(U_1)} = \frac{\partial \Omega_2(U_2)}{\partial U_2} \cdot \frac{1}{\Omega_2(U_2)} \quad (\text{A.7})$$

Using the chain rule, we finally receive:

$$\frac{\partial \ln \Omega_1(U_1)}{\partial U_1} = \frac{\partial \ln \Omega_2(U_2)}{\partial U_2} \quad (\text{A.8})$$

This is a necessary condition for a maximum of  $\Omega^*(U^* = U_1 + U_2)$ . Moreover, we know that in thermal equilibrium both systems exhibit the same temperature  $T_1 = T_2$ . The resemblance of equation (necessary condition) and  $T_1 = T_2$ , and the

<sup>2</sup>Generally, this requirement is fulfilled for all macroscopic systems, except at low temperature close to the absolute zero point.

experience that the inner energy increases with higher temperature, let Boltzmann to reason the following correlation between **temperature T** and the state function  $\Omega(U)$ :

$$T = \frac{1}{k_B} \left( \frac{\partial \ln \Omega(U)}{\partial U} \right)^{-1} \quad (\text{A.9})$$

Accordingly, this statistical approach is also known as **Boltzmann** or **statistic temperature** definition. The Boltzmann constant  $k_B = 1.3806 \cdot 10^{-23} \text{J/K} = 8.6173 \cdot 10^{-5} \text{eV/K}$  is a proportional factor, which has been identified by comparing theory and experiment.

In many textbooks, the ideal gas is used as a comparison between experiment and theory, because this simple model is already sufficient to describe many properties of real gases in a large extend (see [39] for more details about the ideal gas). An ideal gas describes a system of moving particles, which can only interact elastically with each other. Hence, only kinetic energy and no potential energy can be stored in such a system. For this reason, temperature is often **falsely** associated solely with the translation energy of the microscopic particles. However, the Boltzmann definition of the temperature is much more general and is a function of the complete inner energy  $U$ . Depending on the character of the system, the inner energy  $U$  can contain kinetic, but also potential energy. An example of a system whose temperature is solely given by potential energy would be misaligned spins in a magnetic field.

To summarize this part, we found a microscopic description of the macroscopic state function temperature. Boltzmann's statistical approach is based on the conservation of energy and the observation that two system in thermal equilibrium exhibit the same temperature.

## A.4 Clausius' Entropy Concept

William H. Cropper describes in his work "*Rudolf Clausius and the road to entropy*" [146] the development of Clausius entropy concept. Here, I summarize the most important steps.

In the 1850s Rudolf Clausius investigated the efficiency of heat engines, a system that converts energy in form of heat  $Q$  to mechanical work  $W$ . As Sadi Carnot (1796-1832) already noticed, mechanical work can be transformed completely to heat, but the inverse transformation from heat to mechanical work only happens partly. Even in the best heat engine, some energy is uselessly lost, *i.e.* some part of



the energy could not be used for mechanical work. Clausius tried to quantify Sadi's conclusion and found for cyclic processes:

$$\oint \frac{\delta Q}{T} = 0 \quad (\text{reversible, cyclic processes}) \quad (\text{A.10})$$

$$\oint \frac{\delta Q}{T} < 0 \quad (\text{irreversible, cyclic processes}) \quad (\text{A.11})$$

Here,  $\delta Q$  describes the energy at temperature  $T$ , transmitted from a heat reservoir to the system of the heat engine. The  $\delta$  assigns an inexact differential, indicating that the heat transfer is path-dependent. The equal sign applies for **reversible** cycling processes and the smaller-than sign for **irreversible** cycling processes. A reversible process can be inversed without remaining any change in the surrounding.

In a next step, Clausius was able to generalize his ideas from cyclic process only to transitions from any state  $A$  to another state  $B$ . In order to make such a general conclusion, he considered a cyclic process, starting with an irreversible path from state  $A$  to  $B$ , followed by the reversible path from state  $B$  returning back to  $A$ . With  $\int$  and  $\int_r$  denoting integrations over the irreversible and reversible parts of the cycle it gives

$$\begin{aligned} 0 > \oint \frac{\delta Q}{T} &= \int_A^B \frac{\delta Q}{T} + \int_{B^r}^A \frac{\delta Q}{T} \\ &= \int_A^B \frac{\delta Q}{T} - \int_{A^r}^B \frac{\delta Q}{T} \end{aligned} \quad (\text{A.12})$$

and it follows that the integral over the reversible path is always larger than the integral over the irreversible path:

$$\int_{A^r}^B \frac{\delta Q}{T} > \int_A^B \frac{\delta Q}{T} \quad (\text{A.13})$$

He then introduced for such an integral the state function entropy  $S$

$$S(B) - S(A) \geq \int_A^B \frac{\delta Q}{T}. \quad (\text{A.14})$$

Again, the equal sign applies for the reversible transition and the greater-than sign for irreversible transitions. In this regard, Clausius stated the **second law of thermodynamics** for two consecutive equilibrium positions in an isolated system at time  $t_2 > t_1$  it follows:

$$S(t_2) - S(t_1) \geq 0. \quad (\text{A.15})$$

Accordingly, in an isolated system, entropy can only increase or remain the same in time. Here, it is important to point out that this rule only applies for an isolated system. In an open system an energy transfer might induce an entropy decrease in the system. However, this entropy decrease is always accompanied by an entropy in-

crease of the surrounding in a way that the second law of thermodynamics is fulfilled.

A complete transition of energy  $Q$  in form of heat transfer to work  $W$  would result in a decrease of the entropy. Therefore, the second law of thermodynamics provides an explanation of Sadi Carnot's famous theorem that no perfect heat engine exists. We can even calculate the maximum efficiency  $\eta_{max}$  of any heat engine.

A heat engine receives energy  $Q_{hot}$  in form of a heat transfer from a hot reservoir at temperature  $T_{hot}$ . Some part of that energy is utilized for performing mechanical work  $W$  and the rest of energy  $Q_{cold}$  flows in form of a heat transfer to a second colder reservoir. The efficiency of such a heat engine is defined as

$$\eta = \frac{W}{Q_{hot}}. \quad (\text{A.16})$$

Assuming an isotherm heat transfer, *i.e.*, the temperature is constant, the energy transfer from the hot reservoir to the system of the heat engine is accompanied by an entropy loss in the reservoir of at least  $S_{hot} = Q_{hot}/T_h$ . On the other hand, an entropy of  $S_{cold} = Q_{cold}/T_{cold}$  flows from the heat engine to the cold reservoir. For this cycling process to happen by itself, the second law of thermodynamics requires

$$S_{cold} \geq S_{hot}. \quad (\text{A.17})$$

and it follows:

$$Q_{cold} \geq Q_{hot} \cdot \frac{T_{cold}}{T_{hot}}. \quad (\text{A.18})$$

The energy balance  $Q_{cold} = Q_{hot} - W$  of the heat engine finally gives:

$$W \leq Q_{hot} \left(1 - \frac{T_{cold}}{T_{hot}}\right) = Q_{hot} \cdot \eta. \quad (\text{A.19})$$

Consequently, an ideal heat engine like the Carnot cycle has a maximum efficiency of  $\eta_{max} = 1 - \frac{T_{cold}}{T_{hot}}$ . However, in reality the efficiency is generally much lower, due to friction and non-isotherm heat transfer.

## A.5 Boltzmann's Microscopic Entropy Definition

Analogous to the temperature definition, Boltzmann was able to ascribe the macroscopic state function entropy  $S$  to a system's microscopic particles. His approach is again based on a statistical treatment. Thereby, he was capable to find a correlation between the entropy  $S$  and the total number of possible microstates  $\omega(U)$  with the inner energy  $U$  (see Chapter A.3). Boltzmann's famous entropy definition for an isolated system is given by

$$S = k_B \ln \Omega \quad (\text{A.20})$$

where  $k_B$  is the Boltzmann's constant.

On the basis of Boltzmann's entropy interpretation, the second law of thermodynamics acquires a different and more general meaning compared to Clausius' entropy definition (see Equation A.14): First, due to the countability of  $\Omega$  it is in principle possible to calculate the entropy of every system in equilibrium. While Clausius' entropy definition is limited to processes exchanging heat, Boltzmann's concept of entropy is applicable to any macroscopic system in equilibrium. Second, in Boltzmann's interpretation, the first law is nothing more than a probability statement. For a sufficient large system, one observes (almost) always the same macroscopic state, because most microscopically possible distributions (microstates) yield to the same macrostate. In principle, the system could also be in a different macrostate, but for a large system it is so unlikely that this is basically impossible to observe.

We will exemplarily demonstrate these two points by discussing the entropy change of mixing two ideal gases as shown in Fig. A.3. In the beginning, gases  $a$  and  $b$  are separated in two different containers with volume  $V_a$  and  $V_b$ . Both gases have the same temperature  $T_a = T_b$  and pressure  $p_a = p_b$ . Subsequent, we open the divider between both containers, allowing the molecules to flow into the other container, respectively and, hence, mixing the two gases. We assume the whole process to happen adiabatically, which means that there is no heat exchange with the surrounding. Consequently, the temperature and pressure remain unchanged. The number of microstates  $\Omega$  and entropy  $S$  of an ideal gas is given by (see [39] for derivation):

$$\begin{aligned} S(T, N, V) &= k_B \ln \Omega(T, N, V) \\ &= k_B N \left( \frac{5}{2} - \ln \frac{N}{V} + \frac{3}{2} \ln \frac{2\pi m k_B}{h^2} + \frac{3}{2} \ln T \right) \end{aligned} \quad (\text{A.21})$$

with  $N$  being the number of particles. The total number of particles also remains constant during the here described mixing process. However, the volume of each gas increases to  $V = V_a + V_b$ . Therefore, we can calculate the change of entropy upon mixing by

$$\begin{aligned} \Delta S_{total} &= \Delta S_a - \Delta S_b \\ &= [S_a(V) - S_a(V_a)] - [S_b(V) - S_b(V_b)] \\ &= k_B \left( N_a \ln \frac{V}{V_a} + N_b \ln \frac{V}{V_b} \right) \\ &> 0 \end{aligned} \quad (\text{A.22})$$

The entropy increases upon mixing, because  $V > V_a$  and  $V > V_b$ . Following the second law of thermodynamics that entropy can only remain equal or increase, we

conclude that mixing of the two gases is an irreversible process. Indeed, from our experience we know that the inverse process, an autonomous separation of two mixed gas, is not observed (see Fig. A.3), because this would require a decrease in entropy of  $\Delta S_{total}$ .

This example illustrates that Boltzmann's concept of entropy is generally applicable, also for process without heat transfer. Furthermore, it opens the question if the second law of thermodynamics is a fixed rule of nature - like conservation of energy - or just a statistical consequence. In principle, it is possible that in the moment of closing the dividing barrier again, all gas molecules of type  $a$  happen to be on one side and those of type  $b$  to be on the other side. However, in large systems containing  $10^{23}$  particles the chance of this unlikely event is going to be zero.

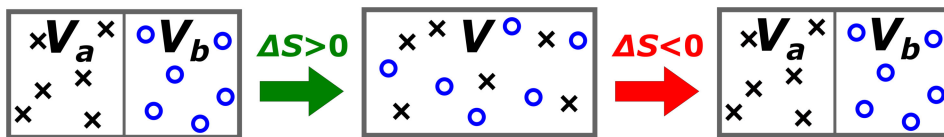


Fig. A.3.: Adiabatic mixing of two ideal gases. Gas  $a$  is marked with black crosses and gas  $b$  with blue rings. The inverse process, autonomous separation of the two gas, is not observed, because it would lead to a decrease of entropy.

## A.6 Classification of Many-Particle Ensembles

In the last sections, we have mostly discussed about isolated systems. An isolated system describes a thermodynamic ensemble, which is completely independent from the surrounding and has a fixed volume, shape and energy. There is no particle and energy exchange or any interaction between the isolated system and its environment (see Fig. A.4a). Such an isolated ensemble is of great importance in the field of thermodynamics, because the second law of thermodynamics (see Equation A.15) only applies for these ideal systems. That being the case, this important isolated system received its own name called **microcanonical ensemble**.

However, in reality, it is impossible to create a perfect isolated system, *e.g.*, even the best imaginable isolation still conducts some minor thermal flow. In addition, it would be impossible for us to "see" into a perfect isolated system, because the process of observation already requires some kind of exchange with the surrounding.

Therefore, in experiments and in everyday life, one always has to deal with systems that can somehow interact with its environment. Here, the second law of thermody-

dynamic does not apply anymore. In order to solve this problem, one considers the system under investigation and its environment to be subsystems of a much larger isolated system. While the large, isolated system still fulfills energy conservation and a continuous increase of entropy, these conditions are no longer valid for its subsystem. The subsystems can exchange energy with each other without changing the total energy stored in the larger, global system. Thus, the entropy in a subsystem can also decrease over time, but only under the condition that the entropy remains the same or increases in the entire isolated system.

Before discussing in more detail which "new" rules apply to the above-mentioned subsystems, we have a look on a frequently used classification of possible thermodynamic (sub)-systems. Fig. A.4a illustrates the idealized **microcanonical ensemble** completely isolated from its environment.

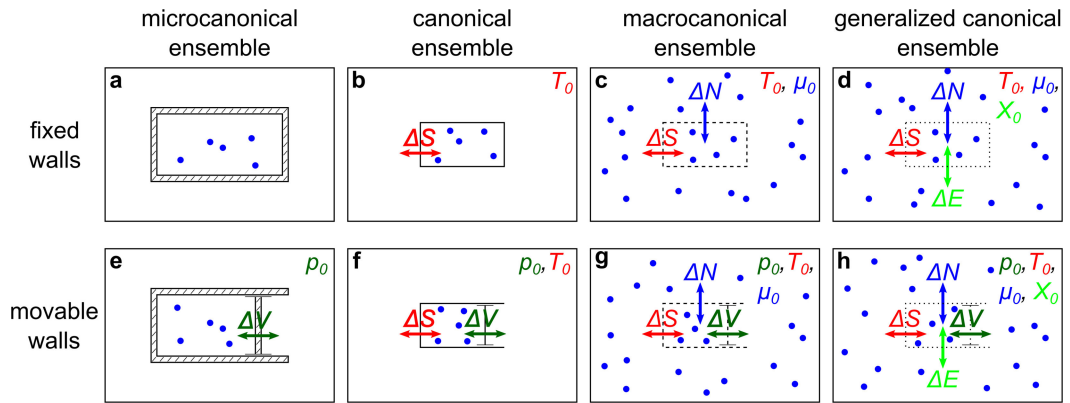


**Fig. A.4.:** Classification of particle ensembles for stationary walls (top row) and moving walls (bottom row). a) An isolated *microcanonical ensemble*. b) A *canonical ensemble* with heat exchange. c) *macrocanonical ensemble* with heat and particle exchange. d) *generalized canonical ensemble* permitting various ways of energy exchange. The corresponding ensembles with moving walls, allowing an exchange in volume, are shown in e)-h).

In the case that energy can be exchanged by heat, *i.e.*, through an entropy flow, the examined subsystem is called a **canonical ensemble** and its environment is described as a heat reservoir (see Fig. A.4b). The term heat exchange is used to describe the process of transferring energy  $Q$  from one system to another, accompanied by an entropy change  $\Delta S = Q/T$ . Generally, the examined subsystem is very small compared to its interacting heat reservoir and, hence, the reservoir's temperature can be assumed to be nearly constant. Accordingly, when energy is exchanged between the canonical ensemble and its reservoir, the temperature of the ensemble changes, in contrast to the temperature of the much larger heat reservoir, which remains constant. For such a canonical ensemble heat is exchanged with its reservoir until equilibrium is reached and the examined ensemble has reached the same temperature as its reservoir.

An ensemble, which can exchange heat and particles, is named a **macrocanonical ensemble** and the environment is described by a heat and particle reservoir (see Fig. A.4c). Analogous to the temperature, the chemical potential  $\mu$  dictates in which direction the particle exchange  $\Delta N$  takes place. The chemical potential  $\mu$  is the energy, which is needed to create a particle at constant volume and entropy. In equilibrium, the chemical potential and the temperature in the macrocanonical ensemble have attained the same value as in the particle and heat reservoir.

Besides a heat and particle exchange, energy can be exchanged between two subsystems in various different ways in nature. For example, in the field of physics, one often looks at the interaction of a system with an externally applied electric or magnetic field. If energy  $\Delta E$  is exchanged by other means than a heat or particle transfer, then the examined subsystem is called a **generalized canonical ensemble** (see Fig. A.4d).

So far, we have only considered systems with static walls and consequently constant volumes. By changing the volume against a pressure  $p$ , mechanical work  $W$  is performed and thus energy can be transferred between two systems. Such a process can be illustrated by moving walls as shown in Fig. A.4e-h. For a subsystem with movable walls, its volume  $V$  will change until the pressure  $p$  of the ensemble and the environment is balanced in equilibrium.

## A.7 Thermodynamic Potentials

The second law of thermodynamics solely applies for isolated systems. A system, which can exchange energy with its environment (reservoir), is called a closed system.<sup>3</sup> Here, we discuss what kind of "new" thermodynamics rules apply to such non-isolated systems like a canonical ensemble, *etc.* More specifically, which structure is thermodynamically favorable in the ensemble?

As described in the last section, a particle ensemble of a closed system, can be regarded as a subsystem  $\sigma$ , which can interact with its much larger reservoirs  $\Sigma$ . The ensemble  $\sigma$  and its reservoirs  $\Sigma$  form together an even larger isolated system (see Fig. A.5). For the complete, isolated system, the energy is conserved. Hence, an energy increase of the ensemble always goes along with an energy decrease in its environment.

Following the second law of thermodynamics, a change in the ensemble  $\sigma$ , *e.g.*,

---

<sup>3</sup>In case of particle exchange between the ensemble and its environment, the ensemble is referred to an open system.

a structural transition, happens automatically when the total change in entropy  $\Delta S_{global}$  of all subsystems is positive

$$\Delta S_{global} = \Delta S_{\sigma} + \Delta S_{\Sigma} > 0. \quad (\text{A.23})$$

Consequently, for the ensemble  $\sigma$  the structural transition could even result in a decrease of entropy. However, it must be accompanied by an even larger increase of entropy  $\Delta S_{\Sigma}$  in its environment  $\Sigma$ . Here, we already notice that an closed ensemble  $\sigma$  behaves quite different to an isolated system. In an isolated system, always the structure having the largest entropy is formed.

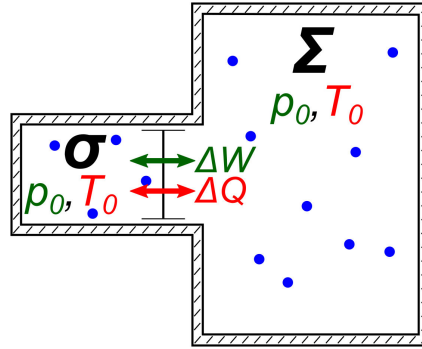


**Fig. A.5.:** Illustration of a canonical ensemble with moving walls  $\sigma$  and its reservoir  $\Sigma$  at temperature  $T_0$  and pressure  $p_0$ . The canonical ensemble and its environment combined form an isolated system. The subsystem can exchange energy by a heat transfer  $Q$  or by performing work  $W$

We first focus on a canonical ensemble with moving walls  $\sigma$  (see Fig. A.5), because it is assumingly the most used thermodynamic model system. For this case, the ensemble can interact with a heat and pressure reservoir  $\Sigma$  at temperature  $T_0$  and pressure  $p_0$ , respectively. In the case of a heat flow  $Q_{\sigma}$  from the reservoir to the ensemble, the entropy in the reservoir decreases. As described above, the reservoir temperature can be assumed to be constant during such a process. Therefore, following Boltzmann temperature definition (see Equation A.9), during the heat exchange  $Q_{\sigma}$  the entropy of the reservoir changes by

$$\Delta S_{\Sigma} = -\frac{Q_{\sigma}}{T_0} < 0. \quad (\text{A.24})$$

The negative sign indicates that energy flows from the reservoir into the ensemble (in the opposite case, heat flowing from the ensemble to the reservoir all signs would be inverse). The additional energy in the ensemble  $Q_{\sigma}$  splits into an increase of the inner energy  $\Delta U_{\sigma}$  and to perform mechanical work, *i.e.*, change of the volume  $\Delta V_{\sigma}$ , against the pressure  $p_0$  of the reservoir. Energy conservation gives

$$Q_{\sigma} = \Delta U_{\sigma} + p_0 \Delta V_{\sigma}. \quad (\text{A.25})$$

Combining Equations A.23, A.24 and A.25, we finally receive an entropy change for the complete system of

$$\begin{aligned}
 \Delta S_{global} &= \Delta S_{\sigma} - \frac{Q_{\sigma}}{T_0} & (A.26) \\
 &= \frac{1}{T_0} [T_0 \Delta S_{\sigma} - \Delta U_{\sigma} - p_0 \Delta V_{\sigma}] \\
 &= \frac{1}{T_0} [\Delta (T_0 S_{\sigma} - U_{\sigma} - p_0 V_{\sigma})] \\
 &= \frac{1}{T_0} [-\Delta G_{\sigma}] \geq 0
 \end{aligned}$$

with  $G_{\sigma}$  being the *free enthalpy* or *Gibbs free energy*. The Gibbs free energy is known as the characteristic *thermodynamic potential* of a canonical ensemble with moving walls. The entropy  $S_{global}$  of the complete, isolated system is maximal when the Gibbs free energy  $G_{\sigma}$  of the ensemble is minimal. Therefore, we can now summarize:

**For a canonical ensemble with moving walls, the structure with the minimal Gibbs energy**

$$G_{\sigma} = U_{\sigma} + p_0 V_{\sigma} - T_0 S_{\sigma} \quad (A.27)$$

**is formed in equilibrium, because then the entropy of the complete system  $S_{global}$  is maximal.**

An analogous approach for other ensembles in contact with various reservoirs, e.g., canonical ensemble with fixed walls and macrocanonical ensemble, leads to the minimization of various characteristic thermodynamic potentials. A summary of commonly used thermodynamic potentials can be found in Fig. A.6. A more comprehensive description of thermodynamic potentials is given in the textbook of Zemansky and Dittmann [147]. Assumingly, next to the Gibbs free energy, the most commonly used thermodynamic potentials are the free energy  $F$ , and the grand potential  $\Omega_G$ :

$$F = U_{\sigma} - T_0 S_{\sigma} \quad (A.28)$$

$$\Omega_G = U_{\sigma} - T_0 S_{\sigma} - \mu N \quad (A.29)$$

As described above, experiments performed in UHV are discussed in this work. For a neglecting volume work  $p_0 V_{\sigma}$ , as in our case working in UHV, one notices that the free energy is equal to the Gibbs free energy  $F = G$ . Hence, the here shown experiments can be either described by a three-dimensional canonical ensemble with moving walls and neglecting volume work or by a two-dimensional canonical ensemble with fixed walls. In the latter case, a constant sample surface is the two-dimensional analogue to a constant volume in three-dimension.



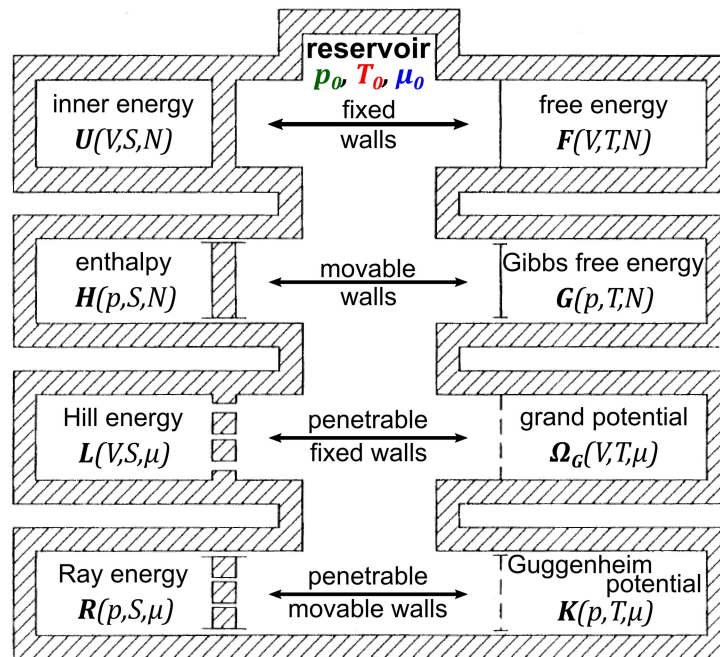


**Fig. A.6.:** Illustration of eight common thermodynamic ensembles connect by various walls with a combined temperature  $T_0$ , pressure  $p_0$  and particle/chemical potential  $\mu_0$  reservoir. There is no interaction with any external field present. The four systems on the left are thermally isolated (shaded wall), while the four system on right exchange heat with the temperature reservoir. The movable wall in the second and third row allow a pressure equalization. The walls with holes in the lower half allow a particle exchange to balance the chemical potential. The characteristic thermodynamic potentials matching to the different ensemble types are displayed (adapted from [147]).

The minimization statement of the thermodynamic potentials, e.g.,  $G$  and  $F$ , is also known as the *principle of minimum in energy*. However, this name is rather confusing, because the total amount of energy remains constant in time. It is the characteristic thermodynamic potential of an ensemble, which strives to a minimum. Furthermore, the principle of minimum in energy is not a new axiom; it is a consequence of the second law of thermodynamics. However, in practice it is often useful to work with the thermodynamic potentials instead of counting the microstates of the complete system. The thermodynamic potential of a particle ensemble only depends on macroscopic, intensive state functions of its reservoirs like temperature and pressure. Therefore, in order to determine the thermodynamically most favorable structure in the observed ensemble, one does not need to know the microscopic details and exact entropy of the reservoir.

## A.8 Summary

Based on the here presented introduction about thermodynamics, we can now try to answer the following questions:

### 1. *What is temperature?*

Temperature  $T$  is an intensive state function of a macroscopic system. Boltzmann has been able to ascribe a systems temperature  $T$  to the systems number of microstates  $\Omega(U)$  and the inner energy  $U$ :

$$T = \frac{1}{k_B} \left( \frac{\partial \ln \Omega(U)}{\partial U} \right)^{-1}$$

### 2. *What is entropy?*

Entropy is an extensive state function of a large, many particle system. In statistical thermodynamic, the entropy of an isolated macroscopic system is defined as

$$S = k_B \ln \Omega(U)$$

where  $k_B$  is the Boltzmann's constant and  $\Omega(U)$  the number of possible microstates, which lead to the observed macrostate.

### 3. *What is the principal of minimum in energy?*

The principal of minimum in energy dictates which macroscopic structure is thermodynamically favorable in a non-isolated, many-particle system. In this context, *energy* refers to the corresponding thermodynamic potential like the Gibbs free energy  $G$  or the free energy  $F$  of the examined non-isolated system and must not be confused with the kinetic and potential energy stored in the system. Typical non-isolated systems are the canonical and generalized canonical ensemble. In equilibrium, for such non-isolated, many particle systems, the structure with the smallest corresponding thermodynamic potential is formed. For example, in a canonical ensemble with moving walls, the structure with the minimal Gibbs free energy  $G$  is observed in equilibrium. This correlation can be explained by the fact that the entropy of the complete, isolated system - ensemble plus reservoir - is maximal, when the thermodynamic potential of the ensemble is minimal. Therefore, the principal of minimum in energy is a consequence of the second law of thermodynamics - entropy can only increase or remain equal in an isolated system – transferred to non-isolated systems interacting with large reservoirs.

**4. *What is the driving force for entropy maximization and how do the particles know, which position has the highest entropy?***

Entropy maximization does not mean that the molecules are forced into a fixed position. In contrast, the particles are free to occupy any microstate, which follows the fundamental laws of physics like energy and momentum conservation. Actually, Boltzmann's statistical approach for entropy assumes all possible microstates to be equally likely in an isolated system. Therefore, the second law of thermodynamics is nothing more than a statistical consequence:

A system can be in various macrostates with different statistical probabilities. The macroscopic structure to which the most possible different microstates yield (highest entropy), is most likely to be observed. For a many particle system at room temperature, a huge number of microstates exists and nearly all of them lead to the same macrostate. Hence, it is practically impossible to measure any other macrostate in equilibrium.



# Bibliography

- [1] G. M. Whitesides, B. Grzybowski, “Self-Assembly at All Scales”, *Science* **2002**, *295*, 2418–2421.
- [2] S. E. Chung, W. Park, S. Shin, S. A. Lee, S. Kwon, “Guided and fluidic self-assembly of microstructures using railed microfluidic channels”, *Nature Materials* **2008**, *7*, 581–587.
- [3] A. Aliprandi, M. Mauro, L. De Cola, “Controlling and imaging biomimetic self-assembly”, *Nature Chemistry* **2016**, *8*, 10–15.
- [4] K. R. Phillips, G. T. England, S. Sunny, E. Shirman, T. Shirman, N. Vogel, J. Aizenberg, “A colloidoscope of colloid-based porous materials and their uses”, *Chemical Society Reviews* **2016**, *45*, 281–322.
- [5] A. E. Willner, R. L. Byer, C. J. Chang-Hasnain, S. R. Forrest, H. Kressel, H. Kogelnik, G. J. Tearney, C. H. Townes, M. N. Zervas, “Optics and Photonics: Key Enabling Technologies”, *Proceedings of the IEEE* **2012**, *100*, 1604–1643.
- [6] N. Nilius, T. Risse, S. Schauermaun, S. Shaikhutdinov, M. Sterrer, H. J. Freund, “Model Studies in Catalysis”, *Topics in Catalysis* **2011**, *54*, 4–12.
- [7] D. Karnaushenko, T. Kang, V. K. Bandari, F. Zhu, O. G. Schmidt, “3D Self-Assembled Microelectronic Devices: Concepts, Materials, Applications”, *Advanced Materials* **2019**, 1902994.
- [8] C. Joachim, J. K. Gimzewski, A. Aviram, “Electronics using hybrid-molecular and mono-molecular devices”, *Nature* **2000**, *408*, 541–548.
- [9] L. Xing, Z. Peng, W. Li, K. Wu, “On Controllability and Applicability of Surface Molecular Self-Assemblies”, *Accounts of Chemical Research* **2019**, *52*, 1048–1058.
- [10] S. Chiang, “Scanning Tunneling Microscopy Imaging of Small Adsorbed Molecules on Metal Surfaces in an Ultrahigh Vacuum Environment”, *Chemical Reviews* **1997**, *97*, 1083–1096.
- [11] S. De Feyter, F. C. De Schryver, “Two-dimensional supramolecular self-assembly probed by scanning tunneling microscopy”, *Chemical Society Reviews* **2003**, *32*, 139–150.
- [12] S. Stepanow, N. Lin, J. V. Barth, K. Kern, “Surface-Template Assembly of Two-Dimensional Metal-Organic Coordination Networks”, *The Journal of Physical Chemistry B* **2006**, *110*, 23472–23477.

- [13] M. Kittelmann, P. Rahe, A. Kühnle, “Molecular self-assembly on an insulating surface: interplay between substrate templating and intermolecular interactions”, *Journal of Physics: Condensed Matter* **2012**, *24*, 354007.
- [14] J. Schnadt, W. Xu, R. T. Vang, J. Knudsen, Z. Li, E. Lægsgaard, F. Besenbacher, “Interplay of adsorbate-adsorbate and adsorbate-substrate interactions in self-assembled molecular surface nanostructures”, *Nano Research* **2010**, *3*, 459–471.
- [15] T. W. White, N. Martsinovich, A. Troisi, G. Costantini, “Quantifying the “Subtle Interplay” between Intermolecular and Molecule–Substrate Interactions in Molecular Assembly on Surfaces”, *The Journal of Physical Chemistry C* **2018**, *122*, 17954–17962.
- [16] R. P. Feynman, “Forces in Molecules”, *Physical Review* **1939**, *56*, 340–343.
- [17] A. Kühnle, “Self-assembly of organic molecules at metal surfaces”, *Current Opinion in Colloid & Interface Science* **2009**, *14*, 157–168.
- [18] C. A. Hunter, J. K. M. Sanders, “The nature of  $\pi$ - $\pi$  interactions”, *Journal of the American Chemical Society* **1990**, *112*, 5525–5534.
- [19] C. Steiner, J. Gebhardt, M. Ammon, Z. Yang, A. Heidenreich, N. Hammer, A. Görling, M. Kivala, S. Maier, “Hierarchical on-surface synthesis and electronic structure of carbonyl-functionalized one- and two-dimensional covalent nanoarchitectures”, *Nature Communications* **2017**, *8*, 14765.
- [20] J. N. Israelachvili, *Intermolecular and surface forces*, 3rd edition, Academic Press, **2011**.
- [21] L. Chi, *Nanotechnology: Volume 8: Nanostructured Surfaces*, Wiley-VCH, **2010**.
- [22] P. A. Rahe, PhD thesis, **2011**.
- [23] D. Lawton, R. Mason, “The Molecular Structure of Molybdenum(II) Acetate”, *Journal of the American Chemical Society* **1965**, *87*, 921–922.
- [24] N. Kalashnyk, J. Ledieu, m. Gaudry, C. Cui, A.-P. Tsai, V. Fournée, “Building 2D quasicrystals from 5-fold symmetric corannulene molecules”, *Nano Research* **2018**, *11*, 2129–2138.
- [25] P. Rahe, M. Kittelmann, J. L. Neff, M. Nimmrich, M. Reichling, P. Maass, A. Kühnle, “Tuning Molecular Self-Assembly on Bulk Insulator Surfaces by Anchoring of the Organic Building Blocks”, *Advanced Materials* **2013**, *25*, 3948–3956.
- [26] A. Schiffrin, A. Riemann, W. Auwärter, Y. Pennec, A. Weber-Bargioni, D. Cvetko, A. Cossaro, A. Morgante, J. V. Barth, “Zwitterionic self-assembly of L-methionine nanogratings on the Ag(111) surface”, *Proceedings of the National Academy of Sciences* **2007**, *104*, 5279–5284.
- [27] J. L. Neff, M. Kittelmann, R. Bechstein, A. Kühnle, “Decisive influence of substitution positions in molecular self-assembly”, *Physical Chemistry Chemical Physics* **2014**, *16*, 15437–15443.
- [28] S. Maier, L.-A. Fendt, L. Zimmerli, T. Glatzel, O. Pfeiffer, F. Diederich, E. Meyer, “Nanoscale Engineering of Molecular Porphyrin Wires on Insulating Surfaces”, *Small* **2008**, *4*, 1115–1118.

- [29] L. Nony, E. Gnecco, A. Baratoff, A. Alkauskas, R. Bennewitz, O. Pfeiffer, S. Maier, A. Wetzel, E. Meyer, C. Gerber, "Observation of Individual Molecules Trapped on a Nanostructured Insulator", *Nano Letters* **2004**, *4*, 2185–2189.
- [30] L. Laflör, F. A. Schlage, L. Kantorovich, P. J. Moriarty, M. Reichling, P. Rahe, "Quadruped Molecular Anchoring to an Insulator: Functionalised Ferrocene on CaF<sub>2</sub> Bulk and Thin Film Surfaces", *The Journal of Physical Chemistry C* **2020**.
- [31] S. Freund, A. Hinaut, R. Pawlak, S.-X. Liu, S. Decurtins, E. Meyer, T. Glatzel, "Morphology Change of C<sub>60</sub> Islands on Organic Crystals Observed by Atomic Force Microscopy", *ACS Nano* **2016**, *10*, 5782–5788.
- [32] P. Rahe, R. Lindner, M. Kittelmann, M. Nimmrich, A. Kühnle, "From dewetting to wetting molecular layers: C<sub>60</sub> on CaCO<sub>3</sub>(10-4) as a case study", *Physical Chemistry Chemical Physics* **2012**, *14*, 6544–6548.
- [33] N. Stock, S. Biswas, "Synthesis of Metal-Organic Frameworks (MOFs): Routes to Various MOF Topologies, Morphologies, and Composites", *Chemical Reviews* **2012**, *112*, 933–969.
- [34] M. Child, *Molecular Collision Theory*, Dover Publications, **1996**.
- [35] C. Paris, A. Floris, S. Aeschlimann, M. Kittelmann, F. Kling, R. Bechstein, A. Kühnle, L. Kantorovich, "Increasing the Templating Effect on a Bulk Insulator Surface: From a Kinetically Trapped to a Thermodynamically More Stable Structure", *The Journal of Physical Chemistry C* **2016**, *120*, 17546–17554.
- [36] G. Tammann, *Kristallisieren und Schmelzen - Ein Beitrag zur Lehre der Änderungen des Aggregatzustandes*, Barth / Leipzig, **1903**.
- [37] N. Schupper, N. M. Shnerb, "Inverse melting and inverse freezing: A spin model", *Physical Review E* **2005**, *72*, 046107.
- [38] L. Vitos, A. V. Ruban, H. L. Skriver, J. Kollár, "The surface energy of metals", *Surface Science* **1998**, *411*, 186–202.
- [39] K. Stierstadt, *Thermodynamik: Von der Mikrophysik zur Makrophysik*, Springer-Verlag Berlin Heidelberg, **2010**.
- [40] L. Bragg, "Nobel Lecture: The Diffraction of X-Rays by Crystals", *Nobel Media AB 2020* **1922**.
- [41] E. J. Scheibner, L. H. Germer, C. D. Hartman, "Apparatus for Direct Observation of Low-Energy Electron Diffraction Patterns", *Review of Scientific Instruments* **1960**, *31*, 112–114.
- [42] L. H. Germer, C. D. Hartman, "Improved Low Energy Electron Diffraction Apparatus", *Review of Scientific Instruments* **1960**, *31*, 784–784.
- [43] W. Ehrenberg, "A new method of investigating the diffraction of slow electrons by crystals", *The London Edinburgh and Dublin Philosophical Magazine and Journal of Science* **1934**, *18*, 878–901.
- [44] E. Ruska, "Noble Prize in Physics for his fundamental work in electron optics, and for the design of the first electron microscope", *The Royal Swedish Academy of Sciences* **1986**.

- [45] H. Sawada, N. Shimura, F. Hosokawa, N. Shibata, Y. Ikuhara, “Resolving 45-pm-separated Si-Si atomic columns with an aberration-corrected STEM”, *Microscopy* **2015**, *64*, 213–217.
- [46] J. Brew, “<https://commons.wikimedia.org/w/index.php?curid=5309032>”, *Wikipedia* **2020**.
- [47] NIAID, “<https://www.niaid.nih.gov/news-events/novel-coronavirus-sarscov2-images>”, **2020**.
- [48] E. W. Müller, “Das Feldionenmikroskop”, *Zeitschrift für Physik* **1951**, *131*, 136–142.
- [49] E. W. Müller, K. Bahadur, “Field Ionization of Gases at a Metal Surface and the Resolution of the Field Ion Microscope”, *Physical Review* **1956**, *102*, 624–631.
- [50] E. W. Müller, “Field Ion Microscopy”, *Science* **1965**, *149*, 591–601.
- [51] G. L. Kellogg, “Field ion microscope studies of single-atom surface diffusion and cluster nucleation on metal surfaces”, *Surface Science Reports* **1994**, *21*, 1–88.
- [52] G. Binnig, H. Rohrer, C. Gerber, E. Weibel, “Surface Studies by Scanning Tunneling Microscopy”, *Physical Review Letters* **1982**, *49*, 57–61.
- [53] G. Binnig, H. Rohrer, “Noble Prize in Physics for their design of the scanning tunnelling microscope”, *The Royal Swedish Academy of Sciences* **1986**.
- [54] J. Brew, “[https://de.wikipedia.org/wiki/Rastertunnelmikroskop#/media/Datei:First\\_STM.jpg](https://de.wikipedia.org/wiki/Rastertunnelmikroskop#/media/Datei:First_STM.jpg)”, *Wikipedia* **2020**.
- [55] I. Ekvall, E. Wahlström, D. Claesson, H. Olin, E. Olsson, “Preparation and characterization of electrochemically etched W tips for STM”, *Measurement Science and Technology* **1999**, *10*, 11–18.
- [56] M. Schmid, “[https://en.wikipedia.org/wiki/Scanning\\_tunneling\\_microscope#/media/File:ScanningTunnelingMicroscope\\_schematic.png](https://en.wikipedia.org/wiki/Scanning_tunneling_microscope#/media/File:ScanningTunnelingMicroscope_schematic.png)”, *Wikipedia* **2020**.
- [57] SecretDisc, “<https://commons.wikimedia.org/w/index.php?curid=3335479>”, *Wikimedia* **2020**.
- [58] D. M. Eigler, E. K. Schweizer, “Positioning single atoms with a scanning tunnelling microscope”, *Nature* **1990**, *344*, 524–526.
- [59] M. F. Crommie, C. P. Lutz, D. M. Eigler, “Confinement of Electrons to Quantum Corrals on a Metal Surface”, *Science* **1993**, *262*, 218–220.
- [60] E. J. Heller, M. F. Crommie, C. P. Lutz, D. M. Eigler, “Scattering and absorption of surface electron waves in quantum corrals”, *Nature* **1994**, *369*, 464–466.
- [61] H. C. Manoharan, C. P. Lutz, D. M. Eigler, “Quantum mirages formed by coherent projection of electronic structure”, *Nature* **2000**, *403*, 512–515.
- [62] R. Wiesendanger, H. J. Güntherodt, G. Güntherodt, R. J. Gambino, R. Ruf, “Observation of vacuum tunneling of spin-polarized electrons with the scanning tunneling microscope”, *Physical Review Letters* **1990**, *65*, 247–250.
- [63] R. Wiesendanger, M. Bode, A. Kubetzka, O. Pietzsch, M. Morgenstern, A. Wachowiak, J. Wiebe, “Fundamental studies of magnetism down to the atomic scale: present status and future perspectives of spin-polarized scanning tunneling microscopy”, *Journal of Magnetism and Magnetic Materials* **2004**, *272-276*, 2115–2120.



- [64] C. Chen, *Introduction to Scanning Tunneling Microscopy*, Oxford University Press, **1993**.
- [65] G. Binnig, C. F. Quate, C. Gerber, “Atomic Force Microscope”, *Physical Review Letters* **1986**, *56*, 930–933.
- [66] S. Lounis, “Theory of Scanning Tunneling Microscopy”, *Lecture Notes of the 46th IFF Spring School: Computing Solids-Models ab initio methods and supercomputing* **2014**.
- [67] J. Bardeen, “Tunnelling from a Many-Particle Point of View”, *Physical Review Letters* **1961**, *6*, 57–59.
- [68] J. Tersoff, D. R. Hamann, “Theory and Application for the Scanning Tunneling Microscope”, *Physical Review Letters* **1983**, *50*, 1998–2001.
- [69] J. Tersoff, D. R. Hamann, “Theory of the scanning tunneling microscope”, *Physical Review B* **1985**, *31*, 805–813.
- [70] C. J. Chen, “Tunneling matrix elements in three-dimensional space: The derivative rule and the sum rule”, *Physical Review B* **1990**, *42*, 8841–8857.
- [71] C. J. Chen, “Origin of atomic resolution on metal surfaces in scanning tunneling microscopy”, *Physical Review Letters* **1990**, *65*, 448–451.
- [72] M. J. Kittelmann, PhD thesis, **2013**.
- [73] J. L. Neff, PhD thesis, **2016**.
- [74] H. Söngen, R. Bechstein, A. Kühnle, “Quantitative atomic force microscopy”, *Journal of Physics: Condensed Matter* **2017**, *29*, 274001.
- [75] S. Aeschlimann, Bachelor thesis, **2014**.
- [76] M. Schunack, PhD thesis, **2002**.
- [77] J. V. Barth, “Molecular Architectonic on Metal Surfaces”, *Annual Review of Physical Chemistry* **2007**, *58*, 375–407.
- [78] L. Porte et al., “Self-organised growth of molecular arrays at surfaces”, *International Journal of Nanotechnology* **2012**, *9*, 325–354.
- [79] J. V. Barth, G. Costantini, K. Kern, “Engineering atomic and molecular nanostructures at surfaces”, *Nature* **2005**, *437*, 671–679.
- [80] F. Klappenberger, “Two-dimensional functional molecular nanoarchitectures - Complementary investigations with scanning tunneling microscopy and X-ray spectroscopy”, *Progress in Surface Science* **2014**, *89*, 1–55.
- [81] D. P. Goronzy, M. Ebrahimi, F. Rosei, Arramel, Y. Fang, S. De Feyter, S. L. Tait, C. Wang, P. H. Beton, A. T. S. Wee, P. S. Weiss, D. F. Perepichka, “Supramolecular Assemblies on Surfaces: Nanopatterning, Functionality, and Reactivity”, *ACS Nano* **2018**, *12*, 7445–7481.
- [82] Y. Zhao, J. Wang, “How To Obtain High-Quality and High-Stability Interfacial Organic Layer: Insights from the PTCDA Self-Assembly”, *The Journal of Physical Chemistry C* **2017**, *121*, 4488–4495.

- [83] Y. Li, H. Wang, Z. Wang, Y. Qiao, J. Ulstrup, H.-Y. Chen, G. Zhou, N. Tao, "Transition from stochastic events to deterministic ensemble average in electron transfer reactions revealed by single-molecule conductance measurement", *Proceedings of the National Academy of Sciences* **2019**, *116*, 3407–3412.
- [84] G. Czap, P. Wagner, J. Li, F. Xue, J. Yao, R. Wu, W. Ho, "Detection of Spin-Vibration States in Single Magnetic Molecules", *Physical Review Letters* **2019**, *123*, 106803.
- [85] G. Czap, P. J. Wagner, F. Xue, L. Gu, J. Li, J. Yao, R. Wu, W. Ho, "Probing and imaging spin interactions with a magnetic single-molecule sensor", *Science* **2019**, *364*, 670–673.
- [86] H. Liang, Y. He, Y. Ye, X. Xu, F. Cheng, W. Sun, X. Shao, Y. Wang, J. Li, K. Wu, "Two-dimensional molecular porous networks constructed by surface assembling", *Coordination Chemistry Reviews* **2009**, *253*, 2959–2979.
- [87] C. Copéret, M. Chabanas, R. Petroff Saint-Arroman, J.-M. Basset, "Homogeneous and Heterogeneous Catalysis: Bridging the Gap through Surface Organometallic Chemistry", *Angewandte Chemie International Edition* **2003**, *42*, 156–181.
- [88] Z.-T. Wang, Y.-G. Wang, R. Mu, Y. Yoon, A. Dahal, G. K. Schenter, V.-A. Glezakou, R. Rousseau, I. Lyubinetsky, Z. Dohnálek, "Probing equilibrium of molecular and deprotonated water on TiO<sub>2</sub>(110)", *Proceedings of the National Academy of Sciences* **2017**, *114*, 1801–1805.
- [89] D. Hötger, P. Abufager, C. Morchutt, P. Alexa, D. Grumelli, J. Dreiser, S. Stepanow, P. Gambardella, H. F. Busnengo, M. Etzkorn, R. Gutzler, K. Kern, "On-surface transmetalation of metalloporphyrins", *Nanoscale* **2018**, *10*, 21116–21122.
- [90] J. M. Gottfried, "Surface chemistry of porphyrins and phthalocyanines", *Surface Science Reports* **2015**, *70*, 259–379.
- [91] J. Liu, C. Wöll, "Surface-supported metal-organic framework thin films: fabrication methods, applications, and challenges", *Chemical Society Reviews* **2017**, *46*, 5730–5770.
- [92] J. Liu, W. Wang, D. Wang, J. Hu, W. Ding, R. D. Schaller, G. C. Schatz, T. W. Odom, "Spatially defined molecular emitters coupled to plasmonic nanoparticle arrays", *Proceedings of the National Academy of Sciences* **2019**, *116*, 5925–5930.
- [93] T. Classen, G. Fratesi, G. Costantini, S. Fabris, F. L. Stadler, C. Kim, S. de Gironcoli, S. Baroni, K. Kern, "Templated Growth of Metal-Organic Coordination Chains at Surfaces", *Angewandte Chemie International Edition* **2005**, *44*, 6142–6145.
- [94] O. M. Yaghi, M. O’Keeffe, N. W. Ockwig, H. K. Chae, M. Eddaoudi, J. Kim, "Reticular synthesis and the design of new materials", *Nature* **2003**, *423*, 705–714.
- [95] G. F. Swiegers, T. J. Malefetse, "New Self-Assembled Structural Motifs in Coordination Chemistry", *Chemical Reviews* **2000**, *100*, 3483–3538.
- [96] B. J. Holliday, C. A. Mirkin, "Strategies for the Construction of Supramolecular Compounds through Coordination Chemistry", *Angewandte Chemie International Edition* **2001**, *40*, 2022–2043.
- [97] A. Kumar, K. Banerjee, P. Liljeroth, "Molecular assembly on two-dimensional materials", *Nanotechnology* **2017**, *28*, 082001.

- [98] R. Hoffmann-Vogel, “Imaging prototypical aromatic molecules on insulating surfaces: a review”, *Reports on Progress in Physics* **2017**, *81*, 016501.
- [99] L. Nony, F. Bocquet, F. Para, F.; Chérioux, E. Duverger, F. Palmino, V. Luzet, C. Loppacher, “Dipole-driven self-organization of zwitterionic molecules on alkali halide surfaces”, *Beilstein J. Nanotechnol.* **2012**, *3*.
- [100] C. M. Hauke, R. Bechstein, M. Kittelmann, C. Storz, A. F. M. Kilbinger, P. Rahe, A. Kühnle, “Controlling Molecular Self-Assembly on an Insulating Surface by Rationally Designing an Efficient Anchor Functionality That Maintains Structural Flexibility”, *ACS Nano* **2013**, *7*, 5491–5498.
- [101] M. Kittelmann, M. Nimmrich, J. L. Neff, P. Rahe, W. Greń, X. Bouju, A. Gourdon, A. Kühnle, “Controlled Activation of Substrate Templating in Molecular Self-Assembly by Deprotonation”, *The Journal of Physical Chemistry C* **2013**, *117*, 23868–23874.
- [102] F. Bocquet, L. Nony, S. C. B. Mannsfeld, V. Oison, R. Pawlak, L. Porte, C. Loppacher, “Inhomogeneous Relaxation of a Molecular Layer on an Insulator due to Compressive Stress”, *Physical Review Letters* **2012**, *108*, 206103.
- [103] J. Gaberle, D. Z. Gao, A. L. Shluger, A. Amrous, F. Bocquet, L. Nony, F. Para, C. Loppacher, S. Lamare, F. Cherioux, “Morphology and Growth Mechanisms of Self-Assembled Films on Insulating Substrates: Role of Molecular Flexibility and Entropy”, *The Journal of Physical Chemistry C* **2017**, *121*, 4393–4403.
- [104] F. Para, F. Bocquet, L. Nony, C. Loppacher, M. Féron, F. Cherioux, D. Z. Gao, F. Federici Canova, M. B. Watkins, “Micrometre-long covalent organic fibres by photoinitiated chain-growth radical polymerization on an alkali-halide surface”, *Nature Chemistry* **2018**, *10*, 1112–1117.
- [105] J. Schütte, R. Bechstein, M. Rohlfing, M. Reichling, A. Kühnle, “Cooperative mechanism for anchoring highly polar molecules at an ionic surface”, *Physical Review B* **2009**, *80*, 205421.
- [106] J. Schütte, R. Bechstein, P. Rahe, M. Rohlfing, A. Kühnle, H. Langhals, “Imaging perylene derivatives on rutile TiO<sub>2</sub>(110) by noncontact atomic force microscopy”, *Physical Review B* **2009**, *79*, 045428.
- [107] F. M. Hossain, G. E. Murch, L. Sheppard, J. Nowotny, “Ab initio electronic structure calculation of oxygen vacancies in rutile titanium dioxide”, *Solid State Ionics* **2007**, *178*, 319–325.
- [108] S. Freund, A. Hinaut, N. Marinakis, E. C. Constable, E. Meyer, C. E. Housecroft, T. Glatzel, “Anchoring of a dye precursor on NiO(001) studied by non-contact atomic force microscopy”, *Beilstein J. Nanotechnol.* **2018**, *9*, 242–249.
- [109] F. Loske, P. Rahe, A. Kühnle, “Contrast inversion in non-contact atomic force microscopy imaging of C<sub>60</sub> molecules”, *Nanotechnology* **2009**, *20*, 264010.
- [110] M. P. Boneschanscher, J. van der Lit, Z. Sun, I. Swart, P. Liljeroth, D. Vanmaekelbergh, “Quantitative Atomic Resolution Force Imaging on Epitaxial Graphene with Reactive and Nonreactive AFM Probes”, *ACS Nano* **2012**, *6*, 10216–10221.
- [111] Personal communication with Lu Lyu, TU Kaiserslautern, **2019**.
- [112] L. Lafuente, J. A. Cuesta, “Phase behavior of hard-core lattice gases: A fundamental measure approach”, *The Journal of Chemical Physics* **2003**, *119*, 10832–10843.

- [113] H. Söngen, Y. Morais Jaques, L. Zivanovic, S. Seibert, R. Bechstein, P. Spijker, H. Onishi, A. S. Foster, A. Kühnle, “Hydration layers at the graphite-water interface: Attraction or confinement”, *Physical Review B* **2019**, *100*, 205410.
- [114] T. R. Albrecht, P. Grütter, D. Horne, D. Rugar, “Frequency modulation detection using high-Q cantilevers for enhanced force microscope sensitivity”, *Journal of Applied Physics* **1991**, *69*, 668–673.
- [115] P. Giannozzi et al., “QUANTUM ESPRESSO: a modular and open-source software project for quantum simulations of materials”, *Journal of Physics: Condensed Matter* **2009**, *21*, 395502.
- [116] D. Vanderbilt, “Soft self-consistent pseudopotentials in a generalized eigenvalue formalism”, *Physical Review B* **1990**, *41*, 7892–7895.
- [117] J. P. Perdew, K. Burke, M. Ernzerhof, “Generalized Gradient Approximation Made Simple”, *Physical Review Letters* **1996**, *77*, 3865–3868.
- [118] S. Grimme, “Semiempirical GGA-type density functional constructed with a long-range dispersion correction”, *Journal of Computational Chemistry* **2006**, *27*, 1787–1799.
- [119] A. L. Greer, “Too hot to melt”, *Nature* **2000**, *404*, 134–135.
- [120] P. M. Tedrow, D. M. Lee, “Liquid-Solid Phase Transition in He<sup>3</sup>-He<sup>4</sup> Mixtures”, *Physical Review* **1969**, *181*, 399–415.
- [121] Z. H. Yan, T. Klassen, C. Michaelsen, M. Oehring, R. Bormann, “Inverse melting in the Ti-Cr system”, *Physical Review B* **1993**, *47*, 8520–8527.
- [122] A. Blatter, M. von Allmen, “Reversible Amorphization in Laser-Quenched Titanium Alloys”, *Physical Review Letters* **1985**, *54*, 2103–2106.
- [123] R. J. Highmore, A. L. Greer, “Eutectics and the formation of amorphous alloys”, *Nature* **1989**, *339*, 363–365.
- [124] C. Michaelsen, W. Sinkler, T. Pfullmann, R. Bormann, “Inverse melting of metastable Nb-Cr solid solutions”, *Journal of Applied Physics* **1996**, *80*, 2156–2168.
- [125] W. Sinkler, C. Michaelsen, R. Bormann, D. Spilsbury, N. Cowlam, “Neutron-diffraction investigation of structural changes during inverse melting of Ti<sub>45</sub>Cr<sub>55</sub>S”, *Physical Review B* **1997**, *55*, 2874–2881.
- [126] H. Y. Bai, C. Michaelsen, R. Bormann, “Inverse melting in a system with positive heats of formation”, *Physical Review B* **1997**, *56*, R11361–R11364.
- [127] S. Rastogi, M. Newman, A. Keller, “Pressure-induced amorphization and disordering on cooling in a crystalline polymer”, *Nature* **1991**, *353*, 55–57.
- [128] S. Rastogi, G. W. H. Höhne, A. Keller, “Unusual Pressure-Induced Phase Behavior in Crystalline Poly(4-methylpentene-1): Calorimetric and Spectroscopic Results and Further Implications”, *Macromolecules* **1999**, *32*, 8897–8909.
- [129] v. C. S. J. Hooy-Corstjens, G. W. H. Hoehne, S. Rastogi, “Inverse melting in syndiotactic polystyrene”, *Macromolecules* **2005**, *38*, 1814–1821.
- [130] V. S. Papkov, M. I. Buzin, S. S. Bukalov, M. N. Il’ina, M. A. Shcherbina, S. N. Chvalun, “Kinetics of Inverse Melting/Crystallization of Poly(dialkoxyphosphazenes)”, *Crystal Growth & Design* **2019**, *19*, 3722–3731.

- [131] L. Merz, M. Parschau, L. Zoppi, K. Baldrige, J. Siegel, K.-H. Ernst, “Reversible Phase Transitions in a Buckybowl Monolayer”, *Angewandte Chemie International Edition* **2009**, *48*, 1966–1969.
- [132] A. Schöll, L. Kilian, Y. Zou, J. Ziroff, S. Hame, F. Reinert, E. Umbach, R. H. Fink, “Disordering of an Organic Overlayer on a Metal Surface Upon Cooling”, *Science* **2010**, *329*, 303.
- [133] J. Kollamana et al., “Control of Cooperativity through a Reversible Structural Phase Transition in MoMo-Methyl/Cu(111)”, *Advanced Functional Materials* **2018**, *28*, 1703544.
- [134] E. Rabani, D. R. Reichman, P. L. Geissler, L. E. Brus, “Drying-mediated self-assembly of nanoparticles”, *Nature* **2003**, *426*, 271–274.
- [135] D. P. Landau, K. Binder, *A Guide to Monte Carlo Simulations in Statistical Physics*, 4th edition, Cambridge University Press, Cambridge, **2014**.
- [136] S. Vinjanampathy, J. Anders, “Quantum thermodynamics”, *Contemporary Physics* **2016**, *57*, 545–579.
- [137] A. V. Kravtsov, S. Borgani, “Formation of Galaxy Clusters”, *Annual Review of Astronomy and Astrophysics* **2012**, *50*, 353–409.
- [138] E. C. Lima, A. Hosseini-Bandegharai, J. C. Moreno-Piraján, I. Anastopoulos, “A critical review of the estimation of the thermodynamic parameters on adsorption equilibria. Wrong use of equilibrium constant in the Van’t Hoof equation for calculation of thermodynamic parameters of adsorption”, *Journal of Molecular Liquids* **2019**, *273*, 425–434.
- [139] J. M. R. Parrondo, J. M. Horowitz, T. Sagawa, “Thermodynamics of information”, *Nature Physics* **2015**, *11*, 131–139.
- [140] T. N. Roach, P. Salamon, J. Nulton, B. Andresen, B. Felts, A. Haas, S. Calhoun, N. Robinett, F. Rohwer, “Application of Finite-Time and Control Thermodynamics to Biological Processes at Multiple Scales”, **2018**, *43*, 193.
- [141] I. Ford, *Statistical Physics: An Entropic Approach*, Wiley, **2013**.
- [142] F. Scheck, “Theoretische Physik 5: Statistische Theorie der Wärme” in, Springer-Verlag Berlin Heidelberg, **2008**.
- [143] H. Weingärtner, *Chemische Thermodynamik: Einführung für Chemiker und Chemieingenieure*, Vieweg+Teubner Verlag, **2003**.
- [144] A. Münster, *Classical thermodynamics*, Wiley-Interscience, **1970**.
- [145] L. Boltzmann, *Vorlesungen über Gastheorie*, Barth Leipzig, **1896**.
- [146] W. H. Cropper, “Rudolf Clausius and the road to entropy”, *American Journal of Physics* **1986**, *54*, 1068–1074.
- [147] M. W. Zemansky, R. H. Dittman, *Heat and Thermodynamics*, 7th edition, McGraw-Hill, **1997**.



## Declaration

Hiermit versichere ich, dass ich die vorliegende Arbeit selbst angefertigt und nur die genannten Quellen benutzt habe.

*Mainz, den 12. Mai 2020*

---

Simon Aeschlimann

## Colophon

This thesis was typeset with  $\text{\LaTeX}2_{\epsilon}$ . It uses the *Clean Thesis* style developed by Ricardo Langner. The design of the *Clean Thesis* style is inspired by user guide documents from Apple Inc.

Download the *Clean Thesis* style at <http://cleanthesis.der-ric.de/>.